Alma Mater Studiorum - Università di Bologna

Dottorato in Ingegneria Civile, Chimica, Ambientale e dei Materiali

Ciclo 34

SC 08/A1 - Idraulica, Idrologia, Costruzioni Idrauliche e Marittime

SSD ICAR/01 - Idraulica

Flow of Complex Fluids in Geological Fractures

Presentata da:

Alessandro Lenci

Superivisore:

Prof. Vittorio Di Federico

Coordinatore Dottorato:

Prof. Alessandro Tugnoli

Co-Supervisore:

Prof. Yves Méheust

Prof. Mario Putti

Contents

Abstract

In this study, the lubrication theory is used to model flow in geological fractures and analyse the compound effect of medium heterogeneity and complex fluid rheology. Such studies are warranted as the Newtonian rheology is adopted in most numerical models because of its ease of use, despite non-Newtonian fluids being ubiquitous in subsurface applications. Past studies on Newtonian and non-Newtonian flow in single rock fractures are summarized in Chapter 1. Chapter 2 presents analytical and semi-analytical conceptual models for flow of a shear-thinning fluid in rock fractures having a simplified geometry, providing a first insight on their permeability. in Chapter 3, a lubrication-based 2-D numerical model is first implemented to solve flow of an Ellis fluid in rough fractures; the finite-volumes model developed is more computationally effective than conducting full 3-D simulations, and introduces an acceptable approximation as long as the flow is laminar and the fracture walls relatively smooth. The compound effect of shear-thinning fluid nature and fracture heterogeneity promotes flow localization, which in turn affects the performance of industrial activities and remediation techniques. In Chapter 4, a Monte Carlo framework is adopted to produce multiple realizations of synthetic fractures, and analyze their ensemble statistics pertaining flow for a variety of real non-Newtonian fluids; the Newtonian case is used as a benchmark. In Chapter 5 and Chapter 6, a conceptual model of the hydro-mechanical aspects of backflow occurring in the last phase of hydraulic fracturing is proposed and experimentally validated, quantifying the effects of the relaxation induced by the flow.

1 | Introduction

In nature and in many industrial applications fluids have a peculiar rheology resulting from their complex microstructure. These fluids, called non-Newtonian, exhibit a relationship between shear stress and shear rate that does not respect Newton's law of viscosity, as their apparent viscosity is dependent on shear rate, and in some cases on shear rate history as well . Typical fluids used in reservoir engineering, drilling operations and hydraulic fracturing show such characteristics. Principal among those fluids are drilling muds, aqueous suspensions, and stimulating fluids such as slurries and foams. In the oil industry, drilling muds provide cooling and lubrication to the drill bit, and hydrostatic containment of formations. Mixtures of water (possibly emulsified with oil), weighting material and clays, as well as small quantities of salts and polymeric fluid additives are frequently used in mining engineering; such physical make-up inevitably leads to complex rheology (Frigaard, Howison & Sobey, 1994); in particular, fluid/solid mixtures often present an inelastic non-Newtonian behaviour because clay particles tend to cross-link chemically, forming bonds between particles . In nature, it was observed that even lava presents a yield stress because of its typical multiphase and chemically heterogeneous structure (Walker, 1967; Robson, 1967).

Reservoir engineering activities, e.g. oil and gas extraction, often take place in fractured media and involve the use of complex fluids under considerable pressure in order to obtain a desired objective, typically enlargement of existing apertures or the creation of new fractures (Detournay, 2016). It is important to notice that all these industrial applications may cause environmental contamination, which in turn produces additional motivation towards the study of flow of complex fluids through fractures: see Birdsell, Rajaram & Viswanathan (2015) for a comprehensive review of pollution issues connected to hydraulic fracturing.

The flow of rheologically complex fluids in naturally and/or artificially fractured media arises in all the aforementioned applications. A parallel with porous media flow of non-Newtonian fluids (see the review on single-phase flow by Sochi (2010)) suggests the existence of specific challenges and com-

pound effects arising from the interaction between the non-linearity of the
flow and the inherent multi scale heterogeneity characterizing the fractured
medium. To capture such interactions, it becomes even more important to
accurately describe the fluid on one hand, and the geometry of individual
fractures or fracture networks on the other. At the single fracture scale, the
simple parallel plate model was used to represent the geometry (Bear, 1972;
Snow, 1970), but experimental evidence showed that the fracture aperture
is characterized by a strong degree of variability (Gale, 1982); in particular,
the existence of rock joints (Engelder & Scholz, 1981) favours the creation
of tortuous flow paths across the fracture (Hakami & Larsson, 1996). Field
observations in crystalline rocks support these findings and confirm the pres-
ence of preferential flow paths (Neretnieks, 1985). Brittle fractures are often
generated by shearing, which can be taken into account by defining a shear
slip between the fracture walls; the slip was proven to control correlations be-
tween the topographies of facing fracture surfaces. Natural fractures present
a roughness that can be represented by a self-affine scale invariance. Sup-
ported by experimental evidence (Schmittbuhl, Gentier & Roux, 1993), the
fractal characterization of fracture walls has gained prominence (Berkowitz,
2002) and nowadays researchers mainly reproduce the spatial aperture varia-
tion starting from the generation of realistic topographies for fracture walls,
or equivalent techniques. There exist several algorithms that permit to gen-
erate fractures as fractional Brownian motion (fBm): the random midpoint
displacement method (RMD), introduced by Fournier, Fussell & Carpenter
(1982); the successive random addition, proposed by Voss (1988) to overcome
the shortcomings of the RMD; the Fourier filtering method, a very time-
efficient technique described in Saupe (1988). The surfaces composing real
fracture are then mated or correlated with each other at long wave lengths;
however they remain uncorrelated at smaller wavelengths, which is observed
in real geological fractures (Brown, 1995; Méheust & Schmittbuhl, 2003) due
to mechanical wear and chemical weathering.

The effects of this fracture aperture variability on single-phase Newtonian
flow has been analysed in detail since the 80s (Brown, 1989; Sahimi, 1993;
Tsang & Tsang, 1987; Durham & Bonner, 1995; Glover, Matsuki, Hikima &
Hayashi, 1998). The need to safeguard the environment from leaks occur-
ring in radioactive and/or toxic waste repositories has encouraged the study
of the influence of fracture roughness on the hydro-mechanical behaviour of
rock joints (Li, Jiang, Koyama, Jing & Tanabashi, 2008), and on transport
properties (Plouraboué, Kurowski, Boffa, Hulin & Roux, 2000). The tradi-
tional approach, dating back to the 80s, is to describe the fracture aperture
as a random field, characterized by an aperture density distribution function,
with or without spatial correlation. This approach was used to study lami-
nar flow in one-dimensional channels (Neuzil & Tracy, 1981; Tsang & Tsang,
1987; Tsang, Tsang, Neretnieks & Moreno, 1988), and extended to two di-
mensions (Tsang & Tsang, 1989; Moreno, Tsang, Tsang, Hale & Neretnieks,

1988). Later, the growing knowledge of fracture topography characteristics has allowed reproducing the complexity of real aperture variations, driving an evolution of models from the simpler series of parallel-plate channels to synthetically-generated 2-D aperture fields that resemble closely those of more closely real fractures (Brown, 1987; Méheust & Schmittbuhl, 2000, 2003). Newtonian flow has been studies extensively in such geometries. The aforementioned tortuous flow paths have been shown to exist due to long range correlations in the aperture field allowing large scale correlated channels of large apertures to connect the inlet and outlet (Méheust & Schmittbuhl, 2001).

Geophysicists and hydrogeologists have recently focused their attention on non-Newtonian fluids to investigate new techniques for soil remediation and enhanced oil recovery. Initially, non-Newtonian modelling was mostly investigated in relation to porous media flow (Barenblatt, Entov & Ryzhik, 1990), while fractured media received little attention. Then, the existing Newtonian background favoured the first attempts to investigate the flow of non-Newtonian fluids through a single fracture, adopting the traditional approaches but with different fluid constitutive laws. The appeal of analytical models led several authors to follow the traditional approach of proposing equivalent aperture formulations also for non-Newtonian fluids. An expression has been proposed by Di Federico (1998) for a power-law fluid, following the work of Silliman (1989), who derived an equivalent aperture for Newtonian fluid in a fracture whose aperture field is along the two in-plane directions.

Despite the geometric oversimplification of the parallel plate model, the latter represents an extremely easily-handled model which often leads to an explicit relationship between the flow rate and the imposed pressure gradients, even considering non-Newtonian fluids (e.g. power-law, Ellis, Prandlt-Eyring). A more sophisticated approach, either including aperture variability and maintaining an analytical or semi-analytical expression, is represented by models where aperture varies along an in-plane direction with flow occurring parallel or orthogonal to it. In a first proposal for Newtonian fluids from (Neuzil & Tracy, 1981), the aperture variability was characterized solely by a probability density function, without information about spatial correlations in the apertures, to simplify computation and show model features. These conceptual models constitute a valid tool to comprehend the role of heterogeneity and rheology, providing a rough estimate of order of magnitudes and trends of the possible quantities of interest.

Recently, we adopted this approach to analyse the effect on flow in fractures due to the different features of the constitutive law. In Lenci & Chiapponi (2020), a power-law fluid, the simplest shear-thinning model, is considered and results are validated with an ad hoc experimental apparatus and a 1-D finite difference scheme; subsequently, in Lenci & Federico (2019), we adopted the Prandlt-Eyring rheology, a smooth shear-thinning model that

exhibits a single low shear-rate plateau. Eventually, we analysed a bi-viscous model to estimate the influence of an yield-stress on flow (Lenci & Di Federico, 2020). However, shear-thinning fluids adopted in the subsurface present both a low and a high shear rate plateau which is typically well represented by the Carreau model. This model lacks an explicit expression of the flow rate as a function of the pressure gradient but can be approximated with a truncated power law (TPL). In (Felisa, Lenci, Lauriola, Longo & Di Federico, 2018) (see chapter 2), the TPL model is considered to characterize the two extreme flow scenarios: the cases of maximum and minimum conductance, where flow occurs orthogonal and parallel to aperture variability, respectively.

The study of non-Newtonian flows in realistic geological fractures is still in its infancy. In order to study the effects of fracture and fluid properties, Lavrov (013a) estimated the equivalent aperture by performing numerical simulations of power-law fluid flow in rough fractures using a lubrication-based approach. Morris, Chochua & Bogdan (2015) proposed a variable aperture flow simulator for Bingham, Herschel-Bulkley and power-law fluids, which iteratively solves a linearised formulation of the flow problem. Numerical studies showed that the lubrication theory constitutes a major approximation when studying the flow in rough fractures (Koyama, Neretnieks & Jing, 2008; Hron, Malek & Turek, 2000), a finding supported by the experiments of Yalamanchili, Sirivat & Rajagopal (1995). Secondary flow (recirculations) may occur between asperities, leading to a systematic error of $5 - 10\%$ in the flow estimation (Koyama et al., 2008). As long as the regime is that of Stokes flow (Reynolds number much smaller than 1) and the aperture field is sufficiently smooth (limited aperture gradients), the lubrication approximation can be adopted to simulate the flow in geological fractures. This approach can be preferred to full 3-D CFD simulation because it results in much more efficient and computationally less intense simulations, with also the possibility to generate much larger meshes. In Lenci, Méheust, Putti & Di Federico (2022a) (see chapter 3), a lubrication-base code is proposed to solve the flow of an Ellis fluid in realistic rough fracture geometries. This efficient and robust tool generates aperture fields with an FFT-based algorithm and is able to solve the flow even for small fluid indices (i.e., exponents defining the power law regime of the rheology) and large applied macroscopic pressure gradients, via an inexact Newton-Krylov method.

A Monte Carlo analysis must be performed to obtain generic characterization of phenomena involving stochastic processes, such as the generation of aperture fields for geological fractures. A stochastic analysis of non-Newtonian flow through rough fractures is presented in Lenci, Putti, Méheust & Di Federico (2022b) (see chapter 4), where we presented the probability density functions of the local flux magnitude and its components. Moreover, we analysed the autocorrelation functions to evaluate the presence of a flow field correlation length.

The characterization of the flow in the subsurface is of uttermost importance to comprehend natural phenomena, optimize industrial activities and minimize the anthropogenic impact on the environment. In unconventional reservoirs, where the solid matrix typically exhibits low porosity and low permeability, the flow occurs in fracture networks, where the hydraulic and the mechanical problem are typically coupled. The by-products of hydraulic fracturing for oil and gas extraction in unconventional reservoirs include fluid wastes that can be recovered for disposal and re-use. During the last phase of the hydraulic fracturing, the flow reverses and a relaxation processes takes place. The fracture closes as the pressure is gradually reduced as a result of the flowback to the extraction well. This flowback reduces wastewater threat on environment. Recently, interest for this topic arose in the scientific community, with authors proposing theoretical models (Dana, Zheng, Peng, Stone, Huppert & Ramon, 2018; Chiapponi, Ciriello, Longo & Di Federico, 2019). In Ciriello, Lenci, Longo & Di Federico (2021) (see Chapter 4) and Lenci, Chiapponi, Longo & Di Federico (2021) (see Chapter 5), a conceptual backflow model for Ellis and power-law fluids is proposed, respectively; the latter present a validation with laboratory experiments for both Newtonian and non-Newtonian fluids, higlighting the importance of rheology on relaxation-induced flow.

2 | Flow of truncated power-law fluid in fracture channels of variable aperture

2.1 Abstract

A conceptual model is presented for non-Newtonian fluid flow in a rough channel representing a single fracture. The fluid rheology is described via a truncated power-law (TPL) model approximating the Carreau constitutive equation, while the aperture variation along the channel is modeled via a stochastic distribution of assigned mean and variance; the lognormal and gamma distributions are considered, together with a deterministic variation of sinusoidal behavior. The flowrate in a fracture subject to an external pressure gradient is derived under the lubrication approximation for the two limiting cases of a pressure gradient which is i) perpendicular and ii) parallel to aperture variation; these parallel and serial arrangements (PA or SA) provide an upper and lower bound to the fracture conductance. Different combinations of the parameters describing the fluid rheology and the variability of the aperture field are considered for a sensitivity analysis. Results are also compared with those valid for a pure power-law (PL) fluid which provides a relevant benchmark. The channel flowrate shows a direct/inverse dependency upon aperture variability for PA/SA. The difference in flowrate between the PL and TPL models is positively affected by aperture variability and pressure gradient, negatively affected by flow behaviour index, while its sign is positive or negative depending on PA/SA. The influence of the specific pdf adopted for the aperture field is moderate, an increasing function of aperture variability and depends on the third and fourth moment of the distribution. The conductance for a deterministic aperture variation exhibits the same trends as a stochastic variation, with differences from the latter depending on aperture variability and flow arrangement.

2.2 Introduction

Hydraulic fracturing is largely used for optimal exploitation of oil, gas and thermal reservoirs. Non-Newtonian fluids are most frequently used in this type of operations (Linkov, 2014; Boronin, Osiptsov & Descroches, 2015); the challenge of modeling flow of these rheologically complex fluids is compounded by the possible interaction of multiple non-Newtonian fluids (Morris et al.,

7

2015). Complex fluids interact with pre-existing rock fractures also during drilling operations (Ozdemirtas, Kuru & Babadagli, 2010; Huang, Griffiths & Wong, 2011), enhanced oil recovery (Auradou, Boschan, Chertcoff, Gabbanelli, Hulin & Ippolito, 2008), and environmental remediation, and other natural phenomena such as magma intrusions, sand intrusions, and mud volcanoes (see Medina *et al.*, 2015 (Medina, Elkhoury, Morris, Prioul, Desroches & Detwiler, 2015) and references therein). Hence, it is important to model non-Newtonian flow in fractured media. A first step in this process is a detailed understanding of flow in a single fracture, as the space between fracture walls (termed fracture aperture) is typically spatially variable (Adler, Thovert & Mourzenko, 2002).

A large bibliography exists on Newtonian flow in single, variable aperture fractures. Neuzil and Tracy (Neuzil & Tracy, 1981) and Tsang (Tsang & Tsang, 1987) adopted a one-dimensional channel model, with channels described by an aperture density distribution and a spatial correlation length. Other authors (Tsang, 1984; Moreno et al., 1988; Tsang et al., 1988; Tsang & Tsang, 1989) extended the model to two-dimensional spatial variability of assigned correlation function, while other studies (Brown, 1987; Mourzenko, Thovert & Adler, 2001; Yan & Koplik, 2008; Talon, Auradou & Hansen, 2010) simulated the fracture surface roughness using fractal models of surface topography. Comprehensive reviews on flow in a single fracture were provided in (Zimmerman & Bodvarsson, 1996; Adler & Thovert, 1999; Berkowitz, 2002; Sahimi, 2011).

Ultimately, stochastic modeling of aperture variability at the single fracture scale leads to determination of the flowrate under a given pressure gradient as a function of the parameters describing the variability of the aperture field and the fluid rheological behaviour. From the flowrate, a flow, or 'hydraulic' aperture can then be derived (Silliman, 1989); a second equivalent aperture can be defined for transport, and usually differs from the 'hydraulic' aperture (Tsang, 1992).

The equivalent flow aperture for flow of non-Newtonian fluids of powerlaw nature in single, variable aperture fractures has been obtained with an heuristic approach by Di Federico for a stochastic variation of assigned distribution (Di Federico, 1998) and for deterministic variations (Di Federico, 1997, 2001). Detailed numerical modeling of flow of a power-law fluid in a variable aperture fracture was performed by Lavrov (Lavrov, 013b, 2014), whose work demonstrated that pronounced channelization effects are associated to a nonlinear fluid rheology; a further study by Lavrov (Lavrov, 013a) validated the simplified model of (Di Federico, 1997). The availability of an equivalent flow aperture as a function of the parameters describing the fluid rheology and the aperture variability is enticing, as it allows taking their interaction into account when modeling flow in fracture networks at a larger scale (Neuman, 2005). Bingham fluid flow in a variable aperture channel was studied analytically and numerically by Roustaei *et al.* (Roustaei, Chevalier, Talon & Frigaard, 2016), highlightning the progressive departure from the lubrication

approximation with increasing heterogeneity, the onset of fouling layers, and the existence of a limiting pressure gradient.

Another relevant issue in non-Newtonian fracture flow is the rheological nature of the fluid. The constitutive model routinely used for hydro-fracturing modeling is the simple, two-parameter power-law (Perkowska, Wrobel & Mishuris, 2016). Yet this model does not characterize real fluids at low and high shear rates, as it implies, for shear-thinning fluids, an apparent viscosity which becomes unbounded for zero shear rate and tends to zero for infinite shear rate. On the contrary, the four-parameter Carreau constitutive equation includes asymptotic values of the apparent viscosity at those limits. Lavrov (Lavrov, 2015) showed the Carreau rheological equation is well approximated by the truncated power-law model, and suggested to adopt the latter model for numerical modeling of flow in variable aperture fractures. To this end, he derived the expressions for flow of a truncated power-law fluid between parallel walls under a constant pressure gradient. A method to predict the flow of yield stress fluids described by a Herschel-Bulkley model and of shear thinning fluids without yield stress described by Carreau model through rough fractures was recently proposed and experimentally validated (Rodríguez de Castro & Radilla, 2016, 2017).

This paper extends the adoption of the truncated power-law model to fractures of variable aperture, in a stochastic or deterministic fashion, with the aim of understanding the joint influence of rheology and aperture spatial variability in a simplified geometrical setup where the variability is confined to one-direction, looking at the two limit cases where the aperture variability is either parallel or perpendicular to the flow direction. This assumption, which admittedly simplifies the real flow field, aims at providing reference benchmarks to be compared with more complex simulations. Section 2 summarizes results on flow of a truncated power-law fluid between parallel walls; Section 3 presents the general expressions of the flowrate for flow perpendicular and parallel to aperture variation; Section 4 deals with a stochastic aperture variation, and illustrates results stemming from the adoption of two different pdfs for the aperture distribution (lognormal and gamma). Section 6 applies the same simplified methodology to a deterministic aperture variation of sinusoidal behaviour. Then results obtained for the truncated model are compared with those earlier obtained for pure power-law fluids. Section 7 reports some conclusions.

2.3 Flow of truncated power-law fluid flow in a constant aperture fracture

Consider the flow of a shear-thinning non-Newtonian fluid in a fracture of length L, width W and constant aperture b; the coordinate system is shown in Figures 2.1(a)-(b); the fracture walls are at $z = +b/2$ and $z = -b/2$. Suppose a uniform, positive pressure gradient $p_x = [p(0) - p(L)]/L$ is applied in the

x direction. Assuming that $b \ll W$, the velocity components in the y and z directions are zero, and the only nonzero velocity component, v_x, is solely a function of z. The fluid is described by the rheological truncated power-law model, reading, in the simple shear situation described above, $\tau = \mu_a \dot{\gamma}$, with τ shear stress, and $\dot{\gamma}$ shear rate. The apparent viscosity μ_a is given by

$$
\begin{aligned}
\mu_a &= \mu_0 \quad \text{for} \quad \dot{\gamma} \leqslant \dot{\gamma}_1; \\
\mu_a &= m\dot{\gamma}^{n-1} \quad \text{for} \quad \dot{\gamma}_1 < \dot{\gamma} < \dot{\gamma}_2; \\
\mu_a &= \mu_\infty \quad \text{for} \quad \dot{\gamma} \geqslant \dot{\gamma}_2;
\end{aligned}
\tag{2.1}
$$

In Eq.(2.1), depicted in Figure 2.1c, μ_0 is the viscosity at zero shear rate, μ_∞ is the limiting viscosity for $\dot{\gamma} \to \infty$, n and m are the rheological and consistency index, respectively, $\dot{\gamma}_1 = (m/\mu_0)^{1/(1-n)}$ is the lower shear rate at which the high viscosity cutoff μ_0 is introduced, and $\dot{\gamma}_2 = (m/\mu_\infty)^{1/(1-n)}$ is the higher shear rate at which the low viscosity cutoff μ_∞ is introduced. The above four-parameter model is identical to the pure power-law model of parameters n and m in the intermediate shear stress range $\dot{\gamma}_1 < \dot{\gamma} < \dot{\gamma}_2$, and overcomes the limitation of having $\mu_a \to \infty$ for $\dot{\gamma} \to 0$ and $\mu_a \to 0$ for $\dot{\gamma} \to \infty$. Lavrov (Lavrov, 2015) showed that the truncated power-law model is practically indistinguishable, for practical purposes, from the Carreau model. He also derived the velocity field $v_x(z)$ and the flowrate per unit width $q_x = Q_x/W$ under a constant pressure gradient p_x. Depending on the aperture value, the flowrate can take three different expressions, namely

$$
q_{xI}(b) = \frac{b^3 p_x}{12\mu_0} \quad \text{for} \quad b < b_1 = \frac{2\mu_0 \dot{\gamma}_1}{p_x};
\tag{2.2a}
$$

$$
q_{xII}(b) = \frac{2(1-n)m^{3/(1-n)}}{3(2n+1)\mu_0^{(2n+1)/(1-n)}p_x^2} + \frac{nb^{(2n+1)/n}}{2n+1}\left(\frac{p_x}{2^{n+1}m}\right)^{1/n}
\tag{2.2b}
$$
$$
\text{for} \quad b_1 < b < b_2;
$$

$$
q_{xIII}(b) = \frac{b^3 p_x}{12\mu_\infty} - \frac{2(1-n)m^{3/(1-n)}}{3(2n+1)p_x^2}\left(\frac{1}{\mu_\infty^{(2n+1)/(1-n)}} - \frac{1}{\mu_0^{(2n+1)/(1-n)}}\right)
$$
$$
\text{for} \quad b > b_2 = \frac{2m\dot{\gamma}_2^n}{p_x};
\tag{2.2c}
$$

According to Eqs. (2.2a)-(2.2b)-(2.2c), three flow regimes (I = low shear rate regime, II = intermediate shear rate regime, and III = high shear rate regime) are possible within the fracture, depending on the relationship between its aperture b and the two threshold apertures b_1 and b_2.

2.4   Flow in a variable aperture channel

In single fracture flow modeling, the fracture aperture $b(x,y)$ is usually taken to vary as a two-dimensional, spatially homogeneous and correlated random
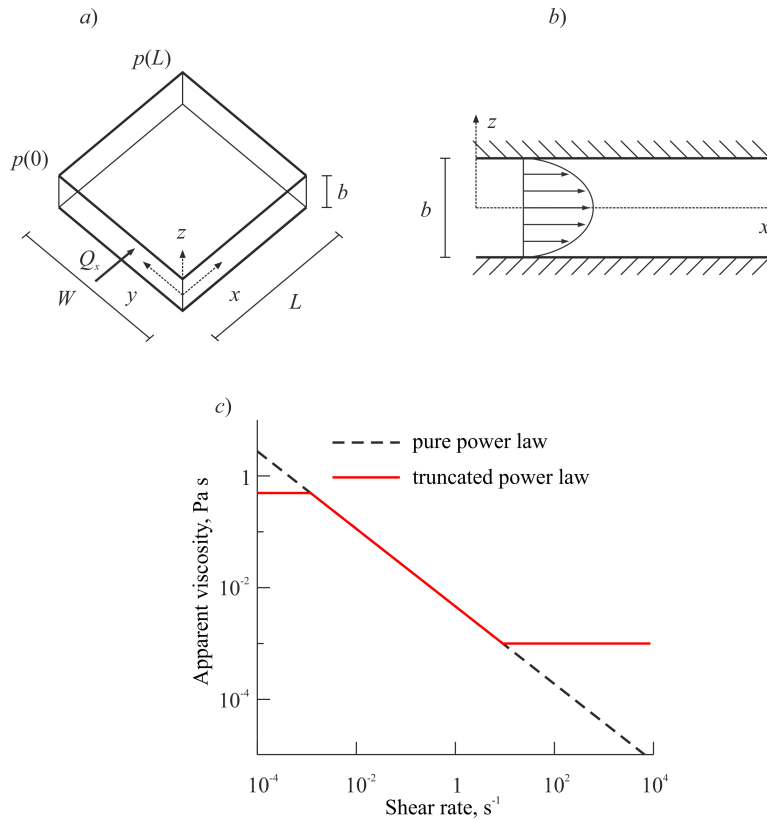
Figure 2.1: Configuration of the fractures and rheological approximation. *a)* Fracture sketch with applied pressure gradient; *b)* fracture profile in the x direction; c) apparent viscosity μ_a as a function of shear rate for the two models: truncated and pure power-law, respectively.

field, characterized by a probability density function $f(b)$ of given mean $\langle b \rangle$ and variance σ_b^2, and possibly spatial correlation described by an aperture autocovariance function of given integral scale I or integral scales I_x and I_y in the anisotropic case (alternatively a fractal distribution of given Hurst coefficient H and correlated at all scales is adopted).

If an anisotropic aperture field of anisotropy ratio $e = I_y/I_x$ is considered, the two limiting cases $e = 0$ and $e = \infty$ give rise to a purely one-dimensional aperture variation; consequently, flow under an external pressure gradient can be considered to take place either transverse (case 1, Figure 2.2a) or parallel to aperture variability (case 2, Figure 2.2b). This approach was used for Newtonian flow by Silliman (Silliman, 1989) to infer estimates of 2-D hydraulic and transport apertures, by Zimmerman (Zimmerman, Kumar & Bodvarsson, 1991) to determine the hydraulic aperture under deterministic sinusoidal variations, and by Di Federico (Di Federico, 1997, 1998) to derive estimates of hydraulic aperture for non-Newtonian power-law flow under both deterministic and stochastic aperture variations, respectively. Lavrov (Lavrov, 013a) validated the approach with two-dimensional numerical simulations conducted for a deterministic, sinusoidal aperture profile in both directions. Comparison of his results with the geometric average of flowrates for one-dimensional sinusoidal variations only along and only across the flow (cases 1 and 2 respectively but with a sinusoidal variation, see Section 5) showed a relative discrepancy in terms of equivalent aperture equal to less than 10% for $\delta < 0.4$, δ being the non-dimensional amplitude of the aperture variation. In the sequel, we consider first case 1, then case 2.

2.4.1   Flow parallel to constant aperture channels

Consider a fracture of dimensions L and W in the x and y direction, respectively, and aperture varying only in the y direction. Consider flow in the direction x parallel to constant aperture channels, i.e., transverse to aperture variation (case 1, Figure 2.2a); the applied pressure gradient is $p_x = [p(0) - p(L)]/L$; the volumetric flux is obtained through the following procedure. The fracture model is discretized into N neighboring parallel channels, each having equal width $\Delta y = W/N$, length L and constant aperture b_i. Depending on the local aperture value, in each channel the flow regime is either I, or II, or III, and the corresponding flowrate per unit width is given either by (2.2a), (2.2b), or (2.2c). The number of channels in each regime is N_I, N_{II}, N_{III}, respectively, and the total width of the channels in each regime is W_I, W_{II}, W_{III} with $N = N_I + N_{II} + N_{III}$ and $W = W_I + W_{II} + W_{III}$; the i-th channel in each regime j ($j = I, II, III$) has width $W_{ji} = W_j/N_j$. Assuming that the shear between neighboring channels and the drag against the connecting walls may be neglected, the total flowrate in the x direction is

$$Q_x = \sum_{i=1}^{N_I} q_I(b_i)W_{Ii} + \sum_{i=1}^{N_{II}} q_{II}(b_i)W_{IIi} + \sum_{i=1}^{N_{III}} q_{III}(b_i)W_{IIIi}. \qquad (2.3)$$
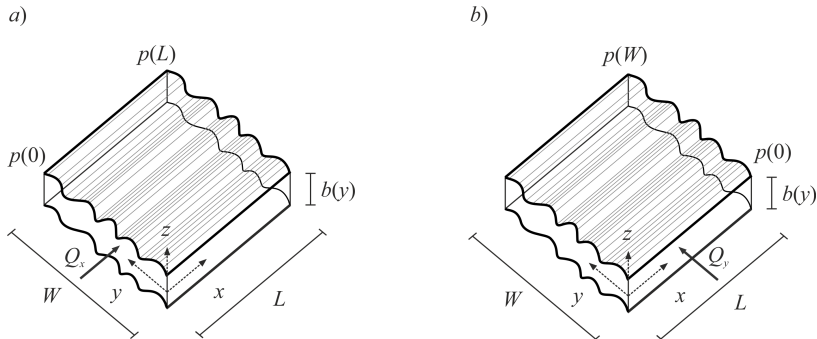
Figure 2.2: Configuration of the fracture. *a*) Case 1: flow perpendicular to aperture variation described by the aperture density function $f(b)$; *b*) case 2: flow parallel to aperture variation described by the aperture density function $f(b)$.

This assumption is acceptable for channels with a smooth variation of the aperture, i.e. with a smooth variation of the flowrate along the y direction, otherwise a linear momentum sharing between the neighbouring channels due to tangential stress in the $x-z$ plane is expected. Taking the limit as $N_j \to \infty$, the width of each channel tends to zero and the discrete aperture variation to a continuous one; then under ergodicity, and exploiting the previous relationships, (2.3) gives for the flowrate per unit width in the x direction the expression

$$q_x = \frac{Q_x}{W} =$$

$$= I_I \frac{p_x}{12\mu_0} + \left[P_{II} \frac{2(1-n)m^{3/(1-n)}}{3(2n+1)\mu_0^{(2n+1)/(1-n)}p_x^2} + \frac{n}{2n+1} I_{II} \left(\frac{p_x}{2^{n+1}m} \right)^{1/n} \right] +$$

$$+ \left[I_{III} \frac{p_x}{12\mu_\infty} - P_{III} \frac{2(1-n)m^{3/(1-n)}}{3(2n+1)p_x^2} \left(\frac{1}{\mu_\infty^{(2n+1)/(1-n)}} - \frac{1}{\mu_0^{(2n+1)/(1-n)}} \right) \right],$$

$$\tag{2.4}$$

where

$$I_I = \int_0^{b_1} b^3 f(b) \mathrm{d}b; \quad I_{II} = \int_{b_1}^{b_2} b^{(2n+1)/n} f(b) \mathrm{d}b; \quad I_{III} = \int_{b_2}^{\infty} b^3 f(b) \mathrm{d}b;$$

$$\tag{2.5}$$

$$P_{II} = F(b_2) - F(b_1); \quad P_{III} = 1 - F(b_2), \tag{2.6}$$

in which $f(b)$ and $F(b)$ are the pdf and cumulative distribution function of the aperture field, respectively.

2.4.2 Flow perpendicular to constant aperture channels

Consider now flow in the y direction perpendicular to constant aperture channels, i.e. parallel to aperture variation (case 2, Figure 2.2b); the fracture

length is W and the applied pressure gradient is $p_y = [p(0) - p(W)]/W$, while L is the fracture width perpendicular to gradient. Discretizing the fracture model into N cells of equal length $\Delta y = W/N$ in series, each cell has width L and constant aperture b_i. By virtue of mass conservation, volumetric flux Q_y through each cell is the same; depending on the local aperture value, in each channel the flow regime is either I, or II, or III, and the corresponding flowrate per unit width $q_y = Q_y/L$ is given, respectively, by the counterparts of Eqs. (2.2a), (2.2b), or (2.2c) upon substitution of the subscript x with the subscript y; this is so neglecting the pressure losses due to the succession of constrictions and enlargements. The number of cells in each regime is N_I, N_{II}, N_{III}, respectively, and the total length of the cells in each regime is W_I, W_{II}, W_{III}, with $N = N_I + N_{II} + N_{III}$ and $W = W_I + W_{II} + W_{III}$; the i-th cell in each regime j ($j = I, II, III$) has length $W_{ji} = W_j/N_j$. The total pressure loss along the fracture, Δp_y, can be expressed as the sum of pressure losses in each cell, Δp_{yi}, as $\Delta p_y = [p(0) - p(W)] = \sum_{i=1}^{N} \Delta p_{yi}$. This in turn yields the mean pressure gradient p_y as

$$p_y = \sum_{i=1}^{N_I} p_{yIi} \frac{W_{Ii}}{W} + \sum_{i=1}^{N_{II}} p_{yIIi} \frac{W_{IIi}}{W} + \sum_{i=1}^{N_{III}} p_{yIIIi} \frac{W_{IIIi}}{W}, \qquad (2.7)$$

where p_{yji} is the pressure gradient in the i-th cell under flow regime j ($j = I, II, III$). Taking the limit as $N_j \to \infty$, the length of each cell tends to zero and the discrete aperture variation to a continuous one; then under ergodicity, and exploiting the previous relationships, Equation (2.7) gives for the mean pressure gradient in the y direction the expression

$$p_y = \int_0^{b_1} p_{yI} f(b) \mathrm{d}b + \int_{b_1}^{b_2} p_{yII} f(b) \mathrm{d}b + \int_{b_2}^{\infty} p_{yIII} f(b) \mathrm{d}b, \qquad (2.8)$$

where the pressure gradient for each infinitesimal cell of constant aperture, i.e. $p_{yj} = p_{yj}(q_y, f(b), b_1, b_2, \mu_0, m, n, \mu_\infty)$, can be expressed as a function of the unknown flowrate per unit width $q_{yI} = q_{yII} = q_{yIII} = q_y$, and the parameters describing the fracture geometry and the fluid rheology, upon inverting Equations (2.2a), (2.2b), or (2.2c), written replacing the subscript x with the subscript y. This allows deriving, albeit numerically, the flowrate per unit width as a function of the applied pressure gradient and problem parameters as done in (2.4) for channels in parallel. An alternative formulation of the problem, using the same formalism adopted for flow parallel to constant aperture channel, is presented in Appendix A and leads to the same results.

2.5   Estimate of flowrate and discussion

Different distributions are adopted for the aperture field, consistently with earlier work on flow and transport in variable aperture fractures (Moreno et al., 1988; Tsang et al., 1988). In the following, i) lognormal, and ii) gamma

distribution are considered, the latter covering for values of the parameter $d > 3 - 4$ also the normal case.

2.5.1 Lognormal distribution

Lognormal distributions for the aperture field were adopted by (Moreno et al., 1988) and (Tsang et al., 1988). Its probability distribution function is given by

$$f(b) = \frac{1}{b\sigma\sqrt{2\pi}} \exp\left[-\frac{(\ln b - \ln b_g)^2}{2\sigma^2}\right], \qquad (2.9)$$

where $b_g = \langle b \rangle \exp(-\sigma^2/2)$ is the geometric mean, $\langle b \rangle$ the arithmetic mean, and σ^2 the variance of $\ln b$. Utilizing Eqs. (2.4)-(2.5) with Equation (2.6) gives for the factors $I_j (j = I, II, III)$ and $P_j (j = II, III)$ the following expressions:

$$I_I = \frac{\langle b \rangle^3}{2} \exp(3\sigma^2) \left[1 + \mathrm{erf}\left(\frac{1}{\sqrt{2}\sigma}\left(\ln\frac{b_1}{\langle b \rangle} - \frac{5\sigma^2}{2}\right)\right)\right];$$

$$I_{II} = \frac{\langle b \rangle^{(2n+1)/n}}{2} \exp\left(\frac{(2n+1)(n+1)}{2n^2}\sigma^2\right) \times$$

$$\times \left[\mathrm{erf}\left(\frac{1}{\sqrt{2}\sigma}\left(\ln\frac{b_2}{\langle b \rangle} - \frac{(3n+2)\sigma^2}{2n}\right)\right) - \mathrm{erf}\left(\frac{1}{\sqrt{2}\sigma}\left(\ln\frac{b_1}{\langle b \rangle} - \frac{(3n+2)\sigma^2}{2n}\right)\right)\right];$$

$$I_{III} = \frac{\langle b \rangle^3}{2} \exp(3\sigma^2)\left[1 - \mathrm{erf}\left(\frac{1}{\sqrt{2}\sigma}\left(\ln\frac{b_2}{\langle b \rangle} - \frac{5\sigma^2}{2}\right)\right)\right],$$

$$(2.10)$$

$$P_{II} = \frac{1}{2}\left[\mathrm{erf}\left(\frac{1}{\sqrt{2}\sigma}\left(\ln\frac{b_2}{\langle b \rangle} + \frac{\sigma^2}{2}\right)\right) - \mathrm{erf}\left(\frac{1}{\sqrt{2}\sigma}\left(\ln\frac{b_1}{\langle b \rangle} + \frac{\sigma^2}{2}\right)\right)\right];$$

$$P_{III} = \frac{1}{2}\left[1 - \mathrm{erf}\left(\frac{1}{\sqrt{2}\sigma}\left(\ln\frac{b_2}{\langle b \rangle} + \frac{\sigma^2}{2}\right)\right)\right],$$

$$(2.11)$$

where $\mathrm{erf}(\ldots)$ is the error function.

The Eqs. (2.4-2.8) of the flow rate are compared with that of a pure power-law fluid (q_{pl}), derived by (Di Federico, 1998), of parameters m and n i.e. for case 1

$$q_{x,pl} = \frac{n}{2n+1}\left(\frac{p_x}{2^{n+1}m}\right)^{1/n} \langle b \rangle^{(2n+1)/n} \exp\left(\frac{(2n+1)(n+1)\sigma^2}{2n^2}\right), \qquad (2.12)$$

and for case 2

$$q_{y,pl} = \frac{n}{2n+1}\left(\frac{p_y}{2^{n+1}m}\right)^{1/n} \langle b \rangle^{(2n+1)/n} \exp\left(-\frac{(2n+1)(n+1)\sigma^2}{n}\right). \qquad (2.13)$$

In Figure 2.3, flowrate and apparent viscosity versus the pressure gradient are depicted, for lognormal aperture distribution and flow perpendicular to
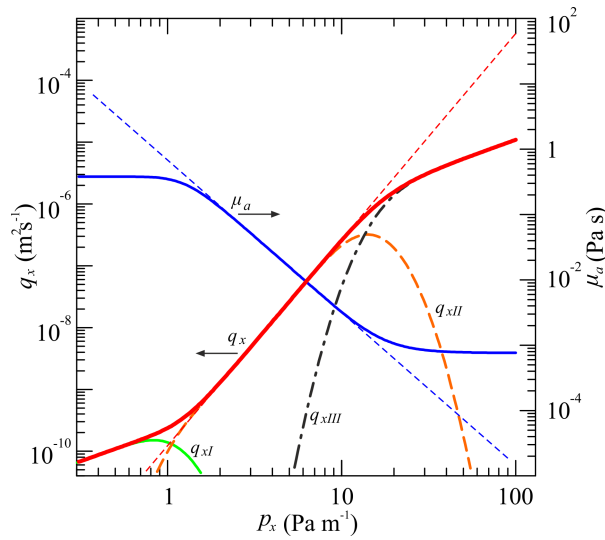
Figure 2.3: Flowrate and apparent viscosity for case 1 (flow perpendicular to aperture variation) and lognormal aperture distribution. The thick red continuous curve refers to the flowrate (left axis), with the three contributions: the low-shear rate regime q_{xI} (continuous green curve), the mid-shear rate regime q_{xII} (dashed orange curve), the high-shear rate regime q_{xIII} (dashdot black curve). The blue continuous curve refers to the apparent viscosity (right axis) and the dashed lines refer to the power-law fluid. The parameters are $n = 0.3$, $\sigma = 0.3$, $\langle b \rangle = 0.001$ m, $\mu_0 = 0.5$ Pa s, $\mu_\infty = 0.001$ Pa s, $m = 0.005$ Pa s^n.

aperture variation (case 1). The contribution of each single flow regime is also represented, in order to quantify their influence on the total flowrate. The presence of three possible flow regime, i.e. (i) low-shear-rate, (II) mid-shear-rate and (III) high-shear-rate allows us to understand why for a certain value of pressure gradient the two models sensibly differ. Clearly, $q_x \to q_{x,pl}$ for $\mu_0 \to \infty$ and $\mu_\infty \to 0$. A similar behavior occurs for different aperture distibutions and direction of flowrate (case 2).

The different trends between q_x and $q_{x,pl}$ are showed in Figures 2.4a - 2.4f, for lognormal distribution and case 1, with $n = 0.3, 0.5, 0.6$, $\mu_0 = 0.5$ Pa s, $\mu_\infty = 0.001$ Pa s, and $m = 0.005$ Pa s^n. Figures 2.4a, 2.4b, and 2.4c depict q_x and $q_{x,pl}$ versus p_x for fixed $\sigma = 0.3$; Figures 2.4d, 2.4e, 2.4f do so versus σ for fixed $p_x = 50$ Pa m^{-1}. It is seen that the flowrate for the truncated model is always decidedly smaller than that associated with the pure power-law, except at very low gradient pressure, where the opposite is true. The difference between the two increases as the external pressure gradient and aperture variability become larger or sufficiently small. Increasing the rheological parameter n, the difference between the truncated power law and pure power law model reduces.

In Figure 2.4a, the truncated power law model, compared with the pure power law model for a fluid with $n = 0.3$, exhibits all flow regimes. Here, it is possible to observe a very small low-shear-rate regime for lower values of pressure gradient, a mid-shear-rate where the two models perfectly match, and a high-shear-rate regime with a lower slope than the pure power law model. Figures 2.4b and 2.4c depict the same behavior for different fluids, respectively with $n = 0.5, 0.6$. In these configurations, the low-shear-rate regime is not present, while the high-shear-rate regime is reached for higher values of pressure gradient and the difference between the models is less marked.

Figures 2.4d, 2.4e, and 2.4f show how aperture variability σ influences the flow rate for a given pressure gradient p_x and different fluids. For both models, the flowrate increases with σ, as the parallel arrangement emphasizes the importance of large-aperture channels asssociated with a larger variability; the truncated model has decidedly smaller flow rates than the pure power-law. The difference between the two models decreases as n increases, until for $n = 0.6$ the difference is very small, and the two models provide identical results in a large range of aperture variability.

Figure 2.5 shows instead the variation of flowrate with respect to pressure gradient, for case 2 (serial arrangement) and both the truncated and pure power-law models. Figure 2.5a highlights the behavior of flowrate versus pressure gradient, for $n = 0.3, 0.5, 0.6$, and fixed $\sigma = 0.5$. Here, a monotonic increasing behavior occurs, with a perfect match between truncated and pure power-law model for low values of pressure gradient. For higher values of the gradient, the truncated model presents a lower slope with respect to the pure power law, but this difference is less marked as n increases; in particular, the truncated model assumes almost the same values, irrespective of the type of fluid. For high gradient values, the truncated model has a lower flowrate than

the pure power-law, like in case 1. Overall, the difference between the two models strongly depends on the type of fluid, as noted for case 1.

Figure 2.5b depicts the influence of aperture variability for $\sigma = 0.1$ to 0.5 and fixed $n = 0.3$. For lower values of pressure gradient, the truncated and pure power-law model perfectly match, in particular for small values of aperture variability. For higher values of pressure gradient, the slope for the truncated model is still lower than the pure power-law, as in case 1. For both truncated and pure power-law, the flowrate decreases with increasing aperture variability as the serial arrangement emphasizes the importance of small apertures.

2.5.2   Gamma distribution

A gamma distribution was adopted by Moreno *et al.* (Moreno et al., 1988) to reproduce the migration of contaminated water in fractured rock in the context of a capillary tube model, and by Tsang *et al.* (Tsang et al., 1988) for one-dimensional channels. Its probability distribution function is given by

$$f(b) = \frac{1}{\Gamma(d)} \frac{b^{d-1}}{b_g^d} \exp\left(-\frac{b}{b_g}\right), \tag{2.14}$$

with the two parameters b_g (geometric mean) and d. For larger values of d, the gamma distribution tends to the normal one. The arithmetic mean and the variance of b are given by $\langle b \rangle = b_g d$; $\sigma_b^2 = b_g^2 d = \langle b \rangle^2 / d$. Utilizing Eqs. (2.4)-(2.5) with Equation(2.6) gives for the factors P_{II}, P_{III} and I_j $(j = I, II, III)$ the following expressions:

$$I_I = \frac{\langle b \rangle^3}{\Gamma(d) d^3} \gamma\left(d + 3, \frac{db_1}{\langle b \rangle}\right);$$

$$I_{II} = \frac{\langle b \rangle^{(2n+1)/n}}{\Gamma(d) d^{(2n+1)/n}} \left[\Gamma\left(d + \frac{2n+1}{n}, \frac{db_1}{\langle b \rangle}\right) - \Gamma\left(d + \frac{2n+1}{n}, \frac{db_2}{\langle b \rangle}\right)\right]; \quad (2.15)$$

$$I_{III} = \frac{\langle b \rangle^3}{\Gamma(d) d^3} \Gamma\left(d + 3, \frac{db_2}{\langle b \rangle}\right),$$

$$P_{II} = \frac{1}{\Gamma(d)} \left[\Gamma\left(d, \frac{db_1}{\langle b \rangle}\right) - \Gamma\left(d, \frac{db_2}{\langle b \rangle}\right)\right];$$

$$P_{III} = \frac{1}{\Gamma(d)} \Gamma\left(d, \frac{db_2}{\langle b \rangle}\right), \tag{2.16}$$

where $\Gamma(z) = \int_0^\infty e^{-t} t^{z-1} \mathrm{d}t$ is the gamma function, $\gamma(\alpha, x) = \int_0^x e^{-t} t^{\alpha-1} \mathrm{d}t = \Gamma(x) - \Gamma(\alpha, x)$ the lower incomplete gamma function, and $\Gamma(\alpha, x) = \int_x^\infty e^{-t} t^{\alpha-1} \mathrm{d}t$ the upper incomplete gamma function. The expression of the flowrate given by Equation (2.4) with Eqs. (2.12) and (2.13) is compared with that of a pure power-law (q_{pl}) fluid of parameters m and n (Di Federico, 1998), i.e. for case
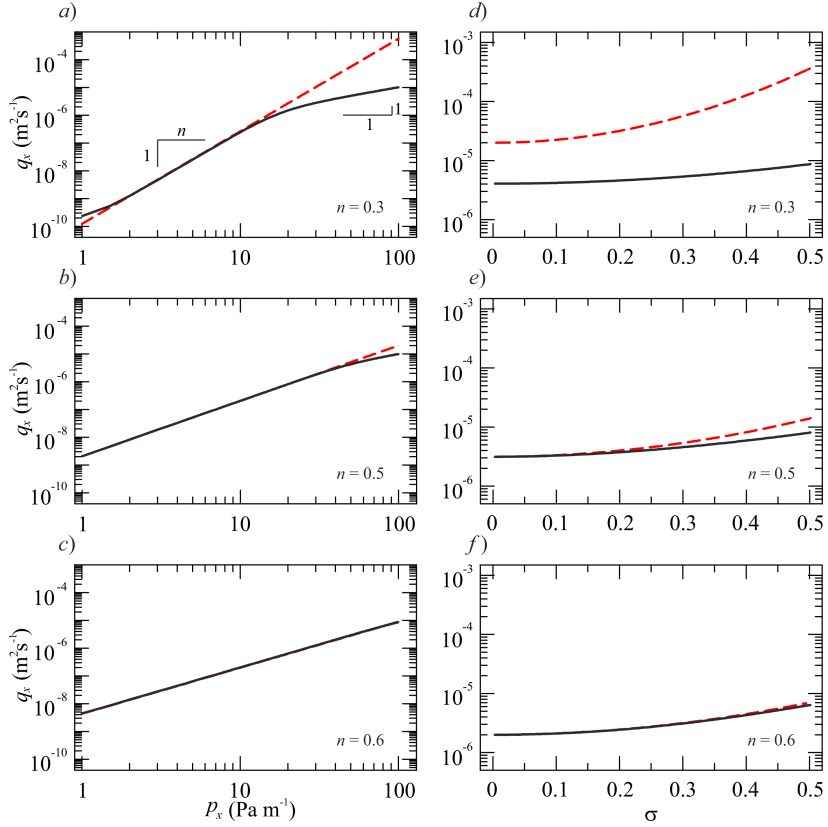
Figure 2.4: Flowrate for case 1 (flow perpendicular to aperture variation) and lognormal aperture distribution. *a-b-c*) Flowrate vs pressure gradient for $n = 0.3, 0.5, 0.6$, $\sigma = 0.3$; *d-e-f*) flowrate vs σ for $n = 0.3, 0.5, 0.6$, $p_x = 50\ \mathrm{Pa\,m^{-1}}$. The other parameters are $\langle b \rangle = 0.001$ m, $\mu_0 = 0.5\ \mathrm{Pa\,s}$, $\mu_\infty = 0.001\ \mathrm{Pa\,s}$, $m = 0.005\ \mathrm{Pa\,s^n}$. The dashed lines refer to the power-law relationships, the continuous lines refer to the truncated power-law relationship.
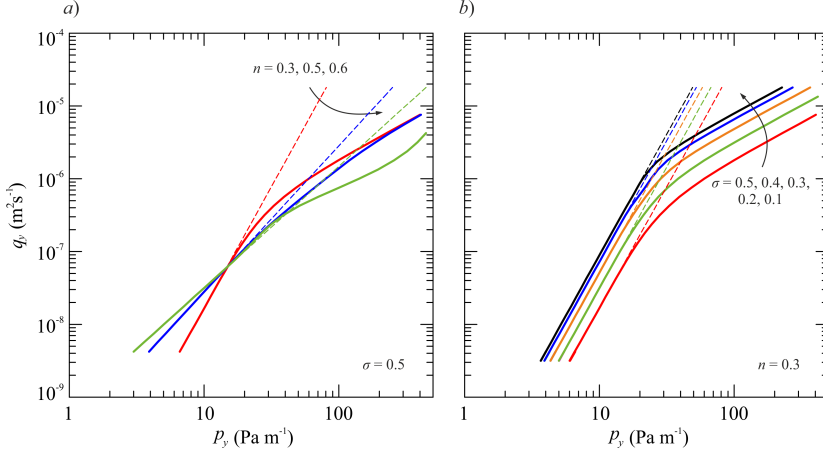
Figure 2.5: Flowrate for case 2 (flow parallel to aperture variation), lognormal distribution. *a)* Flowrate vs pressure gradient for $n = 0.3, 0.5, 0.6$, $\sigma = 0.5$; *b)* flowrate vs pressure gradient for $\sigma = 0.1(0.1)0.5$, $n = 0.3$. The other parameters are $\langle b \rangle = 0.001$ m, $\mu_0 = 0.5$ Pa s, $\mu_\infty = 0.001$ Pa s, $m = 0.005$ Pa s^n. The dashed lines refer to the power-law relationships, the continuous lines refer to the truncated power-law relationship.

1:

$$q_{x,pl} = \frac{n}{2n+1} \left(\frac{p_x}{2^{n+1}m} \right)^{1/n} \left(\frac{\langle b \rangle}{d} \right)^{(2n+1)/n} \frac{\Gamma\left(d + \dfrac{2n+1}{n} \right)}{\Gamma(d)}, \qquad (2.17)$$

while for case 2

$$q_{y,pl} = \frac{n}{2n+1} \left(\frac{p_y}{2^{n+1}m} \right)^{1/n} \left(\frac{\langle b \rangle}{d} \right)^{(2n+1)/n} \left[\frac{\Gamma(d)}{\Gamma(d-2n-1)} \right]^{1/n}. \qquad (2.18)$$

The latter expression is valid only for $d > 2n + 1$. Figures 2.6 and 2.7 depict the comparison between the truncated and pure power-law models, drawn for both lognormal and gamma distributions, for case 1 and case 2, respectively. Here, the two distributions are characterized by the same first two moments. In particular, the parameter d of the gamma distribution is derived by the variance of $\ln b$, σ, previously converted in σ_b, i.e. (Tsang et al., 1988)

$$\sigma_b^2 = \langle b \rangle^2 [\exp(\ln 10\sigma)^2 - 1]. \qquad (2.19)$$

The two distributions differ only by the third and fourth moment. For $\sigma = 0.1$, the skewness is 0.47 for gamma distribution and 0.30 for lognormal, while kurtosis is 3.32 for gamma and 3.16 for lognormal distribution; for $\sigma = 0.2$, the skewness is 0.97 for gamma distribution and 0.61 for lognormal, while kurtosis is 4.42 for gamma and 3.68 for lognormal distribution.
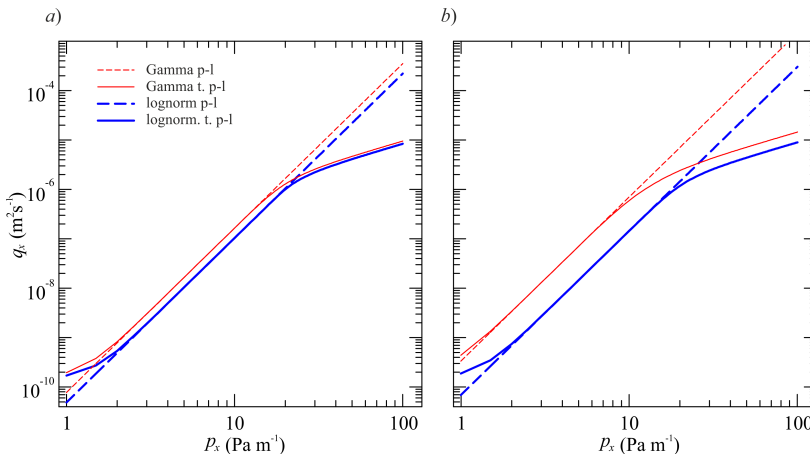
Figure 2.6: Flowrate for case 1 (flow perpendicular to aperture variation), comparison between lognormal and gamma distributions. *a*) Flowrate vs pressure gradient for $\sigma = 0.1$ (lognormal) and $d = 18.37$ (gamma); *b*) flowrate vs pressure gradient for $\sigma = 0.2$ and $d = 4.23$. The other parameters are $n = 0.3$, $\langle b \rangle = 0.001$ m, $\mu_0 = 0.5$ Pa s, $\mu_\infty = 0.001$ Pa s, $m = 0.005$ Pa s^n. The dashed lines refer to the power-law relationships, the continuous lines refer to the truncated power-law relationship.

Figure 2.6, drawn for the parallel arrangement, shows that the models with the two different distributions and with TPL have a similar trend. The slope of the $q_x - p_x$ relationship for the truncated model for both distributions is lower compared with the pure power-law, for high and low values of pressure gradient. The lognormal distribution consistently shows a lower flowrate than the gamma distribution for the same pressure gradient and aperture variability, due to the differences in the distribution shape; the difference in flowrate between distributions increases with increasing aperture variability.

Figure 2.7, drawn for the serial arrangement, shows that for the same values of pressure gradient, the pure power law model for lognormal distribution has a higher flowrate than the gamma distribution, both for $\sigma = 0.1$ and $\sigma = 0.2$. For intermediate pressure gradient, all distributions show a good agreement of the flowrate for the truncated power law and for the pure power law model. Again, the differences between the power law and the truncated power law models become evident whenever the flowrate is in the regime controlled by the high and the low shear rate plateaus.
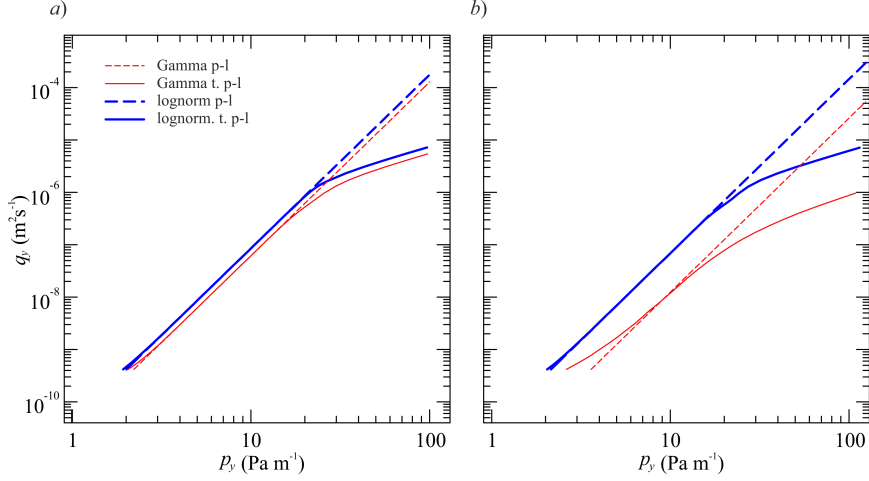
Figure 2.7: Flowrate for case 2 (flow parallel to aperture variation), comparison between lognormal and gamma distributions. For caption see Figure 2.6.

2.6 Deterministic aperture variation

We consider a constant aperture with a sinusoidal perturbation as "rough-walled" fracture (Zimmerman et al., 1991; Di Federico, 1997), as depicted in Figure 2.8:

$$b(y) = \langle b \rangle [1 + \delta \sin(2\pi y/\lambda)] \tag{2.20}$$

where $\langle b \rangle$ is the mean aperture, δ is the magnitude of the "roughness", and λ is the wavelength of the aperture oscillations. Upon comparing the limiting aperture values b_1, b_2 for a given pressure gradient separating the different flow regimes for the truncated power-law model, and the minimum, mean and maximum aperture values $b_{min} = \langle b \rangle(1 - \delta)$, $\langle b \rangle$, and $b_{max} = \langle b \rangle(1 + \delta)$, it is seen that ten possible combinations arise, as reported in Table 2.1. The standard deviation of the aperture distribution σ_b is related to the parameter δ by

$$\sigma_b = \frac{\delta \langle b \rangle}{\sqrt{2}}. \tag{2.21}$$

In the following we compare the behavior, in terms of flowrate for a given value of the pressure gradient, of a deterministic and stochastic aperture variation, both for flow parallel to constant aperture channels (case 1), and flow perpendicular to constant aperture channels (case 2). The lognormal distribution is adopted for the stochastic variation, hence the quantities I_I, I_{II}, and I_{III} and P_{II}, and P_{III} are those reported in Eqs. (2.10) and (2.11). The same quantities, evaluated for the deterministic variation, are listed in Tables 2.2 and 2.3 of Appendix B for all the possible combinations presented in Table 2.1. In Figure 2.9a for case 1, a fluid with rheology index $n = 0.5$ is considered,
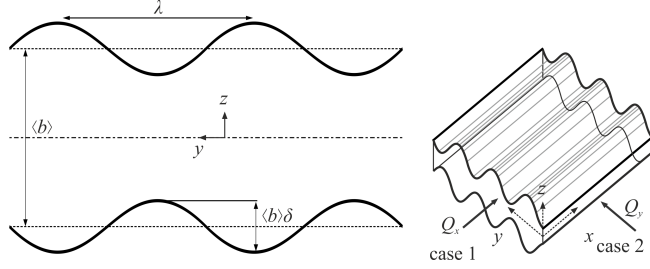
Figure 2.8: Rough-walled fracture profile adopted for the deterministic formulation.
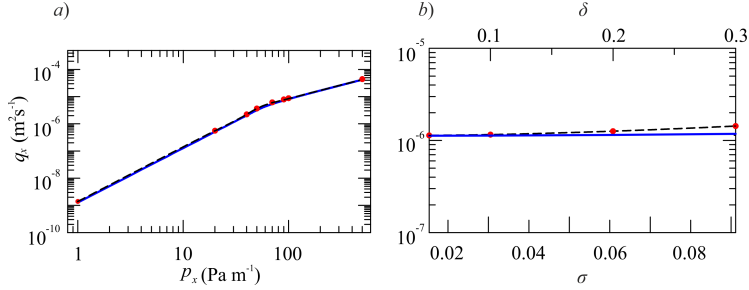
Figure 2.9: Comparison of deterministic (red dots) and stochastic approach (blue line), for case 1 (flow perpendicular to aperture variation). *a)* Flowrate versus pressure gradient, for $\delta = 0.2$, and $n = 0.5$; *b)* flowrate versus standard deviation for $p_x = 30$ Pa m^{-1}, and $n = 0.5$. The other parameters are $\langle b \rangle = 0.001$ m, $\mu_0 = 0.5$ Pa s, $\mu_\infty = 0.001$ Pa s, $m = 0.005$ Pa s^n.

the roughness is taken to be $\delta = 0.2$, and the same variance is considered for both types of variation. The flowrate increases with the pressure gradient, and the agreement between deterministic and stochastic model is good. The comparison between the two models, for case 1, is also shown as a function of σ in Figure 2.9b, for $n = 0.5$, and $p_x = 30$ Pa m^{-1}. Here, the deterministic model tends to predict higher values of the flowrate q_x than the stochastic approach for increasing values of log aperture standard deviation. Figure 2.10a depicts the comparison between deterministic and stochastic aperture variation for case 2, with $n = 0.3$, and $\delta = 0.2$. It is seen that the stochastic variation tends to overestimate the flowrate for increasing pressure gradient, while for lower values of p_x, the agreement between the two models is quite good. This trend in confirmed by Figure 2.10b, drawn for $p_x = 0.5$ Pa m^{-1}, where the deterministic model returns flowrates increasingly lower than the stochastic as σ increases.
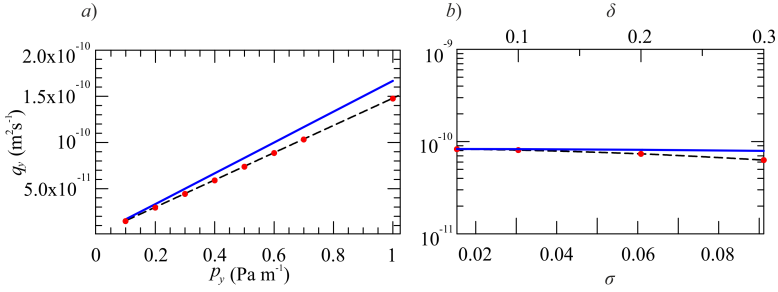
Figure 2.10: Comparison of deterministic (red dots) and stochastic approach (blue line), for case 2 (flow parallel to aperture variation). *a)* Flowrate versus pressure gradient, for $\delta = 0.2$ and $n = 0.3$; *b)* flowrate versus standard deviation for $p_x = 0.5 \, \mathrm{Pa \, m^{-1}}$, and $n = 0.3$. The other parameters are $\langle b \rangle = 0.001 \, \mathrm{m}$, $\mu_0 = 0.5 \, \mathrm{Pa \, s}$, $\mu_\infty = 0.001 \, \mathrm{Pa \, s}$, $m = 0.005 \, \mathrm{Pa \, s^n}$.

Combinations

	Combinations	
1	$b_1 < b_2 < b_{min} < b_{max}$	
2	$b_1 < b_{min} < b_2 < b_{max}$,	$\langle b \rangle > b_2$
3	$b_1 < b_{min} < b_2 < b_{max}$,	$\langle b \rangle < b_2$
4	$b_1 < b_{min} < b_{max} < b_2$	
5	$b_{min} < b_1 < b_{max} < b_2$,	$\langle b \rangle < b_1$
6	$b_{min} < b_1 < b_{max} < b_2$,	$\langle b \rangle > b_1$
7	$b_{min} < b_{max} < b_1 < b_2$	
8	$b_{min} < b_1 < b_2 < b_{max}$,	$\langle b \rangle < b_1 < b_2$
9	$b_{min} < b_1 < b_2 < b_{max}$,	$b_1 < \langle b \rangle < b_2$
10	$b_{min} < b_1 < b_2 < b_{max}$,	$b_1 < b_2 < \langle b \rangle$

Table 2.1: Combinations of deterministic aperture variations.

2.7 Discussion and conclusions

We derived analytical models for flow of non-Newtonian fluids in uneven channels simulating natural or artificial rock fractures. Our approach couples a four-parameter rheological model, the truncated power-law (TPL), with a stochastic variation of the aperture field along a 1-D channel according to a generic probability distribution function (pdf); three different cases are considered including a deterministic variation of sinusoidal shape.

Starting from the solution valid for TPL parallel plate flow, which incorporates three possible flow regimes, the conductance of the channel is determined as a function of rheological fluid parameters, geometry, and the pdf of the aperture distribution. Two limit cases providing an upper and lower bound to the flowrate under an assigned pressure gradient are considered, the parallel (PA) and serial (SA) arrangements, corresponding respectively to an external pressure gradient perpendicular or parallel to aperture variation.

Results for the simpler, two-parameter power-law (PL) rheological model provide the benchmark to discern the impact of the adoption of a more realistic rheological model on the conductance. On one hand, the parallel arrangement emphasizes the importance of large-aperture channels; here the TPL has a smaller conductance than the PL, the difference increasing with aperture variability and pressure gradient and decreasing with flow behavior index. On the other hand, small apertures along the channels play a crucial role in the serial arrangement; here results for the TPL and PL agree for intermediate gradients and differ for larger/smaller ones, when the conductance of the TPL is lower/higher than the PL. The differences between TPL and PL again increase with aperture variability and decrease with flow behavior index.

The impact of the specific pdf adopted for the aperture variation is moderate, with the first two moments being equal. The difference in conductance is an increasing function of aperture variability and depends on the third and fourth moment of the distribution. Specifically, higher values of skewness and kurtosis imply a smaller conductance for the parallel and a larger conductance for the serial arrangement. When a deterministic sinusoidal aperture variation is considered, all trends valid for stochastic variations are confirmed. Differences in conductance with stochastic aperture variation increase with pressure gradient and aperture variability, and are of opposite sign depending on the aperture arrangement.

Our model reveals the coupled effect of aperture heterogeneity and a realistic rheological equation for non-Newtonian fluid flow in rock fractures, a topic of interest in hydraulic fracturing, drilling, EOR, and environmental modelling and remediation. The relevance of rheological properties of real fluids and of the stochastic nature of the fractures suggest a more in depth analysis of the coupling effects. Polymer flooding is often used for EOR since the addition of polymers to the injected brine favors an improved sweep, a reduction of fingering with a more stable displacement. Whilst EOR polymers in

a rheometer display Newtonian and shear thinning behaviour, approximated by a TPL relationship, in the field polymers show a quite complex behavior partially captured in the present model, dictated by the flow geometry driven by fractures networks. Recovery mechanism in fractured reservoirs (carbonate reservoirs usually are extensively fractured but show a low porosity) is strongly influenced by the fractures, which show a well different transmissivity than the matrix and carry most of the flow limiting a large differential pressure and the efficiency of recovery. The nature of the fluid and the characteristics of the fractures counteract this negative aspect. As a matter of evidence, the TPL fluids show a reduction (increment) of flowrate at high (low) shear rates for a given pressure gradient with respect to the PL fluids. The relevance of this reduction/increment and its onset are controlled by the Newtonian plateaus and by the fractures parameters, mainly the average and the variance of the aperture of the fractures.

Results suggest to investigate further this coupling expanding the investigation to two-dimensional modeling of the aperture variation, inclusion of local pressure losses, and adoption of yield-stress rheological models or more complex models. A further element adding complexity to the model is shear-thickening behaviour due to elongation of the polymer molecules, typical of flow in capillary tubes with a sharp contraction (Nguyen & Kausch, 1992). At large flowrates, depending on the fractures characteristics, an elongational contribution adds up to the total pressure drop, showing a shear-thickening effect which can be included in the present model.

2.8   Appendix A - Alternative formulation for serial configuration

The pressure gradient can be estimated as the inverse of Eqs.(2.2–2.2c). We notice that while for a given pressure gradient the condition $b < b_1$ (and $b_1 < b < b_2$, $b > b_2$) must be satisfied in order to guarantee a low-shear, $\dot{\gamma} \leq \dot{\gamma}_1$ (intermediate -$\dot{\gamma}_1 \leq \dot{\gamma} \leq \dot{\gamma}_2$ and high-shear - $\dot{\gamma} \geq \dot{\gamma}_2$) regime, for a given inflow rate q_y the new conditions are

$$p_{yI}(b) = q_{yI}^{-1} \equiv \frac{12\mu_0 q_y}{b^3} \quad \text{for} \quad b > b_1' \equiv \sqrt{\frac{6q_y}{\dot{\gamma}_1}}; \qquad (2.22a)$$

$$p_{yII}(b) = q_{yII}^{-1} \quad \text{for} \quad b_2' < b < b_1'; \qquad (2.22b)$$

$$p_{yIII}(b) = q_{yIII}^{-1} \quad \text{for} \quad b < b_2' \equiv \sqrt{\frac{q_y}{\dfrac{m\dot{\gamma}_2^n}{6\mu_\infty} - \dfrac{a}{4m^2\dot{\gamma}_2^{2n}}}},$$

$$a = \frac{2(1-n)m^{3/(1-n)}}{3(2n+1)} \left(\frac{1}{\mu_\infty^{(2n+1)/(1-n)}} - \frac{1}{\mu_0^{(2n+1)/(1-n)}} \right), \qquad (2.22c)$$

with $b_2' < b_1'$. The inverse functions for the low-shear regime, $p_{yI} = q_{yI}^{-1}$, and the high-shear regime, $p_{yIII} = q_{yIII}^{-1}$, can be found analytically. At intermediate regime the inverse function $p_{yII} = q_{yII}^{-1}$ can be found analytically only for $n = 1/2, 1/4, 1/6$, while in general a numerical inversion is requested. We notice that for $n = 1/2$ the inverse function has two real-valued positive branches. This mathematical aspect could bring to hysteretic behaviour of the flow in the fracture, with different paths in the space $p_y - q_y$ according to the initial state: (i) a low pressure gradient regime and (ii) a high pressure gradient regime for the same flow rate. However, upon introduction of further dissipative effects, mainly due to expansion of the troughs, the hysteresis should be mitigated and eventually cancelled. We will not pursue this aspect, which requires an experimental validation, and we choose the branch of the inverse function corresponding to the high pressure gradient regime. Taking the limit as $N_j \to \infty$, the length of each cell tends to zero and the discrete aperture variation to a continuous one; then under ergodicity, and exploiting the previous relationships, Equation (2.7) gives for the mean pressure gradient in the y direction the expression

$$p_y = \int_{b_1'}^{\infty} p_{yI} f(b) \mathrm{d}b + \int_{b_2'}^{b_1'} p_{yII} f(b) \mathrm{d}b + \int_{0}^{b_2'} p_{yIII} f(b) \mathrm{d}b. \qquad (2.23)$$

2.9 Appendix B - Quantities of interest for deterministic aperture variation

For the deterministic, sinusoidal aperture variation of Section 5, Table 2.2 reports the integrals I_I, I_{II}, I_{III}, while Table 2.3 shows P_{II}, P_{III} for the different combinations reported in Table 2.1. In both tables, consider $\theta_i = \arcsin\left[\frac{1}{\delta}\left(\frac{b_i}{\langle b \rangle} - 1\right)\right]$.

Combinations	I_I	I_{II}	I_{III}
1	0	0	0
2	0		$\frac{\langle b\rangle^3}{2\pi}(1+\frac{3\delta^2}{2})$
3	0	$\frac{\langle b\rangle^{\frac{2n+1}{n}}}{3\pi-2\theta_2}\int_{\theta_2}^{3\pi-\theta_2}(1+\delta\sin\theta)^{\frac{2n+1}{n}}\mathrm{d}\theta$	$\frac{\langle b\rangle^3}{\pi-2\theta_3}\int_{\theta_3}^{\pi-\theta_3}(1+\delta\sin\theta)^3\mathrm{d}\theta$
4	0	0	0
5	$\langle b\rangle^3\left[\frac{1}{\theta_1}\int_0^{\theta_1}(1+\delta\sin\theta)^3\mathrm{d}\theta+\frac{1}{\pi-\theta_1}\int_{\pi-\theta_1}^{2\pi}(1+\delta\sin\theta)^3\mathrm{d}\theta\right]$	$\langle b\rangle^{\frac{2n+1}{n}}\left[\frac{1}{\theta_2}\int_0^{\theta_2}(1+\delta\sin\theta)^{\frac{2n+1}{n}}\mathrm{d}\theta+\frac{1}{\pi+\theta_2}\int_{\pi-\theta_2}^{2\pi}(1+\delta\sin\theta)^{\frac{2n+1}{n}}\mathrm{d}\theta\right]$	0
6	$\frac{\langle b\rangle^3}{3\pi-2\theta_1}\int_{\theta_1}^{3\pi-\theta_1}(1+\delta\sin\theta)^3\mathrm{d}\theta$	$\frac{\langle b\rangle^{\frac{2n+1}{n}}}{\pi-2\theta_2}\int_{\theta_2}^{3\pi-\theta_2}(1+\delta\sin\theta)^{\frac{2n+1}{n}}\mathrm{d}\theta$	0
7	$\frac{\langle b\rangle^3}{2\pi}(1+\frac{3\delta^2}{2})$	$\frac{\langle b\rangle^{\frac{2n+1}{n}}}{\theta_1}\frac{\pi}{1}$	0
8	$\langle b\rangle^3\left[\frac{1}{\theta_1}\int_0^{\theta_1}(1+\delta\sin\theta)^3\mathrm{d}\theta+\frac{1}{\pi+\theta_1}\int_{\pi-\theta_1}^{2\pi}(1+\delta\sin\theta)^3\right]\mathrm{d}\theta$	$\frac{\langle b\rangle^{\frac{2n+1}{n}}}{\theta_2-\theta_1}\int_{\theta_1}^{\theta_2}(1+\delta\sin\theta)^{\frac{2n+1}{n}}\mathrm{d}\theta+\int_{\pi-\theta_2}^{\pi-\theta_1}(1+\delta\sin\theta)^{\frac{2n+1}{n}}\mathrm{d}\theta+\frac{1}{\theta_1-\pi}\int_{3\pi-\theta_1}^{2\pi}(1+\delta\sin\theta)^{\frac{2n+1}{n}}\mathrm{d}\theta$	$\frac{\langle b\rangle^3}{\pi-2\theta_3}\int_{\theta_3}^{\pi-\theta_3}(1+\delta\sin\theta)^3\mathrm{d}\theta$
9	$\frac{\langle b\rangle^3}{3\pi-2\theta_1}\int_{\theta_1}^{3\pi-\theta_1}(1+\delta\sin\theta)^3\mathrm{d}\theta$	$\frac{\langle b\rangle^{\frac{2n+1}{n}}}{\theta_2-\theta_2}\int_{\theta_2}^{?}(1+\delta\sin\theta)^{\frac{2n+1}{n}}\mathrm{d}\theta$	$\frac{\langle b\rangle^3}{\pi-2\theta_3}\int_{\theta_3}^{\pi-\theta_3}(1+\delta\sin\theta)^3\mathrm{d}\theta$
10	$\frac{\langle b\rangle^3}{3\pi-2\theta_1}\int_{\theta_1}^{3\pi-\theta_1}(1+\delta\sin\theta)^3\mathrm{d}\theta$	$\langle b\rangle^{\frac{2n+1}{n}}\left[\frac{1}{\theta_2-\theta_2}\int_{\theta_2}^{\theta_2}(1+\delta\sin\theta)^{\frac{2n+1}{n}}\mathrm{d}\theta+\int_{\theta_1-\pi}^{3\pi-\theta_2}(1+\delta\sin\theta)^{\frac{2n+1}{n}}\mathrm{d}\theta+\frac{1}{3\pi-\theta_2}\int_{3\pi-\theta_2}^{2\pi}(1+\delta\sin\theta)^{\frac{2n+1}{n}}\right]\mathrm{d}\theta$	$\langle b\rangle^3\left[\frac{1}{\theta_3}\int_0^{\theta_3}(1+\delta\sin\theta)^3\mathrm{d}\theta+\frac{1}{\theta_3-\pi}\int_{3\pi-\theta_3}^{2\pi}(1+\delta\sin\theta)^3\mathrm{d}\theta\right]$

Table 2.2: Integrals I_I, I_{II}, and I_{III} for the deterministic case.

Combinations	P_{II}	P_{III}
1	0	1
2	$\left\| \dfrac{\pi - 2\theta_2}{2\pi} \right\|$	$1 - \left\| \dfrac{\pi - 2\theta_2}{2\pi} \right\|$
3	$\left\| \dfrac{\pi - 2\theta_2}{2\pi} \right\|$	$1 - \left\| \dfrac{\pi - 2\theta_2}{2\pi} \right\|$
4	1	0
5	$\left\| \dfrac{\pi - 2\theta_1}{2\pi} \right\|$	0
6	$\left\| \dfrac{\pi - 2\theta_1}{2\pi} \right\|$	0
7	0	0
8	$\left\| \dfrac{\pi - 2\theta_2}{2\pi} \right\|$	$1 - \displaystyle\sum_{k=1}^{2} \left\| \dfrac{\pi - 2\theta_k}{2\pi} \right\|$
9	$\left\| \dfrac{\pi - 2\theta_2}{2\pi} \right\|$	$1 - \displaystyle\sum_{k=1}^{2} \left\| \dfrac{\pi - 2\theta_k}{2\pi} \right\|$
10	$\left\| \dfrac{\pi - 2\theta_2}{2\pi} \right\|$	$1 - \displaystyle\sum_{k=1}^{2} \left\| \dfrac{\pi - 2\theta_k}{2\pi} \right\|$

Table 2.3: P_{II}, and P_{III} for the deterministic case.

3 | A Lubrication-based Solver for Shear-thinning Flow in Rough Fractures

3.1 Abstract

The lubrication theory, a depth-averaged (2-D) approach, is often adopted to simulate Newtonian flow in rough fractures. Such simulations are computationally much less expensive than those based on 3-D CFD solvers, and thus allow addressing large ensembles of stochastic fracture realizations. For creeping flow, the degree of approximation introduced is limited, as long as the apertures vary relatively smoothly. We extend this approach to address the flow of fluids whose rheology, described by the Ellis model, is shear-thinning (ST) above a crossover shear stress, and Newtonian (of viscosity μ_0) below. We obtain a nonlinear relation between the depth-integrated velocity and the 2-D pressure gradient, leading to a novel non-linear Reynolds equation for pressures. We solve it for a vast range of realistic rheological parameter values (in particular, the ST power law exponent) using a novel finite volume method. The symmetry of the Newton Jacobian allows for an inexact conjugate gradient-based Newton-Krylov strategy, which is combined with parameter continuation to enlarge Newton's basin of attraction and increase code robustness. Using the code to investigate realistic synthetic rough fracture geometries, which exhibit both self-affinity and a correlation length, we show that the ST rheology mitigates the effects of aperture heterogeneities, increasing fracture transmissivity by several orders of magnitudes as compared to the Newtonian flow of viscosity μ_0 if the imposed macroscopic gradient is sufficiently large, and even rendering the rough fracture up to 10 times more permeable than a smooth fracture of identical mean aperture.

3.2 Introduction

The comprehension of the hydraulic, mechanical and chemical behaviours of fluids in geological formations is fundamental to the success of subsurface techniques aimed at a variety of applications: resources recovery (Suleimanov, Ismailov & Veliyev, 2011; Ciriello et al., 2021), geothermal exploitation (Sanner, Karytsas, Mendrinos & Rybach, 2003), carbon sequestration (Leung, Caramanna & Maroto-Valer, 2014) and soil reclamation (Mulligan, Yong & Gibbs, 2001). The decreasing prospects of new oil reservoir discoveries is stimulat-

ing companies to invest in unconventional reservoir exploitation (Sheng, Su & Wang, 2019) and enhanced oil recovery (EOR), to maximize the recovery factor of mature oilfields (Muggeridge, Cockin, Webb, Frampton, Collins, Moulds & Salino, 2014). Reservoir stimulation via hydraulic fracturing is a well-established approach to increase formation permeability, allowing to extend existing reserves. In unconventional reservoirs, where the pore space is poorly-connected, induced stimulation permits the production of oil and gas from formations of low-permeability (e.g., shale) (Curtis, 2002), reactivating natural fractures (Gale, Laubach, Olson, Eichhuble & Fall, 2014), and generating new ones (Cipolla, Lolon, Erdle & Rubin, 2010). Induced stimulation is also utilized in enhanced geothermal systems (EGS), which constitute an innovative power system (Lu, 2018): they involve the injection of fluids in artificially fractured hot rocks to exploit an abundant renewable heat source. CO_2-based EGS (Aminu, Nabavi, Rochelle & Manovic, 2017) or CO_2-EOR (Dowell, Fennell, Shah & Maitland, 2017) in fractured geological formations have also been proposed to offset the costs of the subsurface storage of CO_2, which is currently considered a viable approach to reduce anthropogenic CO_2 emissions, responsible for two thirds of the increased greenhouse effects (Leung et al., 2014).

These applications have led in the last ten years to renewed scientific interest for flow in subsurface porous media, in particular, fractured porous media. In igneous rocks in particular, and more generally in low permeability formations, fractures provide preferential pathways of high conductance with respect to the almost impervious rock matrix. The fractures are organized in connected networks (Bonnet, Bour, Odling, Davy, Main, Cowie & Berkowitz, 2001), and the overall hydraulic behaviour of the medium subjected to Newtonian flow is mainly governed by their connectivity (Bour & Davy, 1998) and by the distribution of fracture permeabilities throughout the network (de Dreuzy, Davy & Bour, 2002). In discrete fracture networks (DFN), the parallel plate conceptualization has traditionally been used to model Newtonian flow in a single fracture from the simplified geometry of two planar and parallel fracture walls, leading to a fracture permeability proportional to the square of its aperture. However, fracture wall topographies are in fact rough as a result of the fracturing process, and exhibit self-affine and long-range correlated topographies (Brown & Scholz, 1985; Brown, 1987; Schmittbuhl, Schmitt & Scholz, 1995b; Schmittbuhl, Vilotte & Roux, 1995a). This geometric property is transferred to the aperture field at scales smaller than the correlation length between the two fracture walls (Brown, 1995). The resulting spatial variability of the aperture controls the heterogeneity of Newtonian flow, all the more as the fracture is more closed (i.e., as aperture fluctuations relative to the mean aperture are larger) (Brown, 1987; Glover et al., 1998; Méheust & Schmittbuhl, 2000, 2001), while the ratio of the correlation length to the fracture size controls the impact of the flow heterogeneity on the fracture's hydraulic behavior (Méheust & Schmittbuhl, 2003). Moreover, flow heterogeneity below the fracture plane can in some cases modify the (Newtonian)

flow connectivity at the network scale, thus strongly impacting the permeability of the fractured formation (de Dreuzy, Méheust & Pichot, 2012).

Consequently, Newtonian flow in a single rough fracture has been the topic of many past studies, some of which are cited above. And though simple deterministic wall geometries (Elsworth & Goodman, 1986; Zimmerman & Bodvarsson, 1996; Di Federico, 1997) or an aperture probability density function without spatial correlations (Lenci & Di Federico, 2020; Felisa et al., 2018) allow for analytical or semi-analytical investigation of the flow, the study of the aforementioned realistic geometries must rely on numerical modeling. A vast number of studies, including the seminal work of Brown (1987), have relied on solving the Reynolds equation. It states that the local flux, defined as the integral of the fluid velocity over the local fracture aperture, and is thus conservative, can be expressed in terms of the local in-plane pressure gradient according to a local cubic law, i.e., a Darcy law where the local fracture transmissivity is proportional to the cube of the local aperture (Brown, 1987; Zimmerman & Bodvarsson, 1996). Other studies, following the recent increases in computational power, have simulated Newtonian flow in the 3-D space between the fracture walls (among the first such studies see Mourzenko, Thovert & Adler (1995); Brush & Thomson (2003)), by means of commercial or open source software, either able to numerically solve the Navier-Stokes equation in 3-D flow domains or adopting Lattice Boltzmann method (LBM) (Wang, Chen, Ma, Zhou & Zhou, 2016a) to obtain the velocity field. They have rightfully pointed to the moderate underestimation, by the Reynolds equation, of the fracture transmissivity's deviation from that of a smooth fracture of identical mean aperture; this underestimation results from the inability to model out-of-plane flow tortuosity. However, such 3-D simulations are computationally expensive, limiting applications to the study of a few fracture realizations, and making a full stochastic analysis impossible. The lubrication theory, which reduces the flow problem to two dimensions, allows for very efficient numerical solvers, and is thus useful for stochastic analyses. This approximation can be assumed to be valid as long as the variation of the aperture field w is sufficiently smooth ($\boldsymbol{\nabla} w \ll 1$) and the fluid can be considered in creeping motion ($Re \ll 1$).

In this paper the fluids of interest are those used in the aforementioned applications; they are water-based but contain surfactants or macropolymers (e.g., xanthan gum) that boost fluid viscosity and lower surface tension. Various additives can be introduced depending on the application and the geological formation: i) crosslinkers, to increase molecular weight and proppant-carrying capacity; ii) friction reducers, to increase pump efficiency and keep proppant particles evenly-distributed in the suspension; iii) breakers, to provide rheoreversibility, favouring flowback or fluid-disposal process; iv) biocides, to kill bacteria; v) gellants, to adjust the viscosity and form a gel (Barati & Liang, 2014). A vast range of fluids have been adopted in the various steps of the hydraulic fracturing process: natural polysaccharides, synthetic polymer solutions, organic or chemical gels, emulsions, muds, micel-

lar surfactant solutions and aqueous physical (Barbati, Desroches, Robisson & McKinley, 2016). The complex micro-structure of these fluids inevitably induces a non-Newtonian mechanical behaviour. Solid particles such as proppants will typically lead to jamming effects and thus to shear-thickening of the flow, while most additives will provide the fluid with a soft matter-type microstructure (colloids, polymers, droplets, bubbles, micelles) resulting in a shear-thinning behavior (hereinafter ST). This behaviour is by far prevalent in fluids engineered for subsurface applications (Economides, 2000; Barbati et al., 2016). Recently, non-toxic inexpensive CO_2-based alternatives to conventional fluids have been considered because of their high viscosity and rheoreversibility; these fluids show the desirable ST behaviour without incorporating toxic chemical agents (Jung et al., 2015; Li, Huang, Sun, Gao, Zeng, Tontiwachwuthikul & Liang, 2017; Chen et al., 2016).

Hence, better understanding the flow of ST fluids in rough fractures is crucial to predicting the outcome of various subsurface operations. The coupling of ST rheology and domain heterogeneity is known to produce higher flow localization and channeling in porous media (Sullivan, Gladden & Johns, 2006; Zami-Pierre, de Loubens, Quintard & Davit, 2016) as compared to Newtonian flow in the same geometry. But the topic of ST fluid flow in rough fracture geometries has been little addressed in the literature. Morris et al. (2015) have proposed a lubrication-based model for the flow of Herschel-Bulkley fluids in simple deterministic geometries, while Lavrov (013a, 013b) used a similar model to study the flow of power law fluids in relatively small (33x33) size realizations of self-affine rough fractures (without a correlation length), and provided considerations on the impact of the power law exponent on the flow geometry. Zhang, Prodanović, Mirabolghasemi & Zhao (2019) performed 3-D CFD simulations of ST laminar flow, focusing on the impact of the fluid rheology on inertia effects and the transition to a Forchheimer-like regime. To the best of our knowledge, the flow of ST fluids featuring a rheological transition from a Newtonian plateau at low shear rates to a power law ST behaviour at high shear rates in large scale and realistic fracture geometries (featuring a correlation length) has never been addressed in the literature, and no code implementation allowing to easily perform Monte Carlo simulations over a large number of aperture fields has been proposed.

In this study, we propose a model for simulating the flow of a ST fluid in a variable aperture fracture based on the depth-averaged lubrication theory and considering a three-parameter Ellis constitutive model for the fluids' rheology. The latter accounts for both low shear rate quasi-Newtonian and high shear rate ST behaviors. This approach yields a quasilinear partial differential equation (PDE) that is the sum of a linear heterogeneous diffusion term and a nonlinear generalized (heterogeneous) p-Laplace operator. The latter is a mathematically well-studied prototype of nonlinear partial differential equation and is at the heart of many models of nonlinear diffusion (Philip, 1961), including non-Newtonian flows, turbulent filtration and reactive-diffusion (Diaz & De Thelin, 1994), and nonlinear Darcy flows (Firdaouss, Guermond &

Le Quéré, 1997). The reader is referred to Benedikt, Girg, Kotrla & Takac (2018) for a historical perspective. Recently, the interest on p-Laplacian operators has increased, resulting in significant developments of efficient numerical solvers (Loisel, 2020; Facca, Cardin & Putti, 2021). Taking into consideration the aim of running Monte-Carlo simulations, we propose an efficient Finite Volume (FV) discretization for the nonlinear PDE based on the adaptation of the generalized graph p-Laplacians to a uniform square mesh. The proposed scheme turns out to be a slight variant of the lowest order method of the family of schemes analyzed in Andreianov, Boyer & Hubert (2004). The developed approach has the advantage that it leads to a symmetric Jacobian, thus enabling the implementation of a very efficient Newton-Krylov iteration for the solution of the ensuing nonlinear system employing the preconditioned conjugate gradient linear solver. A parameter continuation method is added to increase robustness for wider ranges of p. This allows to address a vast range of geometrical and rheological parameters of practical interest, in particular, small rheological indices (i.e., ST exponents) of order 0.1, without resorting to more sophisticated and computationally expensive methods such as those proposed in Facca et al. (2021). The ensuing solver achieves a favorable compromise between accuracy and computational cost that enables us to address the study of the flow behavior in the fracture within a Monte-Carlo framework, i.e., considering a significant ensemble of different fracture realizations for a given set of statistical geometric parameters (ratio of mean aperture to length, ratio of apertures' standard deviation of mean aperture, ratio of correlation length to length). The impact of the ST rheology on the spatial distribution of the velocity field in the fracture plane and on the resulting fracture scale hydraulic behavior can then be investigated.

Based on these premises, the organization of the paper follows naturally: Section 3.3 describes the geometric properties of fracture apertures and how realistic synthetic aperture fields can be generated; Section 3.4 provides the derivation of the generalized Reynolds equation for an Ellis fluid in a variable aperture fracture; Section 3.5 presents the implementation of this theoretical model into a novel numerical code, while section 3.6 reports on numerical results regarding the impact of the fluid rheology on fracture flow and the fracture's hydraulic aperture; section 3.7 lists our conclusions and prospects for future work.

3.3 Synthetic aperture fields

As depicted in Figure 3.1, the aperture field $w(\mathbf{x})$ of a fracture is typically estimated as the distance between the two rough fracture walls, whose mean planes are parallel. Denoting $\langle w \rangle$ the mean aperture of the fracture, and $z_\mathrm{u}(\mathbf{x})$ and $z_\mathrm{l}(\mathbf{x})$, respectively, the upper and lower topographies of the walls with respect to their mean planes ($\mathbf{x} = (x_1, \ x_2)^\top$ being the position vector in the
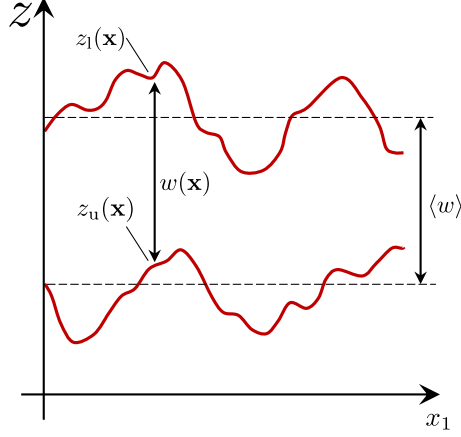
Figure 3.1: Geometry of a fracture profile (i.e., the cut of a 3D fracture by a vertical plane). The separation between the walls' mean planes is the mean aperture $\langle w \rangle$, while $z_u(\mathbf{x})$ and $z_l(\mathbf{x})$ described the topographies of the rough walls with respect to their mean planes.

.

fracture plane), $w(\mathbf{x})$ is simply

$$w(\mathbf{x}) = z_u(\mathbf{x}) - z_l(\mathbf{x}) + \langle w \rangle \ . \tag{3.1}$$

Typically, the walls of a fracture surface can be described as isotropic self-affine topographies, exhibiting long-range correlations up to their linear size (Schmittbuhl et al., 1995a; Bouchaud, 1997) characterized by an exponent H (the so-called Hurst exponent). For a fresh fracture, the two wall topographies are identical, so the fracture aperture depends on the shear slip history of the walls. Shear slip induces an anisotropic decorrelation of the two topographies along the shear direction and at scales smaller than the slip distance (Plouraboué, Kurowski, Hulin, Roux & Schmittbuhl, 1995). In geological fractures, however, the aperture field is usually measured to be isotropic, but also with a decorrelation between the wall topographies at a scale smaller than a correlation length L_c (Brown, 1995). Above that scale, the walls can be considered to be matched, but below it, the aperture field, being a linear combination of two independent self-affine topographies, is also self-affine. In the Fourier space this translates into a power spectral density in the form of a power law of exponent $-2(H + 1)$ at scales smaller than L_c, and flat above that length (see Fig. 3.2(a)). Note that the Hurst exponent H has been measured to a quasi-universal value of around 0.8 over a wide range of scales and materials, including ceramics, metals, and rocks such as granite and basalt (Bouchaud, Lapasset & Planès, 1990), with a few exceptions such as sandstones ($H \sim 0.45$, see Boffa, Allain & Hulin (2000)). This property of the fracturing process in sandstones has been attributed to its intergranular

nature.

Recursive algorithms can be implemented to generate rough surfaces with spatial correlations (by successive random addition (Liu, Bodvarsson, Lu & Molz, 2004)), but the generation of large fractures with these algorithms is inefficient. Alternatively, we adopt a method proposed by Méheust & Schmittbuhl (2003) and relying on the Fourier spectrum's properties (see also Barnsley, Devaney, Mandelbrot, Peitgen, Saupe & Voss (1988)). Generating a random Fourier transform of the aperture field with the spatial correlation properties described above, allows us to obtain an appropriate synthetic aperture field without the need to generate the two wall topographies (Méheust & Schmittbuhl, 2003). The procedure is very fast as it relies on the fast Fourier transform. We start with a spatially-uncorrelated white noise and multiply the modulus of its Fourier transform by the modulus of the wave number $|k| = \sqrt{k_{x_1}^2 + k_{x_2}^2}$ raised to the power $-(H+1)$ (Figure 3.2c). The resulting aperture field can then be scaled and translated so as to tune its mean value and standard deviation, with consequent negative values set to 0, corresponding to an assumption of perfect plastic closure. Fig. 3.2(b) shows two representations of the aperture field of the same fracture at two different degrees of closure, or coefficients of variations, $\sigma_w / \langle w \rangle$.

Algorithm 1: Fracture aperture field generator pseudocode.

$[k_{x_1}, k_{x_2}] =$ `Grid`(M);
$k = \sqrt{k_{x_1}^2 + k_{x_2}^2}$;
$k(k < k_{\rm c}) = k_{\rm c}$;
$z =$ `invFFT`(`FFT`(`Rand`(M)) $\times k^{-(1+H)}$);
$z = (z -$ `Mean`$(z))/$`Std`(z);
$w = z \times \sigma_w + \langle w \rangle$;
$w(w < w_0) = w_0$;

The aperture field generation is implemented according to Algorithm 1, where the parameters are $\langle w \rangle$ and σ_w, which are respectively the desired distance between the walls' mean planes and the standard deviation of the aperture field prior to implementing the perfect plastic closure; H, which is the Hurst exponent controlling the self-affinity; and $k_{\rm c}$, which is the crossover wave number related to the correlation length through $k_{\rm c} = 2\pi/L_{\rm c}$. The following functions are adopted:

1. `Grid` returns a $2^M \times 2^M$ square grid of coordinates k_{x_1} and k_{x_2};

2. `Rand` generates a $2^M \times 2^M$ square matrix of random numbers extracted from a uniform distribution;

3. `FFT` computes the 2-D Fast Fourier Transform and rearranges by shifting the zero-frequency components to the center of the array;

4. `invFFT` computes the inverse 2-D Fast Fourier Transform.
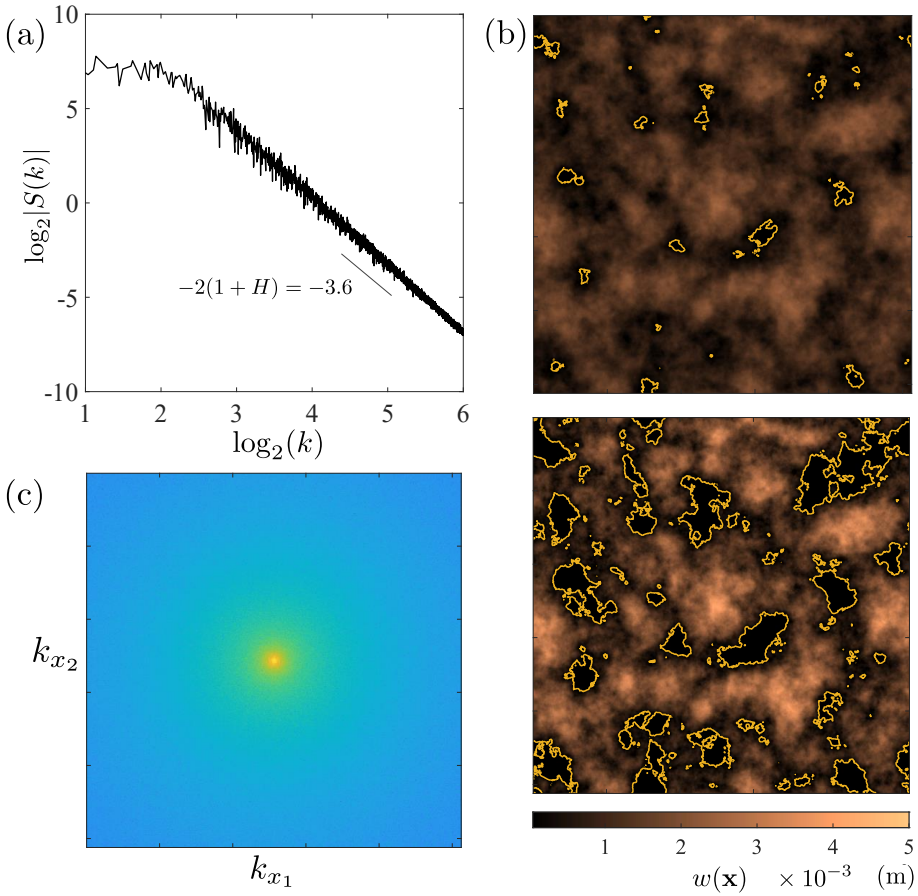
Figure 3.2: (a) Mean radial profile (obtained by angular integration) of the 2-D Fourier transform of a fracture's aperture field, displaying a low-frequency cut-off for wave numbers smaller than $k_c = 2\pi/L_c$, and a power-law trend of negative exponent $-2(1+H)$ for higher frequencies; (b) Aperture field representations for different values of the closure: 0.5 (upper panel), and 1 (bottom panel); (c) Representation of the wave number to the power $-(1+H)$. The set of parameter adopted for the generations is: $L = 80$ cm, $L_c = 10$ cm, $\langle w \rangle = 1$ mm, $H = 0.8$.

5. `Mean` computes the average value.

6. `Std` computes the standard deviation.

In the pseudocode, the parameter w_0 is a non-zero lower cut-off imposed to the aperture field in fractures with closed regions. This regularization parameter is introduced to ensure well-posedness of the flow PDE and guarantee solvability in the numerical solver also in the presence of contact points (zero aperture). Typically, w_0 is chosen to be sufficiently small so as not to affect the accuracy of the solution. In our experiments we employed $w_0 = 10^{-8}$ m.

3.4 Generalized Reynolds equation

Engineered fluids used in subsurface operations typically display an overall sheer-thinning (ST) behaviour, wherein the apparent viscosity μ of the fluid is a decreasing function of shear rate $(\dot{\gamma})$, i.e. the fluid thins with increasing deformation. More specifically, the typical flow curve $\mu = \mu(\dot{\gamma})$ for a ST fluid exhibits two Newtonian plateaus, one of high viscosity at low shear rates, the other one of low viscosity at high shear rates. These plateaus are separated by a shear-thinning regime starting for shear rates higher than a critical threshold value $\dot{\gamma}_c$. The Carreau-Yasuda (CY) five-parameter model (Yasuda, Armstrong & Cohen, 1981) and its original four-parameter version, the Carreau model (see Appendix B for both), exhibit both plateaus and are the most common constitutive laws able to fully capture such a rheology. On the other hand, the power-law (PL) two-parameter model represents the simplest non-Newtonian constitutive equation, but is able to reproduce only the ST behaviour typical of the intermediate range of shear rates in a Carreau-Yasuda or Carreau fluid (Escudier, Gouldson, Pereira, Pinho & Poole, 2001). The CY model is commonly used in CFD applications, but is difficult to handle analytically. Conversely, the more tractable PL model oversimplifies the constitutive law because of its unrealistic apparent viscosity, which is unbounded as the shear rate approaches zero and tends to zero at high shear rates. When dealing with creeping flow in rough fractures, the velocities are usually sufficiently low for high shear rates, corresponding to the low viscosity plateau of the rheological curve, to be rare. In other words, the apparent viscosity attains the low viscosity plateau value in a limited number of spatial locations, so that a rheological model only accounting for the low shear rate plateau and the power law decrease at higher shear rates is an acceptable simplification in practical cases. Such a model is perfectly described by the three-parameter Ellis constitutive law, first introduced by Bird (1987), where, in variance with most generalized Newtonian fluids, the apparent viscosity depends on the local shear stress τ according to

$$\mu = \frac{\mu_0}{1 + \left(\dfrac{\tau}{\tau_{1/2}}\right)^{\frac{1}{n}-1}} \ . \tag{3.2}$$
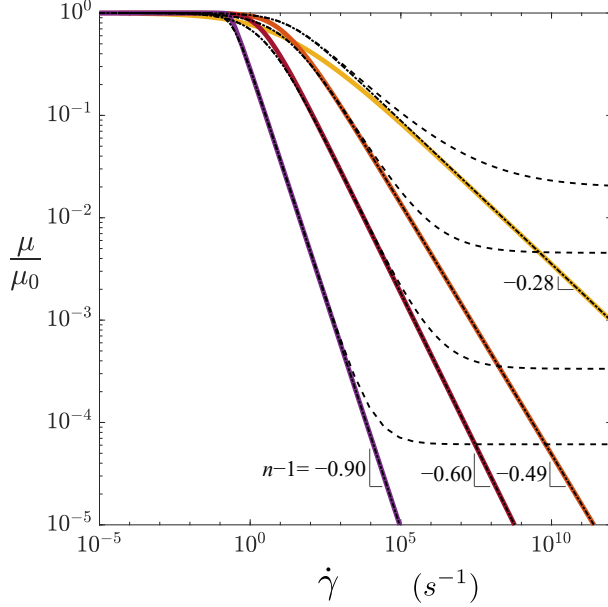
Figure 3.3: Dependence of the dimensionless apparent viscosity μ/μ_0 on the shear rate $\dot{\gamma}$, for the four Ellis fluids listed in Table 3.1: F1 (yellow solid line), F2 (orange solid line), F3 (red solid line), and F4 (purple solid line). The parameters of these fluids are deduced from data originally interpreted with the Carreau-Yasuda model (see Appendix B); the original Carreau model and its low shear rate approximation are reported as dashed and dotted lines, respectively. The high-shear rate power-law exponents for all solid curves are $n - 1$.

As shown in Figure 3.4, μ_0 is the plateau viscosity (having the same dimensions as the dynamic viscosity of a Newtonian fluid), n defines the power law exponent $(n - 1)$ of the shear-thinning regime, and the characteristic $\tau_{1/2}$, defined by $\mu(\tau_{1/2}) = \mu_0/2$, shapes the transition between the two tendencies. The Ellis rheologic parameters depicted in Figure 3.4 and listed in Table 3.1, are those of four real ST fluids taken from the literature that will be used in the following to demonstrate the code.

To derive the flow rate of an Ellis fluid between parallel plates, one of the main building block of the code, we recall the equations governing isothermal flow of an incompressible fluid of density ρ, i.e. the momentum and continuity equations, reading:

$$\rho \mathbf{g} + \boldsymbol{\nabla} \cdot \mathbf{T} = \rho \left(\frac{\partial \mathbf{u}}{\partial t} + (\mathbf{u} \cdot \boldsymbol{\nabla}) \mathbf{u} \right),$$

$$\boldsymbol{\nabla} \cdot \mathbf{u} = 0 \, ,$$

(3.3)

where $\mathbf{u}$ is the velocity, $\mathbf{g}$ is the body force vector and $\mathbf{T}$ is the stress tensor. For a generalized Newtonian fluid, the latter can be written as

Fluid ID	Solution	μ_0 (Pa·s)	$\tau_{1/2}$ (Pa)	n (−)
F1	CMC at 0.3 wt%	0.0510	4.07	0.72
F2	CMC at 0.5 wt%	0.2203	2.50	0.51
F3	CMC at 1.0 wt%	2.9899	5.14	0.40
F4	VES	49	1.07	0.10

Table 3.1: Rheologic parameters μ_0, n and $\tau_{1/2}$ related to the four shear-thinning fluids interpreted with the Ellis models. The fluids considered are: three different Carboxymethylcellulose (CMC) water-based solutions from Sousa et al. (2005), and a visco-elastic surfactant (VES) from Moukhtari & Lecampion (2018). Experimental data have been originally fitted with CY model (parameters listed in table 3.5), and interpreted with the Ellis model as described in Appendix B.

$\mathbf{T} = -p'\mathbf{I} + 2\mu\mathbf{D}$, where p' is the pressure, $\mathbf{I}$ is the identity tensor, $\mathbf{D}$ is the rate of deformation tensor, and μ is the apparent viscosity, which depends on the shear rate tensor $\mathbf{D}$ according to $\dot{\gamma} = \sqrt{2\mathbf{D} : \mathbf{D}}$, where : stands for the tensor double-dot product.

In the following we consider Stokes flow, that is, we assume that the Reynolds number is much smaller than 1 and thus that the non-linear term in the right-hand side of Equation (3.4a) can be neglected. For steady flow between smooth parallel plates of aperture w, the momentum conservation (3.4a) then reduces to

$$\mu \boldsymbol{\nabla}^2 \mathbf{u} = \boldsymbol{\nabla} P \ , \tag{3.4}$$

where $P = p' + \rho g z$ is the reduced pressure.

Taking for simplicity the reduced pressure gradient to be aligned along the x_1 direction, e.g. $\boldsymbol{\nabla} P \equiv (\partial P/\partial x_1, 0, 0)$, and after integrating once over the height z, the one-dimensional formulation of (3.4) becomes

$$\frac{du_1(z)}{dz} = \frac{\partial P/\partial x_1}{\mu} z \ . \tag{3.5}$$

Inserting (3.2) into (3.5) and integrating over z provides the velocity profile as a function of z:

$$u_1(z) = -\left\{ \frac{1}{8\mu_0}\left[w^2 - \left(\frac{z}{2}\right)^2 \right] + \frac{n}{n+1}\left(\frac{1}{2^{n+1}\mu_0^n \tau_{1/2}^{1-n}} \right)^{\frac{1}{n}} \times \right.$$
$$\left. \times \left[w^{\frac{1}{n}+1}\left(\frac{z}{2}\right)^{\frac{1}{n}+1} \right] \left| \frac{\partial P}{\partial x_1} \right|^{\frac{1}{n}-1} \right\} \frac{\partial P}{\partial x_1} \ , \tag{3.6}$$

and averaging over the z-direction leads to a mean velocity in the form

$$\bar{u}_1 = -\left[\frac{w^2}{12\mu_0} + \frac{n}{2n+1}\left(\frac{1}{2^{n+1}\mu_0^n \tau_{1/2}^{1-n}} \right)^{\frac{1}{n}} w^{\frac{1+n}{n}}\left| \frac{\partial P}{\partial x_1} \right|^{\frac{1}{n}-1} \right] \frac{\partial P}{\partial x_1} \ . \tag{3.7}$$

The counterpart to (3.7) for a macroscopic reduced pressure gradient in the x_2 direction can be obtained by replacing x_1 with x_2, and $\bar{u}_1$ with $\bar{u}_2$, in Eq. (3.7).

Under the lubrication theory, (3.7) and its counterpart in the x_2 direction are assumed to hold locally in a fracture of variable aperture $w(x_1, x_2)$. Oron & Berkowitz (1998) demonstrated the validity of this approximation for the Stokes flow of a Newtonian fluid, as long as $\boldsymbol{\nabla} w \ll 1$, with a depth-averaged velocity $\bar{\mathbf{u}}(x_1, x_2) = [\bar{u}_1(x_1, x_2), \bar{u}_2(x_1, x_2)]^{\intercal}$ that depends on both x_1 and x_2. These equations satisfy the momentum conservation, however the velocity and the pressure fields are both unknown and another equation is required.

It turns out that the local flux $\mathbf{q} = w(x_1, x_2)\,\bar{\mathbf{u}}$, which is the integral of the fluid velocity along z and over the local fracture aperture, is conservative (Zimmerman & Bodvarsson, 1996):

$$\boldsymbol{\nabla} \cdot \mathbf{q} = 0 \ . \tag{3.8}$$

Introducing the local flux, expressed as a function of the reduced pressure P through Eq. (3.7), into the mass conservation (3.8) leads to the non-linear lubrication equation:

$$\boldsymbol{\nabla} \cdot \left[\left(\frac{w(x_1, x_2)^3}{12\mu_0} + \frac{n}{2n+1} \left(\frac{1}{2^{n+1}\mu_0^n \tau_{1/2}^{1-n}} \right)^{\frac{1}{n}} w(x_1, x_2)^{\frac{2n+1}{n}} |\boldsymbol{\nabla} P|^{\frac{1}{n}-1} \right) \boldsymbol{\nabla} P \right] = 0 \ , \tag{3.9}$$

which reduces to the classical, linear, Reynolds equation for a Newtonian fluid ($n = 1$), with the solution depending only on fracture aperture in that case. For $n < 1$, conversely, the non-Newtonian pressure field also depends on the fluid's rheology, which renders the problem non-linear.

The fraction of the fracture plane that is concerned by the nonlinear rheology, and to which extent it is, can be visualized from maps of the local depth-averaged apparent viscosity, which must be estimated a posteriori (i.e., once the flow velocity field has been computed):

$$\bar{\mu}(\mathbf{x}) = \frac{\mu_0}{w} \int_{-w/2}^{w/2} \left[1 + \left(\frac{\|\boldsymbol{\nabla} P\| z}{\tau_{1/2}} \right)^{\frac{1}{n}-1} \right]^{-1} dz \ . \tag{3.10}$$

This 2D viscosity field allows introducing the Reynolds number for a generalized Newtonian fluid (Re_G), as

$$Re_G = \frac{\rho \langle \bar{u} \rangle \langle w \rangle}{2 \langle \bar{\mu} \rangle} \ . \tag{3.11}$$

where ρ is the fluid density (in the following it will be assumed equal to the water density 10^3 kg/m^3) and $\langle \bar{\mu} \rangle$ is the average over the fracture plane of the depth-averaged apparent viscosity (or, equivalently, the average of the 3D velocity over the entire fracture volume); similarly, $\langle \bar{u} \rangle$ is the mean velocity computed over the fracture volume. That definition of the Reynolds number

allows us to verify a posteriori that the Stokes flow assumption is still verified in the computed ST flow, a condition that is requested for the lubrication approach to be valid.

Note that an estimate of the critical macroscopic pressure gradient $\overline{\nabla P} = \|\overline{\nabla P}\|$ above which non-Newtonian effects begin to appear in the flow, which we denote $\overline{\nabla P}_c$, can be obtained by considering the aperture in the parallel plate configuration equal to the rough fracture's mean aperture. From the rheological law (3.2), it is seen that the viscosity begins to deviate from the Newtonian plateau viscosity μ_0 when the largest shear stress locally occurring in the fracture, $\tau_{\max}$, is on the same order as the crossover shear stress τ_c in the Carreau-Yasuda rheological law relating the apparent viscosity to the shear rate (see Eq. (3.39)). The crossover shear stress τ_c can be estimated numerically from the transition shear stress $\tau_{1/2}$ and plateau viscosity μ_0 of the Ellis model Eq. (3.2) (see Appendix B).

Given the 1-D momentum conservation (3.5), the largest shear stress occurs at the walls for any fluid and is equal to $\tau_{\max} = \langle w \rangle \overline{\nabla P}/2$. Hence the condition $\tau_{\max} \simeq \tau_c$ provides the following crossover value for the applied macroscropic pressure gradient:

$$\overline{\nabla P}_c = \frac{2\tau_c}{\langle w \rangle} \ . \tag{3.12}$$

If the imposed $\overline{\nabla P}$ is much smaller than $\overline{\nabla P}_c$, the flow is expected to be Newtonian, whereas if it is much larger than the crossover pressure gradient the flow can be expected to be strongly shear-thinning.

3.5 Numerical modeling

3.5.1 Finite volume scheme formulation

We consider a ST fluid flowing through a fracture whose projection on its mean plane is square ($\Omega = (0, L) \times (0, L)$), as depicted in Fig. 3.1. The flow in the fracture is driven from left to right by an externally-applied pressure drop ΔP corresponding to an average pressure gradient $\overline{\nabla P} = \Delta P/L$. Without loss of generality, we assume the following Dirichlet boundary conditions: for $0 < x_2 < L$, the pressure is taken to be zero at the downstream end ($P(L, x_2) = 0$), while upstream $P(0, x_2) = \overline{\nabla P} L$ is assumed. The upper and lower sides of the domain are both assumed impervious, imposing Neumann boundary conditions such that: $\partial_2 P(x_1, 0) = \partial_2 P(x_1, L) = 0$, for $0 < x_1 < L$.

The generalized Reynolds equation (3.9) results in a quasilinear PDE problem of the second order written as:

$$\begin{cases} -\boldsymbol{\nabla} \cdot \left[\left(a(\mathbf{x}) + b(\mathbf{x}) \|\boldsymbol{\nabla} P\|^{\frac{1}{n}-1} \right) \boldsymbol{\nabla} P \right] = 0 & \mathbf{x} \in \Omega \\ P = P_0 & \mathbf{x} \in \partial\Omega_{\mathrm{D}} \\ \boldsymbol{\nabla} P \cdot \boldsymbol{\nu} = 0 & \mathbf{x} \in \partial\Omega_{\mathrm{N}} \end{cases} \tag{3.13}$$
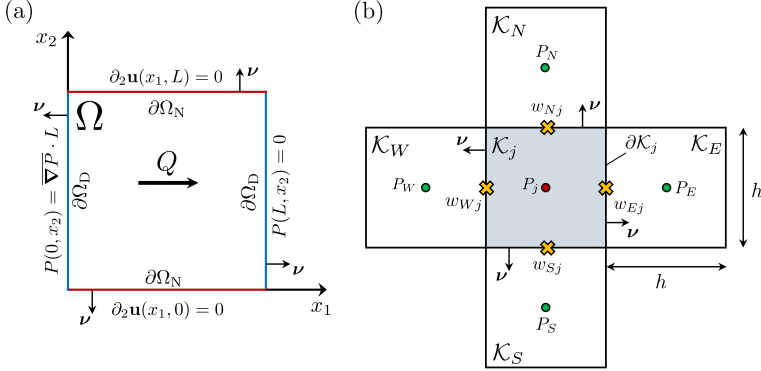
Figure 3.4: (a) Fracture plane representation with boundary conditions. (b) Finite volume method: five-point stencil. Pressures are defined at the centre of each cell, while the fracture's local apertures are defined on the edges.

where $\mathbf{x}$ is the position vector, $\boldsymbol{\nu}$ is the outward unit normal vector defined on the boundary, and the coefficients $a(\mathbf{x})$ and $b(\mathbf{x})$ are defined as

$$a(\mathbf{x}) = \frac{w(\mathbf{x})^3}{12\mu_0} \tag{3.14}$$

and $\qquad b(\mathbf{x}) = \frac{n}{2n+1}\left(\frac{1}{2^{1+n}\mu_0^n\tau_{1/2}^{1-n}}\right)^{\frac{1}{n}} w(\mathbf{x})^{\frac{2n+1}{n}} . \tag{3.15}$

The latter equation is the sum of two terms, the first one involving a linear heterogeneous Laplacian differential operator and the second one involving a nonlinear heterogeneous p-Laplacian operator, with $p = 1/n + 1$. To ensure well-posedness of problem (3.13), the two coefficients a and b must be strictly positive and the shear-thinning index must remain in the range $0 < n < +\infty$ corresponding to $1 < p < \infty$. The physical range of n, $[0, 1]$, is thus contained in the well-posedness region. Hence the only condition that needs to be imposed for well-posedness is that the aperture cannot be zero. This is the reason for the introduction of a non-zero aperture w_0 threshold enforced in the contact zones between the two fracture walls in Algorithm 1 of section 3.4.

Equation (3.13) is discretized by means of the following Finite Volume (FV) scheme. In the first step, the fracture domain Ω is partitioned into a set $\mathcal{Q}$ of 4^M non overlapping square control volumes $\mathcal{K}$ (i.e., $\forall j\ K_j \subset \Omega$ and $\bigcup_j \mathcal{K}_j = \Omega$). Let $\mathbf{x}_j$ be the center of the $\mathcal{K}_j$ control volume, and $\mathcal{K}_i$ the set of adjacent control volumes such that $i \in \sigma(j)$, with $\sigma(j) = \{E, W, N, S\}$ the set of neighboring control volumes. The edge between two cells is defined as:

$$\mathcal{K}_i \bigcap \mathcal{K}_j = \begin{cases} e_{ij} & \text{if} \quad i \in \sigma(j) \\ \varnothing & \text{otherwise .} \end{cases} \tag{3.16}$$

Note that $|e_{ij}| = h$ is the length of a side of the square control volume. Eq. (3.13) can be integrated over any of the cells $\mathcal{K}_j$ to obtain, up to an irrelevant plus or minus sign:

$$\forall j \quad \int_{\mathcal{K}_j} \boldsymbol{\nabla} \cdot \left[\left(a(\mathbf{x}) + b(\mathbf{x}) \|\boldsymbol{\nabla} P\|^{\frac{1}{n}-1} \right) \boldsymbol{\nabla} P \right] d\mathbf{x} = 0 \qquad (3.17)$$

Applying the divergence theorem in each finite volume $\mathcal{K}_j$ leads to

$$\int_{\partial \mathcal{K}_j} \left(a(\mathbf{x}) + b(\mathbf{x}) \|\boldsymbol{\nabla} P\|^{\frac{1}{n}-1} \right) \boldsymbol{\nabla} P \cdot \boldsymbol{\nu} \, ds = 0, \qquad j = 1, \dots, 4^M , \quad (3.18)$$

where $\boldsymbol{\nu}$ is now the outward unit normal vector on the finite volume edge $\partial \mathcal{K}_j$, which expresses that the integral of the flux $\mathbf{q} = \left(a(\mathbf{x}) + b(\mathbf{x}) \|\boldsymbol{\nabla} P\|^{\frac{1}{n}-1} \right) \boldsymbol{\nabla} P$ over $\mathcal{K}_j$ is zero:

$$\int_{\partial \mathcal{K}_j} \mathbf{q} \cdot \boldsymbol{\nu} \, ds = \sum_{i=1}^{4} \int_{e_{ij}} \mathbf{q} \cdot \boldsymbol{\nu} \, ds = 0, \qquad j = 1, \dots, 4^M . \quad (3.19)$$

Numerical integration by means of the mid-point quadrature rule over e_{ij} leads to a second-order approximation of the flux through each finite volume edge:

$$\sum_{i=1}^{4} \int_{e_{ij}} \mathbf{q}_i^{(j)} \cdot \boldsymbol{\nu}_i \, ds \cong +h \sum_{i=1}^{4} \mathbf{q}_i^{(j)} \cdot \boldsymbol{\nu}_i = 0 \qquad j = 1, \dots, 4^M , \quad (3.20)$$

where the edge fluxes are defined as $\mathbf{q}_i^{(j)} \cdot \boldsymbol{\nu}_i = \left(a_i^{(j)} + b_i^{(j)} \|\boldsymbol{\nabla} P_i^{(j)}\|^{\frac{1}{n}-1} \right) \boldsymbol{\nabla} P_i^{(j)} \cdot \boldsymbol{\nu}_i$. We then consider a numerical approximation to the pressure gradient's normal component on the edge, defined as

$$|\boldsymbol{\nabla} P_i^{(j)} \cdot \boldsymbol{\nu}_i^{(j)}| = \left| \frac{P_i - P_j}{h} \right| , \qquad (3.21)$$

and use this approximation for the Euclidean norm of the gradient evaluated at edge e_{ij}. This scheme results in a consistent approximation of the p-Laplacian in (3.13) as long as we maintain our discretization on a square mesh. Indeed, the approximation (3.21) is exact for affine functions on $\mathcal{K}$ (Andreianov et al., 2004) and the gradient approximation based on graph-Laplacians converges to the continuous counterpart for both the heterogeneous linear Laplace equation (Singer, 2006) and the nonlinear p-Laplace equation (Calder, 2018). Since the convergence rate is in any case only first order, the aperture in both the expressions for coefficients $a_i^{(j)}$ and $b_i^{(j)}$ is estimated considering the arithmetic mean

$$w_i^{(j)} = \frac{w_i + w_j}{2} . \qquad (3.22)$$

Note that the use of the harmonic mean would preserve the energy of the scheme. In spite of this, we opted for the arithmetic mean because it is less affected by the ill-conditioning induced by the aperture field's variability, which may span several orders of magnitude (Mazzia, Manzini & Putti, 2011).

3.5.2   Model implementation

In this section we describe the implementation details of our FV formulation of the non-linear lubrication equation (3.13). For each cell $\mathcal{K}_j$ we have:

$$\left(a_E^{(j)} + b_E^{(j)}\left|\frac{P_E - P_j}{h}\right|^{\frac{1}{n}-1}\right)(P_E - P_j) + \left(a_W^{(j)} + b_W^{(j)}\left|\frac{P_W - P_j}{h}\right|^{\frac{1}{n}-1}\right)(P_W - P_j)+$$

$$+\left(a_N^{(j)} + b_N^{(j)}\left|\frac{P_N - P_j}{h}\right|^{\frac{1}{n}-1}\right)(P_N - P_j) + \left(a_S^{(j)} + b_S^{(j)}\left|\frac{P_S - P_j}{h}\right|^{\frac{1}{n}-1}\right)(P_S - P_j) = 0,$$

$$(3.23)$$

valid for $j = 1, \ldots, 4^M$. After all the terms have been put together, the following system of non-linear equations is obtained:

$$F(\mathbf{p}) = A(\mathbf{p})\mathbf{p} - \mathbf{f} = 0 \ , \tag{3.24}$$

where $\mathbf{p}$ is the unknown pressure vector, and, for any given $\mathbf{p}$, the matrix $A(\mathbf{p})$ is symmetric positive definite and pentadiagonal, with coefficients A_{ij} given by

$$A_{ij} = \begin{cases} -\sum_{k \in \sigma(j)}\left(a_k^{(j)} + b_k^{(j)}\left|\frac{P_k - P_j}{h}\right|^{\frac{1}{n}-1}\right) & \text{if} \quad i = j; \\ a_i^{(j)} + b_i^{(j)}\left|\frac{P_i - P_j}{h}\right|^{\frac{1}{n}-1} & \text{if} \quad i \in \sigma(j); \\ 0 & \text{otherwise}, \end{cases} \tag{3.25}$$

The components f_j of the right-hand-side vector $\mathbf{f}$ are given by

$$f_j = \begin{cases} -\left(a_W^{(j)} + b_W^{(j)}\left|\frac{P_W - \overline{\nabla P}L}{h}\right|^{\frac{1}{n}-1}\overline{\nabla P}L\right) & \text{if} \quad j = k(t-2) \quad \text{for} \quad k = 1, ..., t-2, \\ 0 & \text{otherwise.} \end{cases}$$

$$(3.26)$$

The system of nonlinear algebraic equations (3.24) is solved by the Newton method, starting with an initial guess $\mathbf{p}_0$ that is the pressure field corresponding to Newtonian flow (exponent $n = 1$). Denoting k the Newton iteration number and $J(\mathbf{p})$ the Jacobian matrix, the Newton scheme takes on the form:

$$\begin{cases} J(\mathbf{p}_k)\mathbf{s}_k = -\mathbf{F}_k(\mathbf{p}_k); \\ \mathbf{p}_{k+1} = \mathbf{p}_k + \mathbf{s}_k. \end{cases} \tag{3.27}$$

Maximum number of PCG iterations (k_{max})	10^3
Drop tolerance (ϵ)	10^{-4}
Diagonal shift compensation coefficient (δ)	10^{-3}
PCG tollerance upper limit ($\eta_{\max}^{\text{lin}}$)	0.99
PCG tolerance scaling factor (η_0)	0.90

Table 3.2: Parameters for numerical integration.

where for the k-th Newton iteration the Jacobian matrix is formally defined as

$$J(\mathbf{p}) = \mathbf{F}(\mathbf{p})' = A(\mathbf{p}) + A(\mathbf{p})'\mathbf{p} , \tag{3.28}$$

where the A' symbol denotes the derivative of matrix A with respect to the pressures at each mesh node.

The calculation of the elements of the Jacobian matrix is provided in Appendix A with its generic ij-th element reported here:

$$J_{ij}(\mathbf{p}) = \begin{cases} \sum_{s \in \sigma(i)} \left(a_s^{(i)} + \dfrac{1}{n} b_s^{(i)} \left| \dfrac{P_s - P_i}{h} \right|^{\frac{1}{n}-1} \right) & \text{if } i = j; \\ -a_i^{(j)} - \dfrac{1}{n} b_i^{(j)} \left| \dfrac{P_i - P_j}{h} \right|^{\frac{1}{n}-1} & \text{if } i \in \sigma(j); \\ 0 & \text{otherwise} . \end{cases} \tag{3.29}$$

The resulting $J(\mathbf{p})$, at any given $\mathbf{p}$ is a symmetric, pentadiagonal, and positive definite matrix. We would like to remark here that the symmetry of $J(\mathbf{p})$ is a consequence of our specific choice of discretization method. Indeed, the symmetry of $J(\mathbf{p})$ arises from the symmetry of the particular operation of differentiation of the absolute value function. This symmetry allows the use of the Preconditioned Conjugate Gradient (PCG) method for the solution of the Newton linear system (3.27), with obvious improvements in computational performance. Row equilibration of the Jacobian matrix is achieved via diagonal scaling to improve the problem conditioning. This means that the left and right hand-side terms of Eq. (3.27) are both left-multiplied by $D(\mathbf{p})^{-1/2}$, $D = \text{diag}(J)$ being a matrix consisting solely of the Jacobian's main diagonal. Applying the scaling transformation results in a more accurate solution and reduces computational time. We obtain

$$D(\mathbf{p})^{-1/2}J(\mathbf{p})D(\mathbf{p})^{-1/2}D(\mathbf{p})^{1/2}\mathbf{s} = -D(\mathbf{p})^{-1/2}\mathbf{F}(\mathbf{p}), \tag{3.30}$$

The preconditioner of choice is a variable-fill-in incomplete Cholesky factorization.This preconditioning constitutes a problem transformation, which results in a smaller condition number, and consequently, improving the rate of convergence of PCG. The entire procedure detailed above is encapsulated within an inexact Newton-Krylov framework (Kelley, 1987). To avoid over-solving, the PCG exit tolerance is decreased as iterations progress using the

following rule:

$$\eta_k^{\text{lin}} = \begin{cases} \eta_{\text{max}}^{\text{lin}} & \text{if} \quad k = 0; \\ \min\left\{\eta_{\text{max}}^{\text{lin}}, \eta_0 \times \left(\dfrac{||\mathbf{F}(\mathbf{p}_k)||_2}{||\mathbf{F}(\mathbf{p}_{k-1})||_2}\right)^2\right\} & \text{otherwise,} \end{cases} \tag{3.31}$$

where the choice of $\eta_{\text{max}}^{\text{lin}} = 0.99$ and $\eta_0 = 0.9$ allows extracting most of the information from the inner iteration and guarantees an upper limit to the sequence $\{\eta_k^{\text{lin}}\}$. Table 3.2 summarizes these choices with the related values of the parameters.

When the exponent of the Ellis rheological model (n) is sufficiently small, and/or the applied macroscopic pressure gradient $(\overline{\nabla P})$ is too large, the pressure field of the solution for the Newtonian rheology $(n = 1)$ may not fall within the Newton basin of attraction of the PCG-based INK scheme, i.e., convergence may not be possible with that initial guess. A parameter continuation strategy has thus been implemented for such strongly non-linear cases. A sequence $\{n_d\}$ converging to the desired fluid ST index/exponent n_D can be constructed to approach the basin of attraction. The solution for the case n_{d-1} is used as initial guess for solving the case n_d. The sequence $\{n_d\}$ is obtained by subdividing the interval from 1 to n_D, according to the following rule:

$$n_d = \begin{cases} 1 & \text{if} \quad d = 0; \\ n_1\left(\dfrac{n_D}{n_1}\right)^{\frac{d}{D}} & \text{for} \quad d = 1, ..., D \end{cases} \tag{3.32}$$

where d indicates the parameter continuation iteration, while n_1 and n_D are the second and final ST indices of the sequence. In general, the index $n_1 = 1$ (Newtonian case) represents a valid candidate, but for strongly non-linear cases, indicatively when $n < 0.5$, the initial ST index can be imposed to 0.5 to reduce the computational time needed to achieve overall convergence.

Algorithm 2: Parameter continuation strategy pseudo-code.

$\mathbf{p}^{(0)} = A\backslash\mathbf{f}$;
for $d =$ **to** D **do**
$\quad$ **for** $k = 1$ **to** k_{max} **do**
$\quad\quad$ $J \leftarrow \texttt{DiagonalScaling}$;
$\quad\quad$ $J \leftarrow \texttt{Reordering}$;
$\quad\quad$ $C = \texttt{Michol}(J, \epsilon, \delta)$;
$\quad\quad$ $\mathbf{s} = \texttt{PCG}(J, F, C, \eta_k^{lin})$;
$\quad\quad$ **if** $||\mathbf{s}|| \leq \eta_d^{nl}$ **then**
$\quad\quad\quad$ $\mathbf{p}^{(d+1)} = \mathbf{p}^{(d)} + \mathbf{s}$;
$\quad\quad\quad$ **break**

The overall algorithm is summarized in Algorithm 2, with the functions having the following meaning:

1. `DiagonalScaling` implements equation (3.30);

2. `Reordering` applies the reverse Cuthill-McKee ordering;

3. `Michol` generates the PCG preconditioner C via incomplete Cholesky factorization;

4. `PCG` solves the linear system of equation (3.28) via PCG, adopting C as a preconditioner and η_d^{lin} as a tolerance stopping criterion.

The parameter continuation strategy estimates $\mathbf{p}^{(d)}$ following the sequence of shear thinning indices $\{n_D\}$ and uses η^{lin} and η^{nl} as tolerances for the linear and nonlinear iterations, respectively. The tolerance adopted for the continuation strategy is also reduced while approaching the final ST index n_D, such that

$$\eta_d^{\mathrm{nl}} = \eta_{\max}^{\mathrm{nl}} \left(\frac{\eta_D^{\mathrm{nl}}}{\eta_{\max}^{\mathrm{nl}}} \right)^{\frac{d}{D}} \quad \text{for} \quad d = 1, ..., D \; , \tag{3.33}$$

with $\eta_{\max}^{\mathrm{nl}} = 10^{-3}$ and $\eta_D^{\mathrm{nl}} = 10^{-8}$. This strategy allows achieving convergence in a limited number of steps even for strongly non-linear cases (e.g. $n \simeq 0.1$), covering essentially all fluids of practical interest.

3.6   Results

3.6.1   Experimental convergence of the proposed method

We first examine the experimental convergence of the proposed solver in practical applications. The test considers the domain described at the beginning of Section 3.5.1. A 2×2 aperture field (mesh level 0) is generated and kept constant as the mesh is refined, resulting in an aperture field of only four different values. A sequence of 8 mesh refinements (labeled level 1 to level 8) is then obtained by uniform subdivision while maintaining the original four-values aperture field for all the refined meshes originating from the same level-0 mesh. Since, as mentioned before, the scheme is consistent, the solution at mesh level 8 is considered as a "proxy" analytical solution against which we can calculate the error at different mesh levels. At each level M the L^2 error norm is evaluated as

$$\|e_M\| = \sqrt{\Delta x^2 \sum_j (P_{M,j} - P_{9,j})^2} \approx \sqrt{\int_\Omega (P_M - P_9)^2} \; . \tag{3.34}$$

Convergence of this sequence of errors together with the scheme consistency implies convergence to the true solution of the overall solver. We repeat these
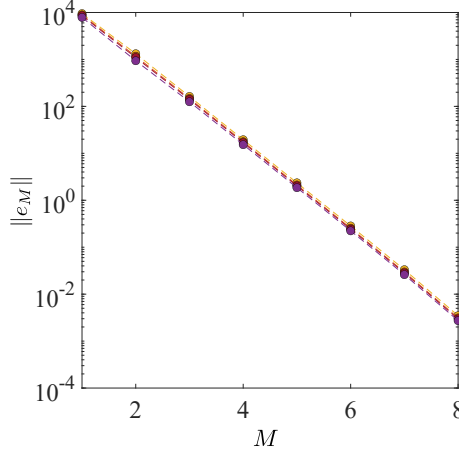
Figure 3.5: Logarithmic plot of $\|e_M\|$, the L^2 norm of the solution error calculated with respect to the finest mesh solution P_8 (mesh level 8), plotted as a function of the mesh level M (i.e., the 2-logarithmic mesh size). The different mesh levels are uniform refinements of a 2×2 initial aperture field. Different curves are related to the different fluids listed in table 3.1: F1 (yellow line), F2 (orange line), F3 (red line), and F4 (purple line). The superimposed lines show the first-order accuracy of the proposed solver.

simulations for all fluid types listed in Table 3.1. The results are shown in Figure 3.5, which shows the log-log plot of the error vs. the mesh level as identified by the value of M.

We now investigate the nonlinear convergence of the solver. Recall that, to minimize nonlinear iterations, the general strategy is to reduce the pre-asymptotic phase of the Newton method as much as possible, thus engaging efficient quadratic convergence as quickly as possible. For fluids characterized by n values in the range $0.5 \leq n \leq 1$ Newton quadratic convergence is always observed (see fluids F1-F3 in table 3.3). Conversely, in the most difficult situations, i.e., for strongly ST fluids characterized approximately by the n-range $0.1 \leq n < 0.5$, we resort to parameter continuation. As depicted in Figure 3.6 and reported in Table 3.3 for the fluid F4, the convergence speed of this latter strategy controls the computational efficiency for these difficult cases. The convergence is shown in Figure 3.6, where the L^2 norms of the difference between two consecutive iterations ($\mathbf{s}_p^{(d)}$) and of the nonlinear residual ($\mathbf{F}^{(d)}$) are plotted against the parameter continuation step. These norms are scaled by a factor $1/2^M$ to remove the dependency on mesh size. The results show an initial linear convergence often followed by superlinear convergence. This behavior can be intuitively expected as a consequence of the adopted scaled tolerance proposed in equation (3.31). In Table 3.3, the performance of the numerical scheme is reported in terms of the non-linear residual and difference between the two last iterations vs. normalized
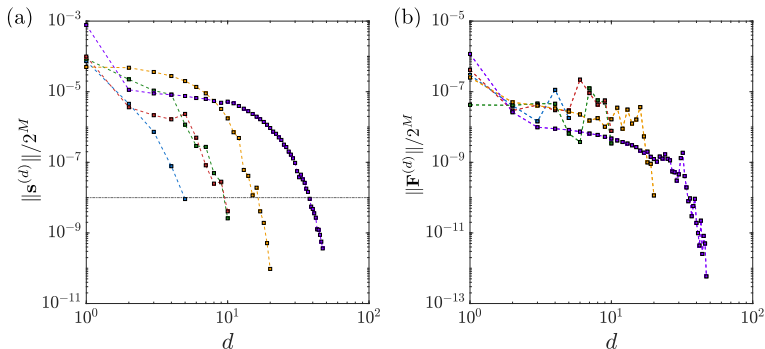
Figure 3.6: Continuation parameter convergence towards the solution for the most strongly ST fluid, F4 ($n = 0.1$). Panels (a) and (b) show the residual and the absolute error scaled norms at each continuation parameter step, respectively (see table 3.3). The aperture field (mesh size $2^M = 2^{10}$) adopted for this simulation has been generated with $L_c = 0.1$ m, $\langle w \rangle = 10^{-3}$ m, $H = 0.8$, $\sigma_w / \langle w \rangle = 1$, $\overline{\nabla P} / \overline{\nabla P_c} = 4.81$, and $L/L_c = 8$. Results refer to simulations reported in Table 3.3: blue (Sim 1), green (Sim 2), red (Sim 3), yellow (Sim 4), and purple (Sim 5). The dotted line in panel (a) represents the tolerance $\eta_{\max}^{\mathrm{nl}}$.

computational time. Different parameter continuation strategies are adopted for fluid F4, showing higher accuracy in the solution for a larger number of continuation iterations and the possibility to reduce computational time by considering a different value of n_1 in rule (3.32) for strongly ST fluids.

3.6.2 Impact of the rheology on the velocity field, apparent viscosity, and fracture transmissivity

The simulated flow field is on average co-current along the direction of $\overline{\nabla P}$, as an obvious consequence of the imposed boundary conditions, which force the flow from the left-hand to the right-hand side of Ω. However, aperture field heterogeneity results in channeling of the flow in the fracture plane along paths of less resistance. This phenomenon, and how it is impacted by fracture closure, has been studied for Newtonian flow for decades (Brown, 1987; Méheust & Schmittbuhl, 2001). The fracture closure $\sigma \simeq \langle w \rangle$ and the ratio L_c/L both control the aperture heterogeneity. The former quantifies aperture fluctuations with respect to the mean fracture aperture, as well as the amount of contact (if the closure is sufficiently large), while the correlation length defines the size of regions of correlated large apertures (or, equivalently, of correlated small apertures), which essentially controls the spatial patterns of flow channeling (Méheust & Schmittbuhl, 2003). In particular, correlated large aperture channels can form if $L \sim L_c$; if such a channel is aligned with the imposed macroscopic pressure gradient, the resulting permeability is larger than that of the smooth fracture of identical mean aperture (Méheust
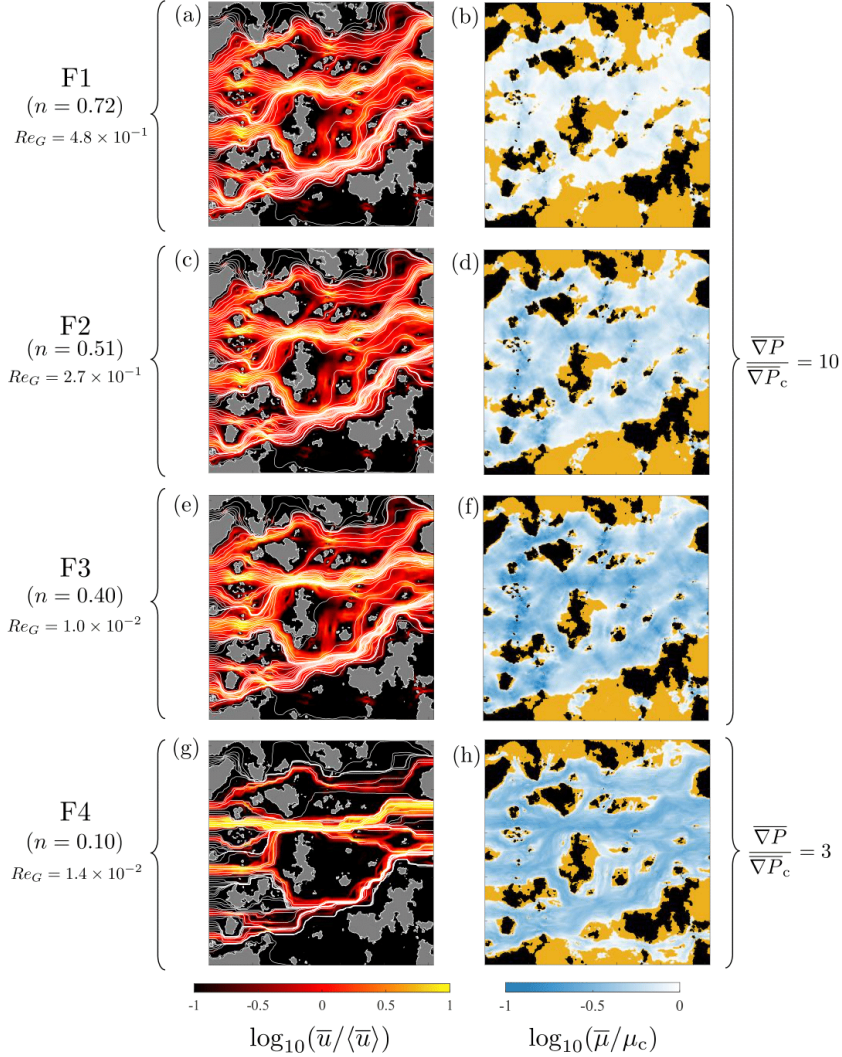
Figure 3.7: Maps of velocity magnitude $\overline{u}/\langle\overline{u}\rangle$ (left column) and depth-averaged apparent viscosity $\overline{\mu}/\mu_{\mathrm{c}}$ (right column) for different fluids. Each row is associated with a fluid listed in Table 3.1, with the fluid rheological index n decreasing from top to bottom. Streamlines (white continuous lines) are shown superimposed to the velocity maps, in the left column. In the viscosity maps (right column), the quasi-Newtonian areas ($\overline{\mu} \geq \mu_{\mathrm{c}}$) are colored in yellow. The aperture field is generated adopting the following parameters: $M = 10$, $H = 0.8$, $L/L_{\mathrm{c}} = 4$, $\langle w \rangle = 1$ mm, $\sigma_w/\langle w \rangle = 1$, $L = 0.4$ m, and $\overline{\nabla P}/\overline{\nabla P_c} = 20$ (fluids F1 to F3) or $\overline{\nabla P}/\overline{\nabla P_c} = 2$ (fluid F4).

Sim.	Fluid	$		\mathbf{F}^{(D)}		/2^M$	$		\mathbf{s}^{(D)}		/2^M$	t/t_0	Parameter Continuation
ID	ID	$(\mathrm{m}^2/\mathrm{s})$	(Pa/m)	(-)	N. Iterations (initial ST index)
Sim 1	F4	1.80×10^{-8}	9.10×10^{-9}	1021	5 ($n_1 = 1$)
Sim 2	F4	3.44×10^{-9}	2.58×10^{-9}	1662	10 ($n_1 = 1$)
Sim 3	F4	7.75×10^{-9}	4.08×10^{-9}	1095	10 ($n_1 = 0.5$)
Sim 4	F4	1.15×10^{-10}	9.56×10^{-11}	2041	20 ($n_1 = 0.5$)
Sim 5	F4	2.00×10^{-12}	6.11×10^{-9}	5960	50 ($n_1 = 0.5$)
Sim 6	F1	4.97×10^{-16}	2.82×10^{-10}	617	-
Sim 7	F2	1.03×10^{-14}	4.01×10^{-11}	678	-
Sim 8	F3	1.94×10^{-14}	1.45×10^{-9}	527	-

Table 3.3: Performance of the parameter continuation strategy for different numbers of iterations and initial ST index n_0. The algorithm performance is measured in terms of residual and absolute error scaled norms at the final continuation step. The normalized computational time is obtained by dividing the computational time (t) by the one of the Newtonian solver ($t_0 = 0.13$ s). The aperture field is generated with $L = 0.4$ m, $\langle w \rangle = 10^{-3}$ m, $H = 0.8$, $\sigma_w/\langle w \rangle = 1$, and $L/L_c = 8$, considering a dimensionless pressure gradient of $\overline{\nabla P}/\overline{\nabla P_c} = 4.81$.

& Schmittbuhl, 2000). Note however that such configurations are not favored statistically, (Méheust & Schmittbuhl, 2001), so, on average, heterogeneity induces higher energy losses across the fracture, which inevitably results in a lower transmissivity as compared to the parallel plate model. If the closure is sufficiently high, contact areas tend to exacerbate the behavior observed at closures that do not allow for fracture wall contact. Fractures where $L_c \sim L$ present few large contact zones, while for $L_c \ll L$ contacts are sparser across Ω and the fracture resembles a quasi-2D porous medium. In summary, flow localization is increased by increased fracture closure.

When a non-Newtonian, shear-thinning rheology is involved, all these effects are relevant, but additionally they are impacted by the fluid's rheology. Figure 3.7 illustrates the compound effect on flow localization of the ST fluid nature and of fracture heterogeneity. For each fluid listed in Table 3.1, the left-hand column shows maps of the ratio of the velocity magnitude $\overline{u} = ||\overline{\mathbf{u}}(\mathbf{x})||$ to the average velocity $\langle \overline{u} \rangle$, while the right-hand column shows the ratio of the depth-averaged apparent viscosity $\overline{\mu}(\mathbf{x})$ to the crossover viscosity $\mu_c = \overline{\mu}(\tau_c)$ (see definition of τ_c in Appendix B).

Figures 3.7a-c-e-g show that the flow localization increases for decreasing values of n (i.e. increasing fluid ST property). High velocities concentrate in areas of higher conductance, and low velocities in the proximity of contact zones, which typically exhibit higher resistance to flow due to aperture heterogeneity. This is similar to what is observed with Newtonian flow, but, in addition, figures 3.7b-d-f-h show that the high velocity regions coincide with low apparent viscosity values, as expected due to the shear-thinning nature of the fluid. Hence the flow of the shear-thinning fluid tends to be even more localized than that of the corresponding Newtonian flow.

Let us first discuss weakly ST cases. In these cases, it is seen that both velocity and apparent viscosity maps show a relatively slight dispersion around
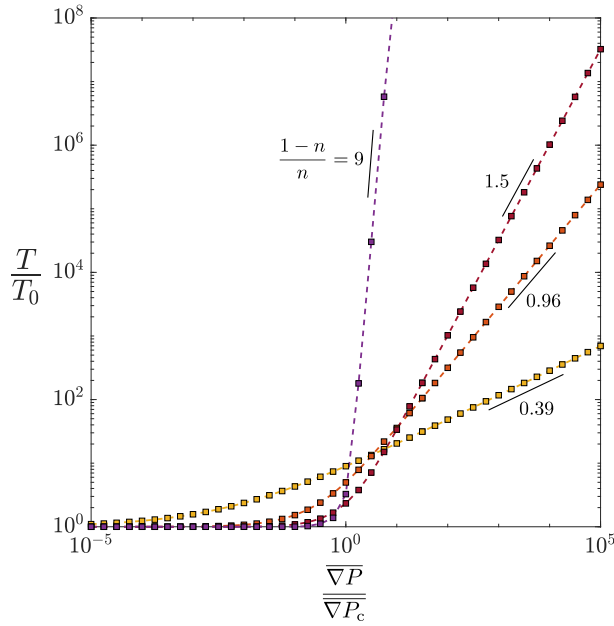
Figure 3.8: Transition from the quasi-Newtonian to the ST behaviour: ratio of the actual transmissivity T to the transmissivity T_0 for a Newtonian fluid of viscosity μ_0 as a function of the dimensionless pressure gradient $\overline{\nabla P}/\overline{\nabla P_c}$, evaluated for fluids F1-F4 in Table 3.1. Simulations have been conducted considering an aperture field generated with parameters: $M = 10$, $H = 0.8$, $\langle w \rangle = \sigma_w = 10^{-3}$ m, and $L/L_c = 4$. The color code for the fluids is the following: yellow line for F1, orange line for F2, red line for F3, and purple line for F4.
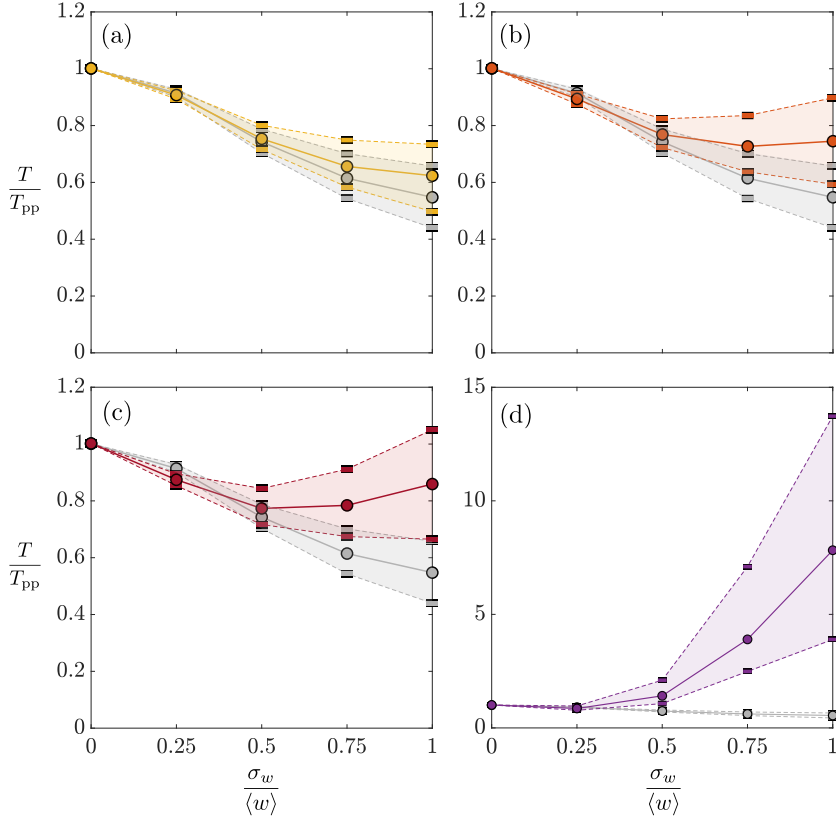
Figure 3.9: Dependence on the closure $\sigma_w / \langle w \rangle$ of the ratio of the actual transmissivity T to the Ellis parallel-plate model transmissivity T_{pp} , plotted in colors for fluids F1-F3 with $\overline{\nabla P} / \overline{\nabla P}_{\mathrm{c}} = 10$ and for fluid F4 with $\overline{\nabla P} / \overline{\nabla P}_{\mathrm{c}} = 3$. Confidence intervals are estimated over 200 simulations. Fracture realizations are generated with: $M = 10$, $H = 0.8$, $\langle w \rangle = 10^{-3}$ m, $L/L_{\mathrm{c}} = 4$ and $L = 0.4$ m. Panels (a) to (d) correspond to the different fluids reported in Table 3.1: (a) F1 in yellow, (b) F2 in orange, (c) F3 in red, (d) F4 in purple. The data plotted in grey shows the Newtonian behavior (which is identical for the four panels). The disks linked by a continuous line represent the median behavior, while the dashed lines show the confidence interval (25th and 75th percentile).

their ensemble average value. Small velocities are located in a limited portion of the fracture near the obstructions, where the apparent viscosity is close to μ_0, implying a quasi-Newtonian behaviour. On the other hand, low values of apparent viscosity are visible in small spots between contact zones, where the fluid is forced to flow under high shear rate conditions. Strongly ST cases exhibit a different behaviour, with a higher dispersion around ensemble averages for both velocity and apparent viscosity. The areas with lower apparent viscosity cover a larger percentage of the fracture plane and appear more elongated, with a more channel-like shape, as the exponent n is closer to its lowest investigated value, 0.1.

Next, we consider the fracture's global transmissivity defined as

$$T = \frac{Q\mu_0}{\overline{\nabla P}} \; . \tag{3.35}$$

Figure 3.8 depicts the transition from a quasi-Darcian flow ($T \propto \overline{\nabla P}$) to a non-linear regime ($T \propto \overline{\nabla P}^{\frac{1}{n}}$) for increasing dimensionless pressure gradients $\overline{\nabla P}/\overline{\nabla P_{\mathrm{c}}}$. As expected, the crossover occurs at the characteristic pressure gradient defined in equation (3.12). The Newtonian transmissivity T_0 is obtained from solving the flow for a ST index $n = 1$ and dynamic viscosity μ_0. The flow regime tends to the quasi-Newtonian behaviour at low imposed macroscopic pressure gradients $\overline{\nabla P}$, and diverges from it as $T \propto \overline{\nabla P}^{\frac{1}{n}}$ when a pressure gradient higher than $\overline{\nabla P_{\mathrm{c}}}$ is imposed.

Figure 3.9 illustrates how the fracture transmissivity T, normalized by the transmissivity T_{pp} of the equivalent parallel plate fracture (i.e., of aperture equal to the rough fracture's mechanical aperture), evolves as a function of the fracture closure, again for the fluids F1-F4 listed in Table 3.1. The behavior of the Newtonian case corresponding to a constant μ_0 viscosity, $T_0/T_{0,\mathrm{pp}}$, is also shown for comparison. Note that, for a fracture subjected to shear-thinning fluid flow, whether the walls are rough or not, T is not an intrinsic property of the fracture, it also depends on the imposed macroscopic pressure gradient $\overline{\nabla P}$ due to the non-linearity of the hydraulic response; on the contrary, T_0 is independent of $\overline{\nabla P}$. Here, the results for fluids F1-F3 refer to a dimensionless pressure gradient $\overline{\nabla P}/\overline{\nabla P_{\mathrm{c}}} = 10$, while for F4 it is $\overline{\nabla P}/\overline{\nabla P_{\mathrm{c}}} = 3$, as setting it to 10 would have brought the Reynolds number Re_G above the 1 upper limit for creeping flow. The results are shown for 200 fracture realizations generated with the same set of parameters (see caption of Figure 3.9). The curves go to 1 at small fractures closures, as expected. The ST property of the shear-thinning fluids increases continuously from (a) to (d), and indeed, the deviation of the ST fluid's behavior from that of Newtonian flow, increases all the more as the fracture closure is larger. Furthermore, this deviation is always positive, and can be so large at sufficiently large closures and for a sufficiently strong ST property (see e.g. the figure 3.9(c-d)), that the median behavior of a rough fracture becomes much more permeable than that of the equivalent parallel plate, by a factor which reaches an order of magnitude. Indeed, as

Fluid ID	F1	F2	F3	F4
$\overline{\nabla P}/\overline{\nabla P}_{\mathrm{c}}$	10	10	10	3
$T_{\mathrm{pp}}/T_{0,\mathrm{pp}}$	2.72	5.34	12.15	972.81

Table 3.4: Parallel-plate transmissivitiy ratios between the Ellis fluids listed in Table 3.1 (T_{pp}) and the corresponding Newtonian fluid ($T_{0,\mathrm{pp}}$), of dynamic viscosity μ_0. A constant separation $\langle w \rangle = 10^{-3}$ m is considered between the plates.

the flow becomes more localized in channels of low apparent viscosity and high velocity, conveying most of the volumetric flow rate of the fracture, the viscous dissipation within the fluid becomes less than what it would be in the homogeneous flow of the equivalent parallel plate configuration. In other words, the ST rheology contrasts the median tendency of transmissivity to decrease due to increasing aperture heterogeneity, and even reverts it in a spectular manner.

In addition, the dispersion over the statistics of the ratio T/T_{pp} also increases much more dramatically with fracture closure for ST flow than for Newtonian flow. This reflects the impact of the spatial arrangement of contact zones and of large permeability regions on the variability of the flow among the individual fracture realizations.

Note also that $T_0/T_{0,\mathrm{pp}}$, the ratio of the parallel plate transmissivity for the ST fluid to that for Newtonian flow, is also strongly dependent on the exponent n of the ST rheological law. Its values for the four fluids F1-4 are shown in Table 3.4. They vary from less than 3 to nearly 1000 as the ST exponent n varies from 0.72 down to 0.1. Finally, note that for all the fracture flow configurations addressed here, the generalized Reynolds number Re_G remains smaller than 1.

3.7 Discussion and Conclusions

This paper studies the combined effects of a nonlinear shear-thinning (ST) rheology and aperture variability on low Reynolds number flow in a single fracture. A Fourier transform based method is used to generate realistic synthetic aperture fields of geological fractures. A novel flow solver is derived to simulate the behavior of a ST fluid, whose rheology is modeled with an Ellis constitutive law, featuring an apparent viscosity with a low shear rate Newtonian plateau and a ST behavior of index n at larger shear rates.

The computational cost often associated with the solution of the non-linear system of equations has been optimized by the developed finite volume based solver, which yields a symmetric Jacobian that allows the implementation of a PCG-based inexact Newton-Krylov (INK) algorithm, to avoid over-solving. Furthermore, a continuation parameter strategy is used to handle strongly nonlinear cases with low n values.

The resulting code is robust for a wide range of ST index values (from 0.1 to 1), even in strongly heterogeneous cases implying a significant percentage of closed areas (e.g. $\sigma_w/\langle w \rangle = 1$), and for pressure gradients typical of forced flow in subsurface industrial applications (e.g. $\overline{\nabla P} = 10^5$ Pa/m), much higher than typical groundwater natural gradients. Computational efficiency is maximized by ensuring that convergence is always achieved. Linear convergence is typically displayed only during the initial Newton iterations and continuation parameters steps, while quadratic asymptotic convergence is always observed.

Concerning the physical effects jointly controlled by fluid rheology and heterogeneity, both the ST behaviour and aperture variability both contribute to flow localization. Elongated zones of high velocity and low apparent viscosity tend to form in a continuous pattern from the inlet to the outlet of the fracture for low ST index n and high coefficient of variation of the aperture field. Streamlines are affected by an increasing ST behaviour of the fluid, with the appearance of stronger localization patterns and zones where the flow is almost stagnant.

A sufficiently high externally-imposed macroscopic pressure gradient induces a non-Darcian flow regime leading to a non-Newtonian transmissivity that is higher than its Newtonian counterpart, possibly by several orders of magnitude. Such a strong non-linear tendency is mainly due to the bulk of the flow being conveyed in marked preferential channels, typically along the path of lowest resistance, where the velocity is high and the apparent viscosity is low. The transition from a (quasi-)Darcian to a non-linear regime occurs when the magnitude of the average shear stress is larger than a characteristic value, itself a function of fluid and fracture properties. Equivalently, this transition occurs close to a characteristic value of the applied macroscopic pressure gradient which is related analytically to the aforementioned characteristic shear stress. Both quantities can be defined analytically from the Ellis constitutive law.

When multiple realizations are examined, an interesting observation becomes evident. The median fracture transmissivity decreases with increasing aperture heterogeneity (and thus closure) as expected (and well-known for Newtonian flow), but the fluid ST behaviour tends to mitigate this effect as a result of the aforementioned enhanced flow channeling. Thus, an increase in non-Newtonian behaviour contrasts the tendency of transmissivity to decrease due to increasing aperture heterogeneity. So much so that for sufficiently large fracture closures and ST properties, the transmissivity is seen to increase again with fracture closure, and to exceed by up to one order of magnitude the Newtonian transmissivity.

The performance achieved with this numerical scheme allows overcoming the limits of the current numerical alternatives. Future prospects include a systematic stochastic analysis of ST flow in geological fractures, considering numerous realizations for the same set of statistical geometric parameters, as well as the impact of the combined effect of fracture heterogeneity and complex rheology on anomalous transport.

3.8   Appendix A - Jacobian analytical formulation

The present Appendix provides details on the analytical evaluation of the Jacobian matrix. The relationship between the Jacobian matrix $J(\mathbf{p})$ and the matrix A is given in equation (3.28). In terms of components, we can write the the Jacobian matrix as:

$$J_{ij} = A_{ij} + \sum_{u=1}^{4^M} \frac{\partial A_{iu}}{\partial P_j} P_u = \begin{cases} A_{ij} + \dfrac{\partial A_{ij}}{\partial P_j} P_j + \dfrac{\partial A_{ii}}{\partial P_j} P_i & \text{if } i \in \sigma(j) \\ A_{ii} + \dfrac{\partial A_{ii}}{\partial P_i} P_i + \sum_{k\in\sigma(i)} \dfrac{\partial A_{ik}}{\partial P_i} P_k & \text{if } i = j \\ 0 & \text{otherwise .} \end{cases}$$

(3.36)

The Jacobian has the same sparsity pattern as A, resulting in a pentadiagonal matrix. The non-zero components in Eq. (3.36) can be derived from those of A as follows:

$$\frac{\partial A_{iu}}{\partial P_j} = \left(\frac{1}{n}-1\right)\begin{cases} -\sum_{k\in\sigma(u)} b_k^{(u)}\left|\dfrac{P_k-P_u}{h}\right|^{\frac{1}{n}-1}\dfrac{1}{P_k-P_u} & \text{if } u=i=j; \\ +b_i^{(j)}\left|\dfrac{P_i-P_j}{h}\right|^{\frac{1}{n}-1}\dfrac{1}{P_i-P_j} & \text{if } u=j \text{ and } i\in\sigma(j); \\ -b_i^{(j)}\left|\dfrac{P_i-P_j}{h}\right|^{\frac{1}{n}-1}\dfrac{1}{P_i-P_j} & \text{if } i=u\neq j; \\ +b_u^{(j)}\left|\dfrac{P_u-P_j}{h}\right|^{\frac{1}{n}-1}\dfrac{1}{P_u-P_j} & \text{if } i=j\neq u; \\ 0 & \text{otherwise,} \end{cases}$$

(3.37)

which defines the matrix A' mentioned in section 3.5.2. Substituting the expression of the components of Eq. (3.37) in Eq. (3.36) leads to the following formulation for the Jacobian

$$J_{ij} = \begin{cases} -a_i^{(j)} - \dfrac{1}{n}b_i^{(j)}\left|\dfrac{P_i-P_j}{h}\right|^{\frac{1}{n}-1} & \text{if } i\neq j \\ \sum_{k\in\sigma(j)}\left(a_k^{(j)} + \dfrac{1}{n}b_k^{(j)}\left|\dfrac{P_k-P_j}{h}\right|^{\frac{1}{n}-1}\right) & \text{if } i=j \\ 0 & \text{otherwise,} \end{cases}$$

(3.38)

where it can be noted that the Jacobian is symmetric (i.e., $J_{ij} = J_{ji}$), since $a_i^{(j)} = a_j^{(i)}$ and $b_i^{(j)} = b_j^{(i)}$.

3.9   Appendix B - Estimation of the parameters of the Ellis model from the Carreau-Yasuda model

This Appendix illustrates how the parameters of the fluids used in the main body of the paper were derived. In general, simple non-Newtonian rheological

Fluid ID	Solution	μ_0' (Pa·s)	μ_∞' (Pa·s)	n' (−)	$\dot{\gamma}_c$ (s⁻¹)	a' (−)
F1	CMC at 0.3 wt%	0.0510	0.001	0.72	17.67	0.71
F2	CMC at 0.5 wt%	0.2203	0.001	0.51	15.85	0.565
F3	CMC at 1.0 wt%	2.9899	0.001	0.40	2.74	0.668
F4	VES	49	0.0003	0.10	0.10	2.00

Table 3.5: Rheologic parameters related to the four fluids: experimental data are fitted with the Carreau-Yasuda models. Parameters for the Carboxymethylcellulose (CMC) solutions are provided in Sousa et al. (2005), while those for the visco-elastic surfactant (VES) are taken from (Moukhtari & Lecampion, 2018). Corresponding Ellis rheological parameters are listed in Table 3.1.

models such as the Ellis constitutive law (Eq. (3.2)) are empirical nonlinear relationship between stress and strain rate that can be adopted to model shear-thinning rheology.

When two different models are fitted to experimental data, rheological parameters are estimated by best fitting and no given correspondence between the two sets of parameters exists. Here, due to the scarcity of Ellis model parameters fitted on rheological data in the literature, and in the interest of comparison and simplification, we inferred the Ellis parameters from existing data hitherto interpreted with the Carreau-Yasuda model. The latter is a five-parameter model, frequently adopted because it typically reproduces the rheology of shear-thinning fluids well; its apparent viscosity is expressed as a function of the shear rate $\dot{\gamma}$ as

$$\mu = \mu_\infty' + \frac{\mu_0' - \mu_\infty'}{\left[1 + (\dot{\gamma}/\dot{\gamma}_c)^{a'}\right]^{\frac{1-n'}{a'}}} \ , \tag{3.39}$$

where μ_0' and μ_∞' are respectively the low and high shear rate apparent viscosity plateaus, $\dot{\gamma}_c$ is the characteristic shear rate separating the low-shear, pseudo-Newtonian regime from the intermediate power-law regime, a' is an index that influences the shape of the transition between the intermediate power-law behaviour and the high shear rate plateau μ_∞, and n' is a shear-thinning index. Fixing the value of a' to 2 results in a four-parameter model, termed the Carreau model.

In low Reynolds number applications, the high shear rate plateau can be neglected ($\mu_\infty' \approx 0$) and a low shear rate approximation of Eq. (3.39) is obtained as

$$\mu = \frac{\mu_0}{\left[1 + (\dot{\gamma}/\dot{\gamma}_c)^{a'}\right]^{\frac{1-n'}{a'}}} \ . \tag{3.40}$$

We consider a given Yasuda-Carreau flow curve and proceed to analytically find the Ellis model (Eq. (3.4)) that best fits the corresponding flow curve $\mu(\dot{\gamma})$. This implies that the low-shear rate viscosity plateaus be identical, and

the power law regimes as well. The former constraint immediately implies that $\mu_0 = \mu_0'$, while the latter implies that the Carreau-Yasuda power law trend, which for $\dot{\gamma} \gg \dot{\gamma}_c$ can be simplified to

$$\mu = \mu_0' \left(\frac{\dot{\gamma}_c}{\dot{\gamma}} \right)^{1-n'} , \tag{3.41}$$

be identical to that of the Ellis model, which for $\tau \gg \tau_{1/2}$ can be approximated to

$$\mu = \mu_0 \left(\frac{\tau_{1/2}}{\tau} \right)^{\frac{1-n}{n}} . \tag{3.42}$$

Substituting the constitutive equation $\tau = \mu\dot{\gamma}$ in Eq. (3.42) and recalling that $\mu_0 = \mu_0'$ yields

$$\mu = {\mu_0'}^{n} \left(\frac{\tau_{1/2}}{\dot{\gamma}} \right)^{1-n} , \tag{3.43}$$

which can now be identified to Eq. (3.41). We thus immediately obtain $n = n'$ and

$$\tau_{1/2} = \mu_0' \dot{\gamma}_c . \tag{3.44}$$

Conversely, when determining the crossover pressure gradient $\overline{\nabla P}_c$ from Eq. (3.12), the crossover shear stress τ_c to be considered is that corresponding to the crossover shear rate $\dot{\gamma}_c$ of the Carreau-Yasuda model. It can thus be estimated from the Ellis model parameters by solving the following implicit equation numerically:

$$\frac{\tau_c}{\tau_{1/2}} = \left[1 + \left(\frac{\tau_c}{\tau_{1/2}} \right)^{\frac{1}{n}-1} \right]^{-1} . \tag{3.45}$$

4 | Monte Carlo Simulations of Shear-thinning Flow in Geological Fractures

4.1 Abstract

The hydraulic behaviour of fractured rocks under non-Newtonian flow conditions is a challenging topic of interest in several fields, related either to environmental remediation or to natural resources recovery. Indeed, many fluids involved in such subsurface operations are non-Newtonian, and the compound effects of fluid rheology and medium heterogeneity strongly affect flow and transport in fractured geological formations. In this work, a stochastic analysis has been conducted via direct numerical Monte Carlo simulations to investigate the behaviour of shear-thinning fluids in fractures subjected to both natural and forced flow (low and high pressure drops respectively), considering different fracture dimensions, for a spatial correlation of the fracture that is an intrinsic parameter of the formation and thus independent of the fracture size. Considering the lubrication approximation, a generalized Reynolds equation for shear-thinning fluids is solved using an ad hoc, finite volume-based, numerical scheme. The influence of the rheology and aperture field heterogeneity on ensemble statistics of the velocity components and magnitude, as well as apparent fracture-scale transmissivity, is quantified over 10^3 fracture realizations. The probability density functions (PDFs) obtained by averaging over the set of realizations and the relative confidence intervals are analysed to comprehend the apparent transmissivity transition from Newtonian to shear-thinning regime. Moreover, the autocorrelation functions of velocity components are computed to understand the impact of rheology on spatial correlations of the flow. Velocity components exhibit narrow PDFs with nearly exponential decay. Under forced flow, elevated pressure gradients emphasize the shear-thinning behaviour, inducing a more marked flow localization for the shear-thinning rheology than for Newtonian flow, under otherwise identical conditions. This translates at the scale of the fracture into a much larger apparent transmissivity, by orders of magnitude.

4.2 Introduction

Flow modelling of complex fluids in geological formations is of interest in numerous industrial applications. Among them are enhanced oil recovery

(Hirasaki, Miller & Puerto, 2011; Leung et al., 2014), geothermal circulations in fractured reservoirs (Bächler, Kohl & Rybach, 2003; Magzoub, Salehi, Li, Fan & Teodoriu, 2021) and fluid losses during drilling operations (Feng & Gray, 2017), where foams, muds, emulsions, colloidal or non-colloidal suspensions are commonly involved. The use of high-viscosity gels in hydraulic fracturing improves the proppant carrying capacity and favours the generation of wider fracture in comparison to the use of slickwater (Pahari, Bhandakkar, Akbulut & Kwon, 2021). Drilling muds provide cooling and lubrication to drill bit and are employed as mechanical stabilizers in the construction of the wellbore to pressurize the borehole against collapse. The constitutive law of these fluids does not respect Newton's law of viscosity, because their microstructure induces a shear-thinning rheology at the continuum scale (Barati & Liang, 2014; Ansari, Turney, Morris & Banerjee, 2021). The non-Newtonian behaviour of these fluids lies in their physical make-up and the ability of mesoscopic components to cross-link chemically (e.g. polymer solutions, see (Wang, Tang, Guo & Wang, 2016b)) or interact electrostatically (e.g. colloidal suspensions, see (Parmar, Méheust & Fossum, 2008; Méheust, Parmar, Schjelderupsen & Fossum, 2011)).

Subsurface geological formations (e.g. crustal rocks) are discontinuous media, consisting in matrix blocks of low permeability separated by fractures, which provide major conduits for flow. The connectivity among fractures and their hydraulic behaviour are the features that control the entire formation permeability (Berkowitz, 1994). The simplest model to study the hydraulic behaviour of a fracture is the parallel plate model or cubic law. This model has been largely used for its simplicity, although it oversimplifies wall topography. Different approaches have been proposed also to represent rough fractures: deterministic saw tooth (Wilson & Witherspoon, 1974), sinusoidal profiles (Elsworth & Goodman, 1986), or profiles with an assigned aperture probability distribution (Neuzil & Tracy, 1981; Felisa et al., 2018; Lenci & Di Federico, 2020). In minerals and rocks, however, field and laboratory measurements on fracture walls highlight the stochastic self-affine nature of the surface morphology, for both natural (Brown & Scholz, 1985; Schmittbuhl et al., 1993; Cox & Wang, 1993) and fresh artificial fractures (Schmittbuhl et al., 1993; Bouchaud, 1997). Several algorithms are able to reproduce this kind of rough surfaces, which are more consistent with the experimental evidence: diamond-square algorithm (Fournier et al., 1982), successive random addition (Lu, Molz & Liu, 2003), and the FFT-based algorithm proposed by (Méheust & Schmittbuhl, 2003), which is far quicker.

Predictions of fracture transmissivities based on the parallel plate model significantly deviate from measurements, especially under elevated normal (Gale, 1990) or cyclic shear stresses (Makurat, 1985), limiting its use to sufficiently smooth fractures. Traditional computational fluid dynamics (Starchenko, Marra & Ladd, 2016), lattice gas (Gutfraind, Ippolito & Hansen, 1995; Stockman, 1997) and lattice Boltzmann methods (Meakin & Tartakovsky, 2009; Tian & Wang, 2017) have been adopted to capture the impact of the complex

geometry of fractures on Newtonian flow, and thus to accurately predict flow and transport attributes, although the simulations are computationally intensive. Alternative numerical methods, based on lubrication theory and computationally more convenient, have been proposed to solve Newtonian creeping flow in rough fractures: standard matrix inversion techniques (Brown, 1987) or pseudospectral methods (Plouraboué, Hulin, Roux & Koplik, 1998). Estimation of the mean hydraulic aperture of a large number of independent fractures show a difference of up to 2 per cent (Mourzenko et al., 1995) between a lubrication-based solver and CFD simulations. Furthermore, due to the stochastic nature of the geometry of geological fractures, fractures described by the same statistical geometrical parameters can display a wide range of hydraulic behaviors (Méheust & Schmittbuhl, 2001, 2003), including behavior that are more permeable than the parallel plate of identical mean aperture (Méheust & Schmittbuhl, 2000), and thus the typical hydraulic behavior of a geological fracture should be understood as the average over a representative statistics, and the dispersion of the behaviors among the statistics should also be investigated. To our knowledge, (Méheust & Schmittbuhl, 2001) performed the first such Monte Carlo simulations of Newtonian creeping flow in geological fractures with realistic geometries.

Monte Carlo simulations have been adopted for decades to simulate different processes in a variety of geologic media: a limited number of realizations of 1-D variable aperture fractures were produced by (Tsang & Tsang, 1987) to investigate flow in fracture channels; the same approach was then generalized to 2-D fractures, although with spatial distributions of apertures that are more relevant to 2-D aquifer permeability fields than to geological fractures (Moreno et al., 1988). The pioneering work of Bellin, Salandin & Rinaldo (1992) investigated the conditions for the validity of first-order flow and transport theories in random porous media; Berkowitz & Scher (1998) adopted a Monte Carlo approach to determine velocity distributions in fracture networks, as a function of the fracture orientations, to study anomalous transport at the network scale; Gómez-Hernández & Wen (1998) analysed the applicability of multi-gaussian random function models in hydrogeology. More recently this methodology has been applied to study transient sequentially coupled radionuclide transport (Hayek, RamaRao & Lavenue, 2020), to investigate flow in two dimensional conductivity field to derive a large-scale transport model (Comolli, Hakoun & Dentz, 2019), to simulate CO2 plume migration (Zhong, Sun & Jeong, 2019), and to perform uncertainty quantification (Yang, Boso, Tchelepi & Tartakovsky, 2020).

Notwithstanding the ubiquitous use of complex fluids in the subsurface, their behaviour is often reduced to the Newtonian rheology, with a limited number of studies having focused on non-Newtonian fluid flow. Several analytical expressions have been proposed to comprehend the flow features in simple geometries (Larson, 1992), or to qualitatively asses the effect of fluid rheology on flow in a variable aperture field of a given distribution (Di Federico, 1997). Different numerical strategies have been adopted to handle problem

non-linearity when dealing with a complex rheology in a variable aperture field: Picard's method (Morris et al., 2015), and sequential sweeping (Lavrov, 013a). A few studies have also addressed non-Newtonian flow in fractures with self-affine geometries (Auradou et al., 2008; Perkowska et al., 2016; Lenci et al., 2022a). Recently, advances in computational power have allowed the investigation of complex processes, such as: multiphase flow (Katiyar, Agrawal, Ouchi, Seleson, Foster & Sharma, 2020), transport in fracture of permeable walls (Dejam, 2019), and hydro-mechanical coupling (Moukhtari & Lecampion, 2018; Wrobel, Mishuris & Papanastasiou, 2021; Chiapponi et al., 2019; Ciriello et al., 2021). Despite this wealth of contributions using different constitutive models and hypotheses, to date Monte Carlo simulations have never been applied to investigate shear-thinning hydrodynamics in rough fractures under natural and artificial flow conditions. Here, we extend the state of art by exploring non-Newtonian fracture hydraulic behaviour, understanding the intertwined role of shear-thinning rheology and fracture heterogeneity.

Recently, (Lenci et al., 2022a) proposed a novel numerical scheme that allows efficiently solving a generalized lubrication equation for the flow of fluids with a markedly shear-thinning (ST) rheology, thus making possible a stochastic analysis of ST flow in rough fractures that does not require excessive computational time. The numerical finite volume scheme is solved with an inexact Newton-Krylov algorithm, yielding results that are sufficiently robust for most fluid cases of practical interest.

The article is organized as follows: section 4.3 presents the non-linear lubrication equation for a non-Newtonian Ellis fluid, the generation process of discrete fractures, and describes the implementation of the lubrication-based numerical code; in section 4.4, the adopted stochastic approach is described; section 4.5 presents the results of the Monte Carlo simulations performed, emphasizing the ensemble statistics obtained: these include the apparent transmissivity, the vertical and longitudinal velocity components, and the velocity modulus; the covariance of the latter is also analyzed. Conclusions and perspectives for future work are formulated in section 4.6.

4.3   Modeling framework

4.3.1   Generation of synthetic fractures

A geological fracture is composed of two rough walls, whose parallel mean planes are separated by $\langle w \rangle$, defined as the mechanical aperture. The topographies of the upper (z_u) and lower wall (z_l), assumed of mean 0, fluctuate with respect to their mean planes, and local apertures can be defined as the distance between them; at positions where the two walls interpenetrate, a zero aperture is imposed.

$$w(x, y) = \max(0, z_u(x, y) - z_l(x, y) + \langle w \rangle) . \tag{4.1}$$

(a)

(b)
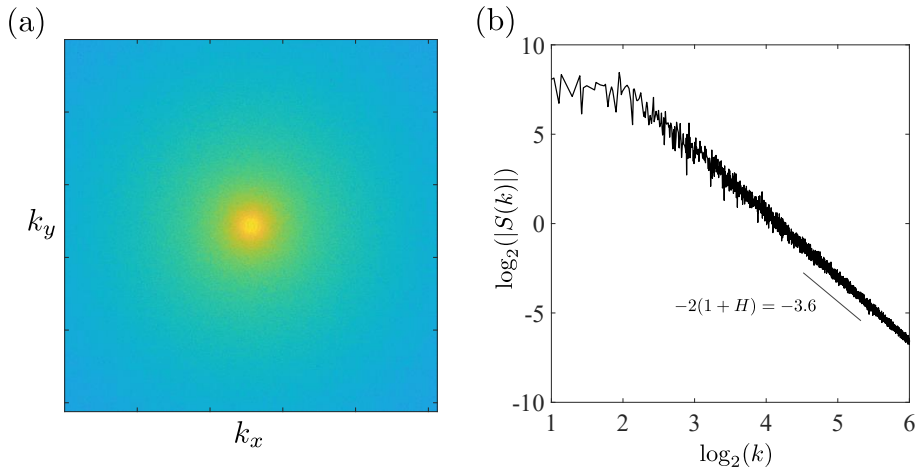
Figure 4.1: (a) Map of the power density spectrum of a synthetic fracture surface distribution: Fourier modes k_x and k_y are in linear scales; the isotropic spectrum is stochastic and exhibits the typical radial power law decay $\propto (k_x^2 + k_y^2)^{-(1+H)}$; (b) radial averaging power density spectrum of a rough fracture's aperture field; it displays the above-mentioned self-affine behaviour for wave numbers larger than k_c, and is constant otherwise for $k \leq k_c$. (a) and (b) are both generated considering: a Hurst exponent $H = 0.8$, a closure of $\sigma_w/\langle w \rangle = 0.8$, a correlation ratio $L/L_c = 0.8$, a mean aperture $\langle w \rangle = 10^{-3}$ m, and a fracture length $L = 1.6$ m.

Fracture surfaces exhibit long-range spatial correlation (Candela, Renard, Bouchon, Brouste, Marsan, Schmittbuhl & Voisin, 2009; Schmittbuhl et al., 1995a). Therefore, the topography of a geological fractures's rough wall topography is an isotropic self-affine surface, with the probability distribution function (PDF) $f(\Delta z, \Delta r)$ scaling as:

$$\forall \lambda \quad f(\Delta z, \Delta r) = \lambda^H f(\lambda^H \Delta z, \Delta r), \tag{4.2}$$

where Δh is the height difference between two points separated by an in-plane segment of length Δr, H is the Hurst exponent, and λ is a scaling factor. Note that fracture surfaces in crystalline rocks consistently show a Hurst exponent of 0.8 (Méheust & Schmittbuhl, 2000), and this value has been proposed as universal by Bouchaud et al. (1990). However, exceptions exist, such as sandstones, in which the grain-induced roughness regime, for high frequencies in the power spectrum, may present values close to 0.5 (Boffa, Allain, Chertcoff, Hulin, Plouraboué & Roux, 1999; Nigon, Englert, Pascal & Saintot, 2017). One consequence of the scaling property of the PDF in Eq. (4.14) is that the two-dimensional power density spectrum of wall topography scales as a power law of the wave number in the form $S(k) \propto k^{-2(1+H)}$, where the wave number k is the norm of the wave vector, i.e., $k = (k_x^2 + k_y^2)^{1/2}$, k_x and k_y being the components of the wave vector.

The two walls of a geological fracture are matched at large length scales but differ at scales smaller than a crossover scale, which we shall denote the correlation length L_c (Brown, 1995). This is due to mechanical wear and chemical weathering over long times. It follows that the aperture field exhibits the same self-affinity as the walls at scales smaller than L_c, and, thus, that the aperture field's Fourier spectrum exhibits the characteristic self-affine power-law scaling at these small scales, and an almost flat behaviour due to the matching of the two walls at scales larger than L_c. Consequently, the spectral power density of the aperture field exhibits the above-mentioned power-law radial decay, of negative exponent $-2(H + 1)$ for wave numbers higher than k_c, the characteristic wave number corresponding to scale L_c (Schmittbuhl et al., 1995b), and is wave numbers smaller than k_c.

This property can be used to generate realistic synthetic aperture fields from a two-dimensional white noise, maintaining its random phase and introducing the spatial correlations by multiplying the Fourier modes corresponding to scales smaller than L_c by the power-law behavior $k^{-(H+1)}$ (Méheust & Schmittbuhl, 2003). Applying an inverse Fourier transform then yields an aperture field with the appropriate geometry, which can then be scaled and translated vertically so as to impose the desired mean aperture and standard deviation of aperture fluctuations. Fig. 4.1a depicts the two-dimensional Fourier spectrum of such a synthetic aperture field, while Fig. 4.1b presents its average radial profile, with the scaling properties discussed above. Fig. 4.2 shows the comparison between two different aperture fields having the same correlation length but different fracture sizes, and thus a markedly different size-to-correlation-length ratio. The latter parameter will be later seen to affect the flow behaviour quite significantly.

4.3.2   Generalized Reynolds Equation

We consider the steady-state, isothermal Stokes flow of an incompressible fluid between two smooth parallel straight walls separated by a uniform distance w. Under the action of a a flow-inducing, externally-applied, pressure gradient $\boldsymbol{\nabla} P = [\partial_x P, \ \partial_y P]^\top$, the flow is parallel (in particular, its vertical component is 0) and the momentum conservation can be written as:

$$\frac{\partial}{\partial z}\left(\mu \frac{\partial \mathbf{u}}{\partial z}\right) = \boldsymbol{\nabla} P, \qquad (4.3)$$

where $\mathbf{u} = [u_x, \ u_y]^\top$ is the velocity vector, and μ is the dynamic viscosity or the apparent viscosity if the fluid is Newtonian or non-Newtonian, respectively. After integrating over the z-direction, the momentum conservation becomes

$$\mu \frac{\partial \mathbf{u}}{\partial z} = \boldsymbol{\nabla} P \ z, \qquad (4.4)$$

which can be re-written using the definition of shear stress as $\tau = \boldsymbol{\nabla} P \cdot z$.
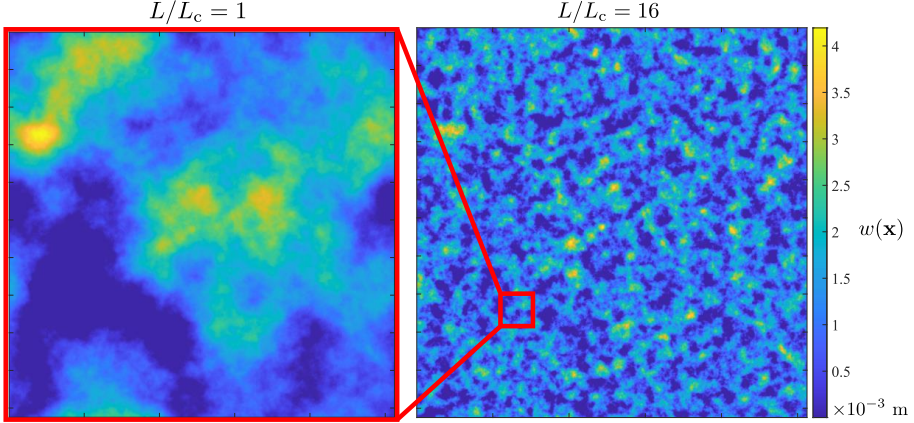
Figure 4.2: Comparison between aperture fields for different values of $L/L_{\rm c}$; the colorbar reports the aperture magnitude in meters for both representations. The two realizations are generated with: a Hurst exponent $H = 0.8$, a closure $\sigma_w/\langle w \rangle = 0.8$, a correlation length of $L_{\rm c} = 10^{-1}$ m, and a mean aperture of $\langle w \rangle = 10^{-3}$ m. The red frames illustrate the size ratio between the two fractures, which is 16.

For a generalized Newtonian model, the apparent viscosity can be expressed in terms of shear stress or shear rate. In particular, the Ellis fluid rheology is a three-parameter model:

$$\mu = \mu_0 \left[1 + \left(\frac{\tau}{\tau_{1/2}} \right)^{\frac{1}{n}-1} \right]^{-1}, \tag{4.5}$$

where μ_0 is the dynamic viscosity at low shear rates, n is the shear-thinning index that defines the power-law trend at high-shear stress, and $\tau_{1/2}$ is a characteristic shear stress such that $\mu(\tau_{1/2}) = \mu_0/2$. This model reduces to the Newtonian rheology for $n = 1$ or $\tau_{1/2} \to \infty$. In Figure 4.3, the dependence of the apparent viscosity on the shear rate is represented in colors for two examples of Ellis fluids, showing the low shear-rate quasi-Newtonian plateau and the high shear rate shear-thinning power-law trend.

If the fluid is Newtonian, the relationship between the volumetric flow rate $\boldsymbol{Q}$ and $\boldsymbol{\nabla}P$ is given by the Hagen-Poiseuille law, which effectively expresses Darcy's law with an intrinsic permeability $w^2/12$. Similarly, for the Ellis model it is possible to analytically derive the velocity profile by introducing Eq. (4.10) in Eq. (4.9) and integrating over the z-direction:

$$u(z) = -\left\{ \frac{1}{8\mu_0} \left[w^2 - \left(\frac{z}{2} \right)^2 \right] + \frac{n}{n+1} \left(\frac{1}{2^{n+1} \mu_0^n \tau_{1/2}^{1-n}} \right)^{\frac{1}{n}} \times \right.$$
$$\left. \times \left[w^{\frac{1}{n}+1} + \left(\frac{z}{2} \right)^{\frac{1}{n}+1} \right] ||\boldsymbol{\nabla}P||^{\frac{1}{n}-1} \right\} \boldsymbol{\nabla}P, \tag{4.6}$$
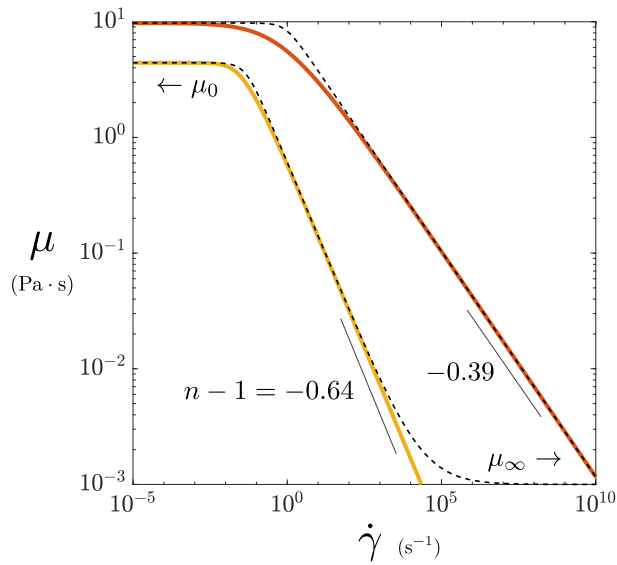
Figure 4.3: Dependence of the apparent viscosity μ on the shear rate $\dot{\gamma}$. The constitutive equation is represented for two Ellis fluids of different shear-thinning behaviour: a xanthan gum, the yellow-solid line, and a silicon oil, the orange-solid solid lines. Both fluids show a low-shear rate Newtonian plateau ($\mu \to \mu_0$), while black-dashed lines report the relative original Carreau model. The black dashed lines are similar curves obtained for two Carreau fluids with the same low-shear plateaus and power law behaviors as each of the two Ellis fluids, respectively, and a high shear asymptotic viscosity of 10^{-3} Pa·s for one of them (the other one's high shear plateau is not visible).

which returns the Newtonian velocity profile for $n = 1$ (or $\tau_{1/2} \to 0$), and leads to a generalized Hagen-Poiseuille law after integration over the aperture and the along the y direction.

The generalized Hagen-Poiseuille law can be assumed to hold locally also in a variable aperture field $w = w(\mathbf{x})$, if the lubrication approximation can be made, i.e., if the aperture field does not fluctuate too abruptly ($\|\boldsymbol{\nabla} w\| \ll 1$) (Brown, 1987). In that case $\mathbf{q}$ is oriented parallel to the mean fracture plane and may vary both in direction and intensity along that plane; it can be rigorously defined as the integral of the three-dimensional fluid velocities over the local fracture aperture $w(x)$ (i.e., along the direction transverse to the mean fracture plane) (Méheust & Schmittbuhl, 2001). Here it is related to the pressure gradient according to

$$\mathbf{q} = -\left[\frac{w(\mathbf{x})^3}{12\mu_0} + \frac{n}{2n+1}\left(\frac{1}{2^{1+n}\mu_0^n \tau_{1/2}^{1-n}}\right)^{\frac{1}{n}} w(\mathbf{x})^{\frac{2n+1}{n}} \|\boldsymbol{\nabla}P\|^{\frac{1}{n}-1}\right]\boldsymbol{\nabla}P \ . \quad (4.7)$$

It follows from the definition of $\mathbf{q}$, from the mass conservation for the incompressible fluid (continuity equation, $\boldsymbol{\nabla} \cdot \mathbf{u} = 0$), and from the nullity of fluid velocities at the fracture's walls, that $\mathbf{q}$ is conservative ($\boldsymbol{\nabla} \cdot \mathbf{q} = 0$). Introducing Eq. (4.5) in the conservation of $\mathbf{q}$ yields the generalized Reynolds equation:

$$\boldsymbol{\nabla} \cdot \left[\frac{w(\mathbf{x})^3}{12\mu_0} + \frac{n}{(2n+1)}\left(\frac{1}{2^{1+n}\mu_0^n \tau_{1/2}^{1-n}}\right)^{\frac{1}{n}} w(\mathbf{x})^{\frac{2n+1}{n}} \|\boldsymbol{\nabla}P\|^{\frac{1}{n}-1}\right]\boldsymbol{\nabla}P = 0 \ , \quad (4.8)$$

which for $n = 1$ (Newtonian fluid) reduces to the classical Reynolds equation (Brown, 1987).

In the literature, the four-parameter Carreau model (Carreau, 1972) is commonly adopted to fit rheological data for shear-thinning fluids, with the apparent viscosity expressed as a function of the shear rate as follows:

$$\mu = \mu'_\infty + \frac{\mu'_0 - \mu'_\infty}{\left[1 + \left(\frac{\dot{\gamma}}{\dot{\gamma}_c}\right)^2\right]^{\frac{1-n'}{2}}} \ . \quad (4.9)$$

This model features a high viscosity ($\mu \simeq \mu'_0$) plateau and a low viscosity ($\mu \simeq \mu'_\infty$) plateau at low and high shear rates, respectively. These plateaus are separated by a power law shear-thinning trend of exponent, or shear-thinning index, n' (see black dashed lines in Fig. 4.3)); $\dot{\gamma}_c$ is a characteristic shear rate that regulates the transition from the low-shear rate viscosity plateau to the shear-thinning behavior.

For the parallel plate scheme, the Carreau constitutive equation does not allow deriving an explicit analytical expression of the flow rate as a function of the imposed pressure gradient. Alternatively, the Ellis model exhibits

the high-viscosity low-shear rate plateau, but lacks the high-shear rate low-viscosity additional cut-off, typical of the Carreau model. Due to the modest influence of the latter low-viscosity cut-off except at exceptionally high imposed macroscopic pressure gradient, the Ellis model represents a valid alternative to the Carreau model to simulate creeping flow of a shear-thinning fluid in variable aperture fractures. In this work, parameters for the Ellis model are inferred from the Carreau parameters fitted to experimental data of real fluids by Uddin, Marston & Thoroddsen (2012). These parameters are obtained assuming the same low-shear rate viscosity plateau ($\mu_0 = \mu_0'$), a negligible low shear viscosity plateau ($\mu_\infty' \sim 0$), and the same large shear rate behavior. The latter conditions imposes both $n = n'$ and the value for the characteristic shear stress $\tau_{1/2}$. In particular, for $\dot\gamma \gg \dot\gamma_c$, the Carreau can be re-written as

$$\mu \underset{\dot\gamma \gg \dot\gamma_c}{\sim} \mu_0'\left(\frac{\dot\gamma_c}{\dot\gamma}\right)^{1-n'}, \tag{4.10}$$

while similarly, for $\tau \gg \tau_{1/2}$, the Ellis model becomes

$$\mu \underset{\tau \gg \tau_c}{\sim} \mu_0\left(\frac{\tau_{1/2}}{\tau}\right)^{\frac{1-n}{n}} = \mu_0\left(\frac{\tau_{1/2}}{\mu\dot\gamma}\right)^{\frac{1-n}{n}}. \tag{4.11}$$

Equations (4.10) and (4.11) thus provide a simple expression of $\tau_{1/2}$ in terms of the Carreau parameters:

$$\tau_{1/2} = \mu_0\dot\gamma_c . \tag{4.12}$$

To quantify the transition from the quasi-Newtonian to the ST behaviour, a critical macroscopic pressure gradient $\overline{\nabla P}_c$ can be analytically derived to evaluate the $\overline{\nabla P}$ above which the non-linear rheology starts to manifest itself in the flow. Considering the parallel plate configuration of aperture equal to the rough fracture's mean aperture, when the maximum shear rate occurring in the flow ($\tau_{\max}$) is higher than the critical shear rate $\tau_c = \tau(\dot\gamma_c)$, the viscosity starts to deviate from the Newtonian plateau viscosity μ_0. Given equation (4.4), the critical pressure gradient can be estimated as

$$\overline{\nabla P}_c = \frac{2\tau_c}{\langle w \rangle} , \tag{4.13}$$

where the critical shear stress τ_c can be numerically evaluated from

$$\tau_c = \mu_0\left[1 + \left(\frac{\tau_c}{\tau_{1/2}}\right)^{\frac{1}{n}-1}\right]^{-1}\dot\gamma_c \tag{4.14}$$

Moreover, a characteristic mean flow velocity u_c for which transition is expected to occur from Newtonian to shear-thinning rheology can be defined as:

$$u_c = \dot\gamma_c\sqrt{k_0} , \tag{4.15}$$

where k_0 is the Newtonian permeability.

(a)

(b)
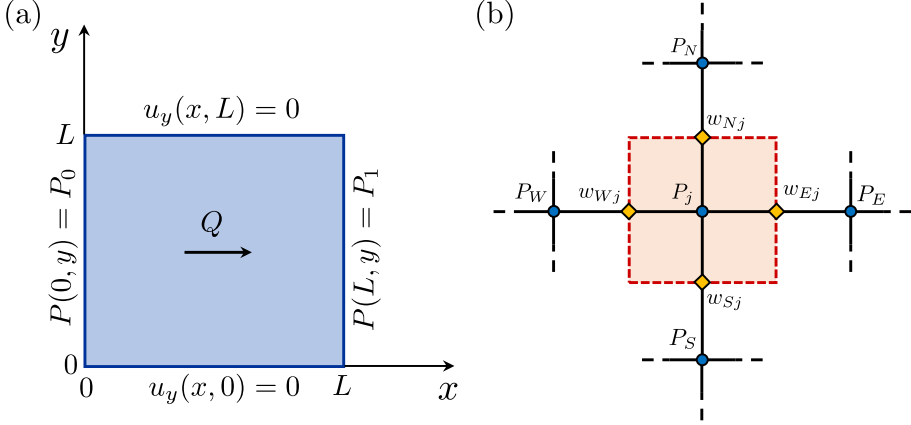
Figure 4.4: (a) Fracture representation with boundary conditions and flow rate direction. (b) Finite volume five-point stencil: the pressure is defined at the centre of the finite volumes (indicated by the blue nodes), the aperture at the center of the edges (indicated by the yellow nodes) via arithmetic mean.

4.3.3 Flow Solver

A lubrication-based numerical code has been implemented to solve the flow of an (shear-thinning) Ellis fluid in a single fracture (Lenci et al., 2022a), whose aperture geometry is generated by means of the synthetic fracture generator described in section 4.3.1. A fracture of dimensions $L \times L$ along its mean plane is discretized on a $N \times N$ regular grid, the flow resulting from an imposed pressure drop $P_0 - P_1$ between the inlet (left-hand boundary) and outlet (right-hand boundary) of the fracture, along the x-direction. The corresponding macroscopic pressure gradient is $\overline{\nabla P} = (P_0 - P_1)/L$. No-flow conditions are imposed along the two transverse boundaries of the flow domain.

A finite volume scheme has been adopted to solve the flow (see Fig. 4.4). The pressure $P(x, y)$ and aperture $w(x, y)$ are defined at different locations, on a staggered grid. The pressure is defined at the centre of each finite volume, the aperture on the boundary between neighbouring cells via arithmetic mean (e.g., $w_i^{(j)} = (w_j + w_i)/2$). The discrete formulation of equation (4.8) can be written for node i as

$$\sum_{i \in \sigma(j)} \left[\frac{w_i^{(j)3}}{12\mu_0} + \frac{n}{2n+1} \left(\frac{1}{2^{n+1} \mu_0^n \tau_{1/2}^{1-n}} \right)^{\frac{1}{n}} w_i^{(j) \frac{2n+1}{n}} \left| \frac{P_i - P_j}{\Delta} \right|^{\frac{1}{n}-1} \right] \left(\frac{P_i - P_j}{\Delta} \right) = 0 ,$$

(4.16)

where $\sigma(j) = \{N, S, E, W\}$ is the set of neighbouring cells of the j-th finite volume, and $\Delta = L/N$ is the mesh size.

The resulting non-linear system of equations is solved with an inexact Newton-Krylov method, wherein the linearised symmetric system of equations is solved via variable-fill-in incomplete Cholesky preconditioned conju-

Fluid (ID)	Carreau Model				Ellis Model		
	n'	μ'_0	μ'_∞	$\dot{\gamma}_c$	n	μ_0	$\tau_{1/2}$
	$(-)$	$(\mathrm{Pa\,s})$	$(\mathrm{Pa\,s})$	(s^{-1})	$(-)$	$(\mathrm{Pa\,s})$	(Pa)
Silicon oil (SO)	0.61	9.75	0	0.045	0.61	9.75	0.20
Xanthan gum (XG)	0.36	4.42	10^{-3}	0.869	0.36	4.42	8.48

Table 4.1: Fluid rheologic parameters for the two considered fluids: a silicon oil (Uddin et al., 2012) and a Xanthan gum produced in the laboratory. Experimental data are originally fitted with Carreau model, while Ellis parameters are inferred from the Carreau parameters.

gate gradient (ICPCG) and a parameter continuation strategy is adopted for configurations with strong non-linearities (i.e., small values of the exponent n).

The numerical code is introduced in a parallel computing framework and outputs are saved and stored using a high-performance hierarchical data format (Koranne, 2010) to reduce the computational time required by the MC simulations and the post-processing.

4.4   Stochastic analysis

4.4.1   Application scenarios

In this study, we consider the Ellis model for two shear-thinning fluids which have been selected such that the power-law exponents n differ sensibly between them and the viscosity cut-offs μ_0 are similar, while no particular requirements are imposed to $\tau_{1/2}$. The Carreau parameters of a silicon oil fluid are taken from (Uddin et al., 2012), while the other fluid is an ad hoc xanthan gum fluid produced in the laboratory. Table 4.4.1 lists the properties of theses two non-Newtonian fluids adopted, while figure 4.3 depicts the corresponding constitutive laws in an apparent viscosity versus shear rate plot. In the following, the flow of the two shear-thinning fluids will be compared to that of Newtonian fluid of dynamic viscosity equal to μ_0.

The analysis is conducted for different imposed macroscopic pressure gradients $\overline{\nabla P}$ and fracture lengths L. The former ranges from 10^2 to 10^3 Pa/m, which corresponds to typical orders of magnitude of groundwater natural potential gradients (Zimmerman & Bodvarsson, 1996), to 10^4 Pa/m, that can be associated with artificially-induced flow in hydraulic fracturing operations (Jung, 1989). Assuming a constant correlation length $L_c = 0.1$ m, a fracture lenght $L = 0.1$ m and larger $L = 1.6$ m are considered to study flow features in smaller. Indeed, if one considers that the correlation length is a property of the formation, resulting from tectonic constrains and chemical weathering posterior to fracturing, then we can assume it to be independent of the fracture's length (de Dreuzy et al., 2012); hence L/L_c decreases as the fracture

Correlation Length	L_{c}	(m)	10^{-1}
Mean Aperture	$\langle w \rangle$	(m)	10^{-3}
Aperture Coefficient of Variation	$\sigma_w / \langle w \rangle$	(-)	0.8
Hurst Exponent	H	(-)	0.8
Mesh size	$N \times N$	(-)	$2^{10} \times 2^{10}$

Table 4.2: List of the fracture generator's inputs that are common to all MC simulations and realizations.

length increases. Regarding the mean aperture, in situ measurements of fracture apertures are challenging (Barbati et al., 2016), thus mean apertures are typically obtained from rough wall measurements on laboratory sample. Typical values of mean fracture aperture ranges from 0.1 mm to 10 mm (Cipolla, Warpinski, Mayerhofer, Lolon & Vincent, 2008). However, values close to 1 mm are more frequent (Yeo, de Freitas & Zimmerman, 1998; Nowamooz, Radilla, Fourar & Berkowitz, 2013).

4.4.2   Monte Carlo simulations

The characteristics of the performed Monte Carlo (MC) simulations are listed in Table 4.3. For each MC set, NMC $= 10^3$ fracture realizations have been generated, changing the seed of the Mersenne Twister random number generator (RNG) (Matsumoto & Nishimura, 1998). For each set, the table reports the parameters μ_0, n and $\tau_{1/2}$ describing the fluid, the correlation length to length ratio, and the pressure gradient. In total, twelve Monte Carlo sets of simulations have been performed for each combination reported in table 4.3, with the geometric parameters listed in table 4.2. The numerical code provides the following quantities of interest (QoI) for each process realization: the pressure field (P), the longitudinal velocity component (u_x), the transversal velocity component (u_y), the velocity magnitude, and the transmissivity (T), as defined by Eq. (4.16).

The post-processing phase elaborates the outputs and produces PDFs of the dimensionless QoIs, for each realization; then, it computes the PDF ensemble average with the relative confidence interval, estimated considering a range of one standard deviation around the mean. In the following section, results concerning the non-Newtonian hydraulic behaviour of variable aperture fractures are discussed with a probabilistic approach; to this end, the velocity components are normalized with respect to the mean velocity magnitude ($\langle ||\mathbf{u}|| \rangle$). The transmissivity for non-Newtonian flow in fractures is defined as:

$$T(\langle ||\mathbf{u}|| \rangle) = \frac{Q\mu_0}{\overline{\nabla P}} \ , \tag{4.17}$$

where Q is the volumetric flow rate. Note that for a shear-thinning rheology

MC set	μ_0 (Pa$\cdot$s)	$\tau_{1/2}$ (Pa)	n (-)	L/L_c (-)	$\overline{\nabla P}$ (Pa$\cdot$m^{-1})	$\overline{\nabla P}/\overline{\nabla P_c}$ (-)
MC1	4.42	8.48	0.36	1	10^2	2.0×10^{-1}
MC2	4.42	8.48	0.36	1	10^3	2.2×10^{0}
MC3	4.42	8.48	0.36	1	10^4	2.2×10^{1}
MC4	4.42	8.48	0.36	16	10^2	2.0×10^{-1}
MC5	4.42	8.48	0.36	16	10^3	2.2×10^{0}
MC6	4.42	8.48	0.36	16	10^4	2.2×10^{1}
MC7	9.75	0.20	0.61	1	10^2	6.5×10^{-4}
MC8	9.75	0.20	0.61	1	10^3	6.5×10^{-3}
MC9	9.75	0.20	0.61	1	10^4	6.5×10^{-2}
MC10	9.75	0.20	0.61	16	10^2	6.5×10^{-4}
MC11	9.75	0.20	0.61	16	10^3	6.5×10^{-3}
MC12	9.75	0.20	0.61	16	10^4	6.5×10^{-2}

Table 4.3: Monte Carlo set ID-numbers and related parameters: fluid rheology (μ_0, $\tau_{1/2}$, n), ratio of aperture correlation to fracture size L/L_c, and pressure gradient $\overline{\nabla P}$. The ratio $\overline{\nabla P}/\overline{\nabla P_c}$ is reported to quantify the significance of non-linear effects. Other parameters common to all simulations are listed in Table 4.4.1.

this transmissivity will depend on the mean velocity, or, equivalently, on the imposed macroscopic pressure gradient. As n goes to 1, T reduces to T_0, which does not depends on the velocity magnitude but only on the fracture's geometry, for a Newtonian fluid.

4.5   Results

4.5.1   Probability density functions of vertically-averaged velocities

A thorough analysis adopting the Monte Carlo framework discussed in the previous section has been conducted to characterize the flow of steady isothermal Stokes flow of shear-thinning fluids in rough fractures. The stochastic velocity dynamics is analysed by means of the ensemble average PDFs of the longitudinal and transversal velocity components, and of the velocity magnitude. Moreover, the confidence interval is provided for each PDF to measure the dispersion of the results around the mean behavior.

The ensemble average PDFs of the longitudinal component of the velocity are depicted in Fig. 4.5 for all parameter combinations listed in Table 4.3. The flow is mainly cocurrent, but local backward flow (i.e. negative $u_x/\langle||\mathbf{u}||\rangle$ values) may occur due to contrasting adjacent aperture values near the fracture contact zones; these, in turn, occupy a good percentage of the fracture total surface (about 30%), for the selected coefficient of variation of the aperture
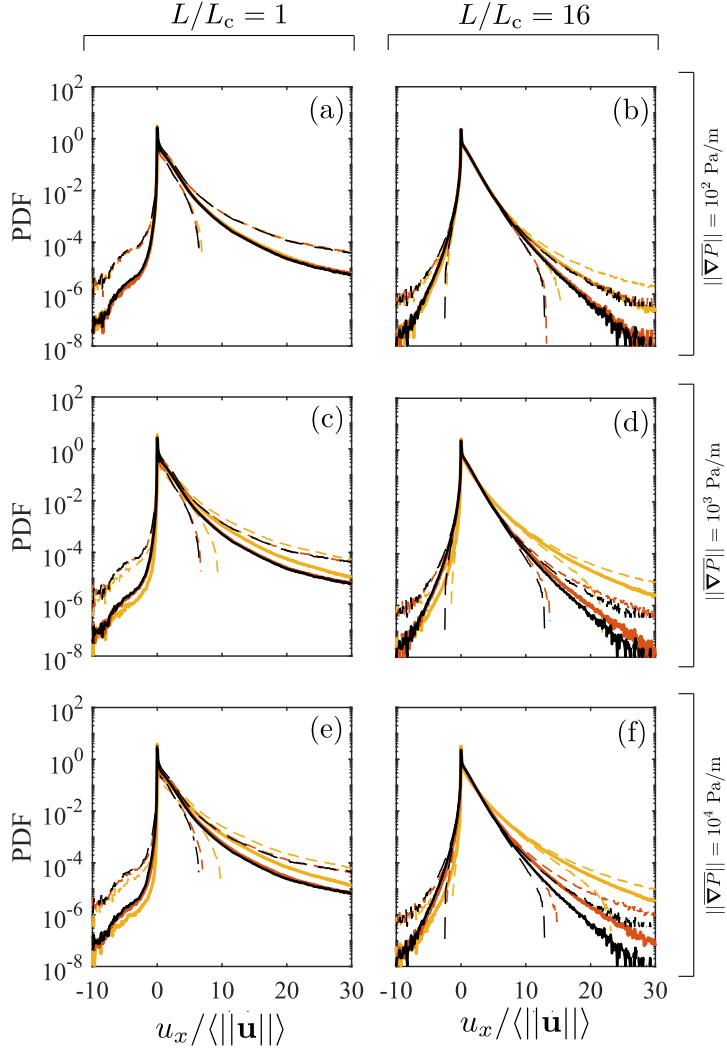
Figure 4.5: Probability density functions of the dimensionless longitudinal velocity component $u_x/\langle||\mathbf{u}||\rangle$ for small (left column) and large (right column) fractures, and for small (top row), intermediate (middle row) and high (bottom row) macroscopic pressure gradients $\overline{\nabla P}$; solid lines represent the mean ensemble PDFs, while dashed lines define the confidence interval, with the range estimated considering the standard deviation. Black lines refers to the Newtonian case ($n = 1$), orange and yellow lines to the silicon oil ($n = 0.61$) and xanthan gum ($n = 0.36$), respectively.

field, which is $\sigma_w/\langle w \rangle = 0.8$. The PDFs of the longitudinal velocity component are distinctly narrow, with the positive cocurrent part exhibiting a decays which approaches an exponential decay for $L/L_c = 16$, and a streched exponential for $L/L_c = 1$. A similar behaviour was observed in two and three dimensional porous media flows, for Newtonian (Siena, Riva, Hyman, Winter & Guadagnini, 2014) and non-Newtonian fluids (Zami-Pierre et al., 2016), which is not surprising since the rough fractures behave all the more as a two-dimensional porous medium as the correlation length is smaller, because a smaller correlation length means that spatial correlations in the apertures (which is essentially what distinguishes a fracture geometry from a uncorrelated 2D porous medium) are restricted to a narrower range of scales, at small scales. Under strongly forced flow conditions, i.e. the highest values of the pressure gradient, the strongly shear thinning fluid ($n = 0.36$) exhibits wider cocurrent and thinner countercurrent tails with respect to the less shear thinning fluid ($n = 0.61$), and even more so when compared to the Newtonian case in the same conditions. On the other hand, under lower pressure gradients the PDFs for Newtonian and non-Newtonian fluids almost overlap, clearly indicating that the fracture heterogeneity governs the flow and the nonlinear effects associated to rheology are quite modest. Results for small fractures (i.e. $L/L_c = 1$) are almost independent of the rheology and flow regime, with a very modest increase/decrease of the cocurrent/countercurrent tail only for the most shear-thinning fluid and the highest pressure gradient. In this type of geometry the strong channeling resulting from the aperture field heterogeneity, which is correlated up to the fracture size, dominates over the effect of rheology. Although the shear-thinning flow is faster than Newtonian flow under identical conditions, the PDF of the longitudinal velocity component normalized by the average velocity is little impacted by the rheology. For large fractures ($L/L_c = 16$) the effect is reversed but remains extremely modest for this low $\overline{\nabla P}$.

Figure 4.6 depicts the ensemble average PDFs of the transversal velocity components: these are nearly symmetric around zero as expected. Results for small fractures (i.e. $L/L_c = 1$) are invariant with respect to the rheology and flow regime, with no significant differences for any combination of parameters. Again this behavior results from the strong geometry-mediated channeling. On the other hand, large fractures ($L/L_c = 16$) under high pressure gradient show wider tails, especially for the most shear thinning fluid.

The PDFs of the transverse velocity components suggest, similarly to the longitudinal case, that under low pressure gradients the flow pattern is mainly dominated by fracture heterogeneity, with contributions due to non-linear rheology that arise only for strongly shear-thinning fluids, especially in large fractures. A Newtonian fluid tends to spread more across the open portion of the fracture as compared to a shear-thinning fluid. In fact, the shear-tinning behaviour induces a more marked flow localization, with the fluid being conveyed in a smaller portion of the fractures and presenting more extreme values of velocities under the same flow conditions.
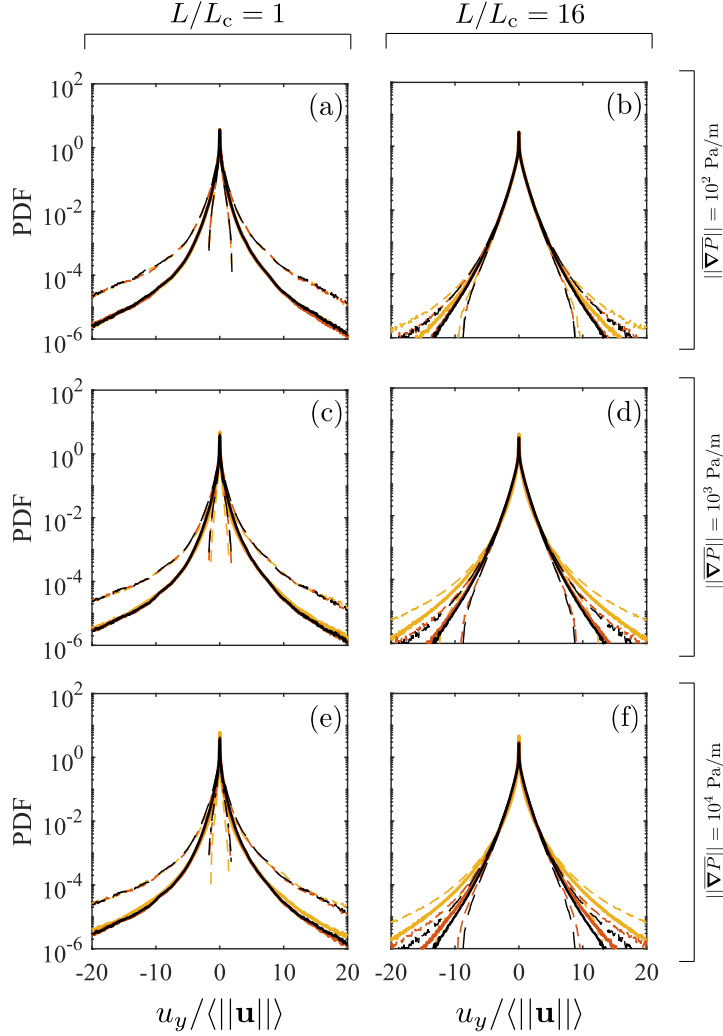
Figure 4.6: Probability density functions of the dimensionless transversal velocity component $u_y/\langle||\mathbf{u}||\rangle$ for small (left column) and large (right column) fractures, and for small (top row), intermediate (middle row) and high (bottom row) pressure gradients $\overline{\boldsymbol{\nabla} P}$; solid lines represent the mean ensemble PDFs, while dashed lines define the confidence interval, with the range estimated considering the standard deviation. Black lines refers to the Newtonian case ($n = 1$), orange and yellow lines to the silicon oil ($n = 0.61$) and xanthan gum ($n = 0.36$), respectively.

The PDF of the velocity magnitude (i.e. the norm of the Eulerian velocity) is related to a typical transport attribute, the spatial-Lagrangian PDF, through flux-weighting (Dentz, Kang, Comolli, Borgne & Lester, 2016). Several studies have aimed at relating the Eulerian velocity PDF to porous medium's geometrical properties (de Anna, Quaife, Biros & Juanes, 2017; Hakoun, Comolli & Dentz, 2019; Puyguiraud, Gouze & Dentz, 2019a; Velásquez-Parra, Aquino, Willmann, Méheust, Le Borgne & Jiménez-Martínez, 2021), and from there, anomalous transport to the Eulerian velocity PDF (Puyguiraud, Gouze & Dentz, 2019b; Velásquez-Parra et al., 2021). In Fig. 4.7, the dimensionless PDF of velocity magnitude is depicted to show the influence of rheology and heterogeneity on the distribution of both high and low velocities. The dimensionless PDFs for the less shear-thinning fluid ($n = 0.61$) overlap with those for the Newtonian fluid for all the combinations considered, meaning that the fluid rheology does not affect the shape of the PDF but only its magnitude. Conversely, the less shear-thinning fluid ($n = 0.36$) shows more extreme values of the velocity magnitude under high pressure gradients, which corresponds physically to a higher localization of flow under a shear-thinning rheology than under the Newtonian rheology, as discussed above. The differences between the two non-Newtonian fluids for intermediate and high pressure gradients increase when a small fractures (i.e. $L/L_c = 1$) is considered, which is expected, since flow channeling at the fracture scale is much stronger in that case, even for Newtonian flow.

4.5.2 Autocorrelation function of the velocity components

In Fig. 4.8, the autocorrelation functions of the velocity components are depicted for the case $L/L_c = 1$. The autocorrelation coefficients $\rho_{xx} = \text{Cov}(u_x, u_x)/\sigma_{u_x}^2$ and $\rho_{yy} = \text{Cov}(u_y, u_y)/\sigma_{u_y}^2$ are evaluated along their respective directions, i.e. the x-direction and y-direction respectively. The autocorrelation functions of the velocity components provide a metric of disorder (Rozenbaum & du Roscoat, 2014), which can be influenced by the the fluid's rheological behaviour. These functions show a more rapid decay for strongly non-Newtonian fluids under elevate pressure gradient and in small fractures ($L/L_c = 1$), while larger fractures are not affected at all. All plots show a hole type covariance with zero integral scale: velocity fluctuations are positively correlated at short distances and negatively correlated at longer distances, and tend to zero exponentially from below. A similar structure has been obtained by Bellin et al. (1992) for 2-D porous media. The influence of rheology and of the external pressure gradient on the autocorrelation coefficients is almost imperceptible in the flow direction, while the transverse component is to some extent affected, showing a faster short-scale correlation decay as the fluid becomes more shear-thinning.

Figure 4.9 depicts the autocorrelation coefficients for the case $L/L_c = 16$.
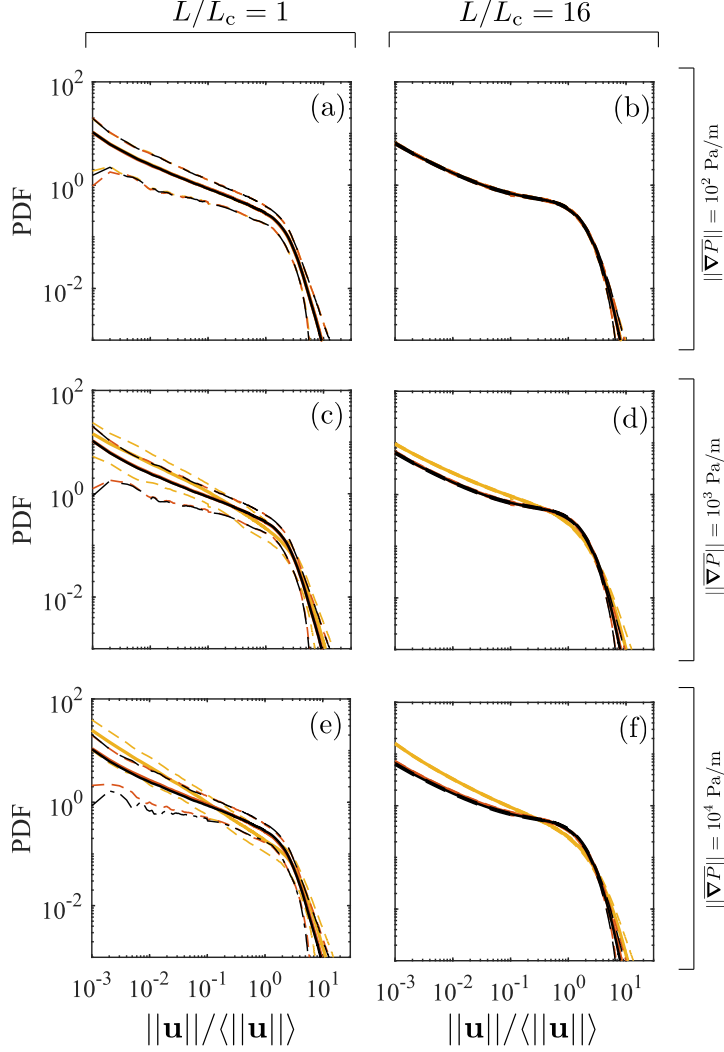
Figure 4.7: Probability density functions of the dimensionless velocity magnitude $||\mathbf{u}||/\langle||\mathbf{u}||\rangle$; for small (left column) and large (right column) fractures, and for small (top row), intermediate (middle row) and high (bottom row) pressure gradients $\overline{\nabla P}$; solid lines represent the mean ensemble PDFs, while dashed lines define the confidence interval, with the range estimated considering the standard deviation. Black lines refers to the Newtonian case ($n = 1$), orange and yellow lines to the silicon oil ($n = 0.61$) and xanthan gum ($n = 0.36$), respectively.
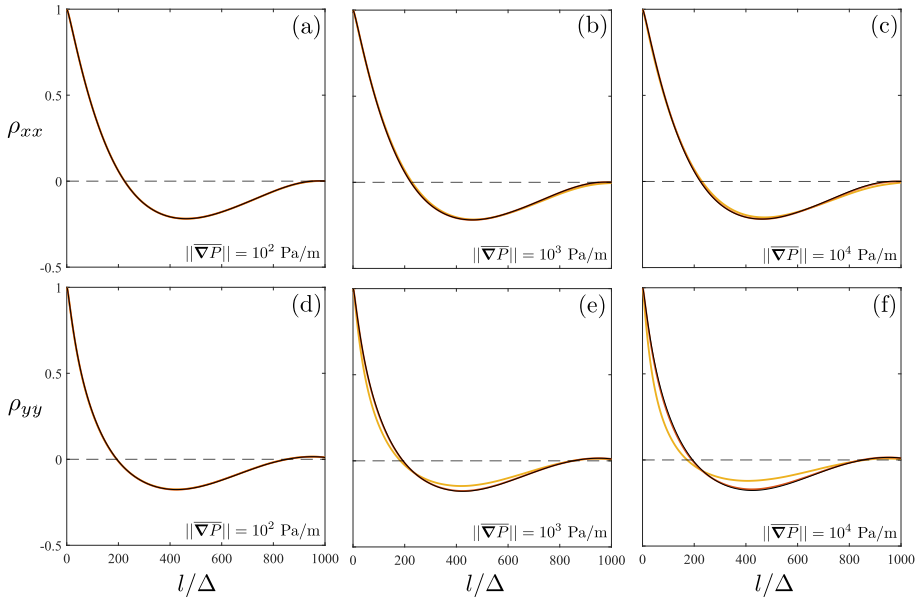
Figure 4.8: Autocorrelation functions of the velocity components (longitudinal ρ_{xx} and transversal ρ_{yy}) as a function of the dimensionless lag (l/Δ), for $L/L_c = 1$. The functions have been averaged over the MC simulations. The dimensionless lag is the ratio of the the distance l to the mesh size Δ. The black solid line represents the Newtonian case, the orange solid line the less shear-thinning fluid ($n = 0.61$), the yellow solid line the strongly shear-thinning fluid ($n = 0.36$).
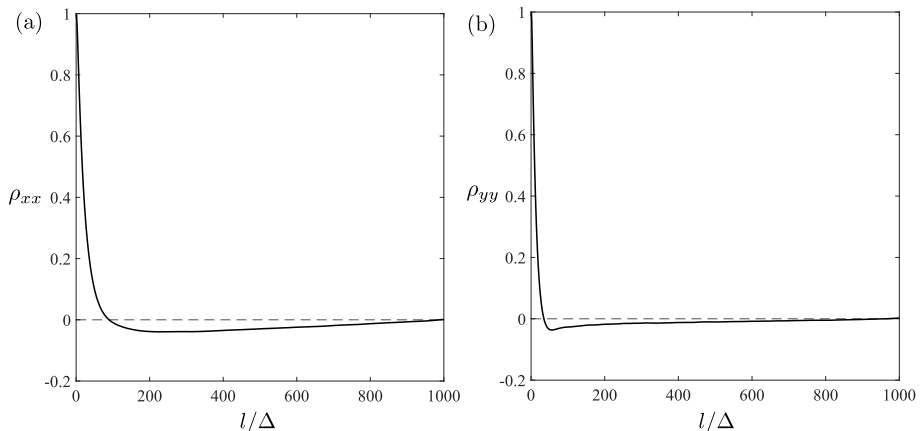
Figure 4.9: Autocorrelation functions of the velocity components (longitudinal ρ_{xx} and transversal ρ_{yy}) as a function of the dimensionless lag (l/Δ), for $L/L_c = 16$. The functions have been averaged over the MC simulations. The dimensionless lag is the ratio of the the distance l to the mesh size Δ. The black solid line represents the Newtonian case, the orange solid line the less shear-thinning fluid ($n = 0.61$), the yellow solid line the strongly shear-thinning fluid ($n = 0.36$).

All combinations of parameters result in the same hole covariances behaviour for ρ_{xx} and ρ_{yy}: a narrow short-scale positive correlation, with a fast short-scale exponential decay, and a long-scale negative correlation, slowly tending to zero from below.

4.5.3 Fracture-scale hydraulic behavior

Considering now the integral flow behaviour, i.e., the hydraulic behavior at the fracture scale, it is seen that the shear-thinning rheology enhances the fracture's apparent transmissivity: this effect becomes relevant under the action of a sufficiently large macroscopic pressure gradient (i.e. sufficiently large average velocity). Fig. 4.10 depicts the dependence of the apparent transmissivity T, normalized with its Newtonian counterpart T_0, on the velocity normalized by the characteristic velocity u_c, for each realization; the average value for each Monte Carlo simulation is also shown. When the normalized velocity is smaller than 1, T/T_0 goes to 1, which is characteristic of the Darcian regime. When T/T_0 is sufficiently larger than 1, it is related to the normalized velocity through a non-linear relation in the form $\langle ||\mathbf{u}|| \rangle^n \propto ||\boldsymbol{\nabla}\langle P \rangle||$, characteristic of the shear-thining (power law) behavior. A similar macroscale transition between two such regimes has been observed for two-dimensional porous media by (Zami-Pierre et al., 2016). Apparent transmissivity values obtained for small fractures ($L/L_c = 1$) are more disperse around their ensemble average as compared to their larger counterpart ($L/L_c = 16$), which better satisfies
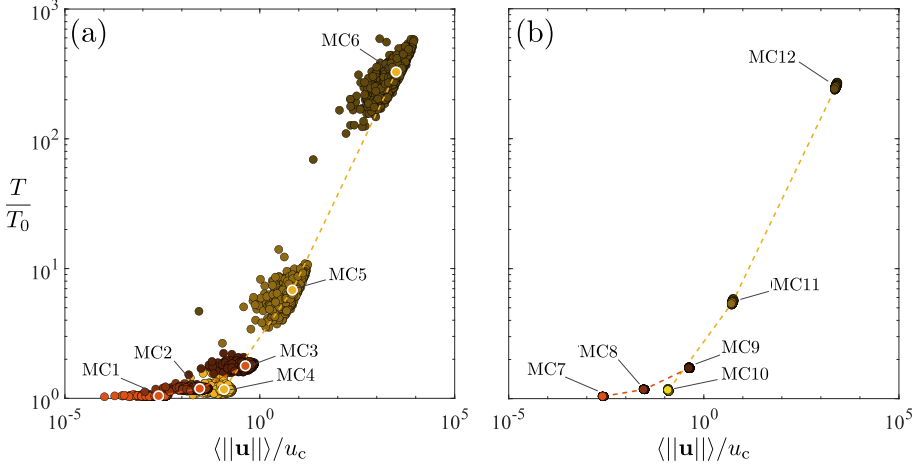
Figure 4.10: Dependence of the dimensionless transmissivity T/T_0 on the dimensionless velocity $\langle ||\mathbf{u}|| \rangle / u_{\mathrm{c}}$, for all realisations and the ensemble average of each Monte Carlo simulation: (a) $L/L_{\mathrm{c}} = 1$, (b) $L/L_{\mathrm{c}} = 16$. Simulation results for the silicon oil and xanthan gum are in orange and yellow, respectively; the darker the color, the higher the imposed global pressure gradient is. Lines are a guide to the eyes.

the ergodic condition, so that values for an individual realisation are almost superimposed with their ensemble average. In other words, since no spatial correlations exist in the aperture field at scales larger than $L/16$, that field is mostly random and all realization of it behave in the same way (see (Méheust & Schmittbuhl, 2003) for a similar result for Newtonian flow). However, comparing results for the two fractures shows that ensemble averages are almost insensitive to the fracture size, or, equivalently, to the ratio L/L_{c}. In other words, the fluid's rheology dominates by far over aperture heterogeneities in controlling the hydraulic behavior for such strongly shear-thinning fluids.

4.6   Conclusions

We conducted a comprehensive stochastic analysis aimed at elucidating how the effects of non-Newtonian rheology and aperture heterogeneity impact the flow in realistic synthetic geological fractures. The shear-thinning behaviour of the fluid, modeled by means of the three-parameter Ellis rheology, is particularly relevant when the fracture is subjected to a sufficiently high macroscopic pressure gradient (typical of forced regimes). A transition from the Darcian regime $\langle ||\mathbf{u}|| \rangle \propto ||\boldsymbol{\nabla} P||$ to the non-linear regime $\langle ||\mathbf{u}|| \rangle^n \propto ||\boldsymbol{\nabla} P||$ occurs when increasing the imposed macroscopic pressure gradient. Under the same conditions, the ensemble statistics of the velocity components differ the most from the Newtonian case for the more shear-thinning fluids. In particular,

the average PDFs of the normalised velocity components show thicker tails for shear-thinning rheologies, indicating a higher frequency of velocities much larger than the mean value. The average PDFs of the velocity magnitude also display a higher dispersion of the velocity around the mean values. These results can be explained by the fact that for strongly shear-thinning fluids the flow localization along correlated large aperture channels is more intense for shear-thinning fluids than for Newtonian flow. This stronger flow localization is consistent with results obtained on two-dimensional porous media in earlier studies. In rough fractures, however, long range spatial correlations create channeling at the scale of the correlation length, which is then the longitudinal scale at which flow localization occurs; this is an ingredient that is not present in uncorrelated 2D porous media.

In sum, the flow pattern is mostly governed by aperture heterogeneities, while the impact of the fluid rheology on the probability density function of velocity component, once normalized by the mean velocity, is relatively limited, except for very shear-thinning fluids. The overall hydraulic behaviour, on the other hand, is strongly affected by the fluid rheology: the ratio of apparent non-Newtonian transmissivities to that of Newtonian fluids increases with the fracture heterogeneity, reaching values much larger than unity. Ensemble averages of the overall hydraulic transmissivity are almost independent of the fracture size (or, equivalently, to the ratio L/L_c), but small fractures, which are more affected by disorder due to flow channeling up to the fracture scale (as for Newtonian flow), show a larger apparent transmissivity around the mean.

Eventually, the analysis of the velocity statistics proposed in this work, as well as fracture and fluid properties, can be adopted to predict transport features that can be implemented in the numerical code and in subsequently introduced in a similar Monte Carlo framework to characterize solute transport (e.g., through spatial dispersion or breakthrough curves).

5 | Experimental investigation on backflow of power-law fluids in planar fractures

5.1 Abstract

In hydrofracturing, we model backflow of a non-Newtonian fluid in a single flat-walled fracture of planar geometry and support our conceptualization with laboratory experiments. We consider a power-law fluid, a spatially homogeneous fracture aperture, and its variation in time depending on the internal fluid pressure and the elastic relaxation of the walls. The relationship between the latter quantities may be linear, akin to a Winkler soil, or nonlinear, due to the progressive softening or stiffening of the boundary associated with the properties of the surrounding rock. The result is an integro-differential problem that generally admits a closed-form solution, albeit implicit for some quantities. In particular, a comparison is conducted between the drainage time in the present configuration and point drainage in radial geometry. The approach is generalized by introducing leak-off, i.e. a loss of fluid at the fracture boundaries that accelerates the fracture closure, when compared to the no leak-off case. To validate the theoretical results, 14 experiments are conducted with an ad-hoc replica of a rectangular fracture of aspect ratio 2.5-2.7, with a maximum height of ≈ 2 mm; the elastic reaction of the walls is due to o-rings, also sealing the fracture without adding friction disturbances. Fluids with different rheology, both Newtonian and shear-thinning, are associated with different boundary conditions of external pressure and overload. The match between theory and experiments is fairly good, with discrepancies of a few percent essentially due to the approximations of the theoretical model, and, for shear-thinning fluids, to the simplified constitutive equation.

5.2 Introduction

Backflow is a term used in the hydrofracturing jargon to represent the third phase of the process following the injection of i) the fracturing fluid and ii) of the proppant (see Sahai and Moghanloo (Sahai & Moghanloo, 2019) and bibliography therein for a recent review). The first phase opens up new fractures, cracks and preferential pathways in the rock mass with a process that initiates at the main well, or borehole, typically located at 1-2 km below ground and having a sub-horizontal orientation; the second phase props them open. At

the beginning of the third phase, the injection ceases and the downstream pressure gradient attenuates and then reverses its direction; this causes part of the fracturing fluid to flow back sequentially from matrix to fractures, fractures to well bore, and finally from well bore to surface, where the fluid is treated and re-used; the phenomenon is commonly described as backflow. The unrecovered portion of hydrofracturing fluid lost as formation leak off represents an economic loss (Economides, Mikhailov & Nikolaevskiy, 2007) as well as a source of environmental pollution: the latter key aspect is clearly summarized by Birdsell *et al.*(Birdsell et al., 2015). During the fourth and final phase, the product of the reservoir under exploitation, typically oil, gas or heat for the deepest reservoirs (Hofmann, Weides, Babadagli, Zimmermann, Moeck, Majorowicz & Unsworth, 2014), follows the backflow and invades the fracture network, eventually reaching the borehole and initiating the productive stage. Any residual fracturing fluid retained in the fracture network or in the formation pore space, as well as the presence of proppant within the fractures (Bolintineanu, Rao, Lechman, Romero, Jove-Colon, Quintana, Bauer & Ingraham, 2017), brings about a reduction of the fracture conductivity, impairing productivity and favouring the stagnation of the fracturing fluid in the subsurface.

While a variety of models examine with varying realism and at various scales (for a review see Britt (Britt, 2012) and Detournay(Detournay, 2016)) the first phase of the hydrofracturing process, the details of backflow were investigated to a lesser degree of attention. In essence, it is seen that typically the reverse flow causes a pressure reduction within the formation and the fracture network upstream of the borehole; this in turn produces the relaxation of the walls, further squeezing the fracture and driving the fluid out. This phenomenon can be captured by numerical models based on a detailed knowledge of the fracture network (Clarkson, Haghshenas, Ghanizadeh, Qanbari, Williams-Kovacs, Riazi, Debuhr & Deglint, 2016), possibly based on AI techniques (see Agwu *et al.*(Agwu, Akpabio, Alabi & Dosunmu, 2018) for a review concerning similar fluids); or represented by models of reduced complexity, characterized by a relatively low number of parameters. This second category includes the model of Lai *et al.*(Lai, Zheng, Dressaire, Ramon, Huppert & Stone, 2016) for radial crack propagation and resulting backflow, the seminal work of Dana *et al.*(Dana et al., 2018), describing the same phenomena in a fracture network built as a succession of plane branches of increasing order, where at each order i two fractures branch out from an order $i-1$ fracture, reminiscent of river networks (Kobchenko, Hafver, Jettestuen, Galland, Renard, Meakin, Jamtveit & Dysthe, 2013), and blood vessels or other biological systems (see Abugattas *et al.* (Abugattas, Aguirre, Castillo & Cruchaga, 2020) and references therein). The model was later extended to include variability in the branching parameters at each order (Dana, Peng, Stone, Huppert & Ramon, 2019). The effect of a bifurcation on single and two-phase flow in a fracture surrounded by a porous medium was investigated by Zhu *et al.* (Zhu, Liu, Liu, Wu & Song, 2021). Quite surprisingly, relatively

few scientific works include non-Newtonian effects, despite the fact that hydrofracturing fluids are rheologically complex by definition. In the first place, they are often engineered so that their viscosity varies over time, typically due to carefully planned chemical reactions within the fluid and/or with the rock matrix (Barbati et al., 2016). This peculiar characteristic permits the optimization of hydrofracturing operations: during the injection phase, a high viscosity allows formation of a clearly defined network of cracks without too much loss of fluid in the surrounding matrix, while in the backflow phase a low viscosity is desirable to minimize pressure losses and maximize the fluid recovery. In principle, this does not necessarily imply a non-Newtonian behaviour, characterized by a viscosity dependent on the velocity vector, or equivalently, by a nonlinear relationship between the stress and the velocity deformation tensors. In practice, however, the rheology of fracturing fluids is mostly non-Newtonian, as explained in detail e.g. by Osiptov (Osiptov, 2017): this is linked to the desirable characteristics of non-Newtonian fluids, whose richness of descriptive parameters allows achieving several engineering objectives at the same time (Lester, Yacob, Morrissey & Linden, 2014).

The adoption of complex constitutive models more apt to represent the rheology of the fracturing fluid has become common (Linkov, 2014) in modelling all phases of the hydrofracturing process. At the scale of an entire formation, or of a domain including several formations, the approach is mostly numerical and includes a detailed description of the newly formed fracture network (Yao, Jiang & Shao, 2015), interacting with the surrounding rock matrix and the fractures possibly already existing in the formation (Rahman & Rahman, 2013). The rheological model adopted is usually power-law, the least detailed model incorporating a nonlinear relationship between stress and strain (Bird, Stewart & Lightfoot, 2002). More detailed formulations, often based on an analytical or semi-analytical approach, focus on a single phase of the hydrofracturing process. In the injection phase, the formation of a plane-strain fracture driven by a power-law fluid is described by Adachi and Detournay (Adachi & Detournay, 2008) and Garagash (Garagash, 2006), and by Mikhailov *et al.* (Mikhailov, Economides & Nikolaevskiy, 2011) with the inclusion of leakoff; anisotropy in the rock matrix was then incorporated in the solution by Dontsov (Dontsov, 2019), while Lakhtychkin *et al.* (Lakhtychkin, Eskin & Vinogradov, 2012) modelled the fracture expansion under the action of two proppant-laden immiscible power-law fluids. An alternative, numerical approach for the propagation phase was adopted by Perkowska (Perkowska et al., 2016). More realistic, and complex rheological models, such as truncated power-law and Carreau, were only recently applied to single fracture propagation (Wrobel, 2020; Wrobel et al., 2021; Pereira & Lecampion, 2021). Much less developed are models for non-Newtonian backflow. To our knowledge, the first was presented by Chiapponi *et al.* (Chiapponi et al., 2019), who modelled radially converging backflow of a non-Newtonian power-law fluid towards a borehole in a single disk-shaped fracture, checking their theoretical findings against laboratory experiments with satisfactory results. Later,

Ciriello *et al.* (Ciriello et al., 2021) developed a similar analysis for plane flow of a non-Newtonian fluid described by the Ellis three-parameter model (Medina, Detwiler, Prioul, Xu & Elkhoury, 2019; Ali, Abbasi & Ahmad, 2021). Here, we consider the same plane geometry and develop novel closed-form expressions for a power-law fluid, widely applied in porous and fractured media flow (Longo, Di Federico & Chiapponi, 2015) with satisfactory results when the rheological parameters in the measuring device are estimated at the same shear rate range of the real phenomenon. We then verify our theoretical result by means of two ad hoc built experimental devices, describing its structure and calibration, exploring different types of wall reaction, and finding a good agreement between experiments and theory.

The manuscript is structured as follows. Section 2 includes the formulation of the problem and the derivation of i) the pressure field in the space/time and ii) the closure pattern of the fracture over time. Section 3 illustrates the experimental set-up, the measurement techniques for the rheological behaviour of the investigated fluids, interpreted with the Newtonian and power-law constitutive equations, and the experimental results with associated uncertainty. Section 4 illustrates a generalization of the problem, including the effects of leak-off from the fracture. Section 5 presents our conclusions and perspectives for future work. Appendices A-C provide additional details on the problem investigated.

5.3   Power-law fluid flow

5.3.1   Formulation

A fluid-filled, rigid rock fracture of length L, width W, time variable aperture $h(t)$ of starting value h_0, and elastic walls is initially ($t = 0$) subject to a no-flow condition at its end $x = L$ and to uniform initial pressure p_e imposed by the value at its outlet $x = 0$, connected with the main well or borehole (see Figure 5.1). The backflow towards the borehole causes a pressure reduction within the fracture that in turn produces the relaxation of the walls, further squeezing the fracture. For a given time, the pressure is $p(x, t)$, while the fracture volume and the outflowing discharge per unit width are $V_f = Lh$ and $q = -dV_f/dt = -L \, dh/dt$. Hereinafter, the pressure within the fracture is taken to include gravity effects (reduced or generalized pressure) caused by the inclination α of the fracture with respect to the horizontal plane. Note that this assumption can be adopted also for the radial geometry, adding generality to the results of Chiapponi *et al.* (Chiapponi et al., 2019) without the need for neglecting gravity effects.

The fracture aspect ratios are $\epsilon_1 = L/W \ll 1$ and $\epsilon_2 = h/L \ll 1$, and the lubrication approximation holds. Hence, the flow is one-dimensional in the x direction; this allows concentrating the relaxation of the fracture entirely in one of the two walls, taken to be the upper one for pure convenience. We further assume that the plane fracture under consideration belongs to a
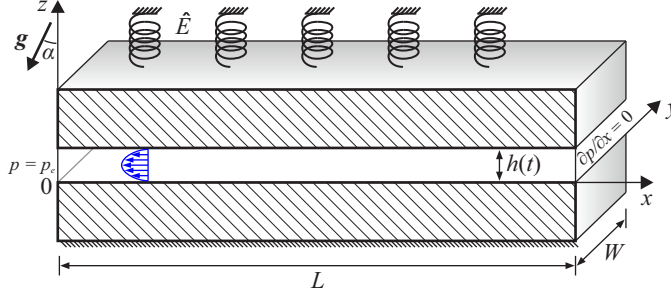
Figure 5.1: Sketch of a smooth fracture with uniform aperture varying over time and elastic wall behaving as a linear/nonlinear ($\lambda = 1/ \neq 1$) foundation of assigned coefficient of subgrade reaction $\hat{E}$ of dimensions $[ML^{-1-\lambda}T^{-2}]$, reverting to a Winkler coefficient $\tilde{E}$ of dimensions $[ML^{-2}T^{-2}]$ for $\lambda = 1$.

series of evenly distributed fractures of spacing l with respect to a horizontal borehole or main well, as it is most often the case in hydraulic fracturing (see Figure 5.2).

To represent in a general form the reaction of the wall we adopt the formulation of Ciriello *et al.* (Ciriello et al., 2021), allowing for generality the Young modulus E of the rock wall to be a function of the strain rate, according to the power-law relationship

$$E = E_0 \left(\frac{h}{l} \right)^{\lambda-1} , \tag{5.1}$$

where E_0 is a reference value of the Young modulus of dimensions $[ML^{-1}T^{-2}]$ and λ a non-negative constant governing the type of wall reaction: linear for $\lambda = 1$, sub-linear or supra-linear for $0 < \lambda < 1$ or $\lambda > 1$ respectively. It is worth noting that $\lambda \neq 1$ also represents possible experimental constraints. Under a Winkler conceptualization of subgrade springs illustrated in Figure 5.1, the rigid wall reacts to the upward fluid pressure with a downward pressure proportional to the aperture given by $r(t) = \tilde{E}h$ where $\tilde{E}$ is the coefficient of subgrade reaction of dimensions $[ML^{-2}T^{-2}]$. For a thin elastic layer, this coefficient is given by the ratio between the Young modulus of the layer's material E $[ML^{-1}T^{-2}]$ and its thickness l (Kerr, 1964), i.e.

$$\tilde{E} = E/l, \tag{5.2}$$

where l in this context is identified with the fracture spacing (Chiapponi et al., 2019). The actual validity, albeit approximate, of eq. (5.2) is conditioned on $l/L < 1$, a requirement often respected in artificial fracture networks produced by fracking (see Ciriello *et al.* (Ciriello et al., 2021) and references therein).

The wall equilibrium, written per unit width, then requires

$$\int_0^L p(x,t)\,\mathrm{d}x = r(t)L = \tilde{E}Lh(t), \tag{5.3}$$
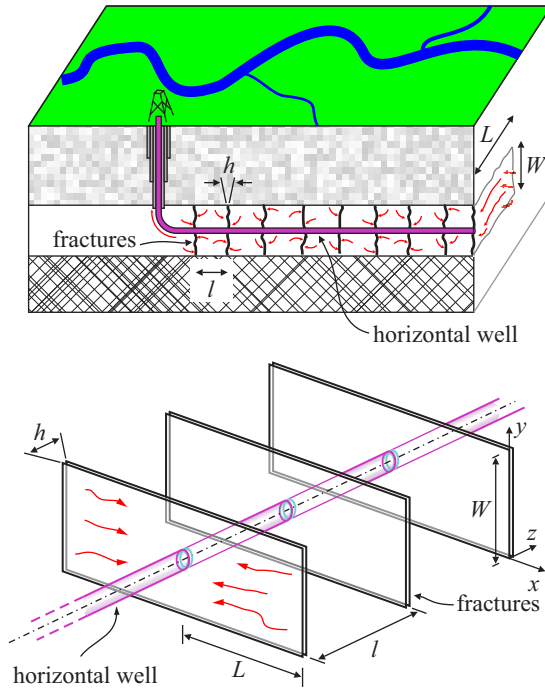
Figure 5.2: Bi-wing planar and symmetric fractures of dimensions L, W and h and equal spacing l originating from a horizontal borehole; here $\alpha = 90°$ as the fractures lie in the vertical plane.

or equivalently using eqs. (5.1)-(5.2)

$$\int_0^L p(x,t)\,\mathrm{d}x = \hat{E}Lh^\lambda(t), \tag{5.4}$$

where $\hat{E} = E_0 l^{-\lambda}$ of dimensions $[ML^{-1-\lambda}T^{-2}]$ is a coefficient of subgrade reaction under the assumption of nonlinear wall reaction and evenly spaced fractures, and reverts to the physical meaning and dimensions of a Winkler subgrade coefficient if $\lambda = 1$. Note that eq. (5.4) stands by itself in the case of a single fracture when the spacing l is not defined and there is no need of eqs. (5.1), (5.2) and (5.3). The wall equilibrium is further generalized by adding a constant force per unit width, defined as overload f_0, on the right-hand side of (5.4), typically opposing the fracture aperture and associated for instance to a residual state of stress within the rock wall generated by its load history. Eq. (5.4) then becomes,

$$\int_0^L p(x,t)\,\mathrm{d}x = \hat{E}Lh^\lambda(t) + f_0, \tag{5.5}$$

completing the schematization of the fluid-wall interaction.

Turning now our attention to the flow, inertial effects are negligible, the regime is viscous, and the fluid has a power-law rheology, described in simple shear flow by the constitutive equation

$$\tau_{zx} = -\tilde{\mu}|\partial u/\partial z|^{n-1}\partial u/\partial z, \tag{5.6}$$

with τ_{zx} shear stress, u velocity, $\tilde{\mu}$ consistency index and n flow behaviour index; for $n = 1$ the fluid is Newtonian, for $n < 1$ shear-thinning, for $n > 1$ shear-thickening. Under the previous assumptions, the pressure distribution is hydrostatic and the velocity profile at any cross-section x is

$$
\begin{aligned}
u(x,z,t) = &-\frac{n}{2^{(n+1)/n}(n+1)}\frac{1}{\tilde{\mu}^{1/n}}\left|\frac{\partial p}{\partial x}\right|^{1/n-1} \\
&\times \frac{\partial p}{\partial x}\left(h^{(1+n)/n} - |2z - h|^{(1+n)/n}\right).
\end{aligned} \tag{5.7}
$$

Shear-thinning fluids ($n < 1$) are most common in practical applications and will be considered henceforth. The wall velocity w_w perpendicular to the wall itself is initially zero at the start of the relaxation phenomenon, i.e.

$$w_w(0) = 0, \tag{5.8}$$

and is given at the generic time t by

$$w_w(h) = \frac{\partial h}{\partial t} = \frac{\mathrm{d}h(t)}{\mathrm{d}t}, \tag{5.9}$$

the last equality holding as the wall is rigid. Further, w_w is related to the fluid velocity u in the x direction by the principle of continuity

$$\frac{\partial w_w}{\partial z} + \frac{\partial u}{\partial x} = 0. \tag{5.10}$$

Substituting eqs. (5.7) and (5.9) in eq. (5.10) and integrating perpendicular to the wall between $z = 0$ and $z = h(t)$ with the boundary conditions (5.8)-(5.9) yields

$$\frac{\mathrm{d}h(t)}{\mathrm{d}t} = \frac{1}{2^{(1+n)/n}(2n+1)\tilde{\mu}^{1/n}} h(t)^{(2n+1)/n}$$

$$\times \left|\frac{\partial p(x,t)}{\partial x}\right|^{1/n-1} \frac{\partial^2 p(x,t)}{\partial x^2}. \tag{5.11}$$

Referring now again to the geometry described by Figure 5.2, showing several bi-wing planar fractures (the schemes for single or multiple fractures do not differ except for the quantities depending on the spacing l), it is noted that consistently with the assumption $L \gg W$ the flow is uniform along most of the fracture half-length L and may be approximately described as planar except in the vicinity the well. Neglecting the convergence of flow lines therein allows simplifying the boundary condition at the fracture outflow, so that the initial and boundary conditions to eqs. (5.5) and (5.11) read

$$h(0,t) = h_0, \quad p(0,t) = p_e, \quad \frac{\partial p(x,t)}{\partial x}(L,t) = 0, \tag{5.12}$$

where i) h_0 is the initial fracture aperture; ii) p_e is the pressure at the fracture outflow, taken to be equal to borehole pressure along the entire fracture height W; iii) the condition at the fracture inflow, representing the upstream network of fractures created by the injection process, is identified as a zero pressure gradient, the least impacting condition on the pressure within the fracture.

5.3.2   Solution

The governing equations (5.5) and (5.11), and the initial and boundary conditions (5.12) can be written in dimensionless form respectively as

$$\frac{1}{H(T)^{(2n+1)/n}} \frac{\mathrm{d}H(T)}{\mathrm{d}T} = \left|\frac{\partial P(X,T)}{\partial X}\right|^{(1-n)/n} \frac{\partial^2 P(X,T)}{\partial X^2}, \tag{5.13}$$

$$\int_0^1 P(X,T)\mathrm{d}X = H^\lambda(T) - P_e + F_0, \tag{5.14}$$

$$H(X,0) = 1, \quad P(0,T) = 0, \quad \frac{\partial P(X,T)}{\partial X}(1,T) = 0, \tag{5.15}$$

by using the dimensionless quantities

$$X = x/L, \ H = h/h_0, \ T = t/t_c, \ P = (p - p_e)/p_c,$$
$$P_e = p_e/p_c, \ F_0 = f_0/(Lp_c), \ Q = (qt_c)/(Lh_0). \quad (5.16)$$

In eq. (5.16), the time and pressure scales t_c and p_c are defined as

$$t_c = \left(\frac{\tilde{\mu}}{\hat{E}}\right)^{1/n} \frac{(2L)^{(n+1)/n}(2n+1)}{h_0^{(n+\lambda+1)/n}}, \quad p_c = \hat{E}h_0^\lambda. \quad (5.17)$$

To solve the problem an auxiliary function is defined as

$$G(T) = \frac{1}{H(T)^{(2n+1)/n}} \frac{dH(T)}{dT}. \quad (5.18)$$

Together with the assumption of backflow, implying $\partial P/\partial x > 0$, eq. (5.18) allows integrating eq. (5.13) with the boundary conditions in eq. (5.15), obtaining the pressure field

$$P(X,T) = \frac{[-G(T)]^n}{n^n(n+1)} \left[1 - (1 - X)^{n+1}\right]. \quad (5.19)$$

Substituting eqs. (5.18) and (5.19) into eq. (5.14) gives

$$\frac{dH}{dT} + n(n+2)^{1/n} H^{(2n+1)/n} \left(H^\lambda - P_e + F_0\right)^{1/n} = 0, \quad (5.20)$$

subject to the initial condition in eq. (5.15).
For $P_e - F_0 = 0$ eq. (5.20) admits the following closed-form solution

$$H(T) = \left[1 + (1 + n + \lambda)(n+2)^{1/n}T\right]^{-n/(1+n+\lambda)}, \quad (5.21)$$

and consequently the pressure is given by

$$P(X, H(T)) = \frac{n+2}{n+1} H^\lambda(T) \left[1 - (1 - X)^{n+1}\right]. \quad (5.22)$$

For $n = 1$ and $\lambda = 1$, equations (5.21) and (5.22) reduce to the expressions derived by Dana *et al.* (Dana et al., 2018) for a Newtonian fluid and $\lambda = 1$ (a linearly elastic wall). Appendix A reports their late-time ($T \gg 1$) approximations. The dimensionless fracture aperture is shown versus time in Figure 5.3, showing the late-time $T^{-n/(n+\lambda+1)}$ scaling; the smaller the flow behaviour index n, the larger the dimensionless aperture. For smaller λ values, the fracture aperture decreases faster with time as the wall reacts less.
For $P_e - F_0 \geq 0$, the function $H(T)$ is obtained implicitly as

$$T = \frac{1}{(n+2)^{\frac{1}{n}}(1+n+\lambda)} \left[\frac{1}{\zeta^{(1+n+\lambda)/n}}\right.$$
$$\times {}_2F_1\left(\frac{1}{n}, \frac{1+n+\lambda}{n\lambda}; \frac{(1+\lambda)(n+1)}{n\lambda}; \frac{P_e - F_0}{\zeta^\lambda}\right)\right]\Big|_1^H, \quad (5.23)$$
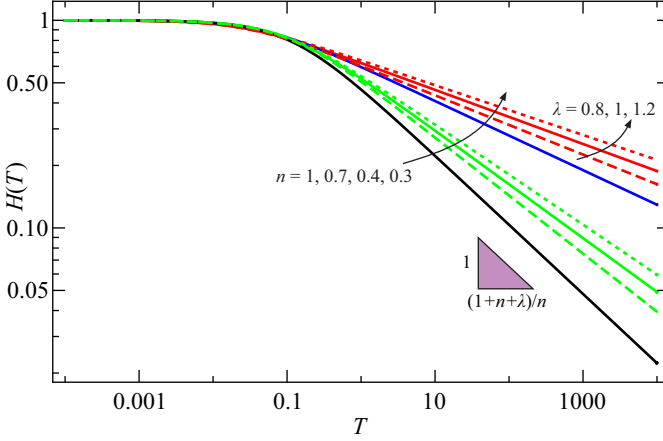
Figure 5.3: Dimensionless fracture aperture versus dimensionless time for $P_e - F_0 = 0$, and $n = 1, 0.7, 0.4, 0.3$. The cases $\lambda = 0.8, 1, 1.2$ are represented by dashed, continuous and dotted lines for $n = 0.7$ and $n = 0.3$ to illustrate the dependence upon λ.

where ζ is a dummy variable, $_2F_1(a, b; c; \zeta)$ is the hypergeometric function of parameters a, b, c and argument ζ and the linear transformation (9.132.2) in Gradshteyn and Ryzhik (Gradshteyn & Ryzhik, 2014) has been used. Early- and late-time approximation of the general equation (5.23) are reported in Appendix B. For the special case $P_e - F_0 = 0$, eq. (5.23) becomes eq. (5.21); for $n = 1$ and $\lambda = 1$, it reduces to equation (2.18) in Dana *et al.* (Dana et al., 2018) via the identity in Appendix C. When a linear wall reaction ($\lambda = 1$) is coupled with a shear-thinning fluid ($n < 1$), eqs. (5.21) and (5.23) reduce to

$$H(T) = \left[1 + (n+2)^{(n+1)/n} T\right]^{-n/(n+2)}, \tag{5.24}$$

$$T = \frac{1}{(n+2)^{\frac{n+1}{n}}}$$
$$\times \left[\frac{1}{\zeta^{(n+2)/n}} \, _2F_1\left(\frac{1}{n}, \frac{n+2}{n}; \frac{2(n+1)}{n}; \frac{P_e - F_0}{\zeta}\right)\right]\Bigg|_1^H. \tag{5.25}$$

The behaviour of the aperture-time function is depicted in Figure 5.4 for different values of n and λ and the case $P_e - F_0 = 0.1$. The aperture tends for large times to $(P_e - F_0)^{1/\lambda}$, and reaches this asymptote later for as the fluid becomes more shear-thinning; the asymptote value is larger when the wall is more rigid (larger λ).

The pressure field for the general case $P_e - F_0 > 0$ is

$$P(X, H(T)) = \frac{n+2}{n+1} H^\lambda(T) \left[1 - \frac{P_e - F_0}{H^\lambda(T)}\right] \left[1 - (1 - X)^{n+1}\right]. \tag{5.26}$$
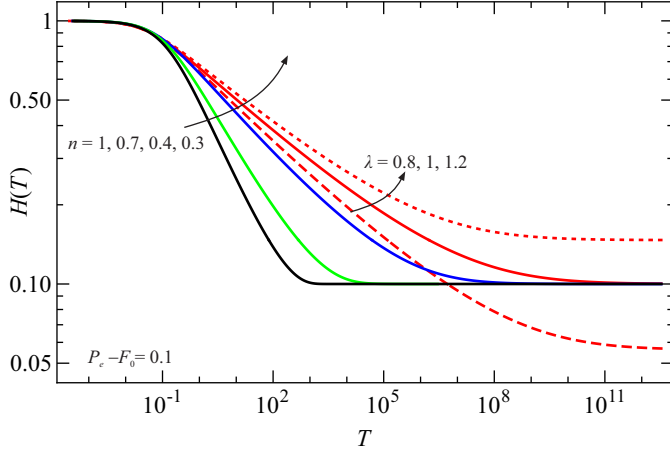
Figure 5.4: Dimensionless fracture aperture versus dimensionless time for $P_e - F_0 = 0.1$ and $n = 1, 0.7, 0.4, 0.3$. The cases $\lambda = 0.8, 1, 1.2$ are represented by dashed, continuous and dotted lines for $n = 0.7$ and $n = 0.3$ to illustrate the dependence upon λ.

Upon plotting the spatial trend of dimensionless pressure within the fracture at different times (Figure 5.5), it is observed that the pressure increases along the fracture and decreases over time; this decrease markedly depends on the value of n and is slower for shear-thinning fluids, more so at late times, while at early times the pressure difference among different fluids is modest.

5.3.3 Drainage analysis

A comparison between the efficiency of the linear and point drainage mechanisms (Holditch, 2007), corresponding to the plane or radial geometry, may be readily obtained by confronting the corresponding solutions for zero outlet pressure and overload, the present eq. (5.21) and eq. (17) of Chiapponi *et al.* (Chiapponi et al., 2019). These two have the general format

$$H(T) = \frac{1}{[1 + \delta(n, \lambda)T]^{n/(1+n+\lambda)}}, \qquad (5.27)$$

where the dependence on the drainage mechanism can be encapsulated in a decay coefficient $\delta(n, \lambda)$ for the fracture aperture, with $1/\delta$ akin to a dimensionless timescale of decay. In dimensionless terms, a larger decay coefficient implies a smaller aperture and residual pressure at any given time and location, hence a more efficient drainage mechanism. Figure 5.6 depicts the behaviour of $\delta(n, \lambda)$, showing that the decay rate: (i) decreases for increasing n, as the fluid behaviour approaches the Newtonian one, (ii) increases for increasing λ, as the fracture wall reacts more to any given pressure within the
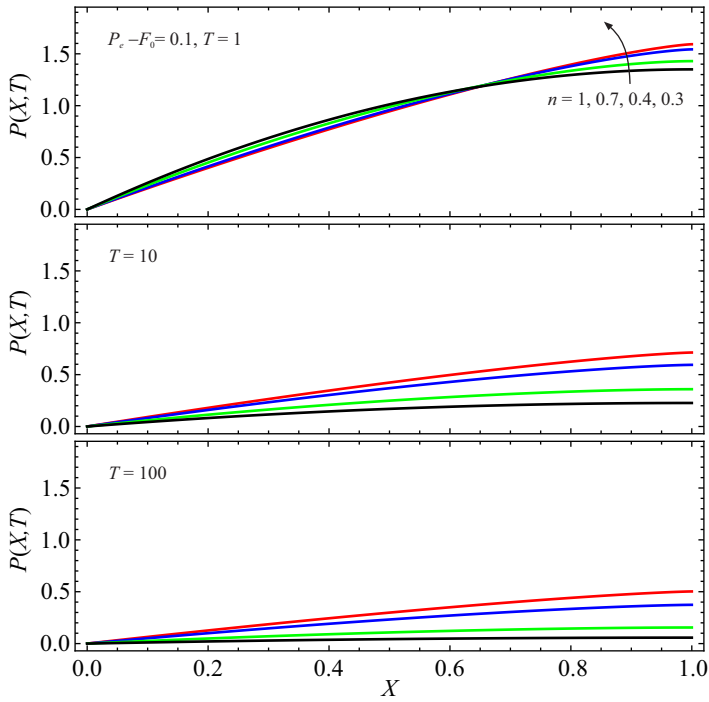
Figure 5.5: Pressure field for $P_e - F_0 = 0.1$, $n = 1, 0.7, 0.4, 0.3$ and $\lambda = 1$.
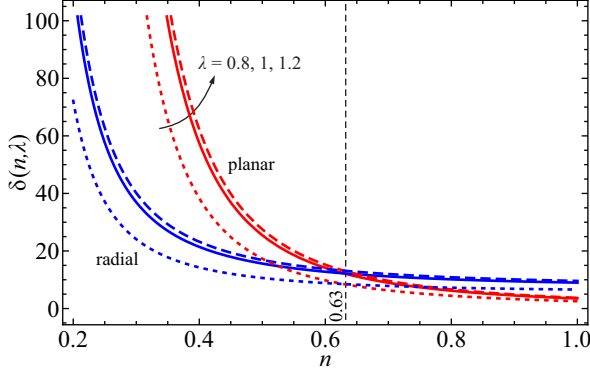
Figure 5.6: Decay ratio for linear and point drainage within a planar fracture and a circular one. The curves refer to softening (dotted), linear (continuous) and stiffening (dashed) fracture wall.

fracture, (iii) is more sensitive to the values of n and λ for small values of these two parameters, and (iv) is smaller for point than for linear drainage for shear-thinning fluids with $n < n_0 \gtrsim 0.63$. These results indicate that, above this threshold, the point drainage is less effective than the linear drainage. This is readily explained, as the average shear stress is homogeneous for the planar geometry with linear drainage, while it increases towards the origin for the radial geometry plate with point drainage. As the draining fluid becomes more shear-thinning, this effect is less pronounced than for Newtonian fluids, and eventually disappears for very shear-thinning fluids. It must be stressed that these conclusions refer exclusively to dimensionless results.

The outflowing discharge can be derived in dimensionless form and in analogy to Chiapponi *et al.* (Chiapponi et al., 2019) as

$$Q = n(n+2)^{\frac{1}{n}} H^{\frac{2n+1}{n}} \left(H^\lambda - P_e + F_0 \right)^{\frac{1}{n}} . \tag{5.28}$$

Analogously, the drainage time T_Y required to drain $Y\%$ of the total fracture volume $(0 - 100\%$ in dimensionless form) is equal to

$$T_Y = \frac{1}{(1+n+\lambda)(n+2)^{1/n}} \left[\left(\frac{100}{100-Y} \right)^{(1+n+\lambda)/n} - 1 \right], \tag{5.29}$$

for $P_e - F_0 = 0$, while for $P_e - F_0 \geq 0$ it is given by

$$T_Y = \frac{1}{(1+n+\lambda)(n+2)^{1/n}} \left[\frac{1}{\zeta^{(1+n+\lambda)/n}} \right.$$
$$\left. \times \,_2F_1 \left(\frac{1}{n}, \frac{1+n+\lambda}{n\lambda}; \frac{(1+\lambda)(n+1)}{n\lambda}; \frac{P_e - F_0}{\zeta^\lambda} \right) \right] \Bigg|_1^b, \tag{5.30}$$
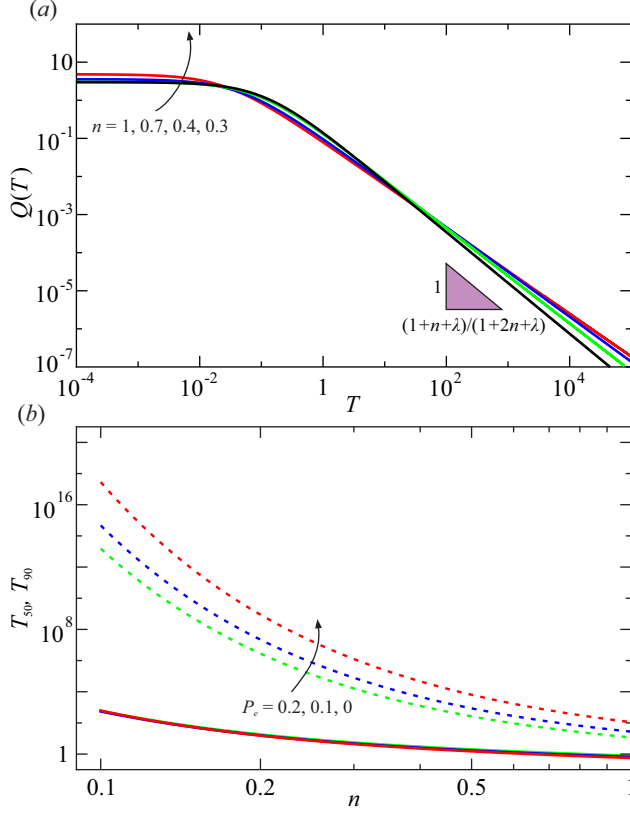
Figure 5.7: *a*) Discharge out of the fracture versus time for $P_e = 0$, $F_0 = 0$, $n = 1, 0.7, 0.4, 0.3$, and $\lambda = 1$. *b*) Time T_{50} (continuous lines) and T_{90} (dashed lines) required to drain 50% and 90% of the total volume versus n, for $\lambda = 1$, $F_0 = 0$, and $P_e = 0, 0.1, 0.2$.

with

$$b = (P_e - F_0)^{1/\lambda} + \frac{100 - Y}{100}\left[1 - (P_e - F_0)^{1/\lambda}\right]. \tag{5.31}$$

Figure 5.7*a* shows the dimensionless discharge out of the fracture for different values of n, zero outlet pressure P_e and overload F_0. The curves almost collapse, and according to eq. (5.28) exhibit an asymptotic scaling with time of exponent $-(2n+\lambda+1)/(n+\lambda+1)$; special values are $-2(n+1)/(n+2)$ for $\lambda = 1$, $-(3+\lambda)/(2+\lambda)$ for $n = 1$, and $-4/3$ for $n = 1$ and $\lambda = 1$. Figure 5.7*b* depicts T_{50} and T_{90}, the times required to drain 50% and 90% of the total fracture volume, for different values of n and P_e with $F_0 = 0$. Results are extremely sensitive to the values of P_e and n; the time needed to achieve a certain recovery decreases as the shear-thinning fluid approaches Newtonian behaviour and drops by orders of magnitude as P_e increases. This may seem

counterintuitive (the fracture drains against a non-zero outer pressure) but it happens as for $P_e > 0$ the fracture does not shut down completely, as opposed to the case $P_e = 0$. Note that in log-linear scale, the curves are practically indistinguishable for a 50% recovery, differ conspicuously for a 90% recovery, and even more so for a 99% recovery (not shown). For a softening model of the Winckler soil ($\lambda < 1$) there is a reduction of the drainage time with respect to the values computed for $\lambda = 1$, and the differences are greater the more the fluid is shear-thinning; the opposite is true for a stiffening model (not shown).

5.4 Experiments

The theory was validated via a set of experiments run in the Hydraulics Laboratory of Parma University. The experimental setup is described in section 3.1, uncertainty quantification in 3.2, and the actual experimental results in 3.3.

5.4.1 Experimental setup

In order to verify the theoretical model and to highlight the possible limitations of the scheme, two experimental devices were built (hereinafter small and large apparata), both consisting of a rigid rectangular flat slat of aluminium alloy, which moves vertically in a sealed cylinder of the same material. The parts were manufactured via a numerically controlled machine (CNC) to guarantee the flatness of the surfaces and therefore the uniformity of the thickness of the rectangular gap.

The seal is created using a neoprene o-ring with a diameter of 6-8 mm, with seats that allow the elastic deformation of the o-ring in a range generally less than 2 mm. The elastic reaction of the fracture wall, a Winkler soil for $\lambda = 1$, is represented by the elastic reaction of the o-ring. The elastic reaction function is taken to be a power-law according to eq. (5.1), and is experimentally evaluated by injecting pressurized air, with pressure measured by a Druck calibrator DPI601 20 kPa full-scale, and by measuring the vertical position of the piston with 3 dial gauges with a resolution of 1/100 mm: for different values of the air pressure, different vertical positions of the piston were measured. The general interpolating function is $p = p_t + \hat{E}h^\lambda$, where p_t is a threshold pressure due to pre- compression of the o-rings. The effect of this threshold pressure is equivalent to an overweight f_0.

The small apparatus shown in figure 5.8 has an internal length of about $2L = 45$ cm and a width of about $B = 9$ cm. In order to ensure uniformity of the gap during testing, the outlet is in the middle of the cylinder, with the two draining trunks of about $L = 20$ cm length discharging symmetrically. Two neoprene o-rings are installed, one between the upper surface of the piston and the closing frame of the cylinder, the other between the lower surface of the piston and the cylinder (bottom neoprene o-ring), with elastic reactions
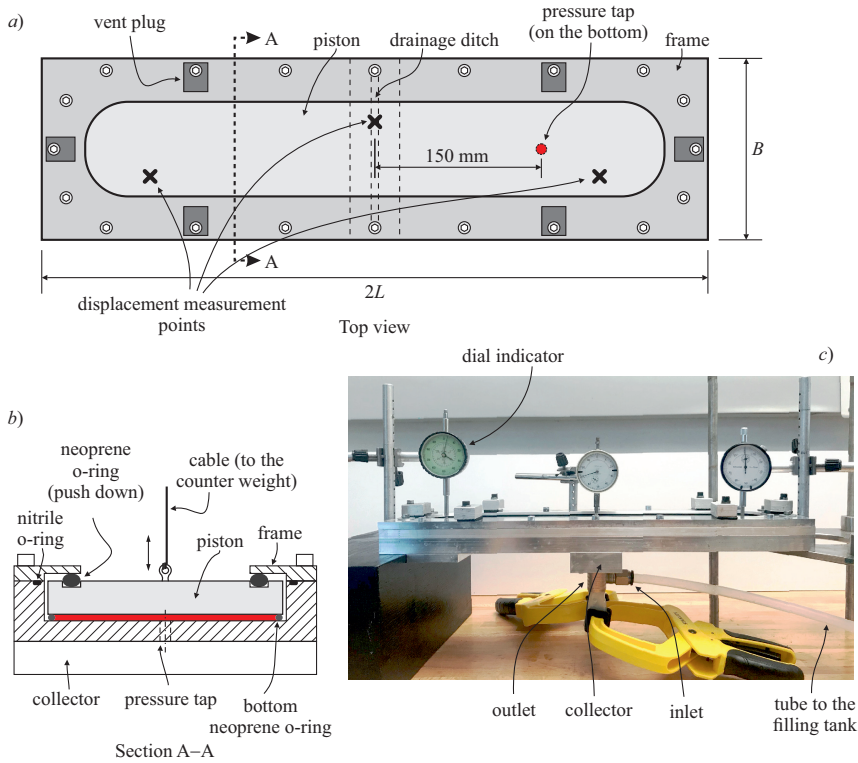
Figure 5.8: Small experimental apparatus. *a*) Top view, *b*) cross view, and *c*) a photo of the apparatus during tests. The bottom neoprene o-ring is missing in the large experimental apparatus.

of the o-rings in opposition. The weight of the piston is 20.20 N. A pressure tap at the bottom of the cylinder allows measurement of the initial pressure.

The large experimental apparatus, shown in figure 5.9, is missing the bottom neoprene o-ring, has an internal length of about $2L = 80$ cm and a width of about $B = 15$ cm. For this device, too, the outlet is in the centreline. In this apparatus, the o-ring is installed between the top surface of the piston and a closing frame of the cylinder (in the same configuration adopted for the first experimental device), with a free gap between the side walls of the piston and the cylinder of about 7/10 mm. The weight of the piston is 78.35 N. This large device has been realized both to check the existence of scale effects and to check the effects of the gap between the lateral surfaces of the piston and the cylinder; this gap could to some extent distort the main flow and could facilitate fluid drainage.

Prior to testing, the elastic reaction of the o-ring was calibrated, with a typical result shown in figure 5.10ab; the single o-ring in the large experimental apparatus shows a stiffening response, while the double o-ring in the small
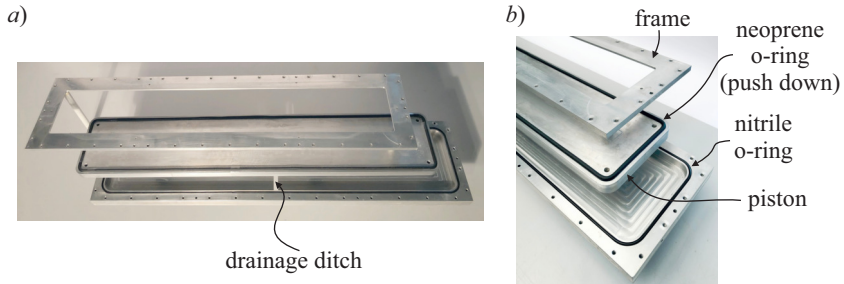
Figure 5.9: Large experimental apparatus. *a*) General view, *b*) details of the frame, the piston and the cylinder.
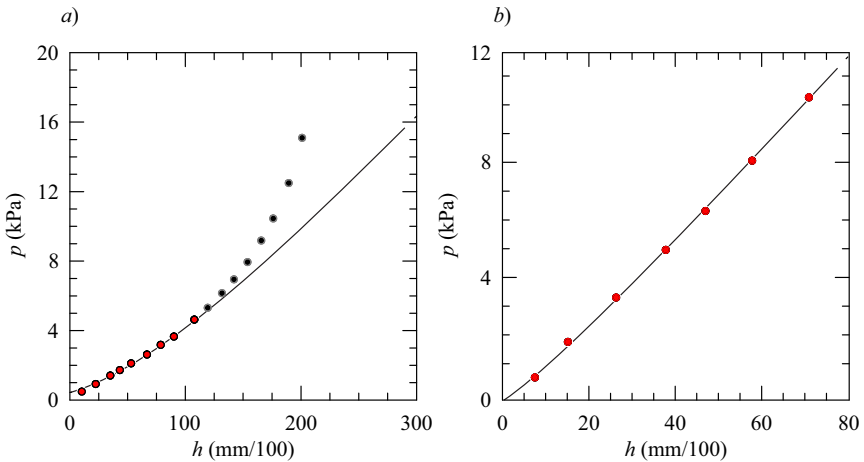
Figure 5.10: Typical experimental elastic response of the system. *a*) Single neoprene o-ring (large experimental apparatus), and *b*) double o-ring in opposition (small experimental apparatus).

experimental apparatus exhibits an almost linear response.

To start an experiment, the inlet pipe was connected to a tank filled with the fluid and positioned at a variable height with respect to the bottom of the cylinder. The purge valves were initially opened to eliminate air bubbles in the fracture and in the hydraulic circuit. Then the valves were closed, and the piston slowly began to move upwards. After reaching the desired position of the piston, the inlet pipe was closed and the outlet pipe was opened rapidly to simulate backflow, with the piston moving downwards. The position in time of the piston was recorded with a video camera at 25 frames per second. The video frames were post-processed to extract the reading of the three dial gauges. For experiments where the external pressure was non-zero, the tank was quickly lowered.

The Newtonian fluids adopted in the experiments were obtained by mixing

glycerol and water in different proportions to obtain different viscosities; the shear-thinning non-Newtonian fluids were obtained by adding Xanthan Gum to the above mixture. The rheological parameters were obtained via a parallel-plate rheometer by Anton Paar (dynamic shear rheometer Physica MCR 101), kept at the same temperature of the experiments. Fluid density was measured with a pycnometer.

5.4.2   Uncertainty quantification

The uncertainties of the experiments derive from the measurement procedures and from the parameters' estimation. The dials indicators have an absolute uncertainty assumed equal to the resolution of 1/100 mm; the absolute uncertainty in time measuring equals half the time step between two subsequent frames, 1/50 s. On the basis of the characteristics of the rheometer and of rheometric data dispersion, we assume a relative uncertainty in fluid behaviour index $\Delta n/n \leq 4\%$ and in consistency index $\Delta \tilde{\mu}/\tilde{\mu} \leq 6\%$. These uncertainties have been minimized by interpolating experimental rheometric data within the same range of shear rate of the experiments, see Longo *et al.* (Longo et al., 2015), yet are larger than the discrepancies typically associated to the adoption of a plate-plate geometry in lieu of a cone-plate geometry. The range of shear rate is computed considering that the maximum value at the wall is

$$\dot{\gamma}_w = \left(\frac{h}{2\tilde{\mu}} \right)^{1/n} \left(\frac{\mathrm{d}p}{\mathrm{d}x} \right)^{1/n} . \tag{5.32}$$

The gap-averaged value is $<\dot{\gamma}> = \dot{\gamma}_w[n/(n+1)]$, decays in time and decreases with the distance from the outlet section. Figure 5.11 shows the typical rheometric data for the shear-thinning fluid adopted in the present experiments, with two interpolating functions for two different ranges of the shear rate, and figure 5.12 shows the gap-average shear rate during Exp. 11.

   The uncertainty in mass density measurement equals $1\,\mathrm{g\,cm^{-3}}$, with $\Delta \rho/\rho \leq 0.1\%$. The elastic response of the neoprene o-ring is affected by partial hysteresis, which represents the most relevant source of uncertainty, with $\Delta \hat{E}/\hat{E} \leq 5.8\%$ and $\Delta \lambda/\lambda \leq 5.5\%$. Other sources of uncertainty are related to the accuracy of CNC machines and are difficult to quantify.

5.4.3   Comparison with model prediction

Fourteen tests were conducted, ten with a Newtonian and four with a shear-thinning fluid, with an initial fracture aperture ranging from 1.47 to 0.73 mm; four test had a non-zero external pressure. Table 5.1 lists the main parameters of the tests. The rheological parameters were obtained by interpolating the rheometrical data in the shear rate range of the experiments. With a similar approach, the elastic parameters $\hat{E}$ and λ were obtained by interpolating a power-function in the range of fracture aperture during the tests. We note that the reaction of the wall was always supra-linear, with λ in the range
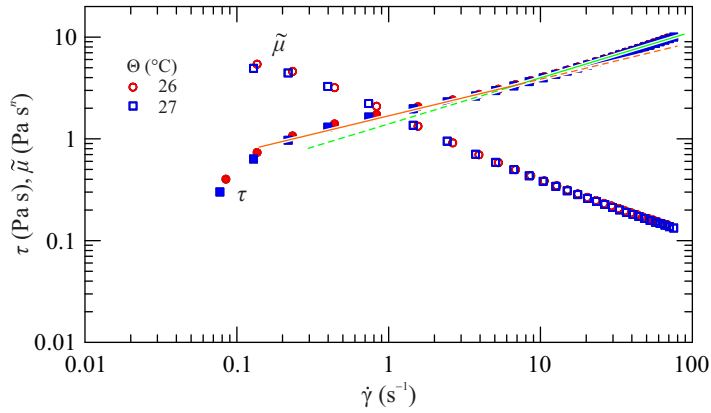
Figure 5.11: Typical rheometric data for the shear-thinning fluid adopted in the experiments, measured at temperatures of 26°C and 27°C. The two interpolating lines indicate that the rheological parameters depend on the range of the shear rate.
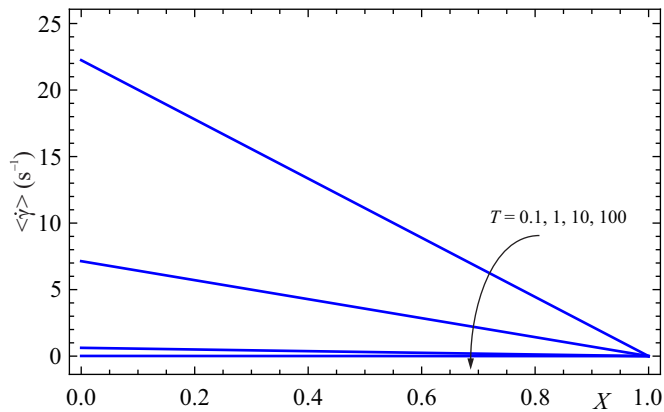
Figure 5.12: Theoretical gap-average shear rate during backflow for Exp. 11, shear-thinning fluid.

Expt.	n	$\tilde{\mu}\,(\mathrm{Pa\,s}^n)$	$\Theta\,(^\circ\mathrm{C})$	$\rho\,(\mathrm{g\,cm}^{-3})$	$h_0\,(\mathrm{mm})$	$p_e\,(\mathrm{Pa})$	λ	$\hat{E}\,(\mathrm{MPa\,m}^{-\lambda})$	$p_t\,(\mathrm{Pa})$	$f_0\,(\mathrm{N})$	Apparatus
1	1	0.24	23.0	1.240	0.97	0	1.36	45.5	1200	78.35	L
2	1	0.24	23.0	1.240	0.73	0	1.36	45.5	1200	78.35	L
3	1	0.50	23.0	1.250	1.21	0	1.43	63.7	950	78.35	L
4	1	1.36	20.0	1.257	1.10	0	1.31	32.5	800	78.35	L
5	1	1.11	19.0	1.257	1.11	0	1.45	88.2	250	78.35	L
6	1	1.06	19.5	1.256	1.46	0	1.60	244.9	450	0.00	L
7	1	0.59	22.6	1.256	1.06	0	1.65	477.5	900	20.20	L
8	1	0.38	23.5	1.256	0.75	0	1.10	29.6	1000	20.20	S
9	1	0.51	22.0	1.250	0.98	2600	1.30	25.3	0	78.35	L
10	1	1.36	20.0	1.257	0.93	1200	1.15	10.9	0	78.35	L
11	0.42	1.52	26.3	1.175	0.98	0	0.69	1.3	0	20.20	S
12	0.46	1.56	27.0	1.175	1.26	11 400	0.80	2.6	0	20.20	S
13	0.46	1.52	27.0	1.175	0.97	6700	0.80	2.6	0	20.20	S
14	0.6	1.90	27.0	1046	0.80	0	0.6	0.4	0	20.20	S

Table 5.1: Parameters adopted for the tests in planar geometry. n and $\tilde{\mu}$ are the fluid behaviour and consistency indexes, Θ is the temperature during the test, ρ is the fluid density, h_0 is the initial fracture height, p_e is the external pressure during backflow, λ, $\hat{E}$ and p_t are the exponent characterizing the nonlinearity of the elastic response, the Winkler subgrade coefficient and the threshold pressure, with $p = p_t + \hat{E}h^\lambda$, where the threshold pressure is the minimum value of pressure required to lift the piston and is due to pre- compression of the o-rings; f_0 is the external load, positive if it favours the fracture closure. In the last column, the symbol "L" and "S" indicates that the large/small experimental apparatus was used.

$1.10 \div 1.65$, for the ten tests with Newtonian fluids, and always sublinear, with λ in the range $0.60 \div 0.80$, for the four tests with shear-thinning fluids. On the contrary, performing experiments in radial flow, the wall reaction was always linear (Chiapponi et al., 2019). This behaviour is dictated by the different geometry of the o-ring seat, with respect to the piston in radial geometry, while in the case of the small apparatus the presence of two o-rings in opposition reduces the value of λ. Exception is made for Exp. 8 for which also in the small apparatus only the upper o-ring was installed. An overload was always present, except for Exp. 6, since for this experiment the piston weight was balanced. Many different values of the Winkler subgrade coefficient $\hat{E}$ were employed, spanning more than three orders of magnitude. The large apparatus was always used with Newtonian fluids except for one case, while the small one was coupled with shear-thinning fluids in all cases. Using two apparata allowed us to verify the lack of scale effects, and to test two different sealing techniques, associated with different elastic responses.

The repeatability of the experiments turned out to be fairly good, as shown by the near overlap of the time series of the fracture aperture for Exp. 1 and 2 conducted under the same conditions except for h_0.

Figure 5.13 compares theoretical predictions and experimental results for the relationship between aperture and time; the two latter quantities are normalized. The experimental apertures match well their theoretical coun-
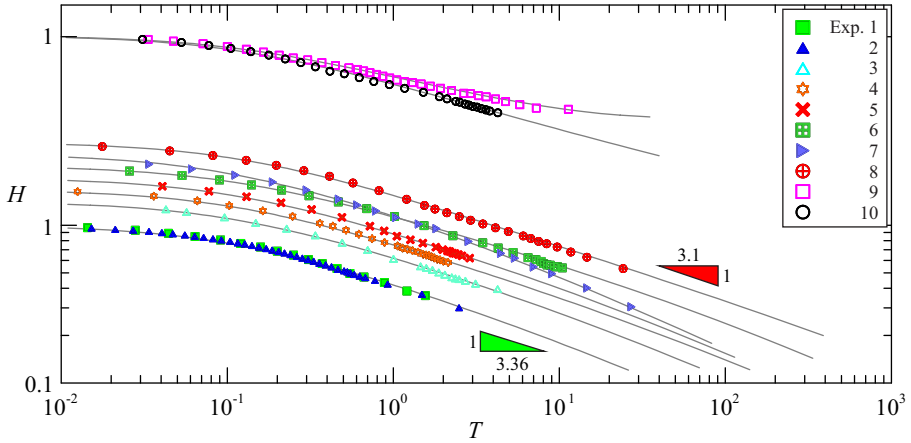
Figure 5.13: Experimental results for the Newtonian fluid, with parameters listed in table 5.1. Symbols represent the experimental data, curves are the theory. Expts. 1-8 are with zero exit pressure, Expts. 9-10 are with non-zero exit pressure. Data and theoretical curves are translated along the vertical for a better visualization, except for Expts.1 and 2, conducted under the same conditions to check the repeatability of the results.
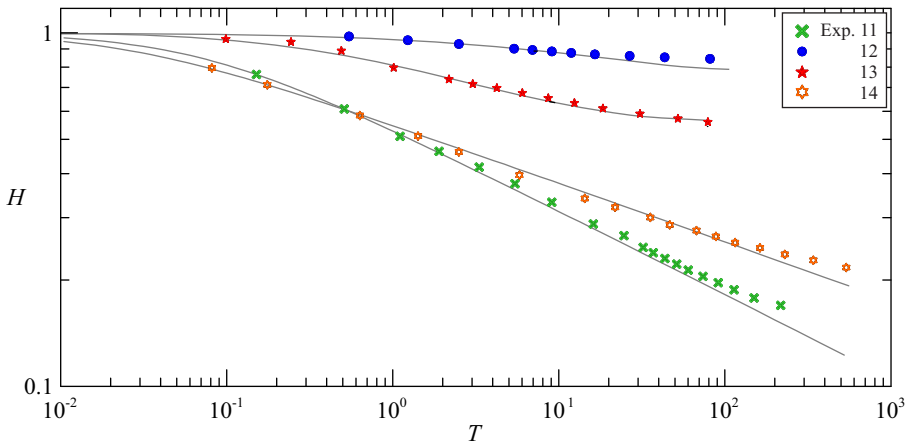
Figure 5.14: Experimental results for non-Newtonian shear-thinning fluid, with parameters listed in table 5.1. Symbols represent the experimental data, curves are the theory. Expts. 11 and 14 are with zero exit pressure, Expts. 12-13 are with non-zero exit pressure.

terparts, capturing the decrease of the aperture versus time towards the respective asymptote; for some experiments there is a slight overestimation, for other experiments the opposite is true with no clear tendency. The same comparison is proposed in Figure 5.14 for shear-thinning fluids; again, the match between theory and experiments is fairly good, with no appreciable differences in accuracy between different experiments. Similarly, no clear trend towards under- or over-estimation is evident, with perhaps a tendency of the residual aperture to exceed the theoretical prediction.

5.5 The effects of leak-off

A further refinement to the conceptual scheme is considering the additional effect of leak-off, with the fluid infiltrating the matrix surrounding the fractures, see Longo and Di Federico (Longo & Di Federico, 2015). This loss of fluid potentially occurs throughout both: i) the border of the fracture, through a surface area of length L_l and height equal to the actual aperture $h(t)$, and ii) the two walls through a surface area A_l. As a simplification, we assume that the details of the fluid flow in the surrounding matrix can be neglected and that the pressure gradient controlling the leak-off is of order $(p - p_0)/l_0$, l_0 being a characteristic length of the process and p_0 a reference pressure within the matrix. The leak-off fluid velocity is assumed equal to

$$u = \left(\frac{k}{\mu_{eff}}\right)^{1/n} \frac{(p - p_0)^{1/n}}{l_0^{1/n}}, \qquad (5.33)$$

where k is the permeability of the matrix and μ_{eff} is the effective viscosity, with (Ciriello, Longo, Chiapponi & Di Federico, 2016)

$$\frac{k}{\mu_{eff}} \equiv \Lambda k^{(1+n)/2},$$

$$\Lambda = \frac{1}{2C_t}\left(\frac{50}{3}\right)^{(n+1)/2}\left(\frac{n}{3n+1}\right)^n \frac{\phi^{(n-1)/2}}{\tilde{\mu}}, \qquad (5.34)$$

where C_t is the tortuosity equal to (Pascal, 1983) $C_t = (25/12)^{(n+1)/2}$. Leak-off can occur along the fracture edge of height $h(t)$, or diffusely through the fracture walls as a consequence, e.g., of pre-existing fractures.

When modified by adding sink terms, eq. (5.11) becomes

$$\frac{\mathrm{d}h(t)}{\mathrm{d}t} = \frac{1}{2^{(1+n)/n}(2n+1)\tilde{\mu}^{1/n}}h(t)^{(2n+1)/n}\left|\frac{\partial p(x,t)}{\partial x}\right|^{1/n-1}$$
$$\times \frac{\partial^2 p(x,t)}{\partial x^2} - \chi_1 h(t)(p - p_0)^{1/n} - \chi_2(p - p_0)^{1/n}, \qquad (5.35)$$

where $\chi_1 = [M^{-1/n}L^{1/n}T^{2/n-1}]$ is

$$\chi_1 = \frac{L_l}{L}\left(\frac{k}{l_0\mu_{eff}}\right)^{1/n}, \tag{5.36}$$

and $\chi_2 = [M^{-1/n}L^{1+1/n}T^{2/n-1}]$ is

$$\chi_2 = \frac{A_l}{L}\left(\frac{k}{l_0\mu_{eff}}\right)^{1/n}. \tag{5.37}$$

Assuming that the reference pressure within the matrix is the well bore pressure, i.e. $p_0 = p_e$, eq. (5.35) becomes in dimensionless form

$$\frac{\mathrm{d}H(T)}{\mathrm{d}T} = H(T)^{(2n+1)/n}\left|\frac{\partial P(X,T)}{\partial X}\right|^{(1-n)/n}\frac{\partial^2 P(X,T)}{\partial X^2}$$
$$- \tilde{\chi}_1 H(T)P(X,T)^{1/n} - \tilde{\chi}_2 P(X,T)^{1/n}, \quad (5.38)$$

where $\tilde{\chi}_1 = \chi_1 t_c p_c^{1/n}$ and $\tilde{\chi}_2 = \chi_2 h_0^{-1} t_c p_c^{1/n}$ are dimensionless coefficients.

The integral equation (5.14) and the boundary and initial conditions (5.15) still hold. We notice that in order to guarantee that $\partial P(1,T)/\partial X = 0$ we assume that no leak-off from the border of the fracture occurs at $X = 1$.

The numerical solution is obtained with a code written in Mathematica, with a parametric solver for $P(X,T)$ as a function of $\tilde{\chi}_1$ of $\tilde{\chi}_2$, n, H_{i+1}, H_i, Δt, where H_i is the value of H at time $i\Delta t$. At each time step, only H_{i+1} is free, all the other parameters are known. Hence, at each step:

- the pressure $P(X)_{i+1}$ is estimated by solving eq.(5.38) in parametric form and approximating the time derivative with $\dot{H} \approx (H_{i+1} - H_i)/\Delta t$, with $P(0)_{i+1} = 0$ and $P'(1)_{i+1} = 0$; H_{i+1} is the free parameter and $H_0 = 1$. Note that the algorithm guarantees a correct treatment of the boundary conditions on the pressure at the inlet and on the pressure gradient at the outlet, which would otherwise appear as hill-posed and requiring for shooting method after converting the problem to an initial value problem.

- The pressure field is numerically integrated in parametric form in the space domain $[0, 1]$; the free parameter is H_{i+1}.

- The parametric integral is used in eq.(5.14) and the equality is forced with a Newton method to estimate H_{i+1}.

- The procedure is repeated at the next time step.

An example code in Wolfram Mathematica 11 is available in https://github.com/sandrolongo2/sandrocodes. A fully explicit advancement in time with an adapted time step guarantees an adequate reproduction of
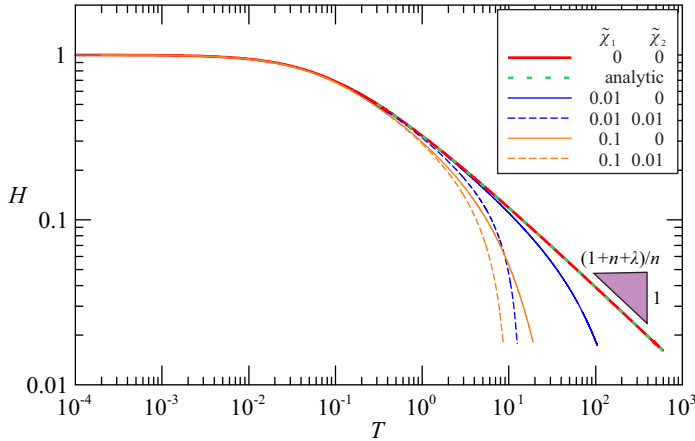
Figure 5.15: Dimensionless fracture aperture versus time for $P_e = 0$, $F_0 = 0$, $n = 1$, $\lambda = 1.37$ and different combinations of $\tilde{\chi}_1$ and $\tilde{\chi}_2$. The asymptotic decay for $\tilde{\chi}_1 \neq 0$ and $\tilde{\chi}_2 = 0$ is exponential.

the analytic solution for $\tilde{\chi} = \tilde{\chi}_2 = 0$, see figure 5.15 showing the results for different combinations of the two parameters controlling leak-off. The dotted green curve and the thick red curve are the analytical solution and the numerical computation, respectively, for the case without leak-off. The remaining curves, associated with either non-zero $\tilde{\chi}_1$ or non-zero $\tilde{\chi}_2$, show the late-time decay is strongly influenced by the leakage effects, with a faster closure of the fracture with respect to the absence of leakage. The effect of the two different leak-off modes is very similar, although the first mode reduces its effect more rapidly due to both the reduction in pressure in the fracture and the progressive closure of the fracture itself; in the second mode it is assumed that the leakage area is invariant and therefore the decay of the effect is due only to the drop in pressure over time.

5.6   Conclusions

Our study tackles the quantitative characterization of the flow back phenomenon of a power-law non-Newtonian fluid taking place in a plane, smooth rock fracture characterized by closing walls associated with various degrees of elasticity. The Newtonian fluid is included as a special case. Closed-from expressions for the fracture aperture, pressure field, discharge rate and drainage time are made available for rigid walls as functions of outlet pressure, overload and recovery rate, and rheological parameters. Our result belong to the category of simplified models and may be used to infer key tendencies and inform upscaling approaches.

Two specific laboratory apparata were built, and an experimental campaign was devised to reproduce the theoretical hypotheses as closely as pos-

sible, overcoming the difficulties inherent in the control of the elastic reaction and with an adequate seal, reducing friction to a minimum, carefully checking that there was adequate air venting during the filling phase to avoid trapped air bubbles. The accuracy of the piston and cylinder geometry is a key element of the experimental work, since the dependence of the flow rate on the third power of the fracture opening (for a Newtonian fluid) amplifies the uncertainties by a factor of 3: the uncertainty in the value of h is tripled when calculating the uncertainty in the value of the flow rate. Special care was also taken with the test fluid, both when creating the mixture and when measuring the rheological parameters, by carefully choosing the interpolation range of the power-law model based on the expected range of shear rate. This is a consequence of the fact that the power-law model, like other rheological laws, is an approximation of the real constitutive equation of non-Newtonian fluids and yields different values of the consistency index and of the flow behaviour index when the model is fitted to different ranges of shear rate. Theoretical results were confirmed by our experiments, generally with a good match and minor under- or over-estimation in the order of a few percent.

Further particular conclusions may be drawn from our work:

- The special case of zero outlet pressure and overload has a simple, explicit closed-form solution tending asymptotically to total closure and zero discharge; its late-time behaviour shows a scaling $t^{-n/(n+\lambda+1)}$ for the aperture and $-(2n + \lambda + 1)/(n + \lambda + 1)$ for the discharge. These exponents clearly elucidate the dependency from flow behaviour index n and exponent λ modulating the wall reaction: very shear-thinning fluids (smaller n) and reactive walls (larger λ) are associated with a more gradual closure.

- The solution for the general case of non-zero outlet pressure p_e and overload f_0 tends asymptotically to a constant value proportional to $(p_e - f_0)^{1/\lambda}$.

- The dimensionless drainage time T_Y required to recover $Y\%$ of the fluid initially residing in the system decreases with increasing n and P_e and decreases with λ, and the differences are greater the more the fluid is shear-thinning. For recovery values close to 100%, T_Y is extremely sensitive to variations of model parameters.

- Experiments can also be conducted on a small geometric scale, but with adequate control of all test steps to limit disturbances and reduce the uncertainty of the results.

- The use of two different apparata allowed exploring both sub- and supra-linear wall reactions and showed the lack of scale effects.

The body of experimental and theoretical work on Newtonian and non-Newtonian power-law backflow from a fracture with relaxing walls towards a

central well or borehole in the two limit flow configurations (plane and radial) allows to describe the phenomenon in a quite comprehensive way within the framework of the single fracture conceptualization. Problem variables are described as functions of system parameters in dimensionless form without the need of specifying any dimensionless number for a Newtonian fluid (Dana et al., 2018), and quantifying the only flow behaviour index n for power-law fluids, having a two-parameter constitutive equation (Chiapponi *et al.* (Chiapponi et al., 2019) and this paper); when a three-parameter rheology such as the Ellis model is adopted the need for an additional dimensionless quantity, namely the ratio between the characteristic shear stress of the Ellis fluid τ_0 and the rock modulus of elasticity E, arises (Ciriello et al., 2021). Similarly, the incorporation of slip effects, relatively common in non-Newtonian flows, would give rise to one or more dimensionless numbers. Another intriguing option is to optimize system performance in terms of geometry and/or rheology using specific metrics , or model inertial flow (Valdés-Parada & Lasseux, 2021). Finally, the need for incorporating uncertainty into modelling of fracking phenomena has recently been brought to attention in the literature (Quosay, Knez & Ziaja, 2020).

5.7 Appendix A - Late-time approximations for $P_e - F_0 = 0$

For late time $(T \gg 1)$, equations (5.21) and (5.22) simplify to

$$H(T) \approx (n+2)^{-1/(1+n+\lambda)}(1+n+\lambda)^{-n/(1+n+\lambda)}T^{-n/(1+n+\lambda)}, \quad (5.39)$$

$$P(X,T) \approx \frac{(n+2)^{(n+1)/(1+n+\lambda)}(1+n+\lambda)^{-\lambda n/(1+n+\lambda)}}{n+1} \times T^{-\lambda n/(1+n+\lambda)} \times \left[1 - (1-X)^{n+1}\right]. \quad (5.40)$$

5.8 Appendix B - Early- and late-time approximations for $P_e - F_0 > 0$

For early time $(T \ll 1)$ eq. (5.23) reduces to

$$T \approx \frac{1}{(n+2)^{\frac{1}{n}}(1+n+\lambda)} \times \left[\frac{1}{H^{\frac{1+n+\lambda}{n}}}\left(1 + \frac{1+n+\lambda}{n(1+n)(1+\lambda)}\frac{P_e - F_0}{H^\lambda}\right)\right]\Bigg|_1^H. \quad (5.41)$$

For late time $(T \gg 1)$ the approximation of eq. (5.23) is

$$
T \approx \frac{H^{-(1+n+\lambda)/n}}{(n+2)^{1/n}\lambda(1-n)} \left(1 - \frac{P_e - F_0}{H^\lambda}\right)^{1-1/n}
$$
$$
+ \frac{H^{-(1+n+\lambda)/n}}{(n+2)^{1/n}(1+n+\lambda)} \frac{\Gamma(1-1/n)\Gamma((\lambda+1)(n+1)/(n\lambda))}{\Gamma(1+(1+n)/(n\lambda))}, \quad (5.42)
$$

which is singular for $n = 1$. The symbol $\Gamma(\cdot)$ is the Gamma function.

5.9 Appendix C - Identity for specific value of the hypergeometric function $_2F_1$

The following identity holds for any positive z (Wolfram, 2020)

$$
_2F_1\left(1, 3; 4; z\right) = -\frac{3}{2z^3}\left[z(z+2) + 2\ln(1-z)\right]. \quad (5.43)
$$

6 | Relaxation-induced flow in a smooth fracture for Ellis rheology

6.1   Abstract

Hydraulic fracturing is a process aimed at improving the productivity of oil, gas or geothermal reservoirs. During hydrofracturing, backflow follows injection and represents the second phase of the process, when part of the fracturing fluid returns from fractures to well, and from well to surface. A conceptual model is presented to grasp the essential features of the phenomenon, conceiving the draining subsurface domain as a planar and rigid fracture. Backflow against an outlet pressure in the injection well is induced by the relaxation of the fracture wall, exerting a force on the fluid proportional to h^λ, with h the time-variable aperture and λ a non-negative exponent; an overload on the fracture may contribute to slowing or accelerating the closure process. The fluid rheology is described by the three-parameter Ellis constitutive equation, well representing the shear-thinning rheology typical of hydrofracturing fluids and coupling Newtonian and power-law behaviour. The interplay between these tendencies is modulated by a dimensionless number N encapsulating most problem parameters; the range of variation of N is discussed and found to vary around unity. The time-variable aperture and discharge rate, the space-time variable pressure field, and the time to drain a specified fraction of the fracture volume are derived as functions of geometry (length and initial aperture), wall elastic parameters, fluid properties, outlet pressure p_e and overload f_0. The late-time behaviour of the system is practically independent from rheology as the Newtonian nature of the fluid prevails at low shear stress. In particular, aperture and discharge scale asymptotically with time as $t^{-1/(\lambda+2)}$ and $t^{-1/(\lambda+3)}$ for $p_e - f_0 = 0$; else, the aperture tends to a constant, residual value proportional to $(p_e - f_0)^\lambda$. A case study with equally spaced fractures adopting realistic geometric, mechanical and rheological parameters is examined: two fluids normally used in fracking technology show completely different behaviours, with backflow dynamics and drainage times initially not dissimilar, later varying by orders of magnitude.

6.2   Introduction

Hydraulic fracturing is a process aimed at improving the productivity of oil, gas or geothermal reservoirs. Analysis of the different phases of hydraulic fracturing is of particular modeling and experimental interest.

An understanding of fractured media flow induced by the relaxation of elastic fracture walls is crucial in modeling fracturing fluid backflow, a complicated phenomenon involving hydrodynamic, mechanical and chemical processes. Backflow is typically the final phase of the hydraulic fracturing process: in the first one, fracturing fluid is injected at high pressure in a rock mass, forming new fractures and enlarging existing ones; in the second phase, proppant is introduced in the subsurface environment to prop fractures open; then when the injection ceases, the pressure drops, existing and new fractures tend to close, and a portion of the injected fracturing fluid, often mixed with proppant (Ezulike, Dehghanpour, Virues, Hawkes & Jones, 2016), flows back towards the injection well and interact with the relaxing walls of the fractures. As the retention of fracturing fluid in the fracture network impairs the fracture conductivity reducing the wellbore productivity (Balhoff & Miller, 2005), and favours migration in the subsurface environment along different pathways (Birdsell et al., 2015), it is of utmost interest to optimize the amount of fluid recovered, irrespective of the reservoir product, be it oil (Zanganeh, Ahmadi, Hanks & Awoleke, 2015), gas (Ghanbari & Dehghanpour, 2016) or heat (McLennan, Walton, Moore, Brinton & Lund, 2015).

The scientific literature offers two main approaches to modeling backflow: (i) detailed numerical simulations involving single fractures (Zeng, Li & Zhang, 2016), fracture networks (Hyman et al.,, 2016) or dual or triple porosity models (Wang, Pan, Zhang & Zhang, 2018b), or (ii) conceptual models capturing the main features of the interaction between fracture flow and wall relaxation (Huang, Hu, Zeng & Zhang, 2019), including the effects of branching networks described at different degrees of complexity (Dana et al., 2018, 2019). A recent addition to the modeling effort is the influence of fluid rheology, following the notion that the backflow fluid is non-Newtonian in the widest sense (Barbati et al., 2016), as not only the relationship between shear stress and shear rate is nonlinear, but also exhibits normal stress and temperature dependency, as well as viscoelasticity, thixotropy, and nonzero yield stress (Hormozi & Frigaard, 2017). At the same time, non-Newtonian fluids allow achieving several engineering objectives, such as (i) minimize the pressure-drop in the entire process; (ii) carry suspended proppant; (iii) minimize the leak-off within the formation; (iv) adapt their characteristics to different environments in terms of temperature and chemical composition; and (v) flow back easily towards the wellbore. Given their versatility and economic value, these fluids are typically treated for reuse once recovered, removing contaminants they may have transported to the surface (Lester et al., 2014). The recovery ratios of backflow fluid vary between 2% and 48% according to Ipatova and Chuprakov (Ipatova & Chuprakov, 2020), with considerable economic value.

Modeling non Newtonian backflow is in its early stage, in variance with the injection and fracture formation stage, for which several conceptualizations and models are available: see Detournay (Detournay, 2016) for a review and the recent work by Wrobel (Wrobel, 2020) comparing different rheological models for fracturing fluids. To the best of our knowledge, only Chiapponi et al. (Chiapponi et al., 2019) considered non-Newtonian fluids in the context of backflow modeling: these authors examined flow of a power-law fluid towards a wellbore in a single fracture of annular geometry, supporting their theoretical findings with laboratory experiments. The present paper develops the analysis of non-Newtonian backflow for a smooth fracture, common in field applications (Osiptov, 2017), and adds realism by employing a three-parameter Ellis model, that well represents the rheology of hydrofracturing (Moukhtari & Lecampion, 2018) and drilling fluids (Shah, Shanker & Ogugbue, 2010). The Ellis model tends to Newtonian for low shear rates, to power-law for high shear rates and allows avoiding the unphysical effect of infinite apparent viscosity at zero shear rate that is typical of the power-law model (Myers, 2005). We note in passing that our results are of a general nature for Newtonian pressurized flow in ducts of variable width and may be of interest for, and be applied also to, deformable microfluidic (Anand, David & Christov, 2019) and biological (Ali, Hussain, Ullah & Anwar Beg, 2019) systems.

The plan of the paper is as follows. Section 2 formulates the problem of relaxation-induced backflow of an Ellis fluid in a fracture with nonlinear wall reaction and subject to overload. Numerical results obtained are presented and discussed in Section 3 as a function of dimensionless groups characterizing the system: the indicial exponent α quantifying the degree of shear-thinning behaviour of the Ellis fluid, the non-negative exponent λ modulating the fracture wall reaction, and a further group N encapsulating most problem parameters. Section 4 illustrates an hypothetical case study adopting realistic geometric and mechanical parameters and two real hydrofracturing fluids decribed by the Ellis model. Section 5 reports the main conclusions and perspectives for future work. In Appendix A the special case of a Newtonian fluid is examined, obtaining results that generalize those of Dana et al. (Dana et al., 2018) to a nonlinear wall reaction, while Appendix B presents an alternative expression for the dimensionless number N, shown to be a combination of well-known dimensionless groups in fluid mechanics.

6.3 Material and methods

6.3.1 Problem statement

A rock fracture produced by hydrofracturing, though of irregular geometry, is often conceptualized for modeling purposes as a 3-D space of length L, width W, and aperture h between two parallel walls (Balhoff & Thompson, 2006); the Cartesian coordinate system x, y, z is illustrated in Figure 6.1 and the fracture is subject to a pressure gradient $\nabla p' \equiv (\partial p'/\partial x, 0, 0)$ in the x
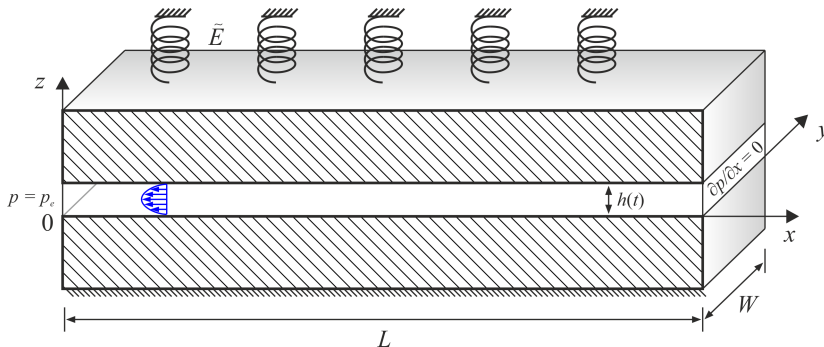
Figure 6.1: Layout of a plane fracture of variable uniform aperture $h(t)$.

direction. In horizontal fractures, the additional gravity-induced pressure gradient is perpendicular the flow plane and has no effect on the flow field. If the (x, y) plane is not horizontal, the z direction perpendicular to the walls is not vertical and gravity effects can be included in a reduced pressure term p, thus leading to a mathematical treatment with no gravity term to consider. For instance, for the Figure 6.3 below representing multiple vertical fractures backflowing to an horizontal well, the reduced pressure p is equal to $p = p' + \rho g y$.

The walls are taken to be rigid, so that the aperture $h(t)$ is solely a function of time, and the deformation is concentrated for mathematical convenience in the upper wall, that behaves as a nonlinear elastic foundation exerting a reaction on the fluid. At $t = 0$ the relaxation of the wall induces a backflow in the negative x direction, and the fracture begins to drain subject to a constant outlet pressure p_e at $x = 0$ and to a no-flow boundary condition at the upstream end $x = L$. Three further hypotheses are adopted: i) the flow is quasi-steady, allowing to neglect the time derivative of the velocity in the momentum equation; ii) the fracture aspect ratio is small, $h_0/L \ll 1$, warranting the lubrication approximation, and iii) the flow is essentially one-dimensional along x, $L \gg W$. The latter conceptualization is usually adopted in hydrogeology also when the two dimensions are comparable, as it is often the case for rock fractures (Wang et al., 2018b).

The flowback fluid is taken to be incompressible of density ρ, non-Newtonian shear-thinning (Barbati et al., 2016) and described by the Ellis three-parameter model (Skelland, 1967). Under the above assumptions, the fluid undergoes simple shear flow in the x direction, and the Ellis rheology is described by the following relationship between shear stress τ_{zx} (hereinafter τ) and shear rate $\dot{\gamma}_{zx}$ (hereinafter simply $\dot{\gamma}$)

$$\tau = \frac{\mu_0}{1 + (\tau/\tau_0)^{\alpha-1}}\dot{\gamma}; \quad \dot{\gamma} = \frac{\partial u}{\partial z}, \tag{6.1}$$

where u is the velocity in the x direction. The rheological law (6.1) features a
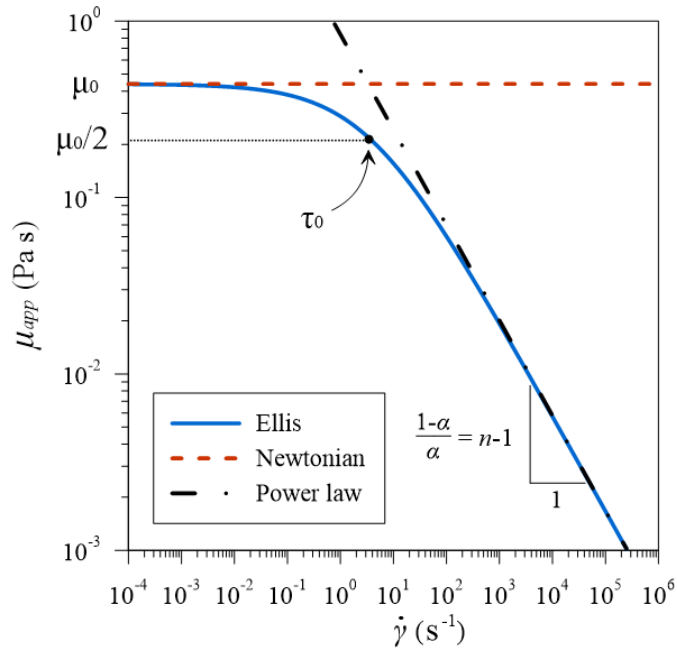
Figure 6.2: Apparent viscosity for three rheological models: Ellis (blue solid line) of parameters μ_0, τ_0, α; Newtonian (red dashed line) of viscosity μ_0; power-law (black dot-dashed line) of consistency index m and rheological index n. The comparison with the latter is drawn assuming: $\alpha = 1/n$ and $\tau_0 = (m/\mu_0^n)^{n/(1-n)}$.

viscosity parameter μ_0, a constant τ_0 defined as the shear stress corresponding to apparent viscosity $\mu_0/2$, and an indicial parameter α, typically larger than one as the fluid is shear-thinning. For $\alpha = 1$, a pseudo-Newtonian behaviour with dynamic viscosity $\mu_0/2$ is recovered, see Figure 6.2 showing the apparent viscosity $\mu_{app} = \tau/\dot\gamma$ for the Ellis model compared to Newtonian and power-law models. Newtonian behaviour in the form of a plateau for low shear rates is also observed for $\gamma \to 0$. For high shear rates the behaviour is power-law, and its two parameters can be determined from the Ellis model parameters, see Appendix A in Balhoff and Thompson (Balhoff & Thompson, 2006); in particular, the rheological index is $n = 1/\alpha$ (Al-Behadili, Sellier, Hewett, Nokes & Moyers-Gonzalez, 2019). Note that when curve fitting is performed on real data, n and $1/\alpha$ may significantly differ (Moukhtari & Lecampion, 2018), as two different models are fitted to the same data set. It is also seen that the Ellis model allows avoiding the unphysical effect of infinite apparent viscosity at zero shear rate that is typical of power-law fluids (Myers, 2005). In the following, we will consider $\alpha > 1$, dealing with the case $\alpha = 1$ in the Appendix, and the parameters μ_0 and τ_0 to be finite and positive. Couette-Poiseuille slit flow of an Ellis fluid under a constant pressure gradient was studied extensively by Steller (Steller, 2001), listing all combinations of parameters leading to Newtonian or pseudo-Newtonian behaviour. In particular, the negative velocity $u(z)$ under a positive reduced pressure gradient $\partial p/\partial$ in the x direction is

$$
\begin{aligned}
u(z,t) = -\frac{1}{8\mu_0}\left[h^2 - (2z-h)^2\right]\frac{\partial p}{\partial x} + \\
- \frac{1}{(\alpha+1)2^{\alpha+1}\mu_0\tau_0^{\alpha-1}}\left[h^{\alpha+1} - |2z-h|^{\alpha+1}\right]\frac{\partial p}{\partial x}\left|\frac{\partial p}{\partial x}\right|^{\alpha-1}.
\end{aligned}
\tag{6.2}
$$

The corresponding average velocity $\overline{u}$ and flow per unit width q_x in the x direction are

$$
\overline{u} = -\frac{h^2}{12\mu_0}\frac{\partial p}{\partial x} - \frac{h^{\alpha+1}}{2^{\alpha+1}(\alpha+2)\mu_0\tau_0^{\alpha-1}}\frac{\partial p}{\partial x}\left|\frac{\partial p}{\partial x}\right|^{\alpha-1} \; ; q_x = \overline{u}h.
\tag{6.3}
$$

For the Newtonian case ($\alpha = 1$) the latter equation reduces to the classical "cubic law" (Zimmerman & Bodvarsson, 1996) written for a fluid with viscosity $\mu_0/2$. The continuity equation reads (Dana et al., 2018)

$$
\frac{\mathrm{d}h}{\mathrm{d}t} + h(t)\frac{\partial \overline{u}}{\partial x} = 0,
\tag{6.4}
$$

and substituting eq. (6.3) in eq. (6.4) gives

$$
\frac{\mathrm{d}h}{\mathrm{d}t} = \frac{h^3}{12\mu_0}\frac{\partial^2 p}{\partial x^2} + \frac{\alpha h^{\alpha+2}}{2^{\alpha+1}(\alpha+2)\mu_0\tau_0^{\alpha-1}}\left|\frac{\partial p}{\partial x}\right|^{\alpha-1}\frac{\partial^2 p}{\partial x^2}.
\tag{6.5}
$$

The problem formulation is completed by the force balance, expressed per unit width of fracture, among the fluid pressure and the elastic reaction of the upper wall, taken to be proportional to aperture h; an overload at the upper wall f_0 (a force per unit width) is included in the balance for generality (Chiapponi et al., 2019); the overload represents an additional force exerted by the walls and usually opposing the fracture opening due, e.g., to a residual stress state generated by the load history of the rocks. It is assumed constant and independent from the fracture aperture. The balance reads

$$\int_0^L p(x,t)\,\mathrm{d}x = \tilde{E}Lh(t) + f_0, \qquad (6.6)$$

where the constant of proportionality $\tilde{E}$ has dimensions $[ML^{-2}T^{-2}]$; for a linear elastic foundation, called a Winkler soil in geotechnical applications, $\tilde{E}$ is equal, for a thin elastic layer of thickness l, to the ratio between the Young modulus of the layer's material E $[ML^{-1}T^{-2}]$ and l, $\tilde{E} = E/l$. In the context of hydraulic fracturing, l may be identified with the fracture spacing (Dana et al., 2018; Chiapponi et al., 2019), a design parameter that depends, among others, on the type of rock; in hydraulically fractured shales, values of l/L equal to 0.057, 0.28, and 0.029 are reported, respectively, by Ghanbari and Dehghanpour (Ghanbari & Dehghanpour, 2016), Wang et al. (Wang et al., 2018b), and Wang et al. (Wang, Elsworth & Denison, 2018a). In the case of vertical/sub-vertical fractures perpendicular to a horizontal/sub-horizontal well or borehole, the geometry of the idealized system is described by Figure 6.3, showing the two wings of equally spaced planar fractures of half-length L, width W, aperture h and spacing l. Albeit the flow very close to the well is radial, the influence of the boundary condition at the well decreases rapidly with distance, and flow in most of the fracture half-length L is uniform, consistently with the assumption $L \gg W$. Hence, as an approximation the boundary condition of assigned pressure p_e at the well is extended to a segment of height W. In the case of planar vertical fractures parallel to, and propagating from, a vertical well, the geometry of the flow is plane without using this approximation.

A further issue deserving investigation is the linearity of the relationship between the wall reaction and the fracture aperture. In fact, a nonlinear elastic behaviour can be the result of the pervasive damage of rocks by microcracks and voids, which determines nonlinearity even for infinitesimal strain, also with an incremental jump in the elastic modulus from tension to compression (Budiansky & O'Connell, 1976; Lyakhovsky, Reches, Weinberger & Scott, 1997). In this case the Young modulus of the material is a function of the strain rate, $E = E_0(h/l)$, and assuming that the latter dependence is expressed with a power-law function one has

$$E = E_0 \left(\frac{h}{l}\right)^{\lambda-1}, \qquad (6.7)$$
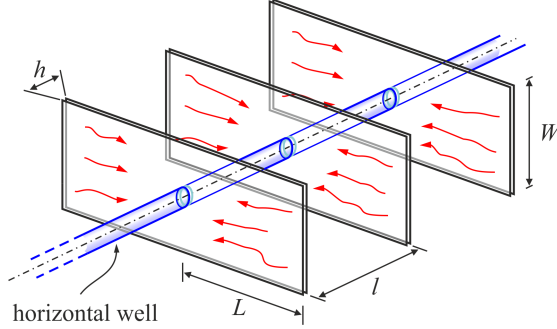
Figure 6.3: Typical scheme for bi-wing planar fractures around a horizontal borehole; L, W and h are the fracture length, width and aperture, l is the fracture spacing.

where λ is a non-negative exponent modulating the nature of the reaction: for $\lambda = 1$ a constant Young modulus is recovered, while $0 < \lambda < 1$ is associated to a softening behaviour, and $\lambda > 1$ to a stiffening one. The assumption results in

$$\tilde{E} = \frac{E_0}{l}\left(\frac{h}{l}\right)^{\lambda-1} \equiv \hat{E}h^{\lambda-1}, \tag{6.8}$$

and eq. (6.6) is modified as

$$\int_0^L p(x,t)\,\mathrm{d}x = \hat{E}Lh^\lambda(t) + f_0, \tag{6.9}$$

with $\hat{E} = E_0 l^{-\lambda}$ of dimensions $[ML^{-1-\lambda}T^{-2}]$.

Equations (6.5) and (6.9) are subject to the following initial and boundary conditions

$$h(0) = h_0, \quad \frac{\partial p(x,t)}{\partial x}(L,t) = 0, \quad p(0,t) = p_e, \tag{6.10}$$

h_0 being the initial fracture aperture, and p_e the exit pressure at the well.

The solution to the above problem yields two relevant quantities expressed per unit width, the flowrate exiting the fracture at the well, $q(t)$, and the residual volume of the fracture at a given time, $v(t)$; these are easily derivable as

$$q(t) = L\frac{\mathrm{d}h(t)}{\mathrm{d}t}, \quad v(t) = Lh(t). \tag{6.11}$$

6.3.2   Dimensionless form

Dimensionless quantities are defined as

$$X = x/L,\, H = h/h_0,\, T = t/t_c,\, P = (p - p_e)/p_c,\, P_e = p_e/p_c,$$
$$Q = qt_c/(h_0 L) = q/(u_0 h_0),\, V = v/(h_0 L), \tag{6.12}$$

where the scales for pressure and time are

$$p_c = \hat{E} h_0^\lambda, \quad t_c = \frac{(2+\alpha)}{\alpha} \left(\frac{2L}{h_0} \right)^{1+\alpha} \frac{1}{h_0^{\alpha\lambda}} \frac{\mu_0 \tau_0^{\alpha-1}}{\hat{E}^\alpha},$$

(6.13)

and $u_0 = L/t_c$ is a velocity scale. This leads to the dimensionless counterpart of eq. (6.5)

$$\frac{dH}{dT} = N H^3 \frac{\partial^2 P}{\partial X^2} + H^{\alpha+2} \left(\frac{\partial P}{\partial X} \right)^{\alpha-1} \frac{\partial^2 P}{\partial X^2},$$

(6.14)

where the pure number

$$N = \frac{2+\alpha}{3\alpha} \left(\frac{2\tau_0 L}{\hat{E} h_0^{\lambda+1}} \right)^{\alpha-1} = \frac{2+\alpha}{3\alpha} \left[\frac{2\tau_0}{p_c (h_0/L)} \right]^{\alpha-1}$$

(6.15)

modulates the relative importance of the Newtonian behaviour of the Ellis fluid at low shear rate, expressed by the first term on the r.h.s. of eq. (6.14), with respect to the second term, the power-law behaviour at high shear rate. For a Newtonian fluid ($\alpha = 1$) N reduces to unity; for a shear-thinning fluid ($\alpha > 1$), N is zero for $\tau_0 = 0$ and/or a rigid wall ($\hat{E} = E_0/l^\lambda \to \infty$), but the latter case renders the scales (6.13) meaningless. In eq. (6.15) defining N, the quantity within brackets represents the ratio between the characteristic shear stress τ_0 of the Ellis fluid and the pressure scale $p_c = \hat{E} h_0^\lambda$ associated with the elastic reaction of the fracture wall; the ratio is in turn corrected by the initial aspect ratio of the fracture h_0/L. This formulation of N includes only parameters defined at the single fracture scale. Note that if the scheme of multiple fractures with spacing l depicted in Figure 6.3 is considered, eq. (6.15) may be rewritten as

$$N = \frac{2+\alpha}{3\alpha} \left[\frac{2 \left(\frac{\tau_0}{E_0} \right) \left(\frac{l}{L} \right) \left(\frac{l}{L} \right)^{\lambda-1}}{\left(\frac{h_0}{L} \right)^2 \left(\frac{h_0}{L} \right)^{\lambda-1}} \right]^{\alpha-1},$$

(6.16)

where τ_0/E_0 is the ratio between the representative shear stress of the fluid and the Young modulus of the host rock, and l/L is the dimensionless fracture spacing. The terms to the power $(\lambda-1)$ represent the contribution due to non-linear elastic behaviour of the walls, and disappear for $\lambda = 1$. An alternative formulation of N as a function of Cauchy, Reynolds, and Ellis dimensionless groups is reported in 6.8. To grasp the order of magnitude of N, we recall that l/L may be taken to vary between 0.03 and 0.3 (with $l/L \approx 0.1$ being appropriate for an order of magnitude analysis), while the initial fracture aspect ratio h_0/L, a number much smaller than 1, may be considered of order $10^{-3} - 10^{-5}$ (Ghanbari & Dehghanpour, 2016; Wang et al., 2018b, 2018a). The latter reference also reports $E_0 = 2.5 \cdot 10^{10}$ Pa for the rock elastic modulus in fractured shales; quite close values, $E_0 = 3 \cdot 10^{10}$ Pa and $E_0 = 2.76 \cdot 10^{10}$

Pa are reported in (Detournay, 2016) and (Fisher & Warpinski, 2012), hence reference values $E_0 = 2.5 - 3.0 \cdot 10^{10}$ Pa are considered.

Actual values of rheological parameters for Ellis fluids are quite scarce in the literature. A reference specific to fracking is (Moukhtari & Lecampion, 2018), where the Ellis parameters are reported for two fracturing fluids, HPG (Hydroxypropylguar) and VES (viscoelastic surfactant). For the first, $\mu_0 = 0.44$ Pa $\cdot$ s, $\tau_0 = 2.01$ Pa, and $\alpha = 1.22$; for the second, $\mu_0 = 49$ Pa $\cdot$ s, $\tau_0 = 8.836$ Pa, and $\alpha = 12$. Adopting as reference geometrical parameters $l/L = 0.1$ and $h_0/L = 10^{-4}$, and a young modulus of $E_0 = 2.75 \cdot 10^{10}$ Pa for the host rock, one obtains $N = 0.209$ for HPG and $N \simeq 0$ for VES, indicating that for the latter fluid the Newtonian component of rheological behaviour is negligible. A further consideration is that VES is very strongly shear-thinning ($\alpha \gg 1$), therefore the value of N is extremely sensitive to variations in parameters: adopting for example $l/L = 0.125$, $h_0/L = 10^{-5}$, and $E_0 = 2.5 \cdot 10^{10}$ Pa, again realistic values, one obtains $N = 0.100$ for VES and $N = 0.618$ for HPG. This second set of parameters is adopted for later reference in Section 6.5 describing a case study and is shown there in dimensional form (see Table 6.1). Trying further combinations of realistic values for fluid and rock properties, it is seen that N may take values smaller or larger than unity, the former case being more frequent. This indicates a certain prevalence of the power-law component of rheology over the Newtonian one, although the asymptotic system behaviour is dominated by the latter, as will be shown in the next section. We bear in mind that a large variety of combinations is possible for the two parameters N and α depending on geometry and properties of fluid and rock, but with the constraint from the definition (6.15) that for $\alpha = 1$ it must be $N = 1$.

The dynamic boundary condition (6.9) and the boundary conditions (6.10) transform as

$$\int_0^1 P(X,T)\,\mathrm{d}X = H^\lambda - P_e + F_0, \qquad (6.17)$$

$$H(0) = 1, \quad \frac{\partial P}{\partial X}(1,T) = 0, \quad P(0,T) = 0. \qquad (6.18)$$

6.3.3 Solution

A solution to eq. (6.14) is sought by integrating in two steps the pressure of the fluid and the fracture aperture. Posing

$$U(X,T) = \frac{\partial P}{\partial X}, \quad \dot{H} = \frac{\mathrm{d}H}{\mathrm{d}T}, \qquad (6.19)$$

eq. (6.14) can be written as

$$B\left(1 + AU^{\alpha-1}\right)\frac{\partial U}{\partial X} = \dot{H} \qquad (6.20)$$

where

$$A = A(T) = \frac{(H)^{\alpha-1}}{N}, \quad B = B(T) = NH^3, \tag{6.21}$$

while the second boundary condition in eq. (6.18) becomes

$$U(1, T) = 0. \tag{6.22}$$

Separating variables in eq. (6.20), and integrating with the boundary condition (6.22) leads to

$$\frac{BU \left(AU^{\alpha-1} + \alpha \right)}{\alpha} = -\dot{H}(1 - X). \tag{6.23}$$

Eq. (6.23) can be rewritten as

$$U^\alpha + CU + D(1 - X) = 0 \tag{6.24}$$

where

$$C = C(T) = \frac{\alpha N}{H^{\alpha-1}}, \quad D = D(T) = \frac{\alpha \dot{H}}{H^{2+\alpha}}. \tag{6.25}$$

Eq. (6.25) is algebraic in U and admits an analytical solution for $\alpha = 1, 2, 3$ and for $\alpha = 1/2, 1/3$ in the form of a combination of functions of H and $\dot{H}$. This solution can be integrated once in space, with the boundary condition $P(0, T) = 0$, obtaining the pressure field. The pressure field is finally integrated in $X \in [0, 1]$ and the integral in eq. (6.17) is computed as a function of H and $\dot{H}$. Then eq. (6.17) is transformed in a nonlinear ODE which is numerically integrated with the initial condition $H(0) = 1$.

These solutions are analytical in the x coordinate and numerical in the time domain and seem quite cumbersome, while their accuracy is comparable to that of a fully numerical solution in space and time; the latter also has the advantage of a free selection of the indicial parameter α. Among the many possible numerical schemes, we adopt a finite difference in time and an implicit resolver in space, with a step size reduction to track solution accurately.

The code is written in Mathematica, introducing a parametric solver for the function $U(X, T)$ as a function of $N, \alpha, H_{i+1}, H_i, \Delta t$, where H_{i+1} and H_i are the values at time $(i+1)\Delta t$ and $i\Delta t$, respectively; the only free parameter is H_{i+1}, all the other parameters are given.

Each time iteration includes the following steps:

- The function $U(X)_{i+1}$ is estimated by solving eq. (6.20) in parametric form, with $\dot{H} \approx (H_{i+1} - H_i)/\Delta t$, with the term H taken to be the average between H_{i+1} and H_i and with the b.c. $U(1)_{i+1} = 0$, where H_{i+1} is the free parameter; $H_0 = 1$ is assumed at the first step.

- The space values of U, known in parametric form, are used to solve the differential problem $\partial P(X)_{i+1}/\partial X = U(X)_{i+1}$, with $P(0)_{i+1} = 0$, obtaining the pressure $P(X)_{i+1}$.

- The pressure field is numerically integrated (in parametric form) in the domain $[0, 1]$.

- The parametric integral is inserted in eq. (6.17), and the equality is forced with a Newton method for finding the value of the parameter H_{i+1}.

- The procedure is repeated for the next time step, shifting the values H_{i+1}.

Once the pressure $P(X, T)$ and aperture $H(T)$ fields are known, the dimensionless flowrate and fracture volume are given by

$$Q(T) = \frac{\mathrm{d}H(T)}{\mathrm{d}T} = \dot{H}, \quad V(T) = H(T). \tag{6.26}$$

Hence at late-time the fracture volume and flowrate behave like the aperture and its time derivative, respectively; for zero borehole pressure and overload the corresponding time scalings are $T^{-1/(\lambda+2)}$ and $T^{-1/(\lambda+3)}$.

6.4   Results and discussion

Figure 6.4 shows the results of the numerical computation for the fracture aperture and different α values, with the analytical solution $H = (1+9T)^{-1/3}$ valid for the Newtonian case and a linearly elastic fracture (Dana et al., 2018), corresponding to $\alpha = 1$, $N = 1$, and $\lambda = 1$. Note that the values $\alpha = 1$, $N = 1$ imply Newtonian behaviour but with a viscosity equal to $\mu_0/2$, thus halving the time scale t_c in eq. (6.13); this requires doubling the dimensionless time T in eq. (6.12) to compare results of equations having a different time scale. The time integration was performed with a time step $\Delta t = 0.01$. Since the results of the numerical integration using this fully explicit scheme fit exceedingly well the analytical solution, it was not necessary to adopt higher order schemes, even considering that the solution has no singularity and behaves rather smoothly.

The asymptotic behaviour of the solution $H(T)$ is dictated by the interplay between the two terms on the r.h.s. of eq. (6.14): the second term scales with the gradient pressure (decaying in time) and with a power of H always larger than 3, since $\alpha > 1$, whereas the first term scales with the third power of H and has N as a coefficient. Since $H \leq 1$ and the gradient pressure quickly decays to values less than unity, the dominant term is the first one, which entails the asymptotic behaviour $H \sim T^{-1/(2+\lambda)}$, see Figure 6.5 where different values of α, for $N = 1$ and $P_e = 0$, produce almost parallel curves for large T. Figure 6.5 also shows how variations in λ significantly affect the late-time behaviour for fixed α: a stiffening $(\lambda > 1)$/softening $(\lambda < 1)$ elastic reaction of the walls delays/facilitates the drainage. It is also seen that the parameter α mainly controls the early stage, the parameter λ the late stage of the backflow process. Figure 6.6 shows results for a fixed $\alpha = 2$, $\lambda = 1$, and
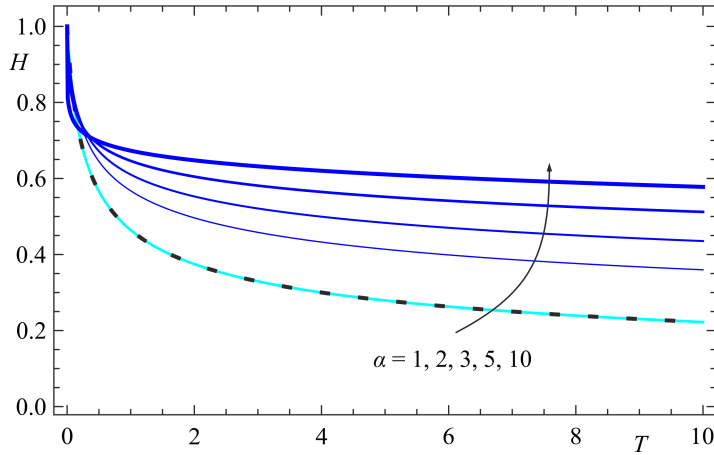
Figure 6.4: Time variation of the fracture aperture H for $N = 0$, $\lambda = 1$, $P_e - F_0 = 0$ and different α values. The black dotted curve refers to the analytical solution for a Newtonian fluid, $H = (1 + 9T)^{-1/3}$. Due to the different time scales adopted for a Newtonian fluid and for the present model, comparison is feasible if the dimensionless time T in the solution for the Newtonian fluid is doubled.
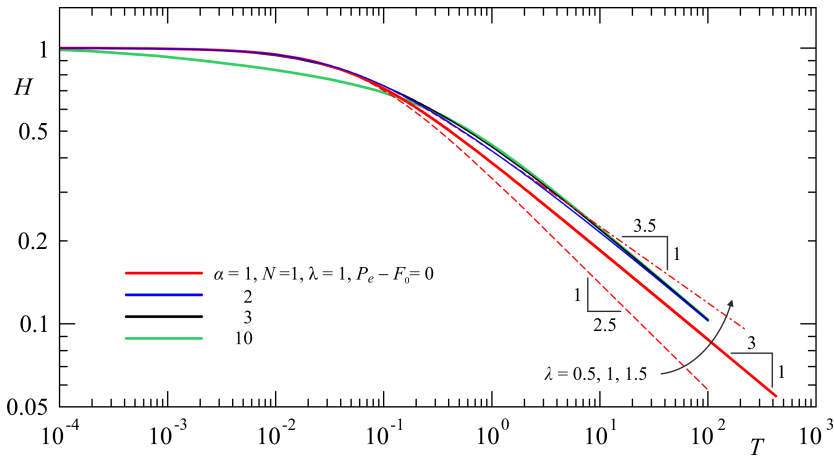
Figure 6.5: Time variation of the fracture aperture H for $N = 1$, $\lambda = 1$ and different α values. For one case ($\alpha = 1$) the effects of a softening/stiffening wall is explored, see the dashed and dash-dotted thin curves for $\lambda = 0.5 - 1.5$, respectively. The asymptotic behaviour is $H \sim T^{-1/(2+\lambda)}$, independent on α.
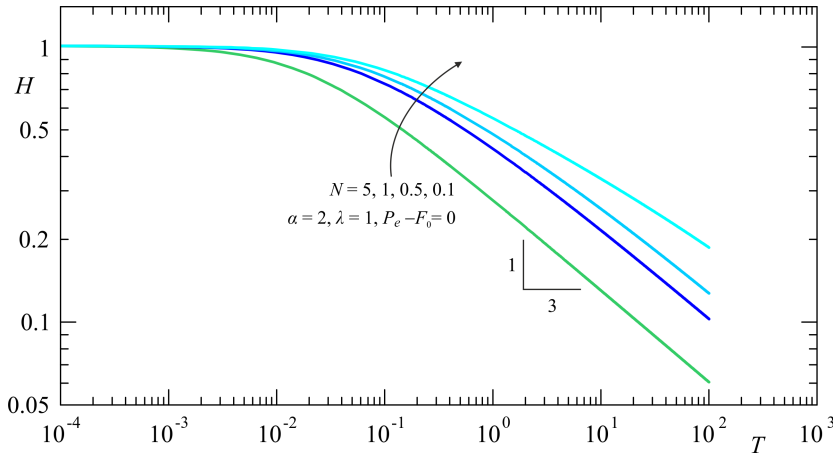
Figure 6.6: Time variation of the fracture aperture H for $\alpha = 2$, $\lambda = 1$ and different N.

different N values; the asymptote is reached much faster for larger N. In sum, the early time behaviour for zero external pressure at the well is in general dominated by the second term in eq. (6.14) unless the coefficient $N \gg 1$; in the latter case both terms substantially contribute to the time evolution of H.

In presence of a non-zero external pressure ($P_e > 0$) or a negative overload F_0 (an additional force per unit of wall surface acting in the same direction of the internal pressure), the asymptotic residual aperture is equal to $(P_e - F_0)^{1/\lambda}$, see Figure 6.7 where both effects are included. The curves coalesce to the asymptote faster for larger N values, implying a dominance of the Newtonian behaviour, while for small N the power-law behaviour prevails and the asymptote is reached for larger dimensionless times. Upon plotting results for $\alpha = 3$ (not shown) the main curves for $\lambda = 1$ and the secondary curves for $\lambda \neq 1$ are very similar to those for $\alpha = 2$.

Figure 6.8 shows the pressure distribution for two different combinations of the parameters and a shear-thinning fluid with $\alpha = 2$. Results for other combinations are similar (and thus not shown), with a pressure decay in space/time quicker or slower depending on the parameter values; at all times the residual pressure within the fracture increases with smaller N values, implying a behaviour closer to Newtonian, and with smaller λ values, i.e. a softening wall; however when the fluid is closer to Newtonian the effect of a λ variation is irrelevant.

An important quantity characterizing the performance of the backflow process is the time required to recover the fluid injected in the fracture network and not lost in the form of leakoff. Here the network is conceptualized as a single fracture and fluid losses are not explicitly represented (they are assumed
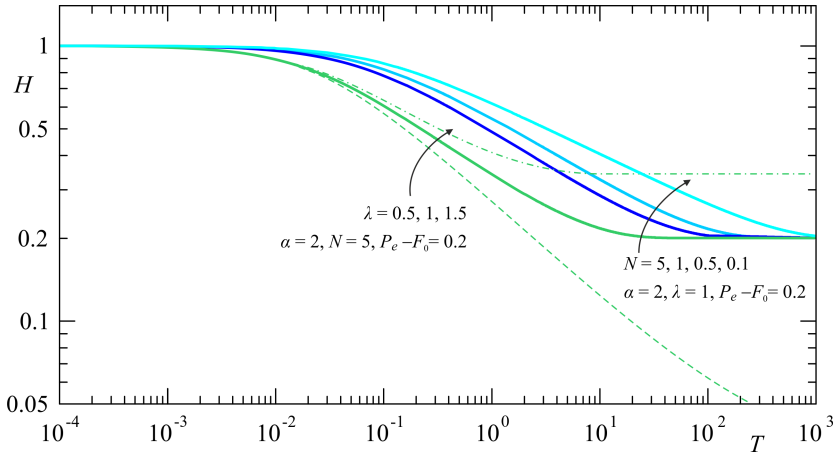
Figure 6.7: Time variation of the fracture aperture H for $\alpha = 2$ and different N values, with given difference between external pressure and overload $P_e - F_0 = 0.2$. For one case ($N = 5$) the effects of a stiffening/softening elastic reaction of the walls is explored, see the dashed and dash-dotted thin curves for $\lambda = 0.5 - 1.5$, respectively.
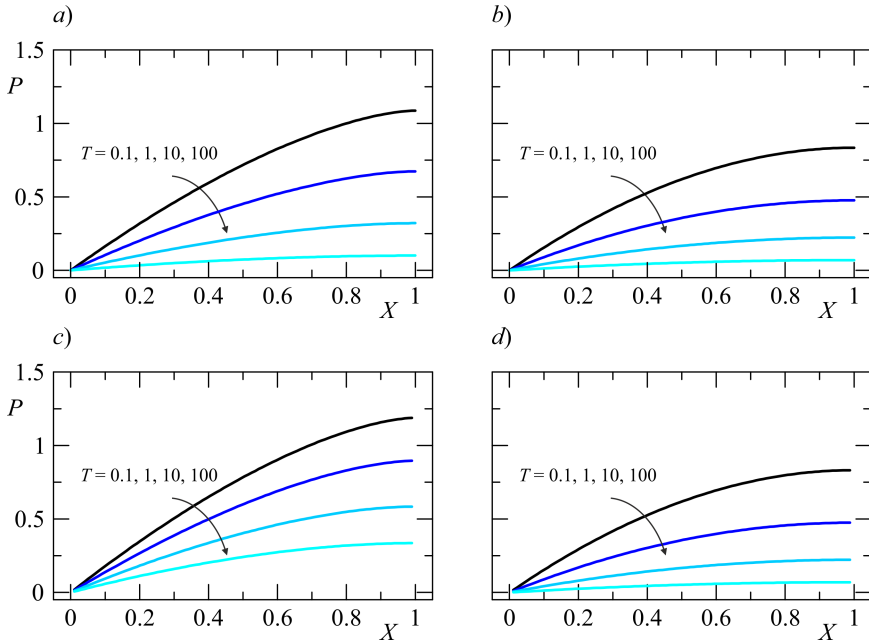
Figure 6.8: Pressure along the fracture at different times for $P_e - F_0 = 0.2$ and a shear-thinning fluid with $\alpha = 2$. Results for *a*) $N = 0.1$ and $\lambda = 1$; *b*) $N = 5$ and $\lambda = 1$; *c*) $N = 0.1$ and $\lambda = 0.5$; *d*) $N = 5$, $\lambda = 0.5$.
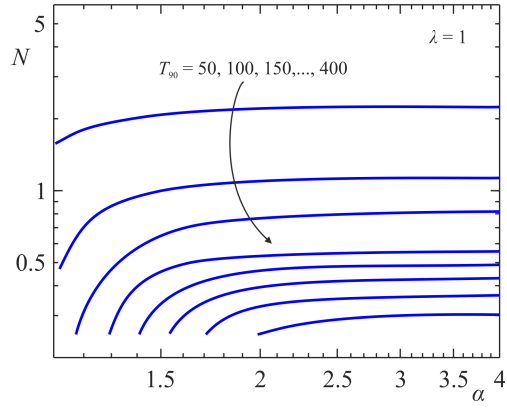
Figure 6.9: Time to recover 90% of the fluid as a function of α and N, with $\lambda = 1$ and $P_e - F_0 = 0$.
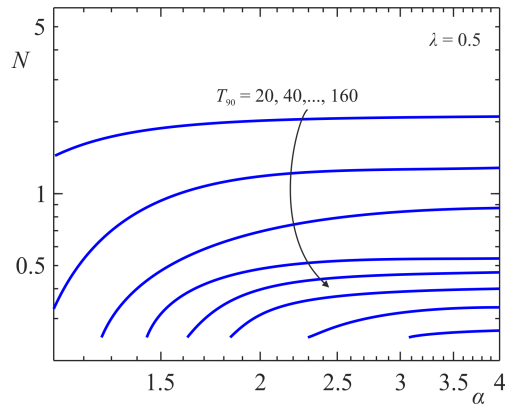
Figure 6.10: Time to recover 90% of the fluid as a function of α and N, with $\lambda = 0.5$ and $P_e - F_0 = 0$.
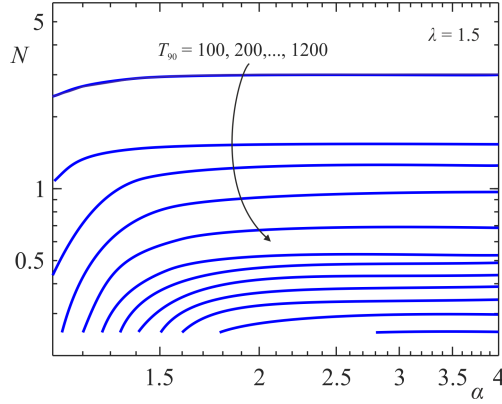
Figure 6.11: Time to recover 90% of the fluid as a function of α and N, with $\lambda = 1.5$ and $P_e - F_0 = 0$.

to take place in the upstream network), however the time T_Y needed to recover $Y\%$ of the fracture volume provides an indication of how rapid the recovery is. Contour maps in the (α, N) space of the dimensionless time T_{90} needed to recover 90% of the fluid are depicted in Figure 6.9 for a linear wall reaction ($\lambda = 1$). As the degree of shear-thinning behaviour rises with α for constant N, there is a sharp increase in dimensionless T_Y for $N < 0.5$, while T_Y is almost independent on α for $N > 2$. Conversely, T_Y for costant α decreases with larger N values, i.e. as the fluid behaviour is closer to Newtonian; this effect is more evident for larger α. Highest values of T_Y are attained for large α and low N, lowest values for small α and large N, the two combinations farthest and closest to Newtonian behaviour. The effect of a sublinear wall reaction ($\lambda = 0.5$) is depicted in Figure 6.10, that of a supralinear wall reaction in Figure 6.11. The dimensionless time to recover the bulk of the stored fluid is decidedly faster or slower with a softening or stiffening wall, demonstrating once again the decisive influence of the parameter λ modulating the wall reaction at late time.

A word of caution is needed when drawing comparisons between non-Newtonian fluids with different rheology as the models are semi-empirical and the time scale used for the dimensionless formulation depends upon the rheological parameters of the Ellis model and is particularly sensitive to the value of the indicial exponent α. Hence model outputs are best compared in dimensional coordinates when quantitative results are needed.

6.5 A case study

A case study is illustrated by comparing the performance of two real hy-drofracturing fluids (Moukhtari & Lecampion, 2018), HPG (Hydroxypropyl-guar) and VES (viscoelastic surfactant) in a realistic setting. The rheological

Fluid	μ_0 (Pa s)	τ_0 (Pa)	α	L (m)	l (m)	h_0 (mm)	E (Pa)	λ	N
HPG	0.44	2.01	1.22	100	12.5	1.00	$2.5 \cdot 10^{10}$	1.00	0.618
VES	49.00	8.836	12.00	100	12.5	1.00	$2.5 \cdot 10^{10}$	1.00	0.100

Table 6.1: Reference parameters for case study: μ_0, τ_0 and α are the reference viscosity, shear stress and indicial exponent of the Ellis fluid, L is the fracture length, l is the fracture spacing, h_0 is the fracture initial height, E is the rock modulus of elasticity, λ is the exponent of the rock wall reaction, N is the dimensionless number governing the interplay between Newtonian and power-law behaviour in an Ellis fluid.
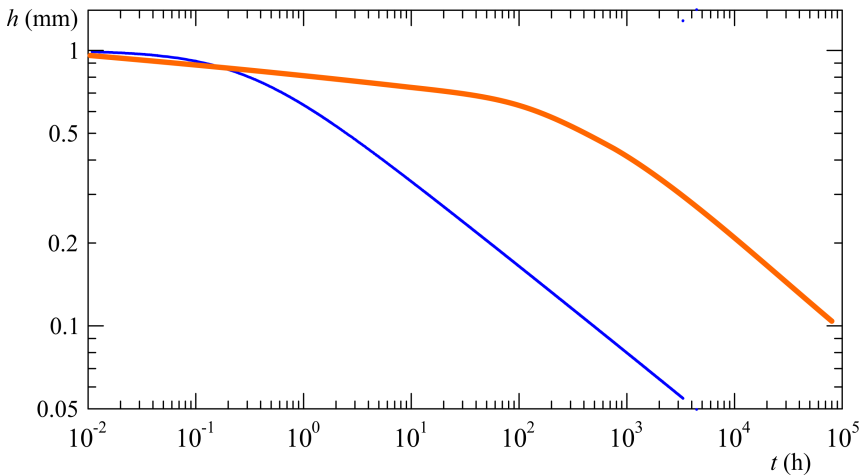
Figure 6.12: Time variation of the fracture aperture h for the HPG (thin line) and VES (thick line) fluids.

parameters according with the Ellis model are reported for both fluids in Table 6.1, together with realistic geometric and mechanical parameters within plausible ranges deduced from the literature, see the earlier discussion in Section 6.3.2. It is seen that HPG is relatively close to Newtonian in behaviour, while VES is extremely shear-thinning, with an equivalent rheological index n less than 0.1 when expressed according to the power-law model.

Figure 6.12 shows the relaxation of the fracture aperture for the two fluids: the aperture for the HPG is only initially slightly larger than for the VES, but then closes more rapidly, reaching one tenth of the initial value at a time around 500 hours. The closure is much more gradual for the VES, requiring about a year to reach the same stage. The difference between corresponding pressure profiles, illustrated in Figure 6.13, shows a decidedly sharper pressure decrease for HPG than for VES in the initial stage.
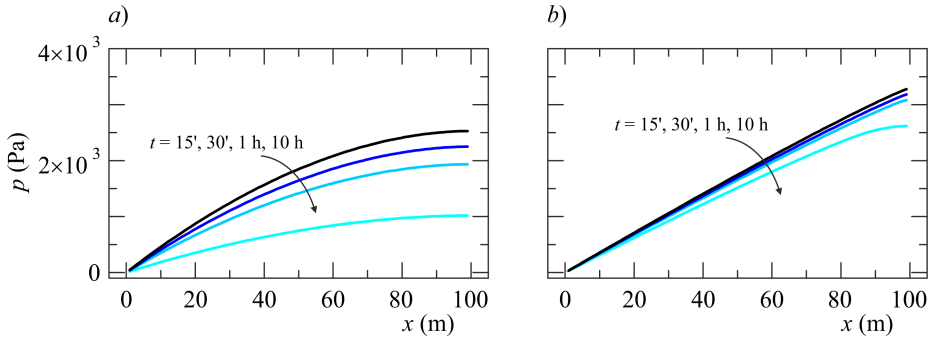
Figure 6.13: Pressure distribution at different time a) for HPG fluid, and b) for VES.
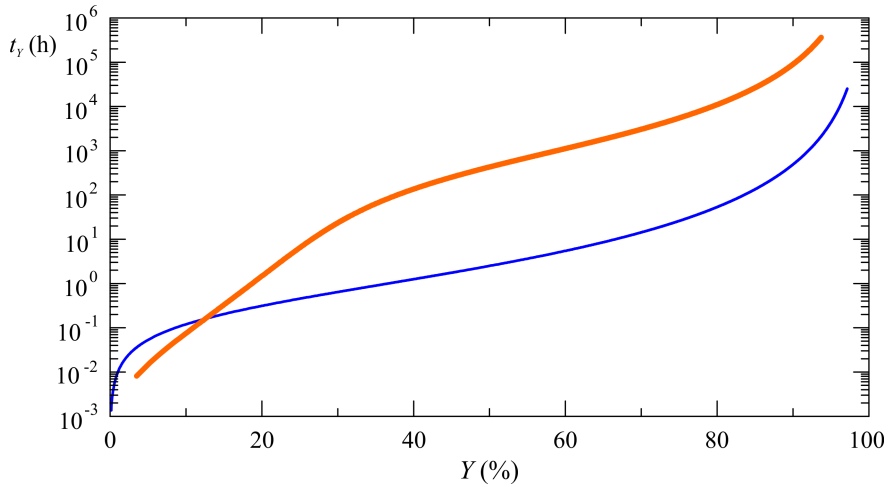
Figure 6.14: Time to recover the fracture volume $Y\%$ for the HPG (thin line) and VES (thick line) fluids.

Figure 6.14 shows the time to recover the volume stored in the fracture for the two fluids. Following the same trend manifested for the evolution of fracture opening, VES demonstrates a higher drainage capacity than HPG in the very early phase, for $Y < 15\%$; subsequently it is much less efficient, and requires an extra time at least three orders of magnitude larger to drain the same percentage of fluid than HPG. Overall the large difference in rheology, mainly encapsulated in the α value, translates into corresponding wide differences in terms of aperture, pressure, and drainage time. This is so because the value of the dimensionless group N is very low for VES, thus allowing the fluid to manifest its essentially power-law nature. We tried a number of other combinations of parameters and found that for very shear thinning fluids like VES the results are very sensitive to relatively small changes in parameters: slightly increasing the modulus of elasticity E to $3 \cdot 10^{10}$ and increasing the spacing to 20 m, leaving the other parameters in Table 6.1 unchanged, leads to $N(HPG) = 0.659$ and $N(VES) = 2.360$. While the change in the N value associated to HPG is modest (6.6%) and implies the system behaviour is essentially unchanged with respecto to the reference case, the increase in N for the VES is dramatic (2260%) and entails a fluid behaviour closer to Newtonian despite the exceedingly high value of α. Upon plotting the aperture variation over time for this case (not shown) the two fluids exhibit a similar behaviour, with only modest differences (less than 10%) in the fracture aperture at early times and an almost identical behaviour later on. The pressure profiles do not show any significant differences.

6.6   Conclusions

A conceptual model for backflow of non-Newtonian fluid from a closing rock fracture was presented in this paper. Under the assumption of Ellis rheology and elastic, but non-deformable wall, the problem in plane geometry is tractable in semi-analytical form to yield the time-variable fracture aperture $h(t)$, pressure field $p(x,t)$ and discharge rate $q(t)$, as well as the drainage time t_Y for a specified recovery rate Y, outlet pressure p_e and overload f_0.

Our results lead to the following specific conclusions:

- The Ellis model adopted herein to describe shear-thinning rheology couples Newtonian and power-law behaviour. When an Ellis fluid backflows from a relaxating fracture the interplay between the two natures is modulated by a dimensionless group N encapsulating the main problem parameters. N can be expressed in terms of i) the indicial exponent α of the Ellis rheology, ii) the parameter λ governing the wall relaxation process, iii) the ratio between the characteristic shear stress of the Ellis fluid τ_0 and the rock modulus of elasticity E, iv) two geometric ratios, the fracture initial aspect ratio h_0/L and dimensionless spacing l/L. An alternative format of N is a modified ratio between the Cauchy number and the product of Reynolds and Ellis numbers.

- The factors N and α mostly influence the early and intermediate time evolution of the system: when $N < 1$ the power-law behaviour prevails; for $N = 1$ the pure Newtonian case is recovered ($\alpha = 1$ entails $N = 1$), while for $N \gg 1$ the behaviour is mixed.

- For late-time the system behaviour tends to Newtonian, is independent of N and is governed by the wall relaxation parameter λ: aperture and discharge scale asymptotically with time as $t^{-1/(\lambda+2)}$ and $t^{-1/(\lambda+3)}$ for $p_e - f_0 = 0$; else, the aperture tends asymptotically to a constant value proportional to $(p_e - f_0)^{1/\lambda}$.

- Very shear-thinning fluids (larger α) and reactive walls (larger λ) are associated with a more gradual closure of the aperture.

- The residual pressure within the fracture increases with smaller N values and with a softening wall ($\lambda < 1$); when the fluid is close to Newtonian the effect of a λ variation is almost irrelevant.

- The dimensionless drainage time T_Y attains the largest values for large α and low N, the lowest values for small α and large N, the two combinations farthest and closest to Newtonian behaviour. A non-linear reaction of the walls result in a faster/slower recovery for $\lambda < 1$ (softening) and $\lambda > 1$ (stiffening). For recovery values close to 100%, T_Y is very sensitive to variations of model parameters.

- Results are discussed in dimensional form for a case study to reinforce the notion that dimensionless results need to be compared with caution as scales include fluid rheological parameters. Realistic geometric and mechanical parameters are adopted for a system of equally spaced fractures, and results are compared for two fluids, HPG and VES, normally used in fracking technology. The time evolution of the aperture and the dependence of the drainage time upon the recovery ratio are similar at early times, then differ by orders of magnitude at intermediate and late times.

The developments presented, together with earlier results (Dana et al., 2018; Chiapponi et al., 2019), provide an overview of the backflow phenomenon in the two basic geometric configurations for a single fracture, plane and radial, and for three rheological models of increasing complexity: Newtonian, power-law, and Ellis. Further improvements of the model remain open in several directions, e.g.: i) a more complex geometry, considering nonplanar fractures with non-negligible curvature; ii) the combination of non-Newtonian rheology with multiple fracture systems, adopting the asymptotic viewpoint of Dana et al. (Dana et al., 2019); iii) the incorporation of particle transport to simulate the settling of solid proppant.

Acknowledgments

6.7   Appendix A - The Newtonian case ($n = 1$)

For $\alpha = 1$ and $N = 1$ eq. (6.25) reduces to

$$C = 1, \quad D = \frac{\dot{H}}{H^3}, \tag{6.27}$$

and integrating eq. (6.24) using these expressions yields

$$P(X, T) = \frac{\dot{H}}{4H^3}[(X - 1)^2 - 1]. \tag{6.28}$$

Substituting in eq. (6.17) and integrating $P(X, T)$ over X gives

$$-\frac{\dot{H}}{3H^3} = H^\lambda - P_e + F_0, \tag{6.29}$$

generalizing eq. (2.14) of Dana et al. (Dana et al., 2018), where $\lambda = 1$ and $F_0 = 0$, to nonlinear wall reaction and non-zero overload. Now define an effective pressure $\tilde{P}_e = P_e - F_0$ at the fracture outflow: this symbol will be used for brevity in the sequel. Consider first the case $\tilde{P}_e = 0$. Integration of eq. (6.29) over time T yields, with the first b.c. in eq. (6.18),

$$H(T) = [1 + 3(2 + \lambda)T]^{-\frac{1}{2+\lambda}}, \tag{6.30}$$

that for $\lambda = 1$ gives back eq. (2.15) of (Dana et al., 2018).

Consider now the case $\tilde{P}_e > 0$. Integration with the help of Mathematica and using transformation formulae for the analytic continuation of hypergeometric functions (Gradshteyn & Ryzhik, 2014) yields for generic λ the following implicit equation

$$T = \frac{1}{3(\lambda + 2)}\left[\frac{1}{H^{\lambda+2}}\,_2F_1\left(1, \frac{\lambda + 2}{\lambda}; \frac{2(\lambda + 1)}{\lambda}; \frac{\tilde{P}_e}{H^\lambda}\right) + \right.$$
$$\left. -\,_2F_1\left(1, \frac{\lambda + 2}{\lambda}; \frac{2(\lambda + 1)}{\lambda}; \tilde{P}_e\right)\right], \tag{6.31}$$

where $_2F_1(\alpha, \beta; \gamma; z)$ is the hypergeometric function of parameters α, β, γ, and argument z. Specific results for $\lambda = 1/2$, $\lambda = 1$, $\lambda = 2$, i.e. a sublinear,

linear or supralinear wall reaction, can be obtained as

$$T = \frac{1}{18\tilde{P}_e{}^5}\left[12\ln\left(\frac{H^{1/2}(1-\tilde{P}_e)}{H-\tilde{P}_e}\right) - \frac{12\tilde{P}_e}{H^{1/2}} - \frac{6\tilde{P}_e{}^2}{H} - \frac{4\tilde{P}_e{}^3}{H^{3/2}} - \frac{3\tilde{P}_e{}^4}{H^2} + \right.$$
$$\left. + 12\tilde{P}_e + 6\tilde{P}_e{}^2 + 4\tilde{P}_e{}^3 + 3\tilde{P}_e{}^4\right], \quad (6.32)$$

$$T = \frac{1}{6\tilde{P}_e{}^3}\left[2\ln\left(\frac{H(1-\tilde{P}_e)}{H-\tilde{P}_e}\right) - \frac{2\tilde{P}_e}{H} - \frac{\tilde{P}_e{}^2}{H^2} + 2\tilde{P}_e + \tilde{P}_e{}^2\right], \quad (6.33)$$

$$T = \frac{1}{6\tilde{P}_e{}^2}\left[\ln\left(\frac{H^2(1-\tilde{P}_e)}{H^2-\tilde{P}_e}\right) - \frac{\tilde{P}_e}{H^2} + \tilde{P}_e\right], \quad (6.34)$$

either by direct integration of eq. (6.31) or using transformations involving the hypergeometric functions (Gradshteyn & Ryzhik, 2014). Eq. (6.33) valid for $\lambda = 1$ is identical to Eq. (2.18) of Dana et al. (Dana et al., 2018). Other results in terms of trascendental and algebraic functions can be obtained for other special values of $\lambda \in \mathbb{N}$ or $1/\lambda \in \mathbb{N}$ but are too cumbersome to report and/or of little technical interest.

Expressions (6.31)-(6.34), when evaluated for for given $\tilde{P}_e$, allow deriving $H(T)$ and the drainage time T_Y needed to drain $Y\%$ of the fracture volume. As the latter quantity is given in dimensionless form by H according to (6.26), to derive T_Y it is sufficient to evaluate (6.31) and its special cases (6.15)-(6.34) for $H = (100 - Y)/100$.

Finally, it is wortwhile to derive the asymptotic behaviour of the general equation (6.31) for the limit case $\lambda \to 0$. According to eq. (5.3), $\lambda = 0$ implies a wall reaction constant over time rather than dependent from the fracture aperture. Integrating (6.29) for $H^\lambda = 1$ gives

$$H = \frac{1}{[1 + 6(1 - \tilde{P}_e)T]^{1/2}}, \quad (6.35)$$

a result that can be simplified for large time to $H = 1/[6(1 - \tilde{P}_e)T]^{1/2}$ and further for $\tilde{P}_e = 0$ to $H = 1/(6T)^{1/2}$. Equation (6.35) can be also obtained directly from eq. (6.31) for $\lambda \to 0$ on the basis of eq. (9.121.1) in (Gradshteyn & Ryzhik, 2014). The late-time scaling for a Newtonian fluid and a wall with constant reaction ($\lambda = 0$) is therefore $H \propto T^{-1/2}$, a result coinciding with the scaling $H \propto T^{-1/(2+\lambda)}$ implied by Figure 6.5 for a Newtonian fluid with $N = 1$, $\alpha = 1$.

6.8 Appendix B - The dimensionless group N

The pure number N may be expressed as a function of well-known dimensionless groups in fluid mechanics (e.g. Massey (1971)). Multiplying and dividing

eq. (6.16) by $\rho\mu_0 h_0 u_0^3$, where u_0 is the reference velocity defined in (6.12), yields

$$N = K \left(\frac{\mathrm{Ca}}{\mathrm{Re} \cdot \mathrm{El}} \right)^{\alpha-1}; \quad \mathrm{Ca} = \frac{\rho u_0^2}{E}; \quad \mathrm{Re} = \frac{2\rho u_0 h_0}{\mu_0}; \quad \mathrm{El} = \frac{\mu_0 u_0}{\tau_0 h_0}, \quad (6.36)$$

$$K = K\left(\alpha, \lambda, l/L, h_0/L\right) = \frac{2+\alpha}{3\alpha} \left[\frac{4\left(\dfrac{l}{L}\right)^{\lambda}}{\left(\dfrac{h_0}{L}\right)^{\lambda+1}} \right]^{\alpha-1} \tag{6.37}$$

where Ca, Re, and El are the Cauchy, Reynolds, and Ellis numbers, and K a geometric factor correcting the ratio $\mathrm{Ca}/(\mathrm{Re} \cdot \mathrm{El})$. In turn, Ca is the ratio between inertial forces and elastic forces transmitted by solid walls, Re is the ratio between inertial and viscous forces, while El is the ratio between the viscous stress associated with the low shear rate Newtonian behaviour and the shear stress τ_0 associated with high shear rate non-Newtonian (power-law) behaviour.

7 | Conclusions and Future Perspectives

In this thesis, analytical, numerical and experimental approaches have been adopted to comprehend and characterize the flow of non-Newtonian fluids involved in fractured rocks. In these media, the flow mainly occurs in fracture networks, where either fractures permeability and connectivity govern the flow. In fractured aquifer or unconventional reservoirs, the characterization of flow is of uttermost importance to quantify oil and gas reservoir storage and the effectiveness of industrial operations, as well as reclamation techniques.

The complex rheology of real fluids and the strong heterogeneity of fractures contribute to the mathematical complexity of the flow problem, introducing non-linearities that may be challenging to treat both analytically and numerically. The use of conceptual analytical models constitute an easily-handled tool to comprehend non-Newtonian fluid flows in a rock fracture. In Felisa et al. (2018) (Chapter 2), a four-parameter truncated power law model has been adopted to model non-Newtonian flow in simplified geometries, each fracture being represented by a series of cylindrical channels of different apertures to reproduce 1-D variability. The flow may occur parallel or orthogonal to the direction of variability, representing the extreme cases of maximum and minimum conductance, respectively. Despite the simplified geometry, this model allows discerning the impact of large and small apertures on permeability, considering a constitutive law that accounts both for the high and low shear rate viscosity plateaus and for the shear-thinning transition between them. For a power-law fluid, this model has been validated via laboratory experiments and with numerical simulations, in (Lenci & Chiapponi, 2020). The impact of other fluid features has been studied in Lenci & Federico (2019) and in Lenci & Di Federico (2020): in the former, the presence of a yield stress has been analysed by adopting a bi-viscous model, while in the latter the Prandlt-Eyring model has been introduced to comprehend the shear-thinning behaviour for low-shear rates regime, reducing the number of rheological parameters by dropping out the high shear rate viscosity plateau, which rarely plays a role in fracture laminar flow. These models provide an upper and a lower bound to fracture permeability and information on order of magnitudes and trends without resorting to numerical techniques.

A more realistic 3D synthetic fracture geometry can be generated, where the flow problem can be solved numerically. In Lenci et al. (2022a) (Chap-

ter3), a FFT-based fracture generator reproduces synthetic isotropic self-affine rough walls, while the flow is solved adopting a lubrication-based approach using a finite volume scheme. The lubrication theory allows reducing the problem to a 2-D depth-averaged formulation, which results in a less time consuming and computationally intensive simulation. This approximation is valid as long as the fracture walls are sufficiently smooth and the flow laminar. 2-D modeling allows better characterizing the flow, which present preferential flow paths and stagnation zones of almost zero velocity, . Such features are also present in Newtonian flow in the same geometries, but the flow localization is more marked with a shear-thinning fluid. The high efficiency achieved by the numerical code has allowed us to produce a stochastic analysis via brute force Monte Carlo. This would be prohibitive with actual commercial or freeware CFD softwares, which solve the (Navier-)Stokes equation in the 3D fracture domain. Furthermore, the homemade code provides a higher control over the algorithm in respect to software which are often closed to users. In the framework of the stochastic analysis, different flow regimes (natural and forced flow), fluid-shear thinning indices, and fracture scales, have been considered. The probability density function and autocorrelation function of the velocity magnitude and its components have been computed to quantify the statistical moments and analyse the tails of the distribution. Moreover, the impact of the shear-thinning index on fracture transmissivity has been quantified to estimate how flow localization impacts the fracture scale hydraulic behavior. Despite the strong channeling phenomena that may develop, with flow occurring in a limited portion of the fracture, the shear-thinning nature of the fluid enhances transmissivity as a results of the lower apparent viscosity of the fluid along the preferential flow channels.

Despite the importance of understanding the motion of a fluid in a heterogeneous fracture, the comprehension of the hydro-mechanical problem which arises from the interaction between a flowing fluid and the fracture walls is of interest. In hydraulic fracturing, after the fracture phase the flow is reversed to recover wastewater so that it can be treated and reused. In (Ciriello et al., 2021) (Chapter 5), a conceptual model to estimate the relaxation induced by this flow back has been proposed considering an Ellis fluid, assuming smooth-walled fracture. The model has been validated experimentally with a power-law fluid in Lenci & Di Federico (2020); good agreement was observed between the laboratory experiments and model prediction.

Our future prospects consist in comparing the outputs of the 2-D lubrication-based numerical code in realistic rough fracture geometries with 3-D CFD simulations to quantify the estimation error resulting from the depth-averaged approach, and define the limits of the lubrication theory considering shear-thinning fluids. For a Newtonian fluid, this analysis has been conducted by Koyama et al. (2008) using COMSOL multiphisics, and they showed a consistent difference between the prediction of the Stokes equation and of the Reynolds equation . Increased aperture field gradient will lead to larger discrepancies between the results from the two approaches.

8 | Acknowledgements

Throughout my PhD years in Bologna, I have received a great deal of support and assistance from my supervisors, co-authors, and colleagues. This dissertation is the result of cooperation and hard work conducted with passion and dedication to the comprehension of natural phenomena and their interaction with human activity. The characterization of the complexity and chaotic behaviour of the surrounding environment can only be achieved by the joint effort of an international and multidisciplinary research team.

I am deeply grateful to my supervisor, Prof. Vittorio Di Federico, for his invaluable expertise and guidance in approaching the research in the field of subsurface hydrology.

My sincere gratitude to my co-supervisors Prof. Yves Méheust and Prof. Mario Putti, who addressed me in identifying relevant research questions, and answering them through a scientific and rigorous method.

The frequent discussions related to the development of the research activity have always been characterized by an open and profitable exchange of ideas with all my supervisors, laying the foundation of a conscious and autonomous scientific path.

References

Abugattas C., Aguirre A., Castillo E., Cruchaga M., 2020, *Numerical study of bifurcation blood flows using three different non-Newtonian constitutive models*, Appl. Math. Model., 88, 529

Adachi J. I., Detournay E., 2008, *Plane strain propagation of a hydraulic fracture in a permeable rock*, Eng. Fract. Mech., 75, 4666

Adler P. M., Thovert J. F., 1999, *Fractures and fracture networks.* Kluwer

Adler P. M., Thovert J. F., Mourzenko V. M., 2002, *Fractured Porous Media.* Oxford University Press

Agwu O. E., Akpabio J. U., Alabi S. B., Dosunmu A., 2018, *Artificial intelligence techniques and their applications in drilling fluid engineering: A review*, J Petrol Sci Eng, 167, 300

Al-Behadili A., Sellier M., Hewett J. N., Nokes R. I., Moyers-Gonzalez M., 2019, *Identification of Ellis rheological law from free surface velocity*, J. Non-Newton. Fluid Mech., 263, 15

Ali N., Hussain S., Ullah K., Anwar Beg O., 2019, *Mathematical modeling of two-fluid electro-osmotic peristaltic pumping of an Ellis fluid in an axisymmetric tube*, Eur. Phys. J. Plus, 134, 141

Ali N., Abbasi A., Ahmad I., 2021, *Channel flow of Ellis fluid due to peristalsis*, AIP Adv., 5, 097214

Aminu M. D., Nabavi S. A., Rochelle C. A., Manovic V., 2017, *A review of developments in carbon dioxide storage*, Appl. Energy, 208, 1389

Anand V., David J., Christov I. C., 2019, *Non-Newtonian fluid-structure interactions: Static response of a microchannel due to internal flow of a power-law fluid*, J. Non-Newton. Fluid Mech., 264, 62

Andreianov B., Boyer F., Hubert F., 2004, *Finite volume schemes for the p-Laplacian on Cartesian meshes*, ESAIM Math. Model. Num. Anal., 38, 931

Ansari M., Turney D. E., Morris J., Banerjee S., 2021, *Investigations of rheology and a link to microstructure of oil-based drilling fluids*, J Petrol Sci Eng, 196, 108031

Auradou H., Boschan A., Chertcoff R., Gabbanelli S., Hulin J. P., Ippolito I., 2008, *Enhancement of velocity contrasts by shear-thinning solutions flowing in a rough fracture*, J. Non-Newton. Fluid Mech., 153, 53

Balhoff M. T., Miller M. J., 2005, *An Analytical Model for Cleanup of Yield-Stress Fluids in Hydraulic Fractures*, SPE J., 10, 5

Balhoff M., Thompson K., 2006, *A macroscopic model for shear-thinning flow in packed beds based on network modeling*, Chem. Eng. Sci., 61, 698

Barati R., Liang J.-T., 2014, *A review of fracturing fluid systems used for hydraulic fracturing of oil and gas wells*, J. Appl. Polym. Sci., 131, n/a

Barbati A., Desroches J., Robisson A., McKinley G., 2016, *Complex fluids and hydraulic fracturing*, Annu. Rev. Chem. Biomol. Eng., 7, 415

Barenblatt G. I., Entov V. M., Ryzhik V. M., 1990, *Theory of Fluid Flows*

Through Natural Rocks. Springer Netherlands, doi:10.1007/978-94-015-7899-8

Barnsley M. F., Devaney R. L., Mandelbrot B. B., Peitgen H.-O., Saupe D., Voss R. F., 1988, *The Science of Fractal Images.* Springer New York, doi:10.1007/978-1-4612-3784-6

Bear J., 1972, *Dynamics of Fluids in Porous Media.* Elsevier

Bellin A., Salandin P., Rinaldo A., 1992, *Simulation of dispersion in heterogeneous porous formations: Statistics, first-order theories, convergence of computations*, Water Resour. Res., 28, 2211

Benedikt J., Girg P., Kotrla L., Takac P., 2018, *Origin of the p-Laplacian and A. Missbach*, Electron. J. Differ. Equ., 2018, 1

Berkowitz B., 1994, *Advances in porous media.* Elsevier, Amsterdam, pp 397–451

Berkowitz B., 2002, *Characterizing flow and transport in fractured geological media: A review*, Adv. Water Res., 25, 861

Berkowitz B., Scher H., 1998, *Theory of anomalous chemical transport in random fracture networks*, Phys. Rev. E, 57, 5858

Bird Armstrong H., 1987, *Dynamics of Polymeric Liquids.* Vol. 1, John Wiley & Sons, https://www.ebook.de/de/product/3635666/bird_armstrong_hassager_liquids_2e_v1.html

Bird R., Stewart W., Lightfoot E., 2002, *Transport Phenomena. 2nd Edition.* John Wiley & Sons Ltd., New York, http://dx.doi.org/10.1115/1.1424298

Birdsell D., Rajaram H., Viswanathan D. D. H., 2015, *Hydraulic fracturing fluid migration in the subsurface: a review and expanded modeling results*, Water Resour. Res., 37, 1

Boffa J., Allain C., Chertcoff R., Hulin J., Plouraboué F., Roux S., 1999, *Roughness of sandstone fracture surfaces: Profilometry and shadow length investigations*, Eur. Phys. J. B, 7, 179

Boffa J., Allain C., Hulin J., 2000, *Experimental analysis of self-affine fractured rock surfaces through shadow length measurements*, Phys. A, 278, 65

Bolintineanu D. S., Rao R. R., Lechman J. B., Romero J. A., Jove-Colon C. F., Quintana E. C., Bauer S. J., Ingraham M. D., 2017, *Simulations of the effects of proppant placement on the conductivity and mechanical stability of hydraulic fractures*, Int. J. Rock Mech. Min. Sci., 100, 188

Bonnet E., Bour O., Odling N. E., Davy P., Main I., Cowie P., Berkowitz B., 2001, *Scaling of fracture systems in geological media*, Rev. Geophys., 39, 347

Boronin S. A., Osiptsov A. A., Descroches J., 2015, *Displacement of yield-stress fluids in a fracture*, Int. J. Multiph. Flow, 76, 47

Bouchaud E., 1997, *Scaling properties of cracks*, J. Phys.: Condens. Matter, 9, 4319

Bouchaud E., Lapasset G., Planès J., 1990, *Fractal Dimension of Fractured Surfaces: A Universal Value?*, Europhysics Letters (EPL), 13, 73

Bour O., Davy P., 1998, *On the connectivity of three-dimensional fault networks*, Water Resour. Res., 34, 2611

Britt L., 2012, *Fracture stimulation fundamentals*, Journal of Natural Gas Science and Engineering, 8, 34

Brown S. R., 1987, *Fluid flow through rock joints: the effect of surface roughness*, Journal of Geophysical Research: Solid Earth, 92(B2), 1337

Brown S., 1989, *Transport of fluid and electric current through a single fracture*, J. Geophys. Res., 94, 9429

Brown S., 1995, *Simple mathematical model of a rough fracture*, J. Geophys. Res. Solid Earth, 100, 5941

Brown S., Scholz C., 1985, *Broad bandwidth study of the topography of natural rock surfaces*, Geophys. Res..

Brush D. J., Thomson N. R., 2003, *Fluid flow in synthetic rough-walled fractures: Navier-Stokes, Stokes, and local cubic law simulations*, Water Resour Res, 39

Budiansky B., O'Connell R. J., 1976, *Elastic moduli of a cracked solid*, Int. J. Solids Structures, 12, 81

Bächler D., Kohl T., Rybach L., 2003, *Impact of graben-parallel faults on hydrothermal convection––Rhine Graben case study*, Physics and Chemistry of the Earth, Parts A/B/C, 28, 431

Calder J., 2018, *The game theoretic p-Laplacian and semi-supervised learning with few labels*, Nonlinearity, 32, 301

Candela T., Renard F., Bouchon M., Brouste A., Marsan D., Schmittbuhl J., Voisin C., 2009, *Characterization of Fault Roughness at Various Scales: Implications of Three-Dimensional High Resolution Topography Measurements*, Pure Appl. Geophys., 166, 1817

Carreau P. J., 1972, *Rheological Equations from Molecular Network Theories*, Trans. Soc. Rheol., 16, 99

Chen Y., et al., 2016, *Phase behavior and interfacial properties of a switchable ethoxylated amine surfactant at high temperature and effects on CO2-in-water foams*, J. Colloid Interface Sci., 470, 80

Chiapponi L., Ciriello V., Longo S., Di Federico V., 2019, *Non-Newtonian backflow in an elastic fracture*, Water Resour. Res., 55, 10144

Cipolla C. L., Warpinski N. R., Mayerhofer M. J., Lolon E., Vincent M. C., 2008, in All Days. SPE, doi:10.2118/115769-ms

Cipolla C. L., Lolon E. P., Erdle J. C., Rubin B., 2010, *Reservoir Modeling in Shale-Gas Reservoirs*, SPE Reservoir Evaluation & Engineering, 13, 638

Ciriello V., Longo S., Chiapponi L., Di Federico V., 2016, *Porous gravity currents: a survey to determine the joint influence of fluid rheology and variations of medium properties*, Adv. Water Res., 92, 105

Ciriello V., Lenci A., Longo S., Di Federico V., 2021, *Relaxation-induced flow in a smooth fracture for Ellis rheology*, Adv. Water Res., 152, 103914

Clarkson C., Haghshenas B., Ghanizadeh A., Qanbari F., Williams-Kovacs J., Riazi N., Debuhr C., Deglint H., 2016, *Nanopores to megafractures:*

Current challenges and methods for shale gas reservoir and hydraulic fracture characterization, Journal of Natural Gas Science and Engineering, pp 513–535

Comolli A., Hakoun V., Dentz M., 2019, *Mechanisms, Upscaling, and Prediction of Anomalous Dispersion in Heterogeneous Porous Media*, Water Resour. Res., 55, 8197

Cox B., Wang J. S. Y., 1993, *Fractal surfaces:measurement and application in earth sciences*, Fractals, 01, 87

Curtis J. B., 2002, *Fractured shale-gas systems*, AAPG Bulletin, 86

Dana A., Zheng Z., Peng G. G., Stone H. A., Huppert H. E., Ramon G. Z., 2018, *Dynamics of viscous backflow from a model fracture network*, J. Fluid Mech., 836, 828

Dana A., Peng G. G., Stone H. A., Huppert H. E., Ramon G. Z., 2019, *Backflow from a model fracture network: an asymptotic investigation*, J. Fluid Mech., 864, 899

Dejam M., 2019, *Advective-diffusive-reactive solute transport due to non-Newtonian fluid flows in a fracture surrounded by a tight porous medium*, Int. J. Heat Mass Transfer, 128, 1307

Dentz M., Kang P. K., Comolli A., Borgne T. L., Lester D. R., 2016, *Continuous time random walks for the evolution of Lagrangian velocities*, Phys. Rev. Fluids, 1, 074004

Detournay E., 2016, *Mechanics of Hydraulic Fractures*, Annu. Rev. Fluid Mech., 48, 311

Di Federico V., 1997, *Estimates of equivalent aperture for non-Newtonian flow in a rough-walled fracture*, International Journal of Rock Mechanics and Mining Sciences and Geomechanics Abstracts, 34, 1133

Di Federico V., 1998, *Non-Newtonian flow in a variable aperture fracture*, Transp. Porous Media, 30, 75

Di Federico V., 2001, *On non-Newtonian fluid flow in rough fractures*, Water Resour. Res., 37, 2425

Diaz J. I., De Thelin F., 1994, *On a nonlinear parabolic problem arising in some models related to turbulent flows*, SIAM J. Math. Anal., 25, 1085

Dontsov E., 2019, *Scaling laws for hydraulic fractures driven by a power-law fluid in homogeneous anisotropic rocks*, Int J Numer Anal Methods Geomech., 43, 519

Dowell N. M., Fennell P. S., Shah N., Maitland G. C., 2017, *The role of CO2 capture and utilization in mitigating climate change*, Nat Clim Change, 7, 243

Durham W., Bonner B., 1995, in Myer L., Tsang C., Cook N., Goodman R., eds, Fractured and Jointed Rock Masses. Proceedings of the conference of fractured and jointed rock masses. Lake Tahoe, California, USA, pp 441–446

Economides M., 2000, *Reservoir stimulation.* Wiley, Chichester, England New York

Economides M., Mikhailov D., Nikolaevskiy V., 2007, *On the problem of fluid leakoff during hydraulic fracturing*, Transp. Porous Media, 67, 487

Elsworth D., Goodman R., 1986, *Characterization of rock fissure hydraulic conductivity using idealized wall roughness profiles*, Int. J. Rock Mech. Min. Sci. Geomech. Abs., 23, 233

Engelder T., Scholz C. H., 1981, in et al. N. L. C., ed., AGU, Vol. 24, Mechanical Behavior of Crystal Rocks. Geophys. Monogr. Ser., Washington D. C., pp 147–152

Escudier M., Gouldson I., Pereira A., Pinho F., Poole R., 2001, *On the reproducibility of the rheology of shear-thinning liquids*, J. Non-Newton. Fluid Mech., 97, 99

Ezulike O., Dehghanpour H., Virues C., Hawkes R. V., Jones R. Steven J., 2016, *Flowback Fracture Closure: A Key Factor for Estimating Effective Pore Volume*, SPE Reservoir Evaluation & Engineering, 19, 567

Facca E., Cardin F., Putti M., 2021, *Branching structures emerging from a continuous optimal transport model*, J. Comput. Phys., p. 110700

Felisa G., Lenci A., Lauriola I., Longo S., Di Federico V., 2018, *Flow of truncated power-law fluid in fracture channels of variable aperture*, Adv. Water Resour., 122, 317

Feng Y., Gray K., 2017, *Review of fundamental studies on lost circulation and wellbore strengthening*, J Petrol Sci Eng, 152, 511

Firdaouss M., Guermond J.-L., Le Quéré P., 1997, *Nonlinear corrections to Darcy's law at low Reynolds numbers*, J. Fluid Mech., 343, 331

Fisher M. K., Warpinski N. R., 2012, *Hydraulic-Fracture-Height Growth: Real Data*, SPE Production & Operations, 27, 8

Fournier A., Fussell D., Carpenter L., 1982, *Computer rendering of stochastic models*, Comm. ACM, 25, 371

Frigaard I. A., Howison S. D., Sobey I. J., 1994, *On the stability of Poiseuille flow of a Bingham fluid*, J. Fluid Mech., 263, 133

Gale J. E., 1982, in Proceedings at 23rd Symposium on Rock Mechanics. Berkeley, California, pp 290–298

Gale J., 1990, *Rock joints.* Brookfield, pp 351–362

Gale J. F., Laubach S. E., Olson J. E., Eichhuble P., Fall A., 2014, *Natural Fractures in shale: A review and new observations*, AAPG Bulletin, 98, 2165

Garagash D. I., 2006, *Transient solution for a plane-strain fracture driven by a shear-thinning, power-law fluid*, Int. J. Numer. Anal. Meth. Geomech., 30, 1439

Ghanbari E., Dehghanpour H., 2016, *The fate of fracturing water: A field and simulation study*, Fuel, 163, 282

Glover P. W. J., Matsuki K., Hikima R., Hayashi K., 1998, *Fluid flow in synthetic rough gractures and application to the Hachimantai geothermal hot rock test site*, Journal of Geophysical Research: Solid Earth, 103(B5), 9621

Gómez-Hernández J., Wen X.-H., 1998, *To be or not to be multi-Gaussian? A reflection on stochastic hydrogeology*, Adv. Water Res., 21, 47

Gradshteyn I. S., Ryzhik I. M., 2014, *Table of integrals, series, and products.* Academic Press

Gutfraind R., Ippolito I., Hansen A., 1995, *Study of tracer dispersion in self-affine fractures using lattice–gas automata*, Phys. Fluids, 7, 1938

Hakami E., Larsson E., 1996, *Aperture measurements and flow experiments on a single natural fracture*, Int. J. Rock Mech. Min. Sci. Geomech. Abs., 33, 395

Hakoun V., Comolli A., Dentz M., 2019, *Upscaling and Prediction of Lagrangian Velocity Dynamics in Heterogeneous Porous Media*, Water Resour. Res., 55, 3976

Hayek M., RamaRao B. S., Lavenue M., 2020, *An Adjoint Sensitivity Model for Transient Sequentially Coupled Radionuclide Transport in Porous Media*, Water Resour. Res., 56

Hirasaki G. J., Miller C. A., Puerto M., 2011, *Recent Advances in Surfactant EOR*, SPE Journal, 16, 889

Hofmann H., Weides S., Babadagli T., Zimmermann G., Moeck I., Majorowicz J., Unsworth M., 2014, *Potential for enhanced geothermal systems in Alberta, Canada*, Energy, 69, 578

Holditch S., 2007, *Hydraulic fracturing: Overview, trends, issues*, Drilling contractor, July-August 2007, 116

Hormozi S., Frigaard I. A., 2017, *Dispersion of solids in fracturing flows of yield stress fluids*, J. Fluid Mech., 830, 93

Hron J., Malek J., Turek S., 2000, *A numerical investigation of flows of shear-thinning fluids with applications to blood rheology*, Int. J. Numer. Methods Fluids, 32, 863

Huang J., Griffiths D. V., Wong S. W., 2011, *Characterizing natural-fracture permeability from mud-loss data*, SPE J., 16, 111

Huang J., Hu J., Zeng W., Zhang Y., 2019, *Investigation of a critical choke during hydraulic-fracture flowback for a tight sandstone gas reservoir*, J Geophys Eng, 16, 1178

Hyman J., et al., 2016, *Understanding hydraulic fracturing: a multi-scale problem*, Philos. Trans. R. Soc. A: Math. Phys. Eng. Sci., 374, 20150426

Ipatova A., Chuprakov D., 2020, *Role of Preexisting Rock Discontinuities in Fracturing Fluid Leakoff and Flowback*, Transp. Porous Media, 135, 137

Jung R., 1989, *Hydraulic in situ investigations of an artificial fracture in the Falkenberg granite*, Int. J. Rock Mech. Min. Sci. Geomech. Abs., 26, 301

Jung H. B., et al., 2015, *Stimuli-responsive/rheoreversible hydraulic fracturing fluids as a greener alternative to support geothermal and fossil energy production*, Green Chem., 17, 2799

Katiyar A., Agrawal S., Ouchi H., Seleson P., Foster J. T., Sharma M. M., 2020, *A general peridynamics model for multiphase transport of non-Newtonian compressible fluids in porous media*, J. Comput. Phys., 402, 109075

Kelley C. T., 1987, *Iterative Methods for Linear and Nonlinear Equations:*. CAMBRIDGE, https://www.ebook.de/de/product/5993482/c_t_kelley_iterative_methods_for_linear_and_nonlinear_equations.html

Kerr A. D., 1964, *Elastic and Viscoelastic Foundation Models*, J. Appl. Mech., 31, 491

Kobchenko M., Hafver A., Jettestuen E., Galland O., Renard F., Meakin P., Jamtveit B., Dysthe D. K., 2013, *Drainage fracture networks in elastic solids with internal fluid generation*, EPL (Europhysics Letters), 102, 66002

Koranne S., 2010, in , Handbook of Open Source Tools. Springer US, pp 191–200, doi:10.1007/978-1-4419-7719-9˙10

Koyama T., Neretnieks I., Jing L., 2008, *A numerical study on differences in using Navier–Stokes and Reynolds equations for modeling the fluid flow and particle transport in single rock fractures with shear*, Int. J. Rock Mech. Min. Sci., 45, 1082

Lai C.-Y., Zheng Z., Dressaire E., Ramon G., Huppert H., Stone H., 2016, *Elastic Relaxation of Fluid-Driven Cracks and the Resulting Backflow*, Phys. Rev. Lett., 15, 24

Lakhtychkin A., Eskin D., Vinogradov O., 2012, *Modelling of transport of two proppant-laden immiscible power-law fluids through an expanding fracture*, The Canadian Journal of Chemical Engineering, 90, 528

Larson R. G., 1992, *Instabilities in viscoelastic flows*, Rheol. Acta, 31, 213

Lavrov A., 2014, *Radial Flow of Non-Newtonian Power-Law Fluid in a Rough-Walled Fracture: Effect of Fluid Rheology*, Transp. Porous Media, 105, 559

Lavrov A., 2015, *Flow of truncated power-law fluid between parallel plates for hydraulic fracturing applications*, Journal of Non-Newtonian Fluid Mechanics, 223, 141

Lavrov A., 2013a, *Numerical modeling of steady-state flow of a non-Newtonian power-law fluid in a rough-walled fracture*, Comput. Geotech., 50, 101

Lavrov A., 2013b, *Redirection and channelization of power-law fluid flow in a rough walled fracture*, Chem. Eng. Sci., 99, 81

Lenci A., Chiapponi L., 2020, *An Experimental Setup to Investigate Non-Newtonian Fluid Flow in Variable Aperture Channels*, Water, 12, 1284

Lenci A., Di Federico V., 2020, *A Channel Model for Bi-viscous Fluid Flow in Fractures*, Transport Porous Med, 134, 97

Lenci A., Federico V. D., 2019, *Shear-Thinning Fluid Flow in Variable-Aperture Channels*, Water, 48, 28

Lenci A., Chiapponi L., Longo S., Di Federico V., 2021, *Experimental investigation on backflow of power-law fluids in planar fractures*, Phys. Fluids

Lenci A., Méheust Y., Putti M., Di Federico V., 2022a, *A Lubrication-based Flow Solver for Shear-thinning Fluids in Geological Gractures*, Water Resour. Res. [In preparation]

Lenci A., Putti M., Méheust Y., Di Federico V., 2022b, *Monte Carlo Simulations of Shear-thinning Flow in Geological Fractures*, Water Resour. Res. [In preparation]

Lester Y., Yacob T., Morrissey I., Linden K. G., 2014, *Can We Treat Hydraulic Fracturing Flowback with a Conventional Biological Process? The Case of Guar Gum*, Environ. Sci. Technol. Lett., 1, 133

Leung D. Y., Caramanna G., Maroto-Valer M. M., 2014, *An overview of current status of carbon dioxide capture and storage technologies*, Renewable Sustainable Energy Rev., 39, 426

Li B., Jiang Y., Koyama T., Jing L., Tanabashi Y., 2008, *Experimental study of the hydro-mechanical behavior of rock joints using a parallel-plate model containing contact areas and artificial fractures*, Int. J. Rock Mech. Min. Sci., 45, 362

Li C., Huang Y., Sun X., Gao R., Zeng F., Tontiwachwuthikul P., Liang Z., 2017, *Rheological properties study of foam fracturing fluid using CO 2 and surfactant*, Chem. Eng. Sci., 170, 720

Linkov A. M., 2014, *On comparison of thinning fluids used for hydraulic fracturing*, Internat. J. Engrg. Sci., 10, 14

Liu H.-H., Bodvarsson G. S., Lu S., Molz F. J., 2004, *A Corrected and Generalized Successive Random Additions Algorithm for Simulating Fractional Levy Motions*, Math. Geol., 36, 361

Loisel S., 2020, *Efficient algorithms for solving the p-Laplacian in polynomial time*, Numer. Math., 146, 369

Longo S., Di Federico V., 2015, *Unsteady flow of shear-thinning fluids in porous media with pressure-dependent properties*, Transp. Porous Media, 110, 429

Longo S., Di Federico V., Chiapponi L., 2015, *A dipole solution for power-law gravity currents in porous formations*, J. Fluid Mech., 778, 534

Lu S.-M., 2018, *A global review of enhanced geothermal system (EGS)*, Renewable Sustainable Energy Rev., 81, 2902

Lu S., Molz F., Liu H., 2003, *An efficient, three-dimensional, anisotropic, fractional Brownian motion and truncated fractional Levy motion simulation algorithm based on successive random additions*, Comput. Geotech., 29, 15

Lyakhovsky V., Reches Z., Weinberger R., Scott T. E., 1997, *Non-linear elastic behaviour of damaged rocks*, Geophys. J. Int., 130, 157

Magzoub M., Salehi S., Li G., Fan J., Teodoriu C., 2021, *Loss circulation prevention in geothermal drilling by shape memory polymer*, Geothermics, 89, 101943

Makurat A., 1985, *The effect of shear displacement on the permeability of natural rough joints*. pp 99–106

Massey B. S., 1971, *Units, dimensional analysis and physical similarity*. Van Nostrand Reinhold

Matsumoto M., Nishimura T., 1998, *Mersenne twister*, ACM Transactions on Modeling and Computer Simulation, 8, 3

Mazzia A., Manzini G., Putti M., 2011, *Bad behavior of Godunov mixed methods for strongly anisotropic advection–dispersion equations*, J Comput Phys, 230, 8410

McLennan J., Walton I., Moore J., Brinton D., Lund J., 2015, *Proppant backflow: Mechanical and flow considerations*, Geothermics, 57, 224

Meakin P., Tartakovsky A. M., 2009, *Modeling and simulation of pore-scale multiphase fluid flow and reactive transport in fractured and porous media*, Rev. Geophys., 47

Medina R., Elkhoury J. E., Morris J. P., Prioul R., Desroches J., Detwiler R. L., 2015, *Flow of concentrated suspensions through fractures: small variations in solid concentration cause significant in-plane velocity variations*, Geofluids, 15, 24

Medina R., Detwiler R., Prioul R., Xu W., Elkhoury J., 2019, *Settling and Mobilization of Sand-Fiber Proppants in a Deformable Fracture*, Water Resour. Res., 54, 9964

Méheust Y., Schmittbuhl J., 2000, *Flow enhancement of a rough fracture*, Geophys. Res. Lett., 27, 2989

Méheust Y., Schmittbuhl J., 2001, *Geometrical heterogeneities and permeability anisotropy of rough fractures*, Journal of Geophysical Research: Solid Earth, 106, 2089

Méheust Y., Schmittbuhl J., 2003, *Scale Effects Related to Flow in Rough Fractures*, Pure Appl. Geophys., 160, 1023

Méheust Y., Parmar K. P. S., Schjelderupsen B., Fossum J. O., 2011, *The electrorheology of suspensions consisting of Na-fluorohectorite synthetic clay particles in silicon oil*, J. Rheol, 55, 809

Mikhailov D., Economides M., Nikolaevskiy V., 2011, *Fluid leakoff determines hydraulic fracture dimensions: Approximate solution for non-Newtonian fracturing fluid*, Internat. J. Engrg. Sci., 49, 809

Moreno L., Tsang Y. W., Tsang C. F., Hale F. V., Neretnieks I., 1988, *Flow and tracer transport in a single fracture: a stochastic model and its relation to some field observations*, Water Resour. Res., 24(12), 2033

Morris J. P., Chochua G. G., Bogdan A. V., 2015, *An Efficient Non-Newtonian Fluid-Flow Simulator for Variable Aperture Fractures*, The Canadian Journal of Chemical Engineering, 93, 1902

Moukhtari F.-E., Lecampion B., 2018, *A semi-infinite hydraulic fracture driven by a shear-thinning fluid*, J. Fluid Mech., 838, 573

Mourzenko V. V., Thovert J.-F., Adler P. M., 1995, *Permeability of a Single Fracture: Validity of the Reynolds Equation*, Journal de Physique II, 5, 465

Mourzenko V. V., Thovert J. F., Adler P., 2001, *Permeability of self-affine fractures*, Transp. Porous Media, 45(1), 89

Muggeridge A., Cockin A., Webb K., Frampton H., Collins I., Moulds T., Salino P., 2014, *Recovery rates, enhanced oil recovery and technological limits*, Philos. Trans. R. Soc. A: Math. Phys. Eng. Sci., 372, 20120320

Mulligan C., Yong R., Gibbs B., 2001, *Surfactant-enhanced remediation of contaminated soil: a review*, Eng. Geol., 60, 371

Myers T. G., 2005, *Application of non-Newtonian models to thin film flow*, PRE, 72, 066302

Neretnieks I., 1985, in Memories of the 17th International Congress of International Association of Hydrologist. Tucson, Arizona, pp 3011–3018

Neuman S. P., 2005, *Trends, prospects and challenges in quantifying flow and transport through fractured rocks*, Hydrol. J., 13, 124

Neuzil C., Tracy J., 1981, *Flow Through Fractures*, Water Resour. Res., 17(1), 191

Nguyen T. Q., Kausch H.-H., 1992, in , Macromolecules: Synthesis, Order and Advanced Properties. Springer, pp 73–182

Nigon B., Englert A., Pascal C., Saintot A., 2017, *Multiscale Characterization of Joint Surface Roughness*, Journal of Geophysical Research: Solid Earth, 122, 9714

Nowamooz A., Radilla G., Fourar M., Berkowitz B., 2013, *Non-Fickian Transport in Transparent Replicas of Rough-Walled Rock Fractures*, Transp. Porous Media, 98, 651

Oron A. P., Berkowitz B., 1998, *Flow in rock fractures: The local cubic law assumption reexamined*, Water Resour. Res., 34, 2811

Osiptov A., 2017, *Fluid Mechanics of Hydraulic Fracturing: a Review*, J Petrol Sci Eng, 156, 513

Ozdemirtas M., Kuru E., Babadagli T., 2010, *Experimental investigation of borehole ballooning due to flow of non-Newtonian fluids into fractured rock*, Int. J. Rock Mech. Min. Sci., 47, 1200

Pahari S., Bhandakkar P., Akbulut M., Kwon J. S.-I., 2021, *Optimal pumping schedule with high-viscosity gel for uniform distribution of proppant in unconventional reservoirs*, Energy, 216, 119231

Parmar K. P. S., Méheust Y., Fossum J. O., 2008, *Electrorheological suspensions of laponite in oil: rheometry studies*, Langmuir, 24, 1814

Pascal H., 1983, *Nonsteady flow of non-Newtonian fluids through a porous medium*, Internat. J. Engrg. Sci., 21, 199

Pereira L., Lecampion B., 2021, *A plane-strain hydraulic fracture driven by a shear-thinning Carreau fluid*, Int. J. Numer. Anal. Methods Geomech.

Perkowska M., Wrobel M., Mishuris G., 2016, *Universal hydrofracturing algorithm for shear-thinning fluids: Particle velocity based simulation*, Comput. Geotech., 71, 310

Philip J. R., 1961, *N-diffusion*, Austr. J. Phys., 14, 1

Plouraboué F., Kurowski P., Hulin J.-P., Roux S., Schmittbuhl J., 1995, *Aperture of rough cracks*, Phys. Rev. E, 51, 1675

Plouraboué F., Hulin J.-P., Roux S., Koplik J., 1998, *Numerical study of geometrical dispersion in self-affine rough fractures*, Phys. Rev. E, 58, 3334

Plouraboué F., Kurowski P., Boffa J.-M., Hulin J.-P., Roux S., 2000, *Experi-

mental study of the transport properties of rough self-affine fractures, J. Contam. Hydrol., 46, 295

Puyguiraud A., Gouze P., Dentz M., 2019a, *Stochastic Dynamics of Lagrangian Pore-Scale Velocities in Three-Dimensional Porous Media*, Water Resour. Res., 55, 1196

Puyguiraud A., Gouze P., Dentz M., 2019b, *Upscaling of Anomalous Pore-Scale Dispersion*, Transp. Porous Media, 128, 837

Quosay A. A., Knez D., Ziaja J., 2020, *Hydraulic fracturing: New uncertainty based modeling approach for process design using Monte Carlo simulation technique*, PLOS One, 15, 1

Rahman M. M., Rahman S. S., 2013, *Studies of Hydraulic Fracture-Propagation Behavior in Presence of Natural Fractures: Fully Coupled Fractured-Reservoir Modeling in Poroelastic Environments*, Int. J. Geomech., 13, 809

Robson G. R., 1967, *Thickness of Etnean Lavas*, Nature, 216, 251

Rodríguez de Castro A., Radilla G., 2016, *Non-Darcian flow experiments of shear-thinning fluids through rough-walled rock fractures*, Water Resour. Res., 52, 9020

Rodríguez de Castro A., Radilla G., 2017, *Flow of yield stress and Carreau fluids through rough-walled rock fractures: Prediction and experiments*, Water Resour. Res., 53, 6197

Roustaei A., Chevalier T., Talon L., Frigaard I., 2016, *Non-Darcy effects in fracture flows of a yield stress fluid*, J. Fluid Mech., 805, 222

Rozenbaum O., du Roscoat S. R., 2014, *Representative elementary volume assessment of three-dimensional x-ray microtomography images of heterogeneous materials: Application to limestones*, Phys. Rev. E, 89, 053304

Sahai R., Moghanloo R. G., 2019, *Proppant transport in complex fracture networks - A review*, J Petrol Sci Eng, 182, 106199

Sahimi M., 1993, *Flow phenomena in rocks: from continuum models to fractals, percolation, cellular automata, and simulated annealing*, Rev. Mod. Phys., 65, 1393

Sahimi M., 2011, *Flow and transport in porous media and fractured rock: from classical methods to modern approaches*, 2nd edition edn. Wiley

Sanner B., Karytsas C., Mendrinos D., Rybach L., 2003, *Current status of ground source heat pumps and underground thermal energy storage in Europe*, Geothermics, 32, 579

Saupe D., 1988, in , The Science of Fractal Images. Springer New York, pp 71–136, doi:10.1007/978-1-4612-3784-6˙2

Schmittbuhl J., Gentier S., Roux S., 1993, *Field measurements of the roughness of fault surfaces*, Geophys. Res. Lett., 20, 639

Schmittbuhl J., Vilotte J.-P., Roux S., 1995a, *Reliability of self-affine measurements*, Phys. Rev. E, 51, 131

Schmittbuhl J., Schmitt F., Scholz C., 1995b, *Scaling invariance of crack surfaces*, Journal of Geophysical Research: Solid Earth, 100, 5953

Shah S., Shanker N. H., Ogugbue C. C., 2010, in 2010 AADE Fluids Conference and Exhibition. Houston, Texas

Sheng G., Su Y., Wang W., 2019, *A new fractal approach for describing induced-fracture porosity/permeability/ compressibility in stimulated unconventional reservoirs*, J Petrol Sci Eng, 179, 855

Siena M., Riva M., Hyman J. D., Winter C. L., Guadagnini A., 2014, *Relationship between pore size and velocity probability distributions in stochastically generated porous media*, Phys. Rev. E, 89, 013018

Silliman S. E., 1989, *An interpretation of the difference between aperture estimates derived from hydraulic and tracer tests in a single fracture*, Water Resour. Res., 25, 2275

Singer A., 2006, *From graph to manifold Laplacian: The convergence rate*, Appl. Comput. Harmon. Anal., 21, 128

Skelland A. H. P., 1967, *Non-Newtonian Flow and Heat Transfer*. John Wiley and Sons, Inc.

Snow D., 1970, *The frequency and apertures of fractures in rock*, Int. J. Rock Mech. Min. Sci. Geomech. Abs., 7, 23

Sochi T., 2010, *Non-Newtonian flow in porous media*, Polymer, 51, 5007

Sousa R., Riethmuller M., Pinto A., Campos J., 2005, *Flow around individual Taylor bubbles rising in stagnant CMC solutions: PIV measurements*, Chem. Eng. Sci., 60, 1859

Starchenko V., Marra C. J., Ladd A. J. C., 2016, *Three-dimensional simulations of fracture dissolution*, Journal of Geophysical Research: Solid Earth, 121, 6421

Steller R. T., 2001, *Generalized slit flow of an Ellis fluid*, Polym Eng Sci, 41, 1859

Stockman H. W., 1997, *A lattice gas study of retardation and dispersion in fractures: Assessment of errors from desorption kinetics and buoyancy*, Water Resour. Res., 33, 1823

Suleimanov B., Ismailov F., Veliyev E., 2011, *Nanofluid for enhanced oil recovery*, J Petrol Sci Eng, 78, 431

Sullivan S., Gladden L., Johns M., 2006, *Simulation of power-law fluid flow through porous media using lattice Boltzmann techniques*, J. Non-Newton. Fluid Mech., 133, 91

Talon L., Auradou H., Hansen A., 2010, *Permeability of self-affine aperture fields*, Phys. Rev. E, 82, 046108

Tian Z., Wang J., 2017, *Lattice Boltzmann simulation of CO2 reactive transport in network fractured media*, Water Resour. Res., 53, 7366

Tsang Y. W., 1984, *The Effect of Tortuosity on Fluid Flow Through a Single Fracture*, Water Resour. Res., 20(9), 1209

Tsang Y. W., 1992, *Usage of "Equivalent Apertures" for Rock Fractures as Derived From Hydraulic and Tracer Tests*, Water Resour. Res., 28, 1451

Tsang Y., Tsang C., 1987, *Channel model of flow through fractured media*, Water Resour. Res., 23, 467

Tsang Y. W., Tsang C. F., 1989, *Flow channeling in a single fracture as a two-*

dimensional strongly heterogeneous permeable medium, Water Resour. Res., 25(9), 2076

Tsang Y. W., Tsang C. F., Neretnieks I., Moreno L., 1988, *Flow and tracer transport in fractured media: a variable aperture channel model and its properties*, Water Resour. Res., 24(12), 2049

Uddin J., Marston J. O., Thoroddsen S. T., 2012, *Squeeze flow of a Carreau fluid during sphere impact*, Phys. Fluids, 24, 073104

Valdés-Parada F. J., Lasseux D., 2021, *Flow near porous media boundaries including inertia and slip: A one-domain approach*, Phys. Fluids, 33, 073612

Velásquez-Parra A., Aquino T., Willmann M., Méheust Y., Le Borgne T., Jiménez-Martínez J., 2021, *Sharp transition to strongly anomalous transport in unsaturated porous media*, Geophys Res Lett, p. e2021GL096280

Voss R. F., 1988, in Peitgen H. O., Saupe D., eds, , The Science of Fractal Images. Springer New York, Chapt. Fractals in nature: From characterization to simulation, pp 21–70, doi:10.1007/978-1-4612-3784-6˙1

Walker G. P. L., 1967, *Thickness and Viscosity of Etnean Lavas*, Nature, 213, 484

Wang M., Chen Y.-F., Ma G.-W., Zhou J.-Q., Zhou C.-B., 2016a, *Influence of surface roughness on nonlinear flow behaviors in 3D self-affine rough fractures: Lattice Boltzmann simulations*, Adv. Water Resour., 96, 373

Wang S., Tang H., Guo J., Wang K., 2016b, *Effect of pH on the rheological properties of borate crosslinked hydroxypropyl guar gum hydrogel and hydroxypropyl guar gum*, Carbohydr. Polym., 147, 455

Wang J., Elsworth D., Denison M. K., 2018a, *Hydraulic fracturing with leakoff in a pressure-sensitive dual porosity medium*, Int. J. Rock Mech. Min. Sci., 107, 55

Wang F., Pan Z., Zhang Y., Zhang S., 2018b, *Simulation of coupled hydro-mechanical-chemical phenomena in hydraulically fractured gas shale during fracturing-fluid flowback*, J Petrol Sci Eng, 163, 16

Wilson C. R., Witherspoon P. A., 1974, *Steady state flow in rigid networks of fractures*, Water Resour. Res., 10, 328

Wolfram 2020, http://functions.wolfram.com/HypergeometricFunctions

Wrobel M., 2020, *On the application of simplified rheological models of fluid in the hydraulic fracture problems*, Internat. J. Engrg. Sci., 150, 103275

Wrobel M., Mishuris G., Papanastasiou P., 2021, *On the influence of fluid rheology on hydraulic fracture*, Internat. J. Engrg. Sci., 158

Yalamanchili R., Sirivat A., Rajagopal K., 1995, *An experimental investigation of the flow of dilute polymer solutions through corrugated channels*, J. Non-Newtonian Fluid Mech., 58, 243

Yan Y., Koplik J., 2008, *Flow of power-law fluids in self-affine fracture channels*, Phys. Rev. E, 77, 036315

Yang H. J., Boso F., Tchelepi H. A., Tartakovsky D. M., 2020, *Method of*

Distributions for Quantification of Geologic Uncertainty in Flow Simulations, Water Resour. Res., 56

Yao C., Jiang Q. H., Shao J. F., 2015, *A Numerical Analysis of Permeability Evolution in Rocks with Multiple Fractures*, Transp. Porous Media, 108, 289

Yasuda K., Armstrong R. C., Cohen R. E., 1981, *Shear flow properties of concentrated solutions of linear and star branched polystyrenes*, Rheol. Acta, 20, 163

Yeo I., de Freitas M., Zimmerman R., 1998, *Effect of shear displacement on the aperture and permeability of a rock fracture*, Int. J. Rock Mech. Min. Sci., 35, 1051

Zami-Pierre F., de Loubens R., Quintard M., Davit Y., 2016, *Transition in the Flow of Power-Law Fluids through Isotropic Porous Media*, Phys. Rev. Lett., 117, 074502

Zanganeh B., Ahmadi M., Hanks C., Awoleke O., 2015, *The role of hydraulic fracture geometry and conductivity profile, unpropped zone conductivity and fracturing fluid flowback on production performance of shale oil wells*, Journal of Unconventional Oil and Gas Resources, 9, 103

Zeng J., Li H., Zhang D., 2016, *Numerical simulation of proppant transport in hydraulic fracture with the upscaling CFD-DEM method*, Journal of Natural Gas Science and Engineering, 33, 264

Zhang M., Prodanović M., Mirabolghasemi M., Zhao J., 2019, *3D Microscale Flow Simulation of Shear-Thinning Fluids in a Rough Fracture*, Transp. Porous Media, 128, 243

Zhong Z., Sun A. Y., Jeong H., 2019, *Predicting CO 2 Plume Migration in Heterogeneous Formations Using Conditional Deep Convolutional Generative Adversarial Network*, Water Resour. Res., 55, 5830

Zhu Z., Liu J., Liu H., Wu M., Song Z., 2021, *Numerical investigation of single- and two-phase flow in porous media with a bifurcated fracture*, Phys. Fluids, 33, 052117

Zimmerman R. W., Bodvarsson G. S., 1996, *Hydraulic Conductivity of Rock Fractures*, Transp. Porous Media, 23, 1

Zimmerman R., Kumar S., Bodvarsson G., 1991, *Lubrification theory analysis of the permeability of rough-walled fractures*, International Journal of Rock Mechanics and Mining Sciences & Geomechanics Abstracts, 28(4), 325

de Anna P., Quaife B., Biros G., Juanes R., 2017, *Prediction of the low-velocity distribution from the pore structure in simple porous media*, Phys. Rev. Fluids, 2, 124103

de Dreuzy J.-R., Davy P., Bour O., 2002, *Hydraulic properties of two-dimensional random fracture networks following power law distributions of length and aperture*, Water Resour Res, 38, 12

de Dreuzy J.-R., Méheust Y., Pichot G., 2012, *Influence of fracture scale heterogeneity on the flow properties of three-dimensional discrete fracture networks (DFN)*, J. Geophys. Res.: Solid Earth, 117, n/a